

SuperNova / Acceleration Probe (SNAP)

An Experiment to Measure the Properties of the Dark
Energy of the Universe

A Letter of Intent to the Department of Energy
and the National Science Foundation

The Institutions of the SNAP Collaboration

Lawrence Berkeley National Laboratory, Berkeley, CA
Space Sciences Laboratory, Berkeley, CA
CNRS-IN2P3, LPNHE, and College de France, France
University of Maryland, College Park, MD
University of California, Berkeley, CA
University of Chicago, Chicago, IL
Space Telescope Sciences Institute, Baltimore, MD
California Institute of Technology, Pasadena, CA
Gemini Observatory, Hilo, HI
European Southern Observatory
University of Stockholm
University of Lisbon

November 24, 1999

Version 1.0

The SNAP Collaboration and authors of this Preview are

S. Perlmutter (PI), M. Levi (co-PI), G. Aldering, S. Deustua, W. Edwards, B. Frye,
S. Holland, D. Kasen, A. Kim, R. Knop, R. Lafever, P. Nugent, K. Robinson
Lawrence Berkeley National Laboratory, Berkeley, CA, USA

R. Lin, D. Curtis, P. Harvey, H. Heetderks, M. Lampton, D. Pankow,
C. Pennypacker, G. Smoot
Space Sciences Laboratory, Berkeley, CA, USA

R. Pain, P. Astier, J.F. Genat, D. Hardin, J-M. Levy, K. Schamahneche
CNRS-IN2P3, LPNHE, and College de France, France

J. Goodman, D. Baden, D. Roberts, G. Sullivan
University of Maryland, College Park, MD, USA

G. Goldhaber
University of California, Berkeley, CA, USA

D. Huterer
University of Chicago, Chicago, IL, USA **

A. Fruchter
Space Telescope Sciences Institute, Baltimore, MD, USA

R. Ellis
California Institute of Technology, Pasadena, CA, USA

I. Hook
Gemini Observatory, Hilo, HI, USA

C. Lidman
European Southern Observatory

A. Goobar
University of Stockholm

A. Mourao
University of Lisbon

** Faculty participation in negotiation

Contents

I	Executive Summary	1
1	Executive Summary	2
1.1	Abstract	2
1.2	Introduction	2
1.3	Scientific Motivation and Background	3
1.4	Proposed Experiment	8
1.5	Control of Statistical and Systematic Uncertainties	10
1.6	Why a New Satellite?: Design Requirements and Ground/Space-Based Alternatives	13
1.7	Overview of Feasibility	15
1.8	Summary of Other Major Science	16
II	SNAP Physics	18
2	Theoretical Overview	19
2.1	Cosmological Parameters	19
2.2	The Dark Energy	19
3	Summary of Current Results from SNe Ia	23
3.1	Introduction	23
3.2	The Physics of Type Ia Supernova	24
3.2.1	Progenitors to Explosion	24
3.2.2	Light Curves	24
3.2.3	Spectra	25
3.2.4	Environmental Influences	25
3.3	Results from the Observation of Type Ia Supernovae	29
4	Science reach of the proposed satellite	35
4.1	Introduction	35
4.2	Constraining the Cosmological Parameters	35
4.3	Exploring higher redshifts ($z \gtrsim 1$)	36
4.3.1	Constraints on Ω_M and Ω_Λ	37
4.3.2	Breaking the parameter degeneracies	40
4.3.3	Measuring the equation of state of the dark energy	40

4.3.4	Further explorations of the dark sector	44
4.4	Previously Identified Sources of Systematic Uncertainty	44
4.5	Proposed Systematic Error Analysis	47
4.5.1	Gray dust	47
4.5.2	Evolution	48
4.5.3	Observables to Correct or Match SNe	52
4.6	Summary	54
5	Comparisons with Alternatives	57
5.1	Introduction	57
5.2	Advantages of Space-Based Observations	61
5.2.1	Reduced Foreground Emission	61
5.2.2	Reduced Atmospheric Distortion	63
5.2.3	Improved Detection Efficiency	67
5.3	Detailed Comparison of SNAP and Ground-based Viewing	67
5.3.1	Searching with HST or NGST	67
5.3.2	Ground-based searching with follow-up using HST or NGST	69
6	Other Scientific Objectives	71
6.1	Introduction	71
6.2	Type II Supernova	71
6.3	Gravitational Strong Lensing	72
6.4	Gravitational weak lensing	77
6.4.1	Introduction	77
6.4.2	Weak Lensing Basics	80
6.4.3	Cosmological Measurements	81
III	Baseline Instrument Description	86
7	Observational Strategy & Data Package	87
7.1	Overview	87
7.2	Observational Strategy & Data Package	88
7.3	Objectives	91
7.4	Instrument Performance	92
8	Telescope	94
8.1	Optical Requirements	94
8.2	Optical Design	94
8.2.1	One-Mirror with Corrector	94
8.2.2	Two-Mirror Ritchey-Chretien with Correctors	95
8.2.3	Two-Mirror Schwarzschild Telescopes	95
8.2.4	Three-Mirror Telescopes	96
8.2.5	Summary	98
8.3	Active Steering Mirror	101
8.4	Primary Mirror Size	101

8.5	Mirror Technology	102
8.6	Conclusion	103
9	Optical Photometry	104
9.1	Optical Photometer Requirements	104
9.2	Technology	105
9.3	Supernovae Detection	105
9.4	Optical Photometer Performance	106
10	IR Photometry	107
10.1	IR Photometer Requirements	107
10.2	IR Photometer Performance	108
11	Spectroscopy	109
11.1	Optical/IR Spectrograph Requirements and Performance	109
11.1.1	Introduction	109
11.1.2	Achieving Wavelength Coverage with a Three-Arm Spectrograph	109
11.1.3	Resolution Requirements and Constraints	110
11.1.4	Integral Field Unit	112
11.1.5	Optics	114
11.1.6	Dispersive Elements	117
11.1.7	Very Low-resolution NIR Spectroscopy Option	117
11.1.8	Internal Adjustment and Calibration	118
11.2	Spectrograph baseline	118
12	Calibration	121
12.1	Introduction	121
12.2	Imager Photometric Calibration	121
12.2.1	Internal Calibration	121
12.2.2	External Flux Calibration	124
12.2.3	Imager Calibration Summary	127
12.3	Spectrograph Wavelength and Photometric Calibration	127
12.4	Imager Astrometric Calibration	128
12.5	Spectrograph Astrometric Calibration	129
12.6	NIR Imager Calibration	129
12.7	Extinction from Foreground Dust in the Galaxy	130
12.8	Photometric Redshift Calibration	133
13	Electronics	135
13.1	Electronics	135
13.1.1	CCD Clocking	136
13.1.2	Double Correlated Sampling	138
13.1.3	Analog to Digital Conversion	138
13.1.4	Digital Processing	138
13.1.5	Power	139

14	Spacecraft Description	140
14.1	Orbit Properties	140
14.2	Spacecraft Description	142
14.2.1	Power system	143
14.2.2	ACS/Propulsion System	143
14.2.3	Telecommunications System	144
14.2.4	Observatory Control Unit	145
14.2.5	Spacecraft Structure	145
14.3	Launch Vehicle	146
14.4	Observatory Integration and Testing	147
15	Mission Operations	151
15.1	Mission Operations	151
15.2	SNAP Operations	152
15.3	Data Handling & Signal Processing	154
15.4	NERSC	154
IV	Research and Development	155
16	Research and Development Plan	156
16.1	Concept/Mission Definition	156
16.2	Cost & Schedule Preparation	156
16.3	CCD R &D	158
16.4	Electronics R &D	158
16.4.1	Analog to Digital Conversion.	158
16.4.2	Correlated Double Sampler	159
16.4.3	Processors	159
16.5	Instrument R &D	159
16.6	Ground Based Studies of Supernova	159
16.7	Optics Design	160
V	Education/Public Outreach	162
17	Education/Public Outreach	163
17.1	Overview	163
17.2	Program Goals and Objectives	163
17.3	Proposed Education Product	163
17.4	Activity Modules	163
17.5	What are Supernovae?	164
17.6	Activity 1: A Simulation of SNe explosions	164
17.7	Activity 2: Making a Hubble Diagram	164
17.8	Activity 3: Supernova Models	164
17.9	Alignment with E/PO Guidelines	165
17.10	Experience of the E/PO team	165

VI	Project Management	166
18	Management of the Project	167
18.1	Organization and Management Plan	167
18.2	Organization	167
18.2.1	Organization Chart	167
18.2.2	Element Function and Responsibility	167
18.2.3	DOE and NSF Organization	167
18.2.4	SNAP Systems and Subsystems Management	171
18.2.5	Management Processes	172
18.2.6	Schedule	176
18.2.7	Cost	176
A	WBS	188
B	CCD's	191
B.1	Overview	191
B.2	Benefits and Goals	194
B.3	Uniqueness of Fully-Depletion Devices	195
B.4	Comparison of CCD's	196
B.5	Technical features of high-resistivity CCD's	199
B.6	Radiation Tolerance	201
B.7	Cosmic Rays	204
B.8	Packaging with 4-side Abutment	204

List of Tables

1.1	Systematic errors	11
1.2	Observational requirements	14
2.1	Some candidates for the dark energy and their respective equations of state.	21
4.1	SNAP constraints on Ω_M , Ω_Λ and Ω_k compared to those expected from SDSS, MAP, and Planck	39
4.2	Constraints on Ω_M and w assuming a flat universe	43
4.3	Potential systematic errors given SNAPSAT's capabilities.	52
4.4	A list of the observables that constrain the various SNe Ia model parameters.	53
4.5	Host galaxy characteristics.	53
5.1	Alternative Facilities	60
5.2	Comparison of Alternative Facilities to SNAP for Baseline Mission . . .	60
5.3	Atmospheric and Space Foregrounds	61
5.4	Wide-field Imaging Comparison	67
5.5	OH Suppression (Follow-up) Imaging Comparison	68
5.6	AO (Follow-up) Imaging Comparison	68
5.7	AO (Follow-up) Spectroscopy Comparison	69
7.1	Redshifted B-band filters	88
7.2	Summary	93
8.1	SNAP Observatory Requirements	94
9.1	Optical Imager/Photometer Requirements	104
9.2	Observation strategy	105
9.3	Optical Photometry	106
10.1	IR Imager/Photometer Requirements	107
10.2	IR Photometry	108
10.3	IR V-band Photometry	108
11.1	Optical Spectrograph Requirements	119
11.2	IR Spectrograph Requirements	120

11.3 Optical Spectroscopy	120
11.4 IR Spectroscopy	120
12.1 Imager Calibration Error Budget	127
12.2 Survey regions with low zodiacal background	130
13.1 Power consumption of CCD readout chain.	139
14.1 Orbit Trade Study Matrix	140
14.2 Attitude control system components	144
14.3 Propulsion system components	144
18.1 SNAP Rough Order Cost Estimate (FY'00\$) Does not include Launch, Launch Vehicle, Spacecraft Bus or OPS/Ground Support	178
18.2 Funding By Fiscal Year (excludes launch and spacecraft)	178
B.1 LBNL $2k \times 2k$ ($15 \mu\text{m}$) ² CCD's as compared with other detectors.	198
B.2 Prometheus Orbit Cosmic Ray Hit Rate	204

List of Figures

1.1	Ω_M — Ω_Λ confidence regions with the current data and with SNAP . . .	5
1.2	Confidence regions in the Ω_M — w plane	7
3.1	Stretch luminosity relationship.	26
3.2	Observed M_B vs. $\mathcal{R}(\text{Si II})$ and $\mathcal{R}(\text{Ca II})$	27
3.3	Spectral temporal evolution of a SN Ia	28
3.4	Metallicity effects in the UV.	30
3.5	Metallicity effects in the optical.	31
3.6	Hubble diagram for 42 high- z SNe	33
3.7	Ω_M — w confidence region	34
4.1	Parameter estimation as a function of maximum redshift	36
4.2	Constraints on parameters Ω_M and Ω_Λ expected from the proposed experiment in a closed universe	38
4.3	Degeneracy breaking in quintessence models	41
4.4	SNAP constraint on parameters Ω_M and w	42
4.5	Quintessence model potential and equation of state reconstruction . . .	45
4.6	Gray Dust FIR Emission	49
4.7	The distribution of restframe B -band magnitude residuals from the best- fit flat cosmology	50
4.8	Peak-to-tail light curve differences.	55
4.9	Metal Abundances of Nearby and Distant Galaxies	56
5.1	Ground and HST Images of a Distant SN	58
5.2	High Redshift SN Discoveries	59
5.3	Atmospheric Emission	62
5.4	Atmospheric Absorption	64
5.5	Ground-Based Image Quality - Optical	65
5.6	Ground-Based Image Quality - NIR	66
6.1	SNe II fit	73
6.2	Thin Lens Diagram	75
6.3	HDFS Gravitational Lens	76
6.4	Microlensing Detectability	78
6.5	Strong lensing by A1689	79
6.6	HST Galaxy Sizes	82

6.7	Weak Lensing Power Spectrum	84
6.8	Weak Lensing Constraints on Ω and Λ	85
7.1	B-band Light-curve for Type Ia Supernovae	89
7.2	SN Ia spectrum with B-band bandpass superimposed.	90
8.1	Example of a 2 meter Ritchey-Chretien.	95
8.2	A Paul-Baker three mirror design.	97
8.3	A Korsch design.	97
8.4	DMT Telescope.	99
8.5	New Planetary Telescope	100
11.1	KAST Spectrograph Layout	111
11.2	Spectral Resolution Trade-Offs	113
11.3	Durham IFU	115
11.4	Durham IFU Pseudo-Slit	116
11.5	NIR Dispersive Element	118
12.1	SNAP imager star counts.	125
12.2	Northern Galactic dustmap.	131
12.3	Southern Galactic dust map	132
13.1	CCD Array Readout Chain.	136
13.2	Analog readout electronics.	137
13.3	Correlated Double Sampling chain Block-Diagram.	137
14.1	Lunar assisted “Prometheus” orbit.	141
14.2	Block diagram of the relationship between the science payload and the spacecraft subsystems.	142
14.3	Planetary mission capability of the Delta III rocket	146
14.4	The 4.0m diameter composite spacecraft fairing for the Delta III launch vehicle.	147
14.5	The 4.0m diameter composite spacecraft fairing for the Delta III launch vehicle enclosing a 2m primary optics design from the Ball Aerospace feasibility study.	148
14.6	The 4.0m diameter composite spacecraft fairing for the Delta III launch vehicle enclosing a 2m primary off-axis optics design.	149
15.1	Ground system showing the flow of data.	151
15.2	Daily coverage from from the SSL ground station for the Prometheus orbit.	152
15.3	Percentage coverage from the SSL ground station as a function of the Prometheus orbit inclination and for different values of the angle of perigee.	153
16.1	Research and Development Plan	157

18.1	SNAP Project Organization Chart	172
18.2	SNAP Project Schedule	177
B.1	Raw test image obtained at Lick Observatory of a back-illuminated 2k \times 2k (15 μm^2 -pixel) LBNL high-resistivity CCD	192
B.2	Measured response of the LBNL “fully-depleted” CCD at -100°C for an unoptimized two-layer AR coating	193
B.3	Absorption length of light in silicon	197
B.4	Back-Illuminated test pattern imaged a back-illuminated 2k \times 2k LBNL high-resistivity CCD tested at Lick Observatory	199
B.5	Lick test CCD images of a heavily obscured region in the Orion Nebula	200
B.6	Cross-section of the back-illuminated, fully-depleted CCD	200
B.7	Degradation of CTE as a function of the Non-Ionizing energy loss	202
B.8	Non-ionizing energy loss metric for CCD displacement damage during solar max.	203
B.9	Differential proton flux in high earth orbit for solar maximum and solar minimum for different shielding thicknesses	205
B.10	Conceptual design for “fully-depleted” CCD packaging	206

Part I

Executive Summary

Chapter 1

Executive Summary

1.1 Abstract

A ~ 2 -meter satellite telescope with a 1-square degree optical imager, a small near-IR imager, and a three-channel near-UV-to-near-IR spectrograph can discover approximately 2000 type Ia supernova in a year at redshifts between $z=0.1$ and 1.7, and follow them with high-signal-to-noise calibrated light-curves and spectra. The resulting data set can determine the cosmological parameters with precision: mass density Ω_M to ± 0.03 , vacuum energy density Ω_Λ to ± 0.05 , and curvature Ω_k to ± 0.06 . The data set can test the nature of the “dark energy” that is apparently accelerating the expansion of the universe: by measuring the ratio of the dark energy’s pressure to its density to ± 0.05 , and by studying this ratio’s time dependence, a cosmological constant dark energy can be differentiated from alternatives such as “quintessence.” The large numbers of supernovae across a wide range of redshifts are necessary but not sufficient to accomplish these goals; the controls for systematic uncertainties are primary drivers of the design of this space-based experiment. These systematic and statistical controls cannot be obtained with other ground-based and/or space-based telescopes, either currently in construction or in planning stages.

1.2 Introduction

In the past few decades the study of cosmology has taken its first steps as an empirical science, combining concepts and tools from astrophysics and particle physics. Already these first results have brought surprises. The simplest model for the universe, flat and dominated by matter, seems not to be true. This implies that our current fundamental physics understanding of particles, forces, and fields is similarly likely to be incomplete.

The empirical evidence comes from just three main complementary lines of attack. Measurements of the mass density of the universe, Ω_M , including measurements from galactic cluster abundance, x-ray flux, and large scale structure, all indicate low Ω_M . If this mass density is the dominant energy density in the universe then according

to General Relativity space itself would have to curve; a higher total energy density ($\rho_{\text{critical}} = 3H_0^2/(8\pi G) \approx 10^{-29} \text{ gm cm}^{-3}$) is required for space to be flat. However, measurements of the curvature of space from the Cosmic Microwave Background hint that its value may be zero. The popular “inflationary” scenario generates just such a flat universe. Assuming that this is confirmed with upcoming CMB measurements, the implication is that there is some other energy component to bring the total to the critical value. The most direct evidence of such a new energy component comes from the supernova measurements of changes in the universe’s expansion rate. These data indicate that the expansion is accelerating, implying the presence of a new, mysterious energy component that can cause acceleration.

To address this new puzzle and begin to establish a solid cosmological picture, each of the three measurement approaches that currently provide the pillars of empirical cosmology must now be extended, tested, and exploited to the fullest extent possible. New measurement approaches, such as the Sunyaev-Zeldovich effect, weak gravitational lensing, galaxy density power spectrum, and type II supernovae, must also be aggressively pursued to provide us with other complementary measurements. The CMB measurements are now going through the extend-test-and-exploit phase, with many ground-based, balloon, and satellite experiments in progress during the upcoming decade. Many years of work have also gone into the development and refinement of cluster mass estimates. In this proposal, we describe a satellite project that is aimed at making a major jump forward for the third approach, supernova-based study of cosmology.

In this letter of intent, we will focus primarily on the driving SN Ia science, although several of the new cosmological measurement methods will also be pursued with this experiment, including type II supernovae and weak lensing. We will describe the scientific background of the SN Ia measurements, their current limitations, and the potential of this experiment to answer the puzzles raised by the current results. The goal of this project is thus to establish one firm footing—ideally, to become one of many—for our cosmological theories.

1.3 Scientific Motivation and Background

A Simple, Direct Approach to the Cosmological Parameters

Type Ia supernovae provide simple cosmological measurement tools. Each one is a strikingly similar explosion event whose physics can be analyzed in some detail from the time record of its intensity and spectrum as it brightens and fades. Most observed SNe Ia have the same peak luminosity, while variations in this brightness can be recognized and, in most cases, calibrated using their intensity/spectrum time records. Their observed peak brightness (magnitude) is then a measure of their distance.

The wavelengths of the photons from the supernova are stretched—“redshifted”—in exact proportion to the stretching of the universe during the period that the photon traveled to us. Thus the comparison of SN Ia redshifts and magnitudes provides a particularly straightforward measurement of the changing rate of expansion of the universe: the apparent magnitude indicates the distance and hence time back to the

supernova explosion, while the redshift measures the total relative expansion of the universe since that time.

This satellite project is designed to establish a Hubble-diagram plot dense with magnitudes and redshifts looking back over two-thirds the age of the universe; with such a history of the expansion of the universe we can determine the contributions of decelerating and accelerating energies—mass density Ω_M , vacuum energy density Ω_Λ , and/or other yet-to-be-studied “dark energies”—as the expansion rate changes over time.

This is an extremely transparent methodology. Almost everyone—even non-scientists—can appreciate and perhaps critique every step. Aside from the basic cosmological equations, there is no model dependence in this empirically-based method, and it is sensitive to only a few parameters of cosmology so there is no fit required in a large-dimensional parameter space. (Conversely, this method of course does not help determine these other parameters, except by narrowing down the whole phase space, as discussed below.) This transparency is an unusual and important feature of this particular very fundamental measurement.

The Current Results: Questions Answered and Posed by an Accelerating Universe

Currently, the cosmological results from the magnitude/redshift measurements of a few score SNe Ia already present surprises and puzzles. Perhaps most striking is that the data indicate that we live in an accelerating universe that must be dominated by a positive cosmological constant or other vacuum energy whose pressure is negative and large. The very simplest cosmological model, the Einstein-de Sitter ($\Omega_M = 1$) universe, which is flat and has zero cosmological constant, is strongly inconsistent with the data. Of the two arguably next-simplest models, only the flat model with the cosmological constant, Λ , fits the data, while the low-mass open universe with zero Λ does not. (All of these statements can be made with very strong statistical confidence; even stretching the range of imagined systematic uncertainties, it is very difficult to fit the data without a cosmological constant in a flat universe.)

These current results immediately raise important questions. Although the data indicate that an accelerating dark energy density—perhaps the cosmological constant—has overtaken the decelerating mass density, they do not tell us the absolute density of either one. These two density values are two of the fundamental parameters that describe the constituents of our universe, and determine its geometry and destiny. The proposed satellite project is designed to obtain sufficient magnitude-redshift data for a large enough range of redshifts ($0.1 < z < 1.7$) that these absolute densities can each be determined to unprecedented accuracy. Taken together, the sum of these energy densities then provides a measurement of the curvature of the universe.

The current data also do not tell us the nature of the dark energy; all we know is that it must have a sufficiently negative pressure to cause the universe’s expansion to accelerate. Our one long-known physical model for the dark energy, the vacuum energy density that Einstein called “the cosmological constant,” presents difficult theoretical problems. Why, for example, is the vacuum energy density so small when compared to

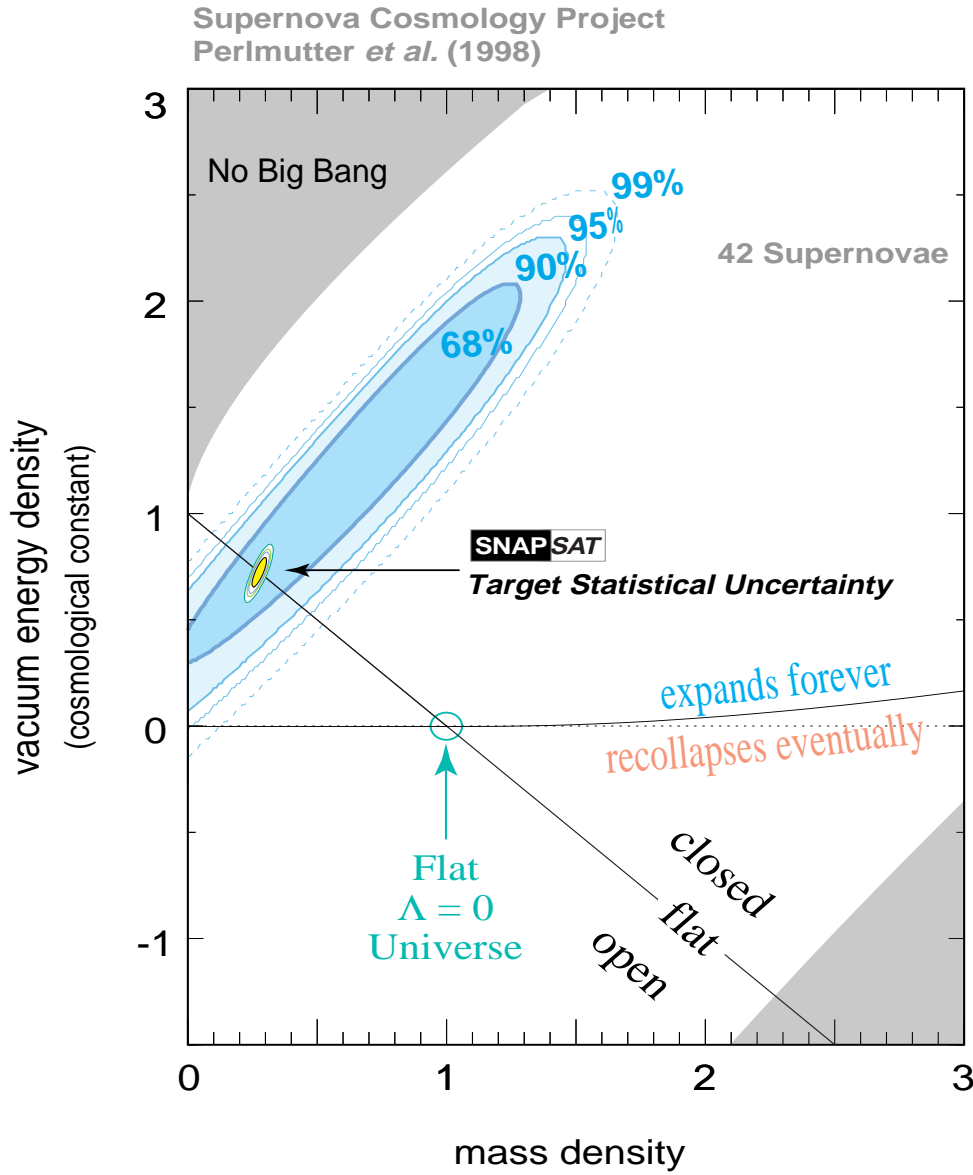


Figure 1.1: 68%, 90%, and 99% confidence regions in the Ω_M — Ω_Λ plane from the 42 distant SNe Ia in Perlmutter *et al.* (1999). These results rule-out a simple flat, $\Omega_M = 1$ cosmology. They further show strong evidence (probability $> 99\%$) for $\Omega_\Lambda > 0$. Also shown is the expected confidence region from the SNAP satellite for an $\Omega_M = 0.28$ flat universe.

the natural energy scales of the particles and fields that would be expected to account for it: the values that are consistent with the current SN Ia results are 10^{120} times smaller than the Planck scale. Moreover, why would a vacuum energy density that remains constant throughout history turn out just now to be within a factor of two or three of the mass energy density, which has fallen by many orders of magnitude since the Big Bang?

In response to these theoretical problems, several alternative physical models have been proposed as candidates for the dark energy. These models can generally be characterized by their equation of state, $p = w\rho$ (the speed of light, c , is set to unity). The ratio of pressure to density, w , can be constant or time-varying depending on the model, and has a constant value of -1 in the case of the cosmological constant.) The current SN Ia data allow some crude constraints on the alternative dark energy models, since not all equations of state fit the data. With the proposed satellite project we can begin to study these alternative dark energy models in some detail, by determining w to much higher accuracy and by studying its evolution as a function of time for the redshift range out to $z \sim 1$ (beyond which current measurements indicate the mass density dominates over the dark energy density).

Scientific Goals of this Proposal

The proposed experiment would provide the strongest probe of the dark energy in the universe and would measure important cosmological parameters to very high accuracy. Assuming that the dark energy is the cosmological constant, this experiment can simultaneously determine mass density, Ω_M , to accuracy of 0.03, cosmological constant energy density, Ω_Λ , to 0.05 and curvature, $\Omega_k = 1 - \Omega_M - \Omega_\Lambda$, to 0.06.

The proposed experiment is one of very few that can study the dark energy directly. Assuming a flat universe with mass density Ω_M and a dark energy component the proposed experiment will be able to measure the equation-of-state ratio w with accuracy of 0.05, at least a factor of five better than the best planned cosmological probes. With such a strong constraint on w we will be able not only to differentiate between, for example, the cosmological constant and topological defect models, but also to severely constrain the scalar-field models. Moreover, with data of such high quality one can relax the assumption of the constant equation of state, and test its variation with redshift. A number of exciting investigations can then be done, including recovering the evolution of the equation of state with redshift and even the shape of the effective potential of the scalar field out to $z \sim 1.5$. These determinations would directly shed light on physics at high energy/small scale and physics of the early universe.

It is important to add that these SN Ia results are not the only available cosmological measurements, nor will they be at the time of the proposed satellite. The estimates of the mass density from large-scale structure (LSS) surveys and cluster evidence are constantly improving, while the CMB results expected this year should give an important measurement of the curvature of the universe. The MAP and Planck satellite experiments are expected to give high-precision fits of ~ 11 cosmological and model-dependent parameters, both before and after the proposed satellite's SN Ia measurements. Perhaps surprisingly, these supernova measurements will provide stronger

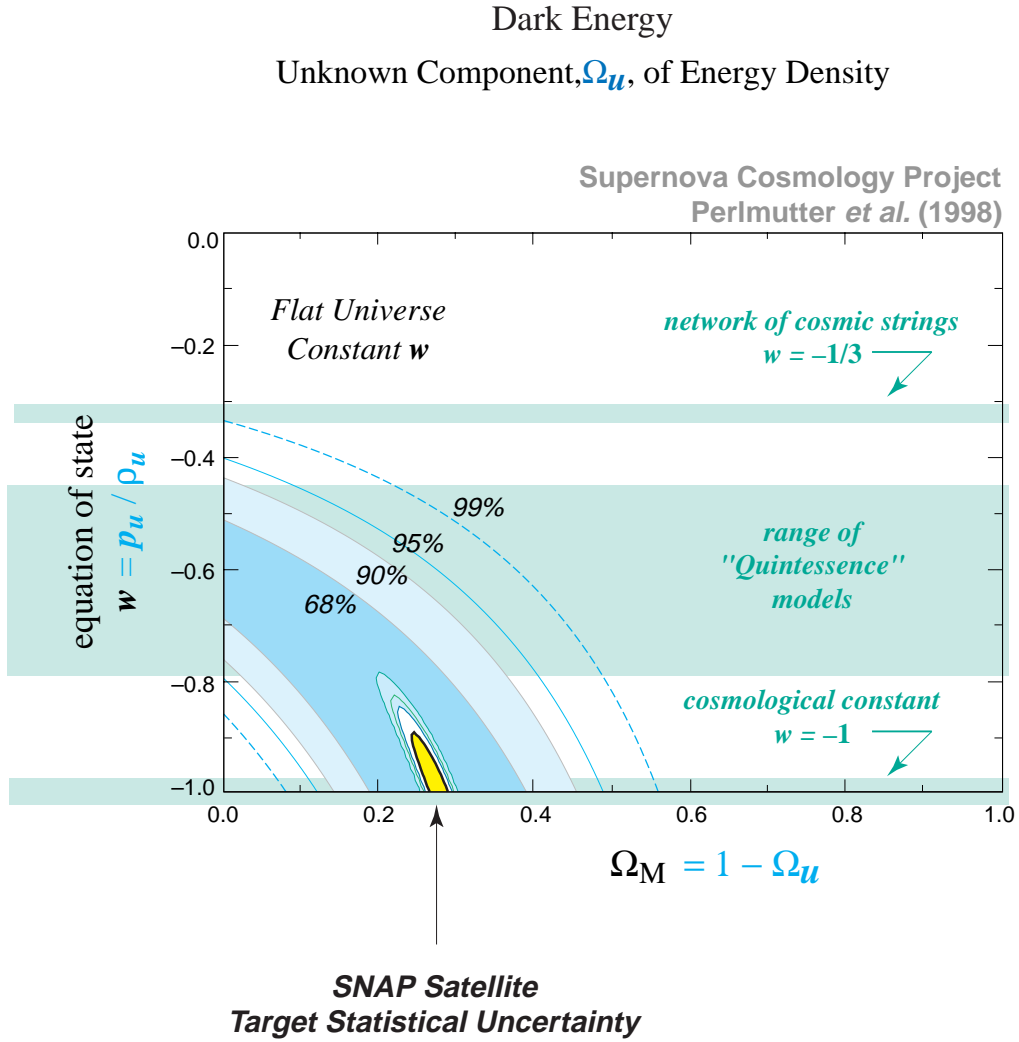


Figure 1.2: Best-fit 68%, 90%, 95%, and 99% confidence regions in the Ω_M - w plane for an additional energy density component, Ω_w , characterized by an equation-of-state $w = p/\rho$. (If this energy density component is Einstein's cosmological constant, Λ , then the equation of state is $w = p_\Lambda/\rho_\Lambda = -1$.) Also shown is the expected confidence region allowed by SNAP.

constraints on Ω_M and Ω_Λ than those expected from either LSS or CMB measurements, and constraints on curvature Ω_k that are comparable with those expected from MAP and Planck. The important cosmological test will be the cross comparison of these and other fundamental measurements — and it is even possible that cosmology will next progress when we discover that they do not agree. In any case, it will be all of these measurements fit simultaneously, that will provide us with our best understanding of the cosmology of the universe; the final results can be as much as an order of magnitude better than the constraints from any one measurement approach..

To accomplish these goals, it is not sufficient simply to discover and study more supernovae and more distant supernovae. The current SN Ia data set already has statistical uncertainties that are only a factor of two larger than the identified systematic uncertainties. There are also several additional proposed systematic effects that might confound attempts at higher precision, in particular the possibilities of “grey dust” and systematic shifts in the population of SN Ia host galaxy environments. Addressing each of these systematic concerns requires a major leap forward in the supernova measurement techniques, and has driven us to the satellite experiment that we describe in this proposal.

1.4 Proposed Experiment

Instrumentation

The baseline proposed satellite experiment is based on a simple, dedicated combination of a 1.8- to 2.0-meter telescope, a 1-square-degree imager, a 1-square-arcminute near-IR imager, and a three-channel near-UV-to-near-IR spectrograph. The 1-square-degree wide field is obtained with a modified three-mirror Paul-Baker design, with a fast-steering mirror located at an intermediate focus to stabilize the image without the need for expensive stabilization of the satellite itself.

The wide-field imager is completely filled with a CCD mosaic for the “optical” wavelengths between 0.3 and 1.0 microns. The near-IR imager will be a single HgCdTe detector to obtain images of specific targets in the wavelengths between 1.0 and 1.7 microns. A dichroic beam-splitter sends the light to these two imaging systems simultaneously.

The spectrograph uses dichroic beam-splitters to send the light into two optical channels ($0.3 - 0.6 \mu\text{m}$ and $0.55 - 1.0 \mu\text{m}$) and one near-IR channel ($0.9 - 1.7 \mu\text{m}$). Each of the three channels employs an “integral field unit” (IFU) to obtain an effective image of a 2 arcsec by 2 arcsec field, split into 0.07 arcsec by 0.07 arcsec regions that are each individually sent to the spectrograph to obtain a three-dimensional data cube of flux at each position and wavelength. In operation, these integral field units will allow simultaneous spectroscopy of a supernova target and its surrounding galactic environment; the 2 arcsec by 2 arcsec field of view also removes any requirement for precise positioning of a supernova target in a traditional spectrograph slit. This point is particularly important for absolute flux calibration, because all of the supernova light is collected with the integral field units. The spectrograph is thus designed to allow the spectra to be used to obtain photometry in any “synthetic” filter band that

one chooses.

Observation Strategy and Baseline Data Package

This instrumentation will be used with a simple, predetermined observing strategy designed to monitor a twenty-square-degree region of sky near the north or south ecliptic poles, discovering and following supernovae that explode in that region. Every field will be visited frequently enough with sufficiently long exposures that at any given redshift up to $z = 1.7$ every supernova will be discovered within, on average, two restframe days of explosion. Every supernova at $z < 1.2$ will be followed as it brightens and fades, while at $z > 1.2$ there will be sufficient numbers of supernovae that it will only be necessary (and possible) to follow a subsample to obtain comparable numbers of supernovae.

The wide-field imager makes it possible to find and follow approximately 2000 SNe Ia in a year. The 1.8- to 2.0-meter aperture of the mirror allows this dataset to extend to redshift $z = 1.7$.

This prearranged observing strategy will provide a uniform, standardized, calibrated dataset for each supernova, allowing for the first time comprehensive comparisons across complete sets of supernovae. The standardized dataset will have the following measurements that will address, and often eliminate, each of the statistical and systematic uncertainties that have been identified or proposed.

- A light curve sampled at frequent, standardized epochs that extends from ~ 2 restframe days to ~ 80 restframe days after explosion.
- Multiple color measurements, including optical and near-IR bands, at key epochs on the light curve.
- Spectrum at maximum light, extending from $0.3 \mu\text{m}$ to $1.7 \mu\text{m}$.
- Final reference images and spectra to enable clean subtraction of host galaxy light.

The quality of these measurements is as important as the time and wavelength coverage, so we require:

- Control over signal-to-noise ratio for these photometry and spectroscopy measurements, to permit comparably high statistical significance for supernovae over a wide range of redshifts.
- Control over calibration for these photometry and spectroscopy measurements, with constant monitoring data collected to ensure that cross-instrument and cross-wavelength calibration remains stable over time.

Note that to date not one single SN Ia has ever been observed with this complete set of measurements, either from the ground or in space, and only a handful have a dataset that is comparably thorough. With the observing strategy proposed here, *every one* of ~ 2000 followed SN Ia will have this complete set of measurements.

In addition to this minimum-required-dataset, a still more extensive set of observations will be performed for a randomly selected subset of SNe Ia (with more at lower redshifts and fewer at higher redshifts). These additional observations will include:

- A time series of spectra, sampled frequently over the entire 80 restframe days of the observed light curve.
- Multiple filter-band light curves. (These are not necessary when the time series of spectra is obtained, since this provides synthetic-filter photometry.)

1.5 Control of Statistical and Systematic Uncertainties

The satellite instrumentation and observation strategy is designed to provide comprehensive control of the previously identified or proposed sources of uncertainty. The completeness of the resulting dataset will make it possible to monitor the physical properties of each supernova explosion, allowing studies of effects that have *not* been previously identified or proposed.

Previously, the identified systematic uncertainty was over half the size of the statistical uncertainty; this would provide the “floor” on the proposed measurement uncertainty, if it were not improved. However, almost every one of the sources of identified systematics is due to limitations of the previous (and even planned NGST baseline SN program) measurements. The dataset described here removes these limitations so that the relevant effects can be measured and the previous systematic uncertainties now become controllable *statistical* uncertainties.

Previously Identified Sources of Systematic Uncertainty

In Table 1.1, we summarize the identified sources of systematic error, and give the uncertainty that each contributed to previous measurements. With the proposed satellite experiment, each of these effects can either be measured so that it can become part of the statistical error budget, or else bounded (the target overall systematic uncertainty is kept below ~ 0.02 magnitudes, so that it will contribute comparably to the final statistical uncertainties). The final column of the table summarizes the observations required to reach this target systematic uncertainty. These previously identified sources of systematic uncertainty are each discussed in more detail in § 4.4.

Proposed Sources of Systematic Uncertainty

Extinction by Proposed “Gray Dust”: *Not previously bounded by any supernova measurements.* The physical models so far proposed for this “gray dust” has dust grains that are large enough that they dim blue and red light equally, however the near-IR light ($\sim 1.2 \mu\text{m}$) is less affected. The same technique can therefore be used to measure this dust as would be used to measure the “ordinary” dust, by extending the broad-wavelength measurements into the near-IR. This will measure dimming due to proposed large-grain gray dust out to $z = 0.5$, and this proposed systematic uncertainty, too, can become part of our statistical error budget.

Systematic	Current δM	Requirement to satisfy $\delta M < 0.02$
Malmquist bias	0.04	Detection of every supernova 3.8 magnitudes below peak in the target redshift range
K-Correction and Cross-Filter Calibration	0.025	Spectral time series of representative SN Ia and cross-wavelength relative flux calibration
Non-SN Ia Contamination	< 0.05	Spectrum for every supernova at maximum covering the rest frame $\approx 6250\text{\AA}$ Si II feature
Milky Way Galaxy extinction	< 0.04	SDSS & SIRTf observations; SNAP spectra of host Galactic subdwarfs
Gravitational lensing by clumped mass	< 0.06	Average out the effect with large statistics with ~ 75 SNe Ia per 0.03 redshift bin. SNAP microlensing measurements.
Extinction by “ordinary” dust outside the Milky Way	0.03	Cross-wavelength calibrated spectra to observe wavelength dependent absorption

Table 1.1: Listed are the main systematic errors in the measurement of the cosmological parameters. Their contribution to magnitude uncertainties in the current analyzed data set is tabulated, along with the observational requirements needed to reduce those uncertainties to $\delta M < 0.02$

Requirement: Cross-wavelength calibrated spectra, at controlled SN-explosion epochs, that extend to rest-frame $1.2\ \mu\text{m}$.

In principle, gray dust models can be constructed that would evade these broad-wavelength measurements, either because the “gray dust” does not exist closer than $z = 0.5$ or because the dust grains are even larger than first proposed and thus absorb light equally at $0.4\ \mu\text{m}$ and $1.2\ \mu\text{m}$. (These larger grain sizes are strongly disfavored by other astrophysical constraints, however.) Even these more contrived dust models can be measured by the proposed dataset because of its large redshift range: at redshifts beyond $z = 1.4$ models with dust would be distinguished from cosmological models with no dust but with Λ at the 50 standard-deviation level.

Requirement: A redshift distribution that extends to $z \geq 1.5$ for followed SNe Ia.

Proposed Uncorrected Evolution: Uncorrected “evolution” has also been proposed as a potential source of systematic uncertainty. Supernova behavior may depend on properties of its progenitor star or binary-star system. The distribution of these stellar properties is likely to change over time—“evolve”—in a given galaxy, and over a set of galaxies.

As galaxies age, generation after generation of stars complete their life-cycles, enriching the galactic environment with heavy elements (the abundance of these elements is termed “metallicity”). In a given generation of stars, the more massive ones will complete their life cycles sooner, so the distribution of stellar masses will also change over time. Such statistical changes in the galactic environments are expected to affect the typical properties of supernova-progenitor stars, and hence the details of supernova explosions. Even the type Ia supernova might be expected to show some differences that reflect the galactic environment in which its progenitor star exploded, even though the SN Ia is triggered under very similar physical conditions every time (as mass is slowly added to a white dwarf star until it approaches the Chandrasekhar limit).

Evidence for such galactic-environment driven differences among SNe Ia has in fact already been seen among nearby, low-redshift supernovae. The range of intrinsic SN Ia luminosities seen in spiral galaxies differs from that seen in elliptical galaxies. So far, it appears that the differences that have been identified are well calibrated by the SN Ia light curve width-luminosity relation. The standard supernova analyses thus already are correcting for a luminosity effect due to galactic-environment-distribution evolution. There are likely to be additional, more subtle effects of changes in the galactic environment and shifts in the progenitor star population, although it is not clear that these effects would change the peak luminosity of the SNe Ia. The proposed satellite experiment is designed to provide sufficient data to measure these second-order effects, which might be collectively called “proposed uncorrected evolution.”

In this discussion it is important to recognize that each individual galaxy begins its life at a different time since the Big Bang, at a different absolute time. Even today, there are newly formed, “young,” first-generation galaxies present that have not yet gone through the life cycles of their high-mass stars, nor yet produced significant heavy element abundance. Thus at any given redshift there will be a large range of galactic environments present and the supernovae will correspondingly exhibit a large range of

progenitor star ages and heavy element abundances. (This is why we can currently observe and correct an evolutionary range of SNe Ia using only low-redshift, nearby SNe Ia.) It is only the relative distribution of these environment ages that will change with universal clock time. By identifying matching sets of supernova that come from essentially the same progenitor stars in the same galactic environments, but across a wide variety of redshifts, we can then perform the cosmological measurements using SNe Ia in the same evolutionary state. This only requires that the SN Ia sample sizes are sufficiently large and varied at each redshift that we can find matching examples in sufficient quantities.

We have identified a series of key supernova features that respond to differences in the underlying physics of the supernova (see § 3.2.3 for a complete list and detailed description). By measuring all of these features for each supernova we can tightly constrain the physical conditions of the explosion, making it possible to recognize sets of supernovae that arise in matching galactic environments. The current theoretical models of SN Ia explosions are not sufficiently complete to predict the precise luminosity of each supernova, but they are able to give the rough relationships between changes in the physical conditions of the supernovae (such as opacity, metallicity, fused nickel mass, and nickel distribution) and changes in their peak luminosities. We can therefore give the approximate accuracy needed for the measurement of each feature to ensure that the physical condition of each set of supernovae is well enough determined so that the range of luminosities for those supernovae is well below the a systematic uncertainty bound ($\sim 2\%$ in total).

In addition to these features of the supernovae themselves, we also study the host galaxy of the supernova. We can measure the host galaxy luminosity, colors, morphology, type, and the location of the supernova within the galaxy, even at redshifts $z \sim 1.7$. (These observations are not possible from the ground.)

1.6 Why a New Satellite?: Design Requirements and Ground/Space-Based Alternatives

The science goals that we have described drive the design requirements of this experiment. The target statistical uncertainties are closely matched by the target systematic uncertainties, so that the numbers of supernovae, their redshift range, and the quality and comprehensive nature of the dataset of measurements for each supernova all together can achieve the stated cosmological measurements.

In particular, the mirror aperture is about as small as it can be before spectroscopy at the requisite resolution is no longer zodiacal-light-noise limited. A smaller mirror design would quickly degrade the achievable signal-to-noise of the spectroscopy measurements, or drastically reduce the number of supernovae followed. The field of view for the optical imager has been optimized to obtain the follow-up photometry of multiple supernovae simultaneously; a smaller field would require multiple pointings of the telescope and again would greatly reduce the number of supernovae that could be followed. The three-channel spectrograph covers precisely the wavelength range

Requirements	Addresses and Resolves
Detection of every supernova 3.8 magnitudes below peak for $z \leq 1.5$	<ul style="list-style-type: none"> • Rise time measurement • Eliminates Malmquist Bias
SNe Ia at $0.3 \leq z \leq 1.2$	<ul style="list-style-type: none"> • Statistics and lever-arm for the precision measurement of Ω_M, Ω_Λ • Detection of Gray Dust • Detection of SN Ia evolution
~ 75 SNe Ia per 0.03 redshift bin	<ul style="list-style-type: none"> • Statistics and lever-arm for the precision measurement of w • The effect of gravitational lensing by clumped mass is averaged out
Well sampled light-curves between ~ 2 restframe days to ~ 80 restframe days after explosion	<ul style="list-style-type: none"> • Determination of the peak magnitude of each SN Ia • Determination of the light-curve shape of each SN Ia • Detection of SN Ia evolution
Multiple IR and optical color measurements at key epochs	<ul style="list-style-type: none"> • Determination of extinction for each SN Ia • Confirmation of the light-curve shape of each SN Ia
Spectrum for every supernova at maximum covering the rest frame $\approx 6250\text{\AA}$ Si II feature and that extend to $1.2\mu\text{m}$	<ul style="list-style-type: none"> • Eliminates non-SN Ia contamination • Measures extinction due to “ordinary” dust outside the Milky Way • Spectral feature – peak magnitude relation
Spectral time series of representative SN Ia with cross-wavelength relative flux calibration	<ul style="list-style-type: none"> • Determine K-corrections • Allow cross-filter comparisons • Detection of Gray Dust • Detection of SN Ia evolution

Table 1.2: Observational requirements to ensure various statistical and systematic errors each contribute uncertainties of $\delta M < 0.02$. The particular sources of error that each requirement addresses are also listed.

necessary to capture, over the entire target redshift range, the Si 6250 Å feature that both identifies the SNe Ia and provides a key measurement of the explosion physics to identify each supernova’s evolutionary state. In general, more than one critical design requirement has driven each of these instrument choices; for example, the wavelength range of the spectrograph also is required to measure the effects of any “gray dust” on the supernova magnitudes.

A comparison with plausible ground- and space-based alternatives makes it particularly clear why this satellite design is required to achieve the science. Simply finding the supernovae near their explosion date from the ground is the first challenge, even for an entirely dedicated 8-meter telescope with a special-purpose 9-square-degree imager. To detect SNe Ia within ~ 2 restframe days of explosion (as required for the risetime measurement) the photometry must extend to 3.8 magnitudes below peak with a signal-to-noise of 10. From the ground, with its bright sky and atmospheric seeing, this limits the search to redshifts less than $z = 0.6$ —and fewer than 300 SNe Ia per year would be discovered. If one begins to degrade the experiment by removing this risetime measurement’s control on systematics, the next key requirement is a measurement of the plateau phase of the light-curve, approximately 2.8 magnitudes below peak, which would limit ground-based searches to redshifts less than $z = 0.7$ (see Table 5.2).

Using the existing Hubble Space Telescope or even the planned Next Generation Space Telescope (NGST) does not improve the ability to discover these supernovae, since neither telescope has a wide-field camera. With the 8-meter NGST’s 16-square-arcminute field of view, it would require tens of years of full-time searching to obtain a comparable sample of SNe Ia in the target redshift range. The NGST does have a quite useful supernova program planned, but all at higher redshifts than this project, and without the extensive controls on systematic uncertainties that we require. This NGST program is aimed at different science, since it is not possible to study the “dark energy” at redshifts much beyond $z \sim 1.2$, when the universe had smaller scale and the dark matter dominated.

One might wonder if the NGST could be used simply to follow up the spectroscopy of the supernovae discovered with this telescope. This would be possible, but it is a rather wasteful use of the 8-meter’s capabilities; most of time for over half a year would be spent simply slewing the NGST from supernova to supernova, with the shutter open for only a small fraction of the time.

1.7 Overview of Feasibility

The essential elements of the project’s feasibility have already been studied. Working with Ball Aerospace Corporation, we were able to establish many of the baseline design feasibility issues by reference to other satellite missions that they have successfully flown, or are currently building.

- We made a top-down cost estimate together with Ball Aerospace, based on other similar satellites designs and costs.

- We performed a trade study of orbit options with Ball Aerospace. We found several options that allowed a workable combination of launch vehicle, mass-to-orbit, thermal control, cosmic-ray load, continuous observing duty cycle, telemetry rates, and power budget.
- Several optical designs appear feasible, including a Ball Aerospace anastigmat design, a Richey-Chretien design, a Paul-Baker design, and an off-axis design. We are likely to adopt a lightweight mirror technology developed for the NGST mirror segments (our monolithic mirror would be the equivalent of just one NGST segment), although our mirror weight requirement is much less severe.
- Pointing requirements can be met using a fast-steering mirror, a legacy technology developed for earth-observing satellites (and the NGST). This image-stabilizing option avoids the need to maintain a precisely stable spacecraft.
- At Lawrence Berkeley National Laboratory's microfabrication facility, we have built and tested high-resistivity CCDs that provide greater than 90% quantum efficiency up to the near-IR ($1\ \mu\text{m}$), and are at least ten times more radiation hard than conventional CCDs. This fabrication process has now been transferred to a high-volume commercial vendor, and two current fabrication runs are currently in their final stages of processing.
- For some years, much larger CCD and silicon strip arrays have been routinely built by the high energy physics community and operated in comparably inaccessible locations, where they are exposed to high radiation levels.
- We have conducted extensive simulation and modeling of the science reach and performance of various observing strategies and instrument trade-offs.

1.8 Summary of Other Major Science

The dataset of images and spectra obtained with this wide-field imager and three-channel spectrograph can address other important science goals with very little additional effort in data collection or in the instrument specifications. Although these science goals will not be discussed in detail in this preview document, it is important in particular to note that we can obtain complementary measurements of the cosmological parameters with completely independent measurement methods.

Weak lensing. Because the observation strategy observes the same patches of sky repeatedly over a year of supernova observations, a very deep, high-resolution image can be added together from thousands of images taken at every orientation of the spacecraft. This is an ideal way to look for weak-lensing elongations of distant galaxies, since the optical distortions of the image will be small and well characterized. Such images of several dozen square-degree fields can constrain the cosmological parameters (see § 6.4) in a manner complementary to the SN Ia measurements, with different systematics.

Type II supernovae. As we discover and follow the SNe Ia, we will also discover and have the option of following SNe II. While these supernovae are not of predictable luminosity, they are close enough matches to a black body that their luminosities can be determined from the size and temperature of their photospheres, along with a fit to any spectral deviations from black body. (Since our experiment provides a very tight constraint on the date of explosion and the velocity of the expanding gas, the size of the photosphere will be easy to determine.) Most SNe II are about six times fainter than the prototypical SNe Ia, so most will not be studied with early detections beyond redshifts $z \sim 0.5$. However since SNe II are much more frequent than SNe Ia, we can afford to study the brightest few percent and this will extend the SN II study beyond $z = 1$. The sources of systematic uncertainty for these SNe II measurements would generally be different from the SNe Ia systematic uncertainties.

There is also important science to be gained from this project that is not aimed specifically at the cosmological models. It is clear, for example, that the final set of very deep, wide field images would become a resource for all of astrophysics, as the Hubble Deep Fields have been.

Current Status

We expect this letter of intent to lead to a further proposal next calendar year. If this proposal is ultimately successful, we envision a joint DOE/NSF-funded science experiment to be launched by NASA.

The next stage of the planned effort will be to initiate the following research and development activities: CCD commercialization, telescope optics design, and specific ground-based supernova studies to refine the experiment design. In addition, we are currently in the process of selecting a spacecraft bus vendor, and this will make it possible to initiate a full-scale cost and schedule analysis.

The fundamental questions and surprising discoveries of recent years make this a fascinating new period of empirical cosmology. This proposed satellite project presents an unusual opportunity to extend this exciting work and advance our understanding of the universe.

Part II

SNAP Physics

Chapter 2

Theoretical Overview

2.1 Cosmological Parameters

The Cosmological Principle states that the universe is homogeneous and isotropic. From this it follows that there is a universal expansion factor $a(t)$ describing the scale of the universe as a function of time. The dynamics of $a(t)$ are determined by General Relativity and depend on the universe's geometry and the energy density of the different components that fill the universe. A universe with nothing but a mass density equal to the critical value $\rho_c = 3H_0^2/(8\pi G) \approx 10^{-29} \text{ gm cm}^{-3}$ is poised between ultimate expansion and ultimate contraction. If there is a non-zero cosmological constant, it too contributes. Importance of the two contributions is expressed by the dimensionless quantities

$$\Omega_M = \frac{8\pi G\rho}{3H_0^2}, \quad \Omega_\Lambda = \frac{\Lambda}{3H_0^2} \quad (2.1)$$

where $H_0 \equiv \dot{a}/a|_{\text{now}}$ is the Hubble parameter today.

Within the Friedmann-Lemaitre-Robertson-Walker cosmological model, the bulk properties of the universe can be described by H_0 , Ω_M , and Ω_Λ . As the only parameters that determine the bulk kinematics of the universe, they fix the age of the universe and specify its past and future dynamics.

These three fundamental cosmological parameters have long been the subjects of investigations. Previous measurements of Ω_M have generally come from the study self-gravitating dynamical systems. Previous Ω_Λ limits have generally come from counting statistics of high-redshift $z \gtrsim 1$ objects, which measure differential volumes. The measurement of H_0 has been controversial and only now are we seeing the slow convergence to a generally accepted value, $H_0 \approx 70 \text{ km/s/Mpc}$.

2.2 The Dark Energy

A standard cosmology based on inflation was established in the early 1980s. In this picture, inflation exponentially expands a small patch of space and produces a flat universe. This would explain why the universe does not have large curvature and why the

Cosmic Microwave Background is so uniform across scales larger than the then-horizon of the universe. Inflation also generates adiabatic scale-invariant perturbations, which serve as seeds for large-scale structure (LSS) formation. Evidence for dark matter, on the other hand, has been present since the early work of Zwicky (1937) six decades ago, when he measured radial velocities of galaxies in the Coma cluster and concluded that they cannot be explained by the visible mass. Starting in the 1970s, comparisons of nuclear abundances with the predictions of big-bang nucleosynthesis established that most matter in the universe is non-baryonic and that baryons contribute no more than 5% of the critical energy density (for reviews of the dark-matter conundrums, see Trimble 1997; Turner 1999; Copi, Schramm, & Turner 1995). Observations of the radial motion of stars within galaxies and of galaxies themselves revealed that there is non-luminous, dark matter.

The simplest cosmological model consistent with inflation is the Einstein - de Sitter universe, $\Omega_{\text{total}} = \Omega_M + \Omega_\Lambda = 1$. The difference between Ω_{total} and unity determines the curvature of the universe and the corresponding (normalized) curvature energy density: $\Omega_k = 1 - \Omega_{\text{total}}$. The Einstein-de Sitter model has no curvature. If the universe is thus flat and the cosmological constant vanishes, then $\Omega_M = 1$. Since $\Omega_B \approx 0.05$, if the universe is flat and there is no cosmological constant most matter in the universe is not only dark, but also non-baryonic.

However, during the last 10 - 15 years cosmologists have begun to doubt this picture for several reasons. First of all, it appeared that there is not enough matter to make a flat universe, and that the energy density in matter (baryonic or otherwise) may be closer to $\Omega_M \approx 0.35 \pm 0.1$. These low values of Ω_M were obtained using several approaches: the evolution of the number-density of rich clusters of galaxies (Bahcall & Fan, 1998); mass estimates of galaxy clusters, either through the Sunyaev-Zeldovich effect (Carlstrom et al., 1999) or through measurement of the x-ray flux (J. Mohr & Evrard, 1999); and the power spectrum of Large Scale Structure (LSS), characterized by the “shape” parameter $\Gamma \approx \Omega_M h \sim 0.25$ (Efsthathiou, Bond, & White, 1992) (where $H_0 = 100 h$ km/sec/Mpc), which for $h \approx 0.7$ implies $\Omega_M \sim 0.4$. Meanwhile, a flat universe was favored not only by theorists who believe in inflation, but also by preliminary evidence from Cosmic Microwave Background (CMB) data (Knox & Dodelson, 1999). A flat universe ($\Omega_{\text{total}} = 1$) together with $\Omega_M < 1$ thus suggested that matter is not the only energy component of the universe.

New, direct evidence for this unidentified energy, which we will call the “dark energy,” came with the magnitude/redshift measurements of type Ia supernovae at high redshifts by two independent teams (Perlmutter et al., 1999; Riess et al., 1998). The observed high-redshift supernovae are fainter than would be expected if all energy density were due to matter or to matter together with space curvature.

This faintness can be understood if, contrary to expectation, the universe is accelerating. The General Theory of Relativity shows that this happens if the *total* equation of state ratio (that is, the total pressure divided by the total density in the universe) is less than $-1/3$. Since the equation of state for (pressureless) matter is zero, this requires the existence of an energy component which has negative pressure, and whose energy density is $\Omega \sim 0.6 \sim 1 - \Omega_M$. If the energy were nearly or exactly smooth, it would not have been seen in large-scale structure surveys. The most obvious candidate

is energy of the vacuum, the cosmological constant (Λ).

The cosmological constant was first introduced by Einstein as a term in his equations of General Theory of Relativity in order to explain a static universe, only to be rejected by him as his “greatest blunder”. Physicists have reintroduced Λ from time to time, only to discard it again. If there is a cosmological constant, its contribution to the energy density of the dark energy cannot be much greater than the critical energy density. This “measurement” presents one of the most serious problems in all of particle physics: why is ρ_Λ so small? A straightforward dimensional argument taking its scale from Newton’s gravitational constant would predict an energy density of the vacuum 10^{120} times bigger than the upper limit quoted above. For an excellent review of the cosmological constant problem, see Weinberg (1989).

Dark energy candidate	w ($p = w\rho$)
Λ	-1
Cosmic strings	$-1/3$
Domain walls	$-2/3$
Quintessence (tracker)	$\gtrsim -0.8$
Quintessence (PNGB)	time-variable

Table 2.1: Some candidates for the dark energy and their respective equations of state.

There are alternative sources of energy density whose equation of state $p = w\rho$ has $w < -1/3$. See Table 2.1. A scalar field rolling down its potential and providing significant energy density has been proposed and investigated in the late 1980’s (Ratra & Peebles, 1987). With recent evidence for the accelerating universe, there was a surge of interest in these scalar fields, also called “quintessence” (Caldwell, Dave, & Steinhardt, 1998; Zlatev, Wang, & Steinhardt, 1999). For certain effective potentials the energy density in the quintessence field tracks that of the dominant component (radiation or matter) and can become dominant at late times (Steinhardt, Wang, & Zlatev, 1999). These “tracker” solutions can thus provide an answer to the “cosmic coincidence problem”: why do we live at a special time in the history of universe when the energy densities in matter and dark energy are the same order of magnitude? Quintessence couples to matter only gravitationally and clusters only on very large scales (larger than the horizon). In order for big-bang nucleosynthesis to proceed unhampered and

for baryonic structure to grow sufficiently on small scales, quintessence is required to be sub-dominant throughout the past history of the universe and can begin dominating the energy density only recently ($z \sim \text{few}$).

Another class of scalar-field models are Pseudo-Nambu-Goldstone Boson (PNGB) models (Frieman et al., 1995; Coble, Dodelson, & Frieman, 1997). In these models, the field is initially at rest on the potential, held by large friction term (large Hubble parameter) in the early universe. The field starts rolling at late times, when the Hubble parameter drops to lower values. This generally happens at redshifts of a few, and that is when the field is dynamical.

Yet another class of candidates are cosmic defects (Vilenkin, 1984; Vilenkin & Shellard, 1994), of which cosmic strings and domain walls are the most likely dark energy candidates. Cosmic defects are produced during a phase transitions in the early universe, and can be thought of as strings or walls with energy density. Cosmic defects have negative pressure ($w = -1/3$ for strings and $w = -2/3$ for domain walls) which makes them candidates for the dark energy.

These dark energy candidates and their respective equations of state are given in Table 2.1. “Ordinary” matter candidates like axions, primordial black holes, and lightest supersymmetric particles are candidates for dark matter, but cannot play the role of dark energy since their equation of state has $w = 0$, not $w < -1/3$.

Chapter 3

Summary of Current Results from Type Ia Supernovae

3.1 Introduction

Numerous studies have shown that Type Ia supernovae (SNe Ia) can be used as calibrated “standard candles” with an intrinsic dispersion in peak magnitudes, corrected for various understood effects, of ~ 0.1 mag (Hamuy et al., 1996; Riess, Press, & Kirshner, 1996). The mass density Ω_M , and the normalized cosmological constant Ω_Λ , together describe the space-time geometry of the universe and can be probed using the *relative* luminosity distances to such calibrated standard candles scattered throughout the observable universe. Over a modest range in redshift the luminosity distance is nearly degenerate for various combinations of $(\Omega_M, \Omega_\Lambda)$. However Goobar & Perlmutter (1995) showed that it is possible to break this degeneracy the data in extend far enough in redshift. Using this approach, two independent research groups have presented compelling evidence for an accelerating universe from the observation of high-redshift Type Ia supernovae (SNe Ia) (Perlmutter et al., 1999; Riess et al., 1998).

Measurements of Ω_M and Ω_Λ use the magnitude-redshift relation for Type Ia supernovae (SNe Ia) over a range of redshifts (Perlmutter et al., 1997, 1998, 1999). The basic procedure consists of *a*) discovering large numbers of high- z SNe Ia (> 20 per observing run) while they are still on the rise, *b*) obtaining spectroscopic follow-up within a few days of discovery to confirm the SN type and redshift, *c*) acquiring ground-based and HST light curve photometry, and *d*) analyzing the data to obtain peak magnitudes and measure Ω_M and Ω_Λ .

In the following section, the physics behind a Type Ia Supernovae explosion is reviewed in some detail. Following this, we briefly summarize the experimental results based on observations of several dozen supernovae.

3.2 The Physics of Type Ia Supernova

3.2.1 Progenitors to Explosion

Type Ia supernovae (SNe Ia) are among the brightest known objects in the universe. The classification of these objects is based purely on their optical spectra: “Type I” corresponds to the absence of hydrogen lines, and “a” for the presence of a strong Si II absorption feature (with a trough at $\approx 6150 \text{ \AA}$). Since they form a nearly homogeneous class and simple selection criteria can make the observed dispersion quite small, they are natural cosmological probes (Vaughan et al., 1995). The observed homogeneity has led to a search for a homogeneous progenitor that would satisfy the requirements of lacking hydrogen and occurring in both spirals and elliptical galaxies. This has led to the assumption that the SNe Ia progenitor involves the thermonuclear disruption of a Chandrasekhar-mass white dwarf. The current status of the search for the identification of the SNe Ia progenitor is reviewed in Branch et al. (1995), with the basic two models both involving white dwarfs in a binary system (either one where hydrogen is accreted and turned into C/O through fusion on the surface layers until it approaches the Chandrasekhar limit or a double-degenerate scenario in which two white dwarfs coalesce as gravitational radiation shrinks their orbits).

Observations of SNe Ia show that they have a characteristic light curve shape that can be understood in terms of the radioactive decay of ^{56}Ni to ^{56}Co to ^{56}Fe (Arnett, Branch, & Wheeler, 1985), in which the γ -rays accompanying these decays get thermalized and power the optical light curve. They also have a characteristic development of the optical spectra: near the time of maximum light the spectrum contains lines of intermediate-mass elements from oxygen to calcium; and at late times the spectrum becomes dominated by iron-peak lines. Hydrodynamic explosion models to explain these observations have included deflagration models such as the “W7” model of Nomoto, Thielemann, & Yokoi (1984). While this model is somewhat hand-crafted to fit the observed spectra and suffers from an overproduction of neutron rich species, it remains the standard in the field. The “DD” (Khokhlov, 1991a; Woosley, 1991, delayed detonation,) and “PDD” models (Khokhlov, 1991b, Pulsating Delayed Detonation,) improve the predicted nucleosynthetic yield and gives qualitative agreement with the observed spectra and light curves (Höflich & Khokhlov, 1996).

3.2.2 Light Curves

The model for the photometric history of SNe Ia has been refined from a homogeneous description (Leibundgut, 1988; Branch & Miller, 1993; Sandage & Tammann, 1995) to one that characterizes a relation between peak luminosity and light-curve shape (Phillips, 1993; Hamuy et al., 1993, 1996; Riess, Press, & Kirshner, 1995; Kim et al., 2000). The slower, broader light-curves are intrinsically brighter at peak than the faster, narrower light-curves. Recognizing and exploiting such relations has led to a great increase in value of SNe Ia as extragalactic distance indicators. Extending luminosity/light-curve relations to multiple passbands separates the competing effects of dust, intrinsic differences, and distance on the light of SNe Ia (Riess, Press, &

Kirshner, 1996). Distances with $\sim 10\%$ uncertainty can be obtained using the light-curve shapes of well-observed supernovae.

In Figure 3.1 we see how knowledge of the B -band “stretch”, s , can help determine the relative luminosity of several well observed nearby SNe Ia. From an $s = 1$ template, which is similar to the Leibundgut template for SNe Ia (Leibundgut, 1988), all known light-curves for SNe Ia can be reproduced quite reasonably from the U -band through the V -band (over the time range $-19 \lesssim t - t_0 \lesssim +40$) by stretching (or compressing) the time axis of the light-curve about maximum light by the factor s . The correlation between the stretch and the SN Ia’s brightness is not surprising. SN Ia which produce more ^{56}Ni are more luminous, and hotter, leading to higher overall opacities (Höflich & Khokhlov, 1996). With higher opacities one increases the diffusion time and thus the time the SN Ia takes to reach peak and fade after peak (Arnett, 1982).

3.2.3 Spectra

The optical spectra of SNe Ia are rich in information [see Filippenko (1997, in press) for a review]. Many of the elements synthesized and ejected in the explosion have been identified despite the blending of their high-velocity profiles (Branch et al., 1983; Nugent, 1997). In addition, the relative strengths of some spectral features have been shown to correlate with SN Ia peak luminosity (Nugent et al., 1995a). This is highlighted in Figure 3.2 where we see the ratios of various spectral features in the maximum light spectra of SNe Ia plotted against their relative peak brightnesses. As the supernova evolves, predictable casts of features appear and disappear, illuminated by the photosphere’s recession through the synthesized layers. Due to the amazing homogeneity of SNe Ia the weekly temporal evolution of these features is sufficiently reliable to be used as a clock to determine the current age of a SN Ia to a precision of 1-2 days (Minkowski, 1939; Riess et al., 1997). Figure 3.3 displays the temporal evolution of a typical SN Ia starting at ≈ 14 days before maximum light sampled from several nearby SNe Ia.

3.2.4 Environmental Influences

One of the more recent developments in SN Ia modeling has been the inclusion of differences in the progenitor’s make-up prior to exploding the model. This has led to a wonderful, and simple explanation for the stretch-luminosity relationship. As stated above differences in the total fused ^{56}Ni mass can account for the relationship between stretch and peak brightness. Yet how do we wind up with these differences in the first place? One explanation can be seen in the models of Höflich, Wheeler, & Thielemann (1998). It is well known that differences in the metallicities of 7-10 M_{\odot} main sequence stars can produce both differences in the total C-O core mass as well as the C/O ratio [see Umeda et al. (1999) for a full explanation]. During the thermonuclear explosion white dwarfs with a smaller C/O ratio ($\approx 2/3$) than a typical white dwarf (≈ 1) will produce less ^{56}Ni and have a smaller amount of kinetic energy. This yields a SN Ia which has a smaller peak brightness and narrower light curve due. This also has an affect on the spectral ratios mentioned above.

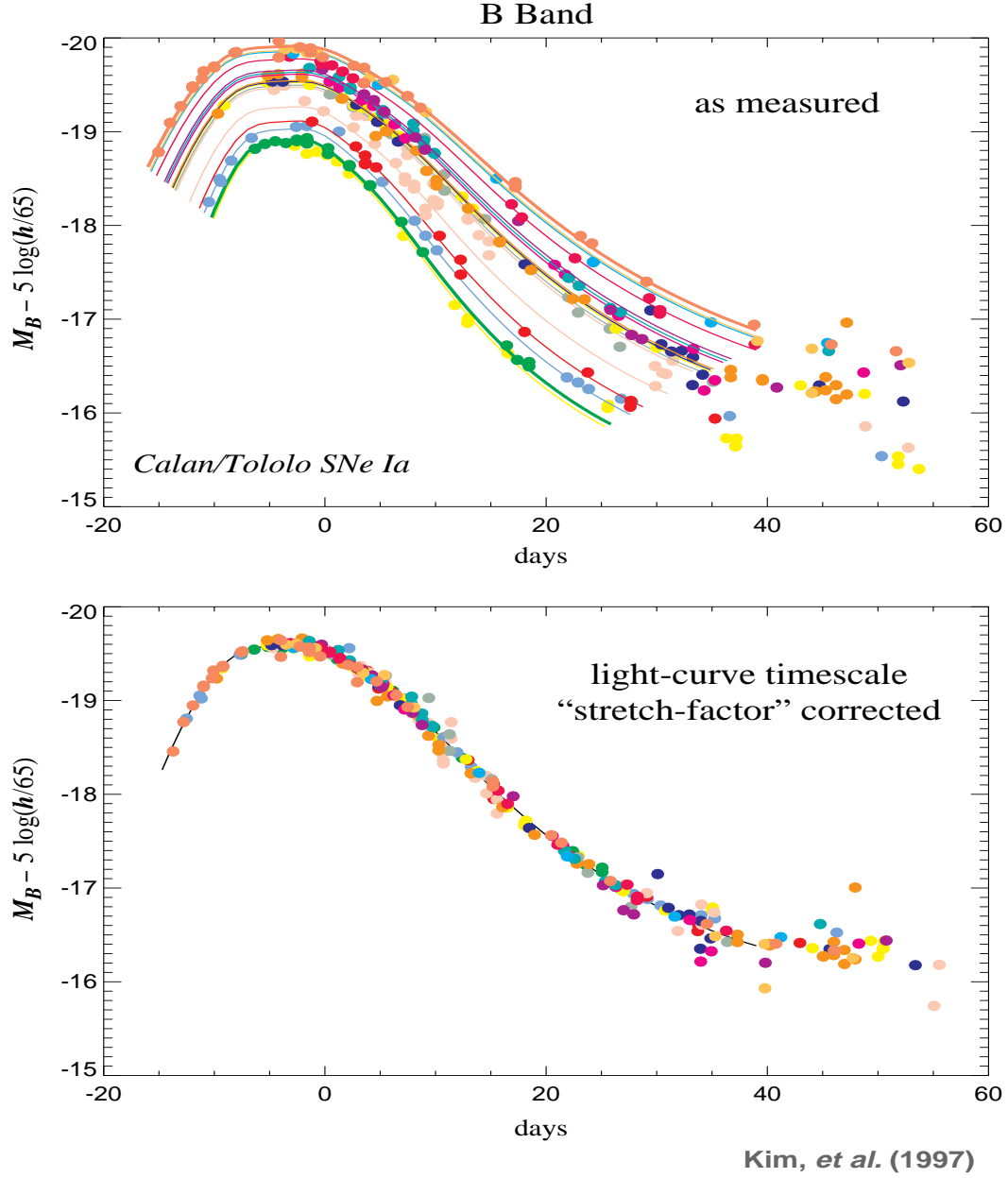


Figure 3.1: The relationship between “stretch” and the luminosity of a Type Ia is seen in these two panels. The top panel shows several SNe Ia from the Calán/Tololo Supernova Survey arranged by their observed relative luminosity (all objects were in the Hubble Flow). The bottom graph shows how “stretch” can be used to describe the light curves with one parameter.

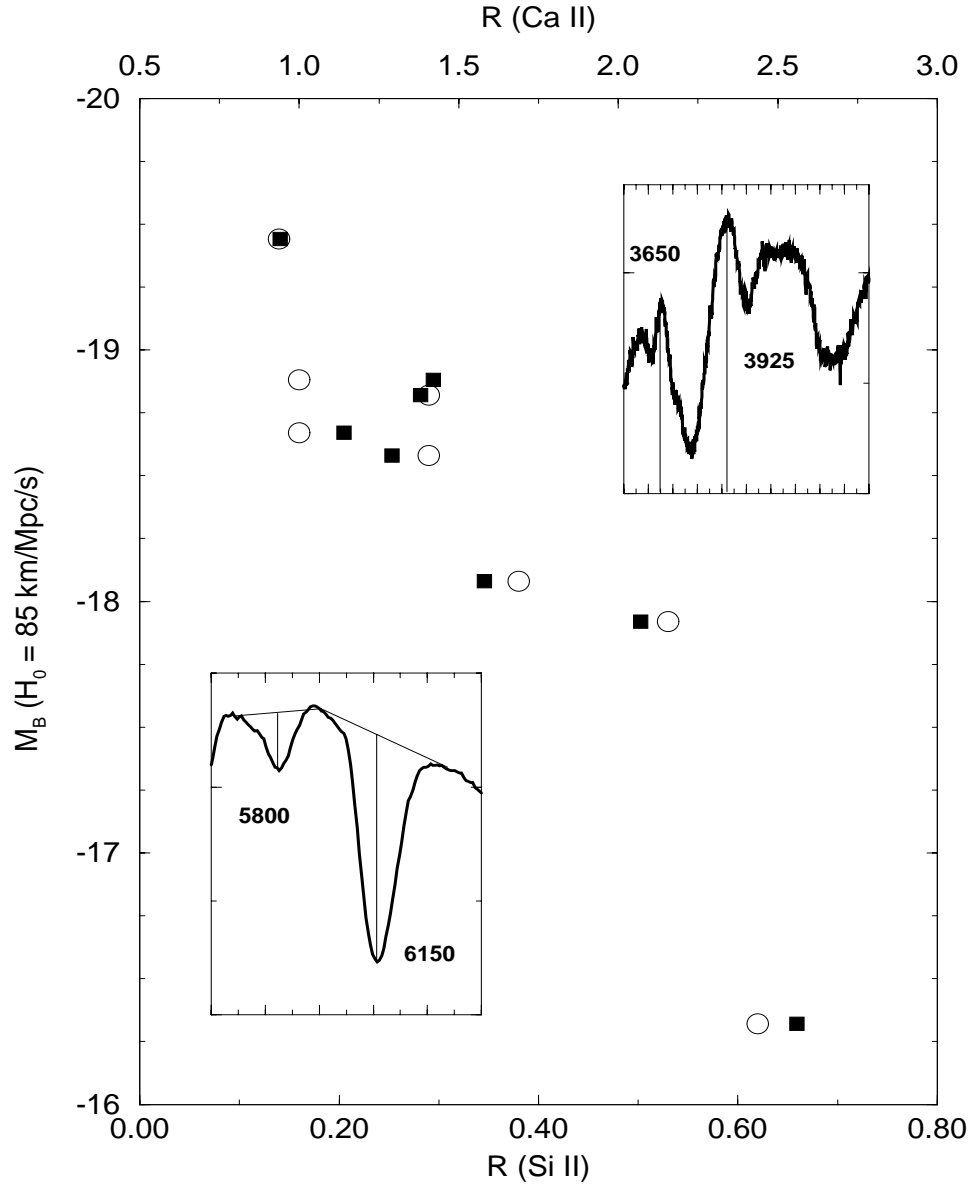


Figure 3.2: Observed M_B vs. $\mathcal{R}(\text{Si II})$ (open circles) and $\mathcal{R}(\text{Ca II})$ (filled squares). The inset graphs illustrate how the ratios were measured. (Nugent et al., 1995a)

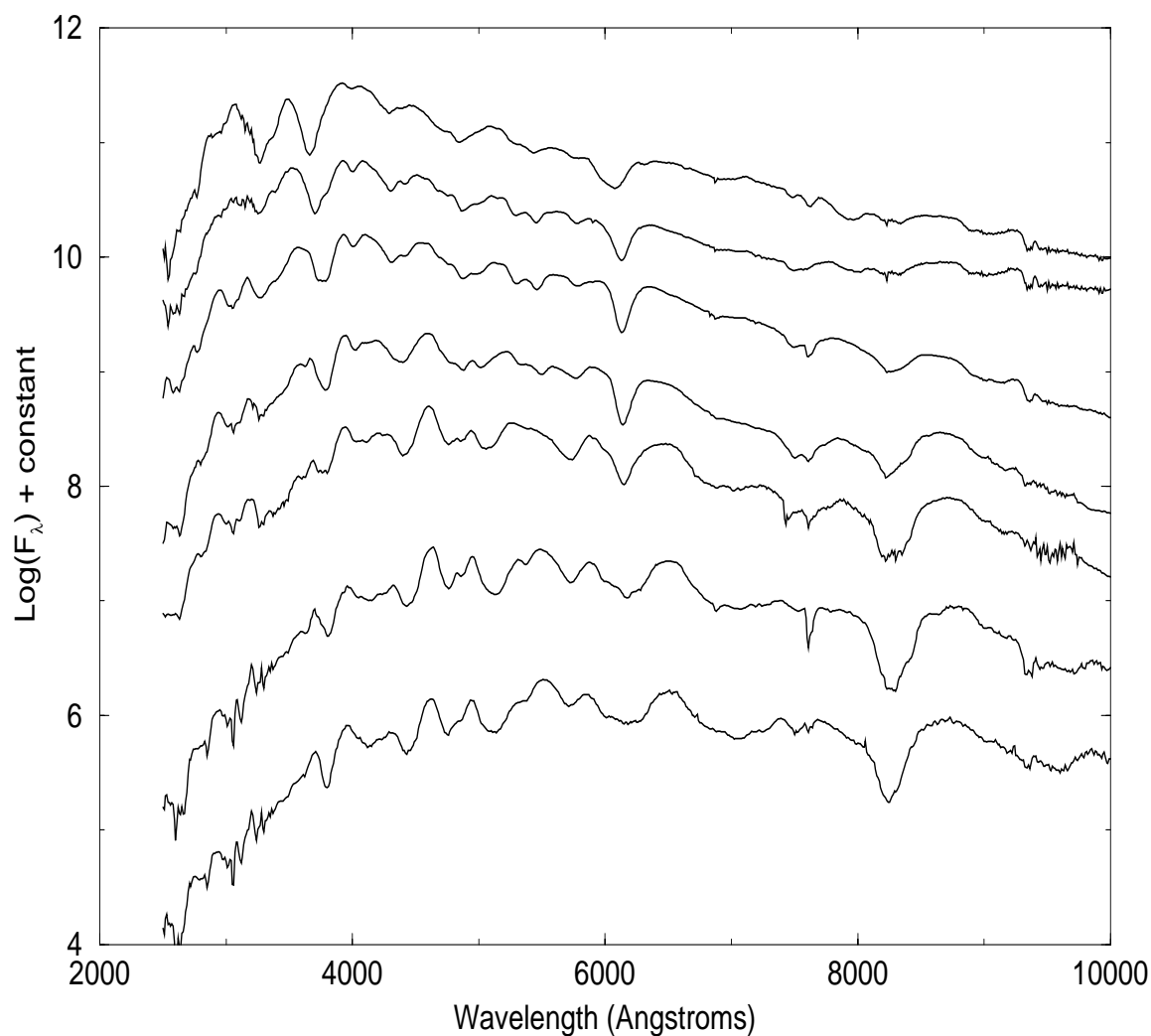


Figure 3.3: A graph of the theoretical weekly temporal evolution of a SN Ia starting at ≈ 14 days before maximum light. (Nugent et al., 1999)

In simulations, Höflich, Wheeler, & Thielemann (1998) have altered the metallicity of the progenitor in the outer, unburned layers. This has a strong influence on the UV spectrum. Lentz et al. (1999) has quantified these effects by varying the metallicity in the unburned layers and computing their resultant spectra at maximum light with the spectrum synthesis code PHOENIX (Nugent et al., 1997; Nugent, 1997). In Figure 3.4 we see the large variations produced in the UV for SNe Ia of differing metallicity. This result is not surprising since the UV spectrum is created by millions of opaque iron-peak lines. Reducing the metallicity results in a lower opacity and higher flux in the UV. Further observations here will be able to quantify these differences at several epochs. In Figure 3.5 we see the affect on the Si II lines in the optical. The metallicity differences are most likely the cause of the 'velocity differences' among SNe Ia that were seen in Branch & van den Bergh (1993).

Further observations in the UV and optical will allow us to quantify these differences at several epochs. We should then be able to look for correlations between these differences and peak brightness, light curve shape and host galaxy type. With these additional data sets we will be able to put very tight constraints on acceptable progenitors, explosion mechanisms and peak luminosities.

3.3 Results from the Observation of Type Ia Supernovae

There are currently two independent teams that are running coordinated search and follow-up observations of high-redshift supernovae. They are the Supernova Cosmology Project (SCP) (Perlmutter et al., 1997, 1998, 1999) which was launched in 1989, and the High-Z Supernova Search Team (HIZ) (Schmidt et al., 1998; Garnavich et al., 1998; Riess et al., 1998) which found their first supernova in 1995.

Both groups use the same basic search techniques and resources and to date have together provided ~ 100 SNe Ia with spectral confirmation discovered at $z > 0.3$. The mean redshifts of the discovered supernovae have been steadily increasing with each successive search run, as we have specifically tailored the filters and exposure times to search at progressively larger distances. We have reached the point where we are now starting to build a statistically significant sample of $1 < z < 1.25$ supernovae.

The current results from both teams (Perlmutter et al., 1999; Riess et al., 1998) using a (largely) disjoint set of high-redshift supernovae studied with different photometry and analysis techniques lead to remarkably similar conclusions. We present here the Perlmutter et al. (1999) results which are statistically more significant.

A Hubble diagram based on results obtained by SCP for 42 SNe with $0.18 < z < 0.83$ is shown in Fig. 3.6. It shows that we live in a low mass-density universe, and presents strong evidence for a cosmological constant [Perlmutter et al. (1999); see also Riess et al. (1998)]. These data indicate that $\Omega_M = 0.28 \pm 0.08$ for a flat universe, and constrain the combination $0.8\Omega_M - 0.6\Omega_\Lambda$ to -0.2 ± 0.1 . Similar results were obtained by HIZ.

The current data imply the existence of a dark energy which might be from the cosmological constant. Alternatively, it could be that this dark energy is due to some other primordial field for which $\rho \neq -p$, leading to different dynamical properties

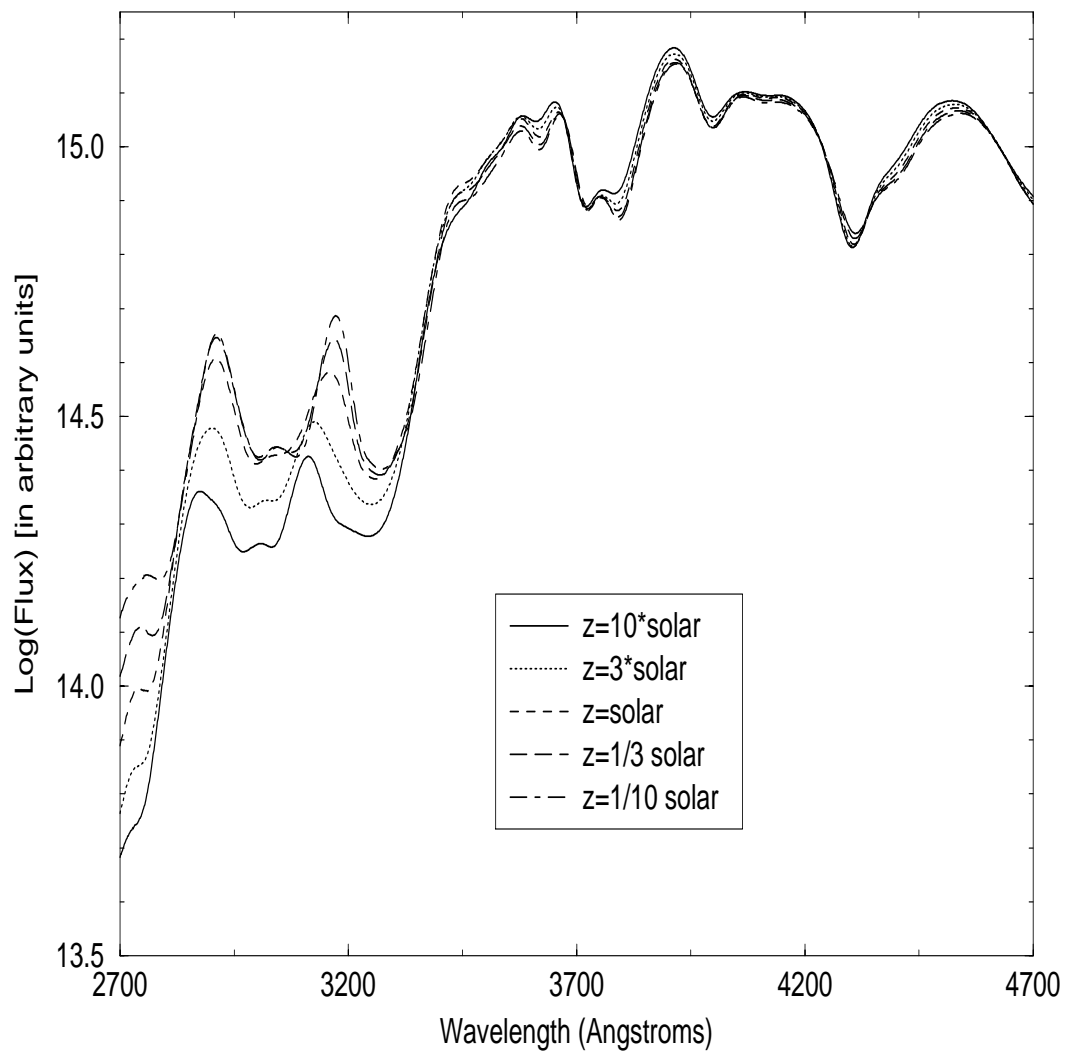


Figure 3.4: Maximum light spectrum synthesis models of W7 (a deflagration model by Nomoto, Thielemann, & Yokoi (1984) of a SN Ia) with varying metallicities.

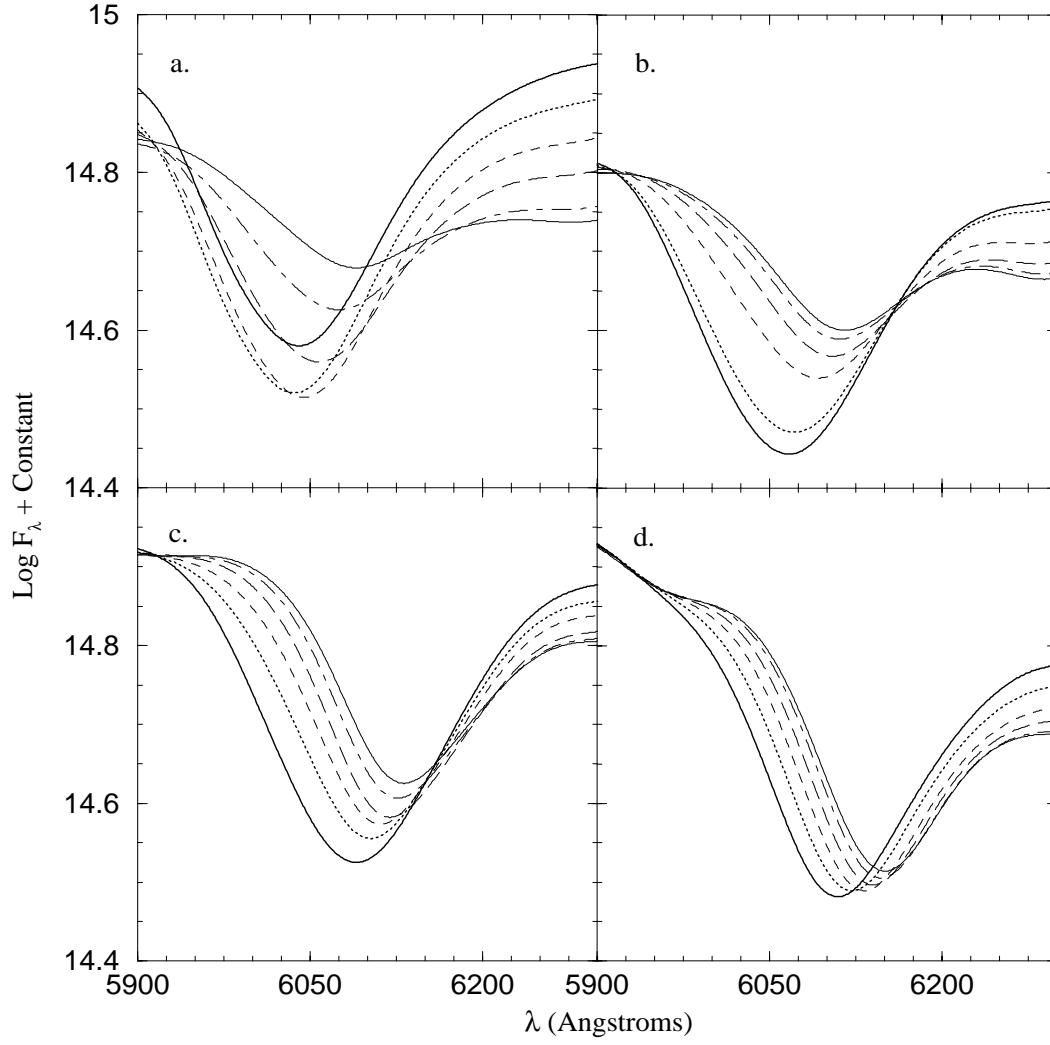


Figure 3.5: Maximum light spectrum synthesis models of W7 (a deflagration model by Nomoto, Thielemann, & Yokoi (1984) of a SN Ia) with varying metallicities.

than a cosmological constant. By parameterizing the field's equation-of-state ratio as $w = p/\rho$, we can currently make some constraints on possible different dark energy models. Perlmutter et al. (1999) finds that for a flat universe, the data are consistent with a cosmological-constant equation of state with $0.2 \lesssim \Omega_M \lesssim 0.4$ (Fig. 3.7). Cosmic strings ($w = -1/3$) are already strongly disfavored.

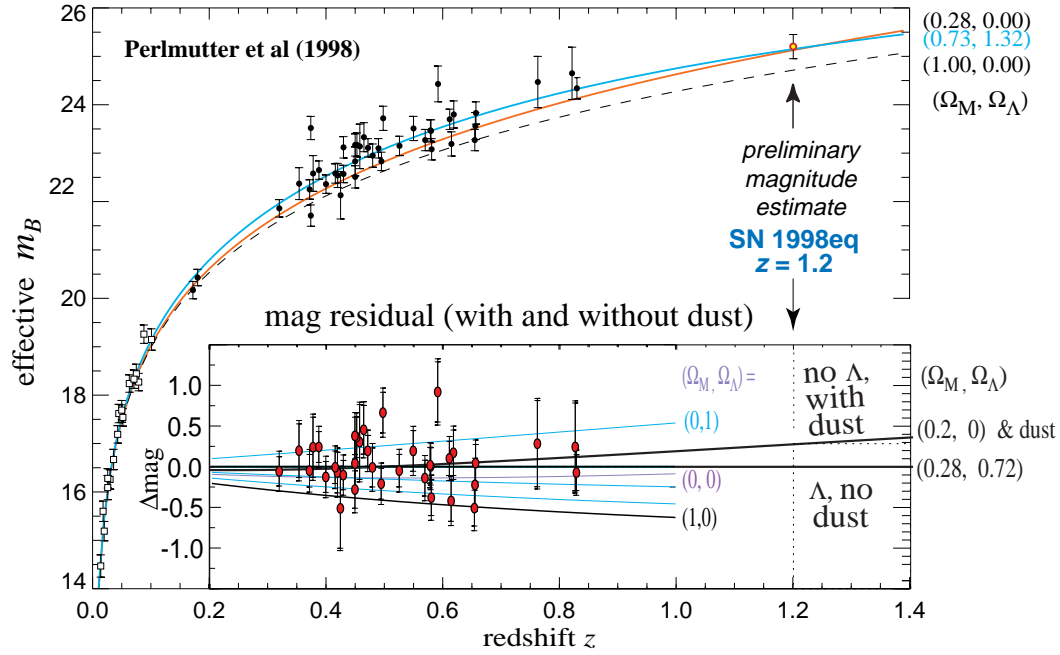


Figure 3.6: Hubble diagram for 42 high- z SNe (Perlmutter et al., 1999). The best-fit world model with $(\Omega_M, \Omega_\Lambda) = (0.73, 1.32)$ is drawn through the data (solid line). The Einstein-de Sitter case $(1.0, 0.0)$ is strongly excluded by the current data (dashed line). The case $(\Omega_M, \Omega_\Lambda) = (0.28, 0.00)$ indicates that some contribution from a cosmological constant is required for values of Ω_M favored by dynamical measurements. The magnitude difference between the best-fit world model and suitable ones with $\Omega_\Lambda = 0$ show redshift dependencies which would be very hard to mimic within the context of SNe evolution or gray dust hypotheses (see inset panel). By extending our survey beyond $z=1$, the *form* of the Hubble diagram alone would become sufficient evidence to support a cosmological constant. The preliminary magnitude estimate of our highest redshift SN1999eq at $z = 1.2$ is suggestive, but more analysis and more SNe at this redshift are necessary.

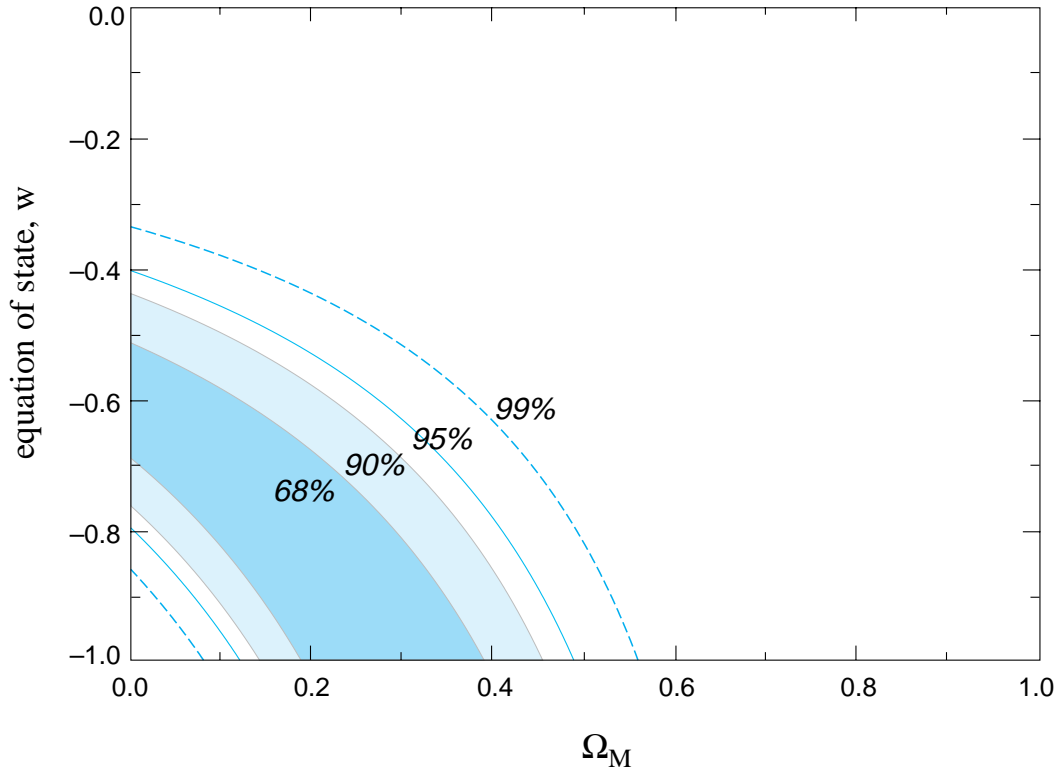


Figure 3.7: Best-fit 68%, 90%, 95%, and 99% confidence regions in the Ω_M - w plane for an additional energy density component, Ω_w , characterized by an equation-of-state ratio $w = p/\rho$. (If this energy density component is Einstein's cosmological constant, Λ , then the equation of state is $w = p_\Lambda/\rho_\Lambda = -1$.) The fit is for the supernova subset of our primary analysis, Fit C, constrained to a flat cosmology ($\Omega_M + \Omega_w = 1$). The two variables \mathcal{M}_B and α are included in the fit, and then integrated over to obtain the two-dimensional probability distribution shown.

Chapter 4

Science reach of the proposed satellite

4.1 Introduction

In this chapter we describe quantitatively the precision with which SNAP will allow us to pin down the cosmological parameters of the universe, and explain how it provides a unique capability to probe the dark energy sector and distinguish between various models. We then present a detailed analysis of the limiting systematic errors, and describe a program of observations that will constrain the sources of systematic error in supernova-based cosmology.

4.2 Constraining the Cosmological Parameters

To estimate the accuracy of parameter determination from the proposed experiment, we performed Monte-Carlo simulations assuming a fiducial model with $\Omega_M = 0.28$, $\Omega_\Lambda = 0.72$ and $w = -1$. Unless otherwise noted, all simulations assume 2366 supernovae distributed from $z = 0$ to $z = 1.7$ with individual uncertainties of 0.15 mag per supernova. The distribution of supernovae in redshift is not uniform; most are in the interval $0.2 < z < 1.2$. Our calculations show that these numbers can reasonably be expected from the baseline version of our proposed experiment after one year of operation. Additional very-low-redshift supernovae that are planned to be observed from ground are not included; their inclusion would further strengthen our arguments about parameter determination.

In the following sections we describe the optimal redshift distribution and present the expected uncertainties on the cosmological parameters using SNAP alone, and by combining SNAP with other complementary experiments. Further sections describe SNAP's ability to distinguish between models that appear degenerate to other experiments, and its ability to explore the dark matter sector

4.3 Exploring higher redshifts ($z \gtrsim 1$)

Energy density in matter scales as $(1+z)^3$, while dark energy scales as $(1+z)^{3(1+w)}$ (with $w \lesssim -1/2$ being favored observationally). Therefore, if the negative-pressure component is dominant or comparable to the energy density in matter today, it had to be sub-dominant throughout the history of the universe, until $z \sim 1$. Supernovae probe precisely the interesting redshift range where dark energy becomes important, $0 < z \lesssim 2$, which makes them a uniquely efficient probe of the dark energy.

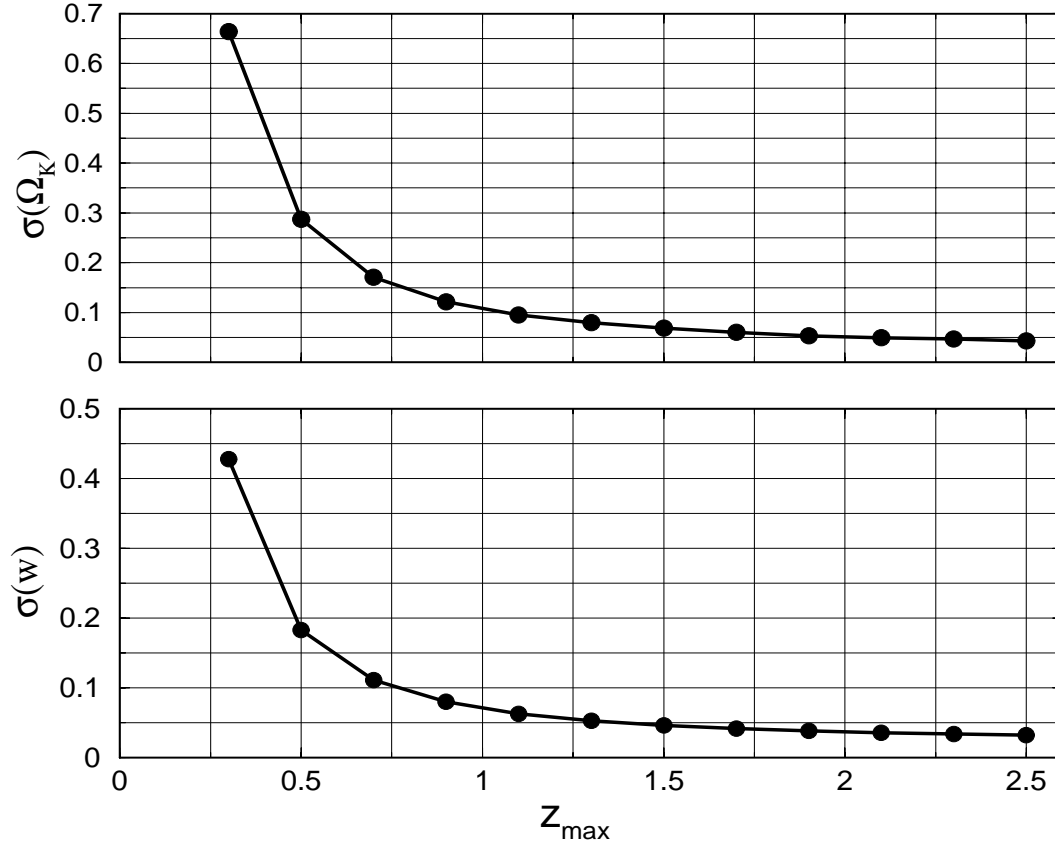


Figure 4.1: Accuracy in parameter estimation as a function of maximum redshift probed in supernova surveys. Shown is the uncertainty in the determination of the curvature energy density Ω_k (upper panel) and equation of state w (lower panel) each as a function of maximum redshift probed z_{\max} . 2366 supernovae distributed from $z = 0$ to z_{\max} are assumed in each case. Exploring redshifts between 0 and 1.5 is optimal, since this is where most of the dark-energy action occurs. Going to redshifts beyond $z \sim 1.8$ would bring very little improvement in parameter-determination accuracy, as the dark energy is dynamically unimportant at such high redshifts.

Figure 4.1 shows the uncertainty in the curvature parameter Ω_k and the uncertainty in the equation of state ratio of the dark energy, w , both as a function of maximum redshift probed. We assumed 2366 supernovae distributed from $z = 0$ to the given

redshift z_{max} with individual calibrated statistical uncertainties of 0.15 magnitudes and distribution in redshift as expected from our experiment and scaled to z_{max} . Fisher-matrix analysis was used to obtain the uncertainties (the Fisher matrix uses expansion of the log-likelihood function about its maximum in parameter space, and gives best statistical errors on parameters calculated from a given data set; see Tegmark, Taylor, & Heavens (1997)). From this figure we conclude the following: 1) using SNe Ia that extend to redshifts of $z = 1$ and higher helps in obtaining higher accuracy because one covers a larger interval of “action” of the dark energy, and 2) going to redshifts much higher than $z \approx 1.5 - 2$ is not useful because dark energy’s contribution to the energy-density is negligible for $z \gtrsim 2$.

4.3.1 Constraints on Ω_M and Ω_Λ

The proposed experiment would put very strong constraints on the energy contents of the universe. Because the distance-redshift relation depends only on a handful of parameters, these parameters would be well determined by the extensive and precise data. Since the experiment would probe redshifts at which the dark component contributes significantly to the total energy density and where it affects evolution of the universe, this especially interesting component would be well characterized.

Assuming that dark energy corresponds to the cosmological constant, this experiment can simultaneously measure Ω_M to an accuracy of 0.03 and Ω_Λ to 0.05. Furthermore, it can test flatness of the universe (that is, measure Ω_k) to 6% independently of the CMB. Assuming further that the universe is flat ($\Omega_\Lambda = 1 - \Omega_M$), Ω_M and Ω_Λ can be determined to accuracy of 0.01. These accuracies are about a factor of ten better than current supernova constraints. Figure 1.1 shows expected constraints from the proposed experiment on the energy densities of matter and vacuum, Ω_M and Ω_Λ , for the case of a flat universe. Figure 4.2 shows the same constraints for the case of a closed universe. Also shown are the current constraints using 42 high-redshift and 18 low-redshift supernovae (Perlmutter et al., 1999).

Table 4.3.1 shows expected uncertainties in the aforementioned parameters for our experiment, for the CMB experiments MAP and Planck with and without the polarization information, for Sloan Digital Sky Survey (SDSS), for MAP and Planck each combined with SDSS, and for MAP with polarization and combined with the knowledge that the universe is flat ($\Omega_k = 0$). It is apparent that the proposed experiment can determine Ω_M and Ω_Λ much more accurately than MAP or Planck by themselves, and it can determine the curvature of the universe, Ω_k , about as well as MAP or Planck, (which is remarkable given that CMB anisotropy probes will be able to measure curvature particularly well). Independent knowledge of cosmological parameters or combination with other experiments helps significantly decrease the (already small) CMB uncertainties; however, the same will in general be true for the supernova experiment.

Our constraints on the cosmological parameters do not depend on the value of the Hubble parameter H_0 . However, one can determine H_0 using supernovae in two ways: 1) by using information from a Cepheid variable in the host galaxy, which would set an absolute distance scale for the given galaxy and 2) by using information from

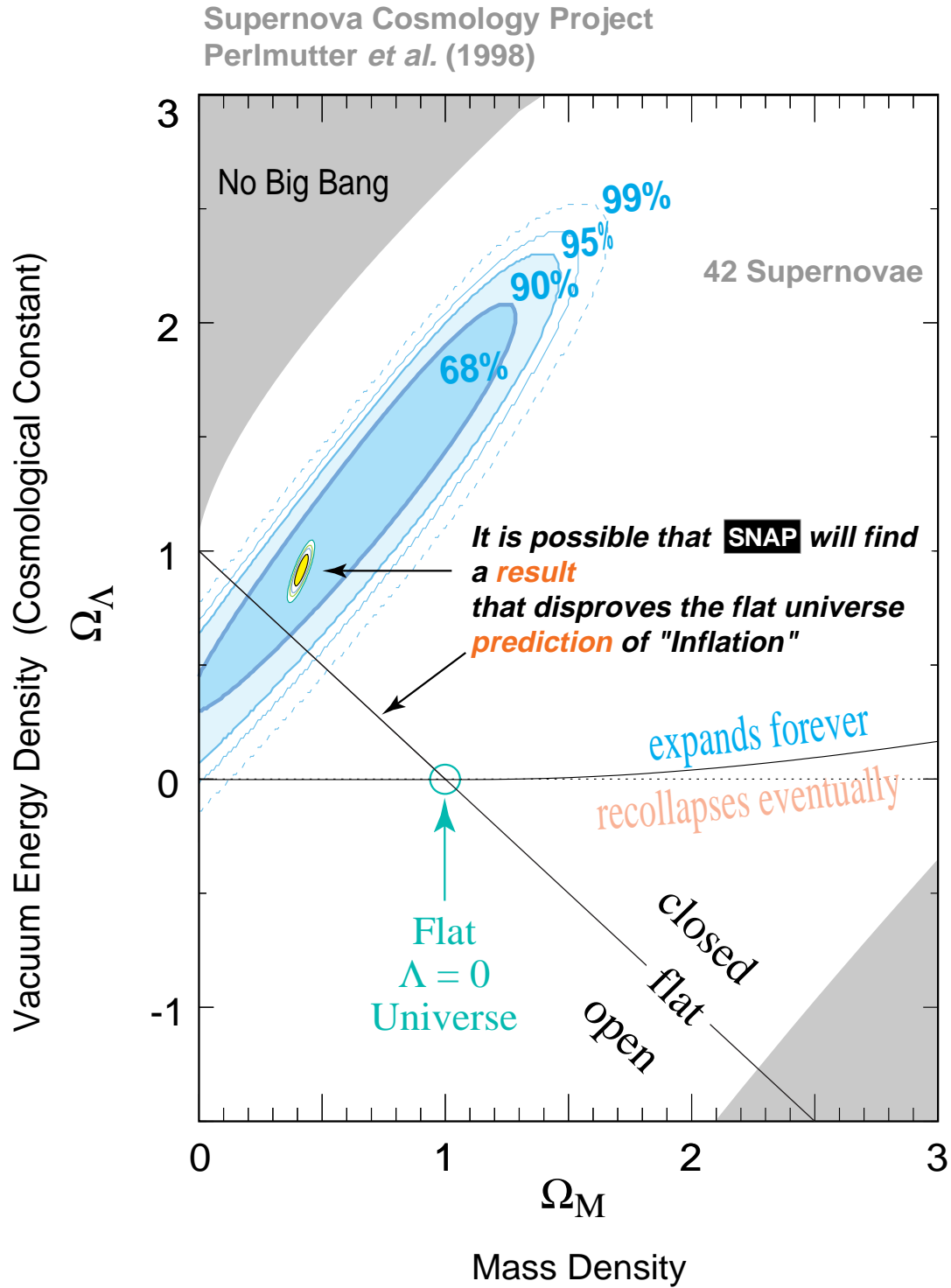


Figure 4.2: Constraints on parameters Ω_M and Ω_Λ expected from the proposed experiment compared to current supernova constraints. This figure shows the case of a closed universe.

	σ_{Ω_M}	σ_{Ω_Λ}	σ_{Ω_k}
SNAP	0.03	0.05	0.06
SDSS	0.23	∞	∞
MAP	1.40	1.10	0.31
MAP(P)	0.24	0.19	0.05
MAP+ Ω_k	0.10	0.10	— — —
Planck	1.20	0.96	0.26
Planck(P)	0.14	0.11	0.03
MAP(P)+SDSS	0.036	0.042	0.015
Planck(P)+SDSS	0.027	0.024	0.005

Table 4.1: SNAP constraints on Ω_M , Ω_Λ and Ω_k compared to those expected from SDSS, MAP, and Planck with various assumptions as indicated. MAP(P)+ Ω_k indicates that the universe is independently known to be flat ($\Omega_k = 0$). SDSS, MAP and Planck results are based on Fisher matrix analysis (Eisenstein, Hu, & Tegmark, 1999), while SNAP constraint is obtained from Monte-Carlo simulations. Parameters considered and their fiducial values were $\Omega_M = 0.35$, $\Omega_B = 0.05$, $\Omega_\Lambda = 0.65$, $h = 0.65$, $T/S = 0$, $n_T = 0$ and cannot vary. The (P) indicates the use of polarization information.

Type II supernovae, which can yield the distance to the supernova using the expanding photosphere method (see § 6.2). Finally, we would be able to accurately determine the combination $H_0 t_0$ (where t_0 is the age of the universe), since the uncertainty regions in the $\Omega_M - \Omega_\Lambda$ plane are almost parallel to contours of constant age (Perlmutter et al., 1999).

4.3.2 Breaking the parameter degeneracies

It is well-known that cosmology experiments suffer from so-called degeneracies, where different combinations of parameters yield the same observable (Goobar & Perlmutter, 1995; Bond, Efstathiou, & Tegmark, 1997; White, 1998; Efstathiou & Bond, 1999). In experiments sensitive to many parameters, these degeneracies can lead to drastic reductions in the accuracy of parameter determination.

Besides determining several important cosmological parameters independently, the proposed SN experiment will have the ability to break degeneracy from other experiments, notably CMB anisotropy probes and, to a lesser degree, LSS surveys. For example, Eisenstein, Hu, & Tegmark (1999) demonstrate that combining CMB and SN measurements can lead to improvement of up to a factor of 10 in determination of Ω_M and Ω_Λ due to breaking of degeneracies – much more than the naively expected $\sqrt{2}$ improvement.

As an example of just how strong the proposed experiment can be in breaking these degeneracies, we show the following example, based on Huey et al. (1999); Wang (1999, private communication). We consider four quintessence models (quintessence is a scalar-field candidate for the dark energy, and is discussed in the next section). These models have different equations of state ratios ($w = -5/6, -2/3, -1/2, -1/3$) and are all degenerate with the fifth, a model with a cosmological constant and cold dark matter. In other words, parameters of each model (quintessence energy density Ω_Q , scaled Hubble parameter h , baryon energy density Ω_B) were chosen so that they are indistinguishable in the CMB data. Upper panel of Figure 4.3 shows overlapping CMB spectra for two of these models, while the middle panel shows matter power spectra for those models, with SDSS projected standard errors (assuming $w = -2/3$ fiducial model). Note that the degeneracy remains even after the SDSS data are taken into account. Lower panel of the same figure shows the magnitude-redshift curves for the same models (with $\Delta m = m - m_{open}$, where m is the magnitude for a given universe and m_{open} that for an open $\Omega_M = 0.3$ universe) and error bars expected from the proposed experiment. The supernova telescope would be able to conclusively distinguish one model from the others and break the degeneracy.

4.3.3 Measuring the equation of state of the dark energy

How can we distinguish between alternative models like quintessence and a cosmological constant? It turns out that the equation of state ratio of the dark energy $w = p/\rho$ is by far the most important parameter. In models with adiabatic initial perturbations w governs the background evolution of the dark energy through Friedmann's equations (Hu, 1999; Hu & Eisenstein, 1999) (the other two parameters in these models, effective

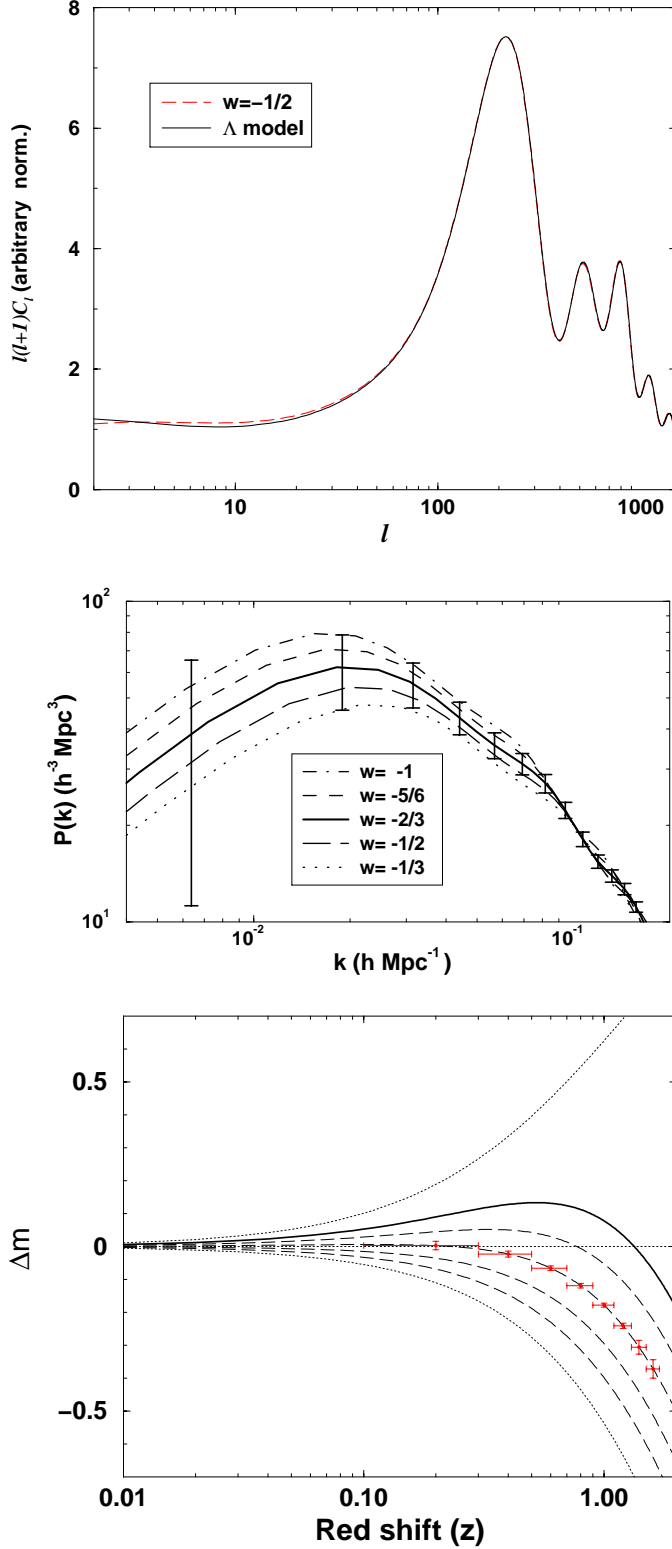


Figure 4.3: Breaking of the degeneracy. Four quintessence models are chosen (with $w = -5/6, -2/3, -1/2, -1/3$), each CMB-degenerate with a vacuum-energy dominated universe ($w = -1$). *Upper panel:* CMB power spectra for two of the five models; note that the power spectra overlap. *Middle panel:* matter power spectra for the same five models with SDSS projected standard errors. Note that the models still cannot be distinguished. *Lower panel:* the same five models shown on a magnitude-redshift graph, with errors predicted from our proposed experiment. The dashed lines are the quintessence models, the solid line is the Λ CDM model, and $\Omega_\Lambda = 1$ (upper dotted) and $\Omega_M = 1$ (lower dotted) curves are added for reference. The models are readily distinguishable by our experiment.

and viscous speeds of sound, govern only the evolution of perturbations, which are super-horizon-sized and difficult to detect with any cosmological probe). The equation of state ratio also parameterizes cosmic defects, such as strings and domain walls, which generate isocurvature perturbations.

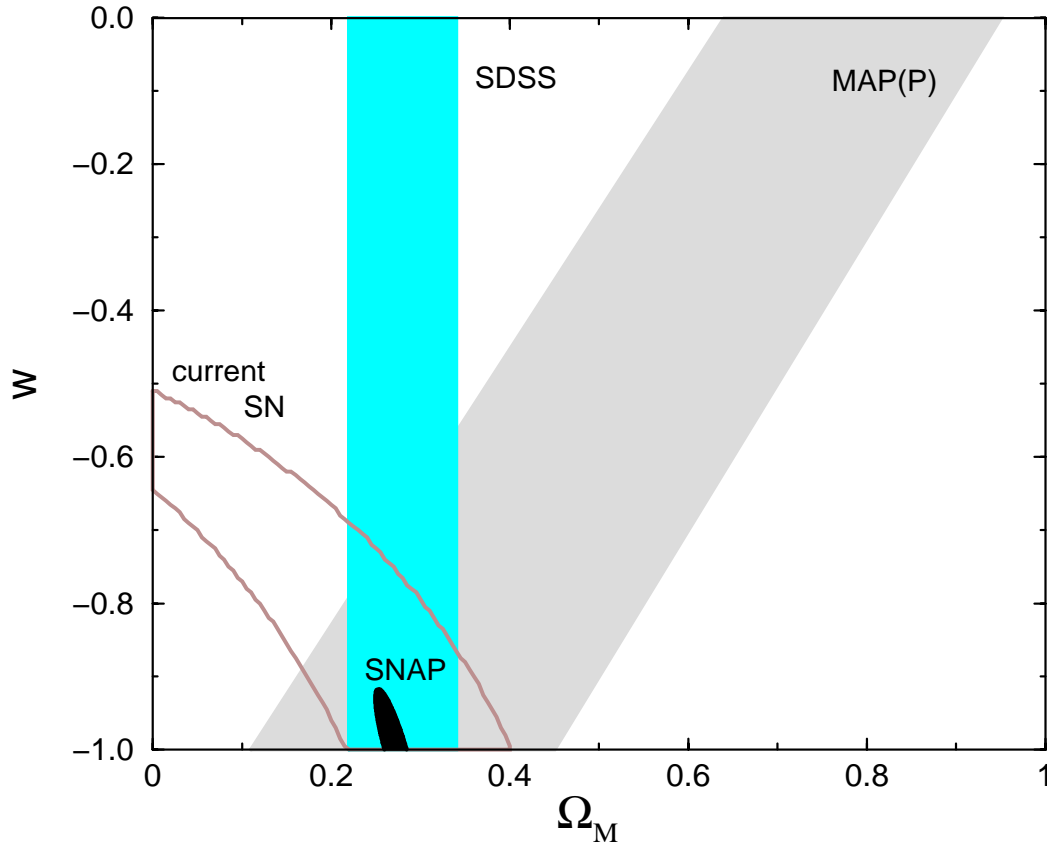


Figure 4.4: SNAP constraint on parameters Ω_M and w compared to those of MAP with polarization information and SDSS (MAP and SDSS constraints are from Hu, Eisenstein, & Tegmark (1999)). Also shown are the present constraints using a total of 54 SN. All constraints assume a flat universe and $\Omega_M = 1 - \Omega_{DARK} = 0.28$, $w = -1$ as fiducial values of the parameters. MAP and SDSS constraint regions are obtained using a Fisher matrix analysis, while SNAP constraint is obtained using a Monte-Carlo simulation.

Figure 4.4 dramatically shows that our experiment is likely to be the strongest single probe of the dark energy. It shows constraints in the Ω_M - w plane, where w is equation of state ratio of the dark energy (assumed constant). A flat universe is assumed. Also shown are the constraints expected from MAP (with polarization) and SDSS, after marginalization over other relevant parameters (taken from Hu, Eisenstein, & Tegmark (1999)). The proposed SNAP experiment would improve upon the present constraint on w by about an order of magnitude, and would also constrain the dark component much better than either CMB or LSS experiments.

Our measurements of the dark energy will complement those of CMB, which have more sensitivity to physics at higher redshifts ($z \lesssim 1100$). Dark energy affects the CMB in three ways: by contributing to the distance to the surface of last scattering, through the Integrated Sachs-Wolfe (ISW) effect and through gravitational clustering. All three effects are small – the first one because dark energy “disappears” at redshifts greater than a few, and the ISW and clustering because they are small and affect low multipoles of the CMB spectrum only, where cosmic variance is significant. Large-scale structure surveys, on the other hand, effectively measure clustering of matter, and are weakly sensitive to the dark energy, which is expected to cluster on super-horizon scales only, if at all. Other cosmological probes, such as Sunyaev-Zeldovich effect in galaxy clusters, gravitational lensing and abundance of galaxy clusters, are generally very weakly sensitive to the presence of the dark energy.

	SNAP	SDSS	MAP	MAP(P)	Planck	Planck(P)
σ_{Ω_M}	0.03	0.04	1.19	0.86	0.11	0.11
σ_w	0.05	55.3	2.45	1.96	0.27	0.25

Table 4.2: Constraints on Ω_M and w assuming a flat universe. SDSS, MAP and Planck results are based on Fisher matrix analysis (Hu, 1999, private communication; Hu, Eisenstein, & Tegmark, 1999), while SNAP constraint is obtained from Monte-Carlo simulations. The (P) indicates use of polarization information. Note that Planck(P) may be able to fit for a value of w but can not measure the *time-dependence* of the expansion.

Table 4.2 shows values for the uncertainties in Ω_M and w from upcoming LSS and CMB surveys and from the proposed SNAP experiment. Again, CMB and LSS results are based on the Fisher matrix analysis (Hu, 1999, private communication; Hu, Eisenstein, & Tegmark, 1999), while those for of our experiment are based on a Monte-Carlo simulation. As this Table shows, the proposed experiment will constrain the equation of state of the dark energy a factor of five better than the Planck satellite with polarization information.

Accurate determination of the equation of state of dark energy is one of the most important and exciting tasks that cosmology faces. The proposed experiment would not only distinguish conclusively between, for example, the cosmological constant and domain walls, but could also probe the properties of dark energy. For example, since tracker quintessence models obey the Ω_M - w relation for any given potential (Steinhardt, Wang, & Zlatev, 1999), obtaining a tight constraint in the Ω_M - w plane would rule out many potentials and possibly shed some light on physics in the early universe.

4.3.4 Further explorations of the dark sector

So far, we have assumed that the equation of state of the dark energy is constant. This may not be so. Some dark energy candidates, such as rolling scalar fields, generally produce a time-varying equation of state. While in the tracker quintessence models this change is often small out to $z \sim \text{few}$ (Zlatev, Wang, & Steinhardt, 1999), other models, such as Pseudo-Nambu-Goldstone-Boson models (Coble, Dodelson, & Frieman, 1997) exhibit variable w at small redshifts.

Our analyses shows that the proposed experiment will be able to put constraints on the redshift variation of w . This can be done in several ways – for example, by parameterizing $w(z)$ as a step function with different values in several redshift intervals. One can go even further and consider a continuous $w(z)$ with no parameterization. As an example, we show that with a large set of distance-redshift supernova measurements, such as those provided by the proposed experiment, one may be able to reconstruct the equation of state of the unknown component out to the maximum redshift probed (Huterer & Turner, 1999). Figure 4.5 shows simulated reconstruction of both the effective potential of a realistic quintessence model (Caldwell, Dave, & Steinhardt, 1998) and its equation of state, using supernovae uniformly distributed out to $z = 1.5$ with individual uncertainties of 5% in distance (or 0.11 mag). Intuitively, knowledge of Ω_M and Ω_Λ leaves one unknown parameter in the luminosity distance, the equation of state w . Supernova measurements probe a range of redshifts, thereby revealing the redshift-evolution of w . In addition, if the dark energy is a scalar field, knowledge of the distance-redshift relation can give us kinetic and potential energies of the field separately. This figure shows that the SNAP experiment would open a direct window to the particle physics of the early-universe.

Finally, accurate knowledge of the luminosity distance out to redshift of ~ 1.7 can be useful for other cosmological tests. For example, Starkman, Trodden, & Vachaspati (1999) derive a critical redshift out to which we need to verify acceleration of the universe to establish that the universe is entering an inflationary phase, and that we are not living in a cosmological-constant-dominated bubble. For the currently favored values of Ω_M and Ω_Λ , this critical redshift is $z \approx 1.8$. Clearly, the proposed experiment would be ideally suited to perform this cosmological test.

4.4 Previously Identified Sources of Systematic Uncertainty

In Table 1.1, we summarized the identified sources of systematic error, and give the uncertainty that each contributed to previous measurements. With the proposed satellite experiment, each of these effects can either be measured so that it can become part of the statistical error budget, or else bounded (the target overall systematic uncertainty is kept below ~ 0.02 magnitudes, so that it will contribute comparably to the final statistical uncertainties). The final column of the table summarizes the observations required to reach this target systematic uncertainty.

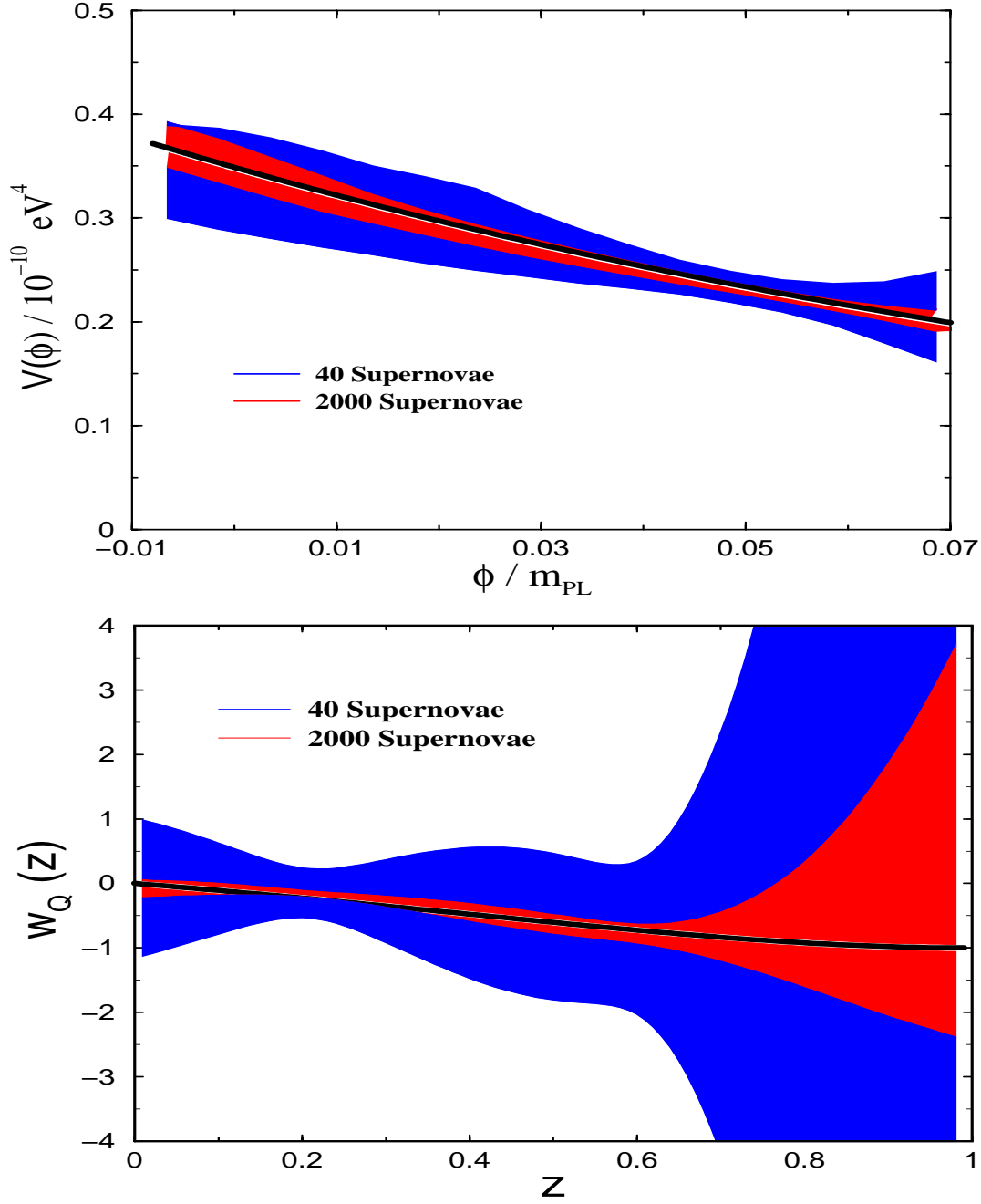


Figure 4.5: *Upper panel:* The 95% confidence interval for the reconstructed potential assuming luminosity distance errors of 5% with 40 and 2000 supernovae (shaded areas) and the original potential (heavy line). This quintessence model has parameters (Caldwell, Dave, & Steinhardt, 1998) $\Omega_M = 0.4$, $V(\phi) = V_0 \exp(-\beta\phi/m_{\text{PL}})$, $V_0 = (2.43 \times 10^{-3} \text{ eV})^4$, $\beta = 8$. The simulated data were fit by a fourth-order polynomial in z . *Lower panel:* Reconstruction of the equation of state for the same potential, except with $\beta = 15$.

Malmquist Bias: *Contributed 0.04 uncertainty on Ω_M^{flat} in previous studies.* This is the sampling bias due to any low-versus-high-redshift difference in detection efficiency of intrinsically fainter supernovae. For the target redshift range, the proposed experiment will detect every supernova in the observed region of sky at 10% of its peak brightness, eliminating this source of systematic uncertainty.

Requirement: Detection of every supernova at least 2.5 magnitudes below peak.

K-Correction and Cross-Filter Calibration Uncertainty: *Contributed 0.025 uncertainty on Ω_M^{flat} in previous studies.* The K -correction uncertainty is the systematic uncertainty due to any uncorrected mismatch between the photometry filters' transmission functions (in the supernova restframe) at high redshift and at low redshift. These generally small mismatches would be corrected perfectly if the supernova's spectral time series were known. The proposed experiment will provide such time series for a representative sample of supernovae. Cross-filter calibration uncertainty reflects the lack of relative calibration of the magnitude systems of the different filters used at low and high redshifts. This “cross-filter,” cross-wavelength calibration has only been measured crudely from the ground (it requires a known source or detailed knowledge of the atmosphere transmission); the satellite experiment will be designed to fill this gap.

Requirement: Spectral time series of representative SN Ia sample and cross-wavelength relative flux calibration.

Non-SN Ia Contamination Bias: *Bounded at <0.05 uncertainty on Ω_M^{flat} in previous studies.* It is possible for occasional type Ib or Ic supernovae to appear very similar to SNe Ia if the spectrum does not extend redward far enough—and with sufficient signal-to-noise—to include and detect the strong 6250 Å Silicon feature that identifies the SN Ia. This feature redshifts into the near-IR and thus becomes very difficult to observe from the ground. The proposed spectrograph will study this feature for every SN in the target redshift range, eliminating this source of systematic uncertainty.

Requirement: Spectrum for every supernova at maximum light covering the 6300 Angstrom restframe wavelength region, i.e. to 1.7 μm at $z = 1.7$.

Milky Way Galaxy Extinction: *Bounded at <0.04 uncertainty on Ω_M^{flat} in previous studies.* Maps of the extinction in our Galaxy provide good measurements of relative extinction, but there is still some residual systematic uncertainty in the absolute “zero point” of this extinction map. This zero-point uncertainty will be improved with observations by SIRTf and SDSS; SNAP itself will constrain this uncertainty using spectra of hot Galactic subdwarfs. *Requirement: Optical and near-IR spectra of ~ 100 hot Galactic subdwarfs in SNAP field.*

Gravitational Lensing by Clumped Mass (MACHOs): *Bounded at <0.06 uncertainty on Ω_M^{flat} in previous studies.* With the large data sample of ~ 2000 SNe Ia proposed here, it will be possible to average out the effect of any gravitational lensing on supernovae at a given redshift, by including both the rare amplified events and the

common deamplified events—which average to give an undistorted value because the total flux is conserved in a lensed image. This is likely to be a quite small range of distortions at lower redshift, but possibly larger at $z > 1$. (Moreover, by studying the distribution of these amplification/deamplification events at redshifts above $z = 1$, it will be possible to statistically study the line-of-sight distribution of the dark matter that would be causing the lensing.) Note that this uncertainty will also be limited by microlensing studies; see § 6.

Requirement: Large samples of SNe Ia (~ 50 per 0.03 redshift bin) at all redshifts in target range.

Extinction by “Ordinary” Dust Outside the Milky Way: *Contributed 0.03 uncertainty on Ω_M^{flat} for all previously-observed dust that diminishes blue more than red light.* The proposed experiment will be able to obtain cross-wavelength-calibrated data with broad wavelength coverage for each supernova, so that the dimming of the spectrum as a function of wavelength can be measured with high signal-to-noise. This eliminates the systematic uncertainty due to “ordinary” dust that will absorb blue more than red light, since this systematic uncertainty now becomes part of our statistical error budget.

Requirement: Cross-wavelength calibrated spectra, at controlled SN-explosion epochs, that extend to rest-frame $1 \mu\text{m}$.

4.5 Proposed Systematic Error Analysis

To obtain high-accuracy measurements of the cosmological parameters and the time-dependent equation of state for the dark energy, it will not suffice simply to discover and study more supernovae and more distant supernovae. The current SN Ia data set already results in statistical uncertainties that are within a factor of two of the identified systematic uncertainties. There are also several additional proposed systematic effects that might confound attempts at higher precision, in particular the possibilities of “gray dust” and systematic shifts in the initial conditions of supernova explosions through properties of their progenitor stars.

The satellite instrumentation and observation strategy were designed to obtain a dataset that provides comprehensive control of the major sources of systematic uncertainty. For each supernova, a set of observations is obtained that will monitor its physical properties. This will also allow studies of effects that have *not* been previously identified or proposed.

Below we first address the sources of systematic errors and then describe the full set of observables that constrain them.

4.5.1 Gray dust

Extinction of light from supernovae can lead to overestimation of their distances. Observed colors are an effective test, since typical dust reddens incoming light. However, it has been suggested by Aguirre (1999) that certain large (up to $\sim 0.1 \mu\text{m}$), and possibly needle-like, dust grains can be expelled from galaxies via radiation pressure and can

have an opacity curve that is shallow in optical bands, thus making them absorptive while producing only small color excess (see Fig. 4.6). The existence of such dust would lead the unwary cosmologist into underestimating Ω_M or overestimating Ω_Λ .

If there is gray dust that has had insufficient time to diffuse uniformly in intergalactic space, different lines of sight would have differing amounts of extinction due to clumping. This would result in an increase of observed supernova magnitude dispersion, an effect that is not seen in current observations. Figure 4.7 compares the magnitude-residual distributions to the Gaussian distributions expected given the measurement uncertainties and an intrinsic dispersion of 0.17 mag. Both the low- and high-redshift distributions are consistent with the expected distributions; the formal calculation of the SN Ia intrinsic-dispersion component of the observed magnitude dispersion ($\sigma_{\text{intrinsic}}^2 = \sigma_{\text{observed}}^2 - \sigma_{\text{measurement}}^2$) yields $\sigma_{\text{intrinsic}} = 0.154 \pm 0.04$ for the low-redshift distribution and $\sigma_{\text{intrinsic}} = 0.157 \pm 0.025$ for the high-redshift distribution.

The Hubble diagram extended to $z \sim 1.3$ also tests for gray dust. Sufficient dust to explain our $z \sim 0.5$ data without Λ predicts fainter SNe at $z \sim 1.2$ than the cosmology with Λ . *Preliminary* data for SN1998eq falls on the brighter (no dust) curve; Fig. 3.6.

As discussed in the Executive Summary, it is also possible to detect $z \lesssim 0.5$ gray dust by comparing optical and near-IR photometry of SNe Ia found in this redshift range.

Finally, as Fig 4.6 shows, the light from galaxies and quasars permeating the intergalactic medium will heat any dust — whether gray or not — causing it to re-emitting in the far-infrared (FIR). Observations limiting the strength, or even detecting, the FIR background place an upper limit on the amount of gray dust allowed. However, normal galaxies heat their own internal dust which also re-emits in the FIR. Only the difference between the FIR emission from galaxies and the total FIR background can come from intergalactic dust. Current SCUBA observations at 850 μm are already close to ruling-out gray dust. Future deeper observations with SCUBA and SIRTf will provide even stronger constraints on the amount of gray dust allowed.

4.5.2 Evolution

Type Ia supernovae with different progenitor properties should result in explosions with slightly differing properties, even if there is only one mechanism for creating Type Ia supernovae, and even if this mechanism has a set “trigger” such as the Chandrasekhar limit. If these differences are not corrected by the light curve width-luminosity relation presently in use, *and if the distribution* of key parameters of the progenitor stars changes with redshift, the Type Ia supernova explosions observed at high redshift could differ in peak luminosity from those at low redshift, leading to a systematic error in the determination of the cosmological parameters. However, the SNAP dataset will allow corrections for these differences, or allow similar SNe Ia to be identified and matched at high and low redshifts thus mitigating against the effects of changing progenitor properties

Parameters which might affect the initial conditions of a supernova explosion include the masses, binary system orbital parameters, and abundance of elements heavier than hydrogen (the abundance of elements starting with oxygen is termed “metallic-

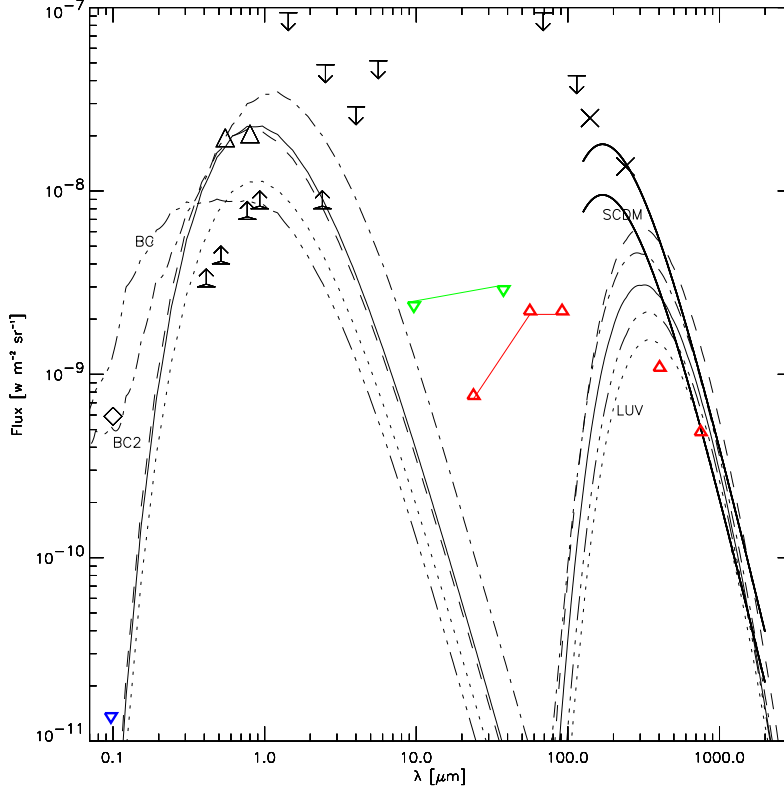


Figure 4.6: FIR dust spectrum (solid line, right) and intergalactic radiation field spectrum (left) for the Aguirre & Haiman (1999) fiducial gray dust model (with the best-fit CMB subtracted) needed to make a $\Omega_M = 0.2$, $\Omega_\Lambda = 0$ cosmology fit the SNe results. Along with the fiducial model, various alternatives for the intergalactic radiation field are shown. These are a model using half the UVB normalization (LUV; dotted), an $\Omega = 1$ model (SCDM; dashed), and models with the Bruzual-Charlot spectral templates (BC; triple-dot-dashed), and reddened B-C templates (BC2; dot-dashed). Observational constraints are the DIRBE FIRB detections (crosses) and upper limits (down arrows), the UVB detections (triangles) and HDF-derived lower limits (up arrows), and the Voyager FUV upper limit (diamond). To the original Aguirre plot we have added lower limits from IRAS galaxy counts at 25, 60, and 100 μm , and from SCUBA source counts at 450 and 850 μm . These are represented with red upward-pointed triangles. We have further added the upper limits in the 10–40 μm region from modeling of the TeV spectra of nearby blazers (green downward triangles), and the EUV upper limits of Donahue, Aldering, & Stocke (1995) (plotted 10 \times too high to fit on the plot). Present SCUBA source counts are close to eliminating the fiducial dust model. Deeper FIR counts from SCUBA and SIRTf should settle the question of whether, or how much, gray dust is allowed.

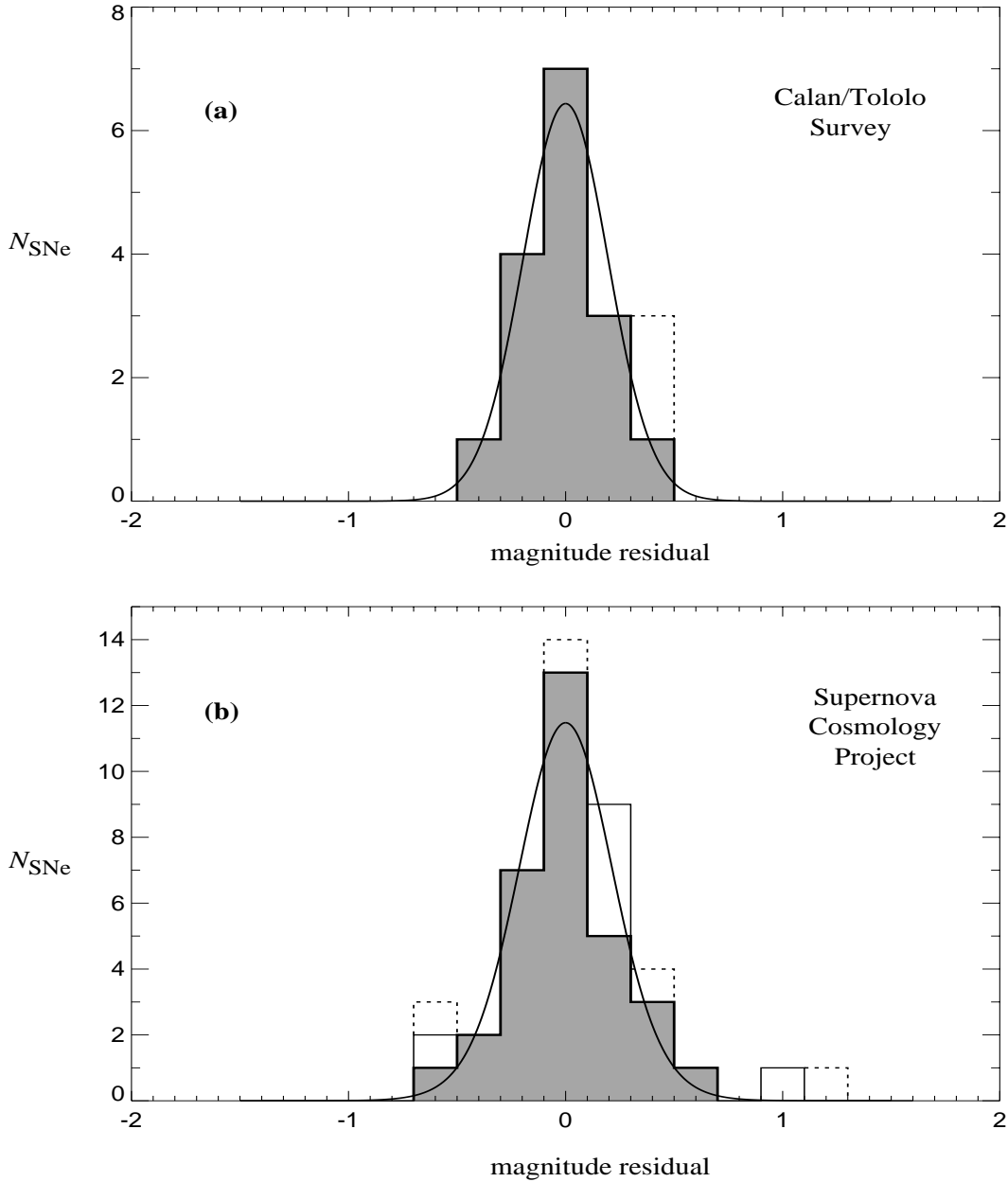


Figure 4.7: The distribution of restframe B -band magnitude residuals from the best-fit flat cosmology for the Fit C supernova subset, for (a) 18 Calán/Tololo supernovae, at redshifts $z \leq 0.1$ and (b) 42 supernovae from the Supernova Cosmology Project, at redshifts between 0.18 and 0.83. The darker shading indicates those residuals with uncertainties less than 0.35 mag, unshaded boxes indicate uncertainties greater than 0.35 mag, and dashed boxes indicate the supernovae that are excluded from Fit C. The curves show the expected magnitude residual distributions if they are drawn from normal distributions given the measurement uncertainties and 0.17 mag of intrinsic SN Ia dispersion. The low-redshift expected distribution matches a Gaussian with $\sigma = 0.20$ mag (with error on the mean of 0.05 mag), while the high-redshift expected distribution matches a Gaussian with $\sigma = 0.22$ (with error on the mean of 0.04 mag).

ity”). The progenitor mass determines the timescale for a star to evolve from birth to the white dwarf stage, and affects the abundance and distribution of heavy elements in the core. The relative masses of stars in a binary system determines which star will become a white dwarf first (the most massive star will), how long that white dwarf will have to wait to accrete mass from — or coalesce with — its companion, and the mass accretion rate (for a Chandrasekhar WD). The binary system orbital parameters likewise affect the later two timescales. Finally, the heavy element abundance affects the stellar evolutionary timescales, the composition and structure of the core, and the mass accretion rate.

As a given galaxy ages, generation after generation of stars complete their life-cycles, enriching the galactic environment with heavy elements over time. In a given generation of stars, the more massive ones will complete their life cycles sooner, so the distribution of stellar masses within that generation will evolve. However, the star formation amongst — or even within — galaxies is not very well synchronized. Some galaxies form new stars fairly uniformly in time, while others experience bursts of star formation followed by billions of years without star formation. There are examples of very young, low-metallicity, galaxies even at the present epoch, and there are examples of old, high-metallicity galaxies at high redshift (see for example Fig. 4.9 where the metallicities of galaxies over the range $0 < z < 1$ are compared). Thus, the distribution of these progenitor parameters is very broad, not well correlated with redshift, and limited only by the age of the universe and the upper mass limit for forming a white dwarf.

There are two complementary paths to searching for and correcting the influence of progenitor properties, and the SNAP dataset will allow both to be pursued. First, the detailed form and development of the supernova spectrum and light curve offers important information of the initial conditions of the explosion itself. In addition, properties of the host galaxy globally and near the location of the supernova can suggest whether a given supernovae might have been young or old, or metal-rich or metal-poor. In particular, although galaxy metallicity and age are difficult to determine, the luminosities, colors, morphology and location within a galaxy can provide an approximate means of determining likely properties of the progenitor each supernova. Indeed, evidence for differences among SNe Ia with differing host galaxy environments has in fact already been seen among nearby, low-redshift supernovae. The range of intrinsic SN Ia luminosities seen in spiral galaxies differs from that seen in elliptical galaxies (Hamuy et al., 1996). So far, it appears that the differences that have been identified are well calibrated by the SN Ia light curve width-luminosity relation. The standard supernova analyses thus already are correcting for a luminosity effect due to the range in progenitor properties. Accounting for more subtle effects requires that the SN Ia sample sizes are sufficiently large and varied at each redshift so that at a minimum we can find matching examples in sufficient quantities, and possibly even correction for such effects, turning a systematic error into a statistical one, and improving Type Ia supernovae as distance indicators in the process.

4.5.3 Observables to Correct or Match SNe

We have identified a series of key observable supernova features that reflect differences in the underlying physics of the supernova. By measuring all of these features for each supernova we can tightly constrain the physical conditions of the explosion, making it possible to recognize supernovae that have similar initial conditions and arise in matching galactic environments. The current theoretical models of SN Ia explosions are not sufficiently complete to predict the precise luminosity of each supernova, but they are able to give the rough correlations between changes in the physical conditions of the supernovae and the peak luminosity (Höflich, Wheeler, & Thielemann, 1998). These conditions include the velocity of the ejecta (a measurement of the kinetic energy of the explosion), the opacity (here we refer to the opacity of the inner layers, which affects the overall light curve shape), metallicity of the progenitor (which affects the early spectra), ^{56}Ni mass (a measurement of the total luminosity), and ^{56}Ni distribution (which might lead to small effects in the light curve shape at early time). We can therefore give the approximate accuracy needed for the measurement of each feature to ensure that the physical condition of each set of supernovae is well enough determined so that the range of luminosities for those supernovae is well below the systematic uncertainty bound ($\sim 2\%$ when all the constraints are used together). The following tables provides a list of these measurements. We also include a table that identifies several characteristics of the host galaxy that will also help us subdivide the SNe Ia into groups that come from very similar environments. There is currently some evidence that some of these host galaxy observables correlate with some of the SNe Ia parameters (Branch, Romanishin, & Baron, 1996).

Observables X	$\partial M_{peak}/\partial X$	Requirement for $m_{sys} < 0.02$
Spectra		
Spectral feature minima	0.04/500 km/s	150 km/s
Spectral feature widths	0.12/100 Å	10 Å
Spectral Feature Ratios	$0.12(B)$, $-0.75(\lambda = 3000\text{Å})$, $1.5(\lambda = 6150\text{Å})$	5%
Light Curves		
Stretch	0.10/5%	1%
Rise Time	0.1/1 day	0.3 days
Peak to tail ratio	0.05/0.2 mag	0.05 mag

Table 4.3: A list of the potential sources and values (m_{sys}) of systematic errors due to unresolved differences among SNe Ia explosion models.

Rise time from explosion to peak. The rise time to peak is an indicator of opacity, fused ^{56}Ni mass and potential differences in the ^{56}Ni distribution. Constraining it to within 0.3 days corresponds to a 0.03 magnitude constraint at peak. To achieve this accuracy requires discovery within ~ 2 days of explosion, on average, i.e. ~ 3.8 magnitudes below peak.

Plateau level 45 days past peak. The light curve plateau level that begins ~ 45 days past peak is an important indicator of the C/O ratio of the progenitor star,

Observables	^{56}Ni Mass	^{56}Ni Distribution	Kinetic Energy	Opacity	Metallicity
Spectral feature minima	◦	—	●	◦	●
Spectral feature widths	◦	—	●	◦	●
Spectral Feature Ratios	●	—	◦	◦	●
Stretch	●	◦	◦	●	—
Rise Time	●	●	◦	◦	◦
Peak to tail ratio	◦	—	◦	●	—

Table 4.4: A list of the observables that constrain the various SNe Ia model parameters. ● = directly related to, ◦ = indirectly related to, and — = slightly related to or no relation to the model parameter.

Parameter	Observable
Host galaxy luminosity	U, B, V, R, I, J, H band photometry
Host galaxy colors	U, B, V, R, I, J, H band photometry
Host galaxy absorption lines	0.3-1.7 μm spectroscopy
Host galaxy emission lines	0.3-1.7 μm spectroscopy
Host galaxy morphology	0.1'' spatial resolution
SNe Ia location in host galaxy	0.1'' spatial resolution

Table 4.5: Host galaxy observables which further constrain the progenitor environment of a SNe Ia.

and fused ^{56}Ni . A 0.1 magnitude constraint on this plateau level corresponds to a 0.02 magnitude constraint at peak. To achieve this accuracy requires a signal-to-noise ratio of 10 for photometry 2.8 magnitudes below peak. Figure 4.8 highlights these differences for two nearby supernovae.

Overall light curve timescale. The “stretch factor” that parameterizes the linear stretching or compression of the light curve time scale is affected by almost all the aforementioned parameters, since it tracks the SN Ia’s evolution from early to late times. It is closely correlated with the two previously mentioned observables, which focus on details of the light curve timescale, and it ties this experiment’s controls for systematics to the controls used in the previous ground-based work. A 1.5% uncertainty in the stretch factor measurement corresponds to a ~ 0.02 magnitude uncertainty at peak. This requires signal-to-noise ratio of 10 for photometry extending from 10 days before peak to 45 days after peak.

Spectral line velocities. The velocities of several spectral features throughout the UV and optical make an excellent diagnostic of the overall kinetic energy of the SNe Ia. The kinetic energy directly influences the overall shape of the light curve. If the velocities are constrained to ≈ 150 km/s then the peak luminosity can be constrained to ~ 0.02 magnitude uncertainty at peak, given a typical SNe Ia velocity of 15,000 km/s.

Spectral Feature Ratios. The ratios of various spectral features in the restframe

UV are strong indicators of the metallicity of the SNe Ia. Since it is well known that the metallicities of *nearby* galaxies vary by large amounts (see Figure 4.9) this is another important parameter to constrain and correlate. As can be seen in Höflich, Wheeler, & Thielemann (1998) the metallicity of the progenitor has a strong influence on the UV spectrum. Lentz et al. (1999) has quantified these effects by varying the metallicity in the unburned layers and computing their resultant spectra at maximum light. By achieving a reasonable signal-to-noise per wavelength bin we will be able to constrain the metallicity of the progenitor to 0.1 dex.

We also note that the ratios of spectral features in the restframe optical (Ca II H&K and Si II at 6150 Å) provide additional constraints on the opacity and stretch of the SN Ia (Nugent et al., 1995a). These features are easily observed given the velocity measurements mentioned above.

All these observables tightly constrain the physical properties of the SN Ia since they either directly or indirectly measure all of the physical parameters that control the light curve and spectral evolution. These parameters include the SN Ia's overall opacity, total ^{56}Ni mass and distribution, and kinetic energy. Each will measure several of these parameters simultaneously, further refining and cross-checking their values. Based on our current understanding of the physics behind SNe Ia, the requirements that we have placed on the observations will allow us to keep the systematics below the 2% level.

4.6 Summary

The satellite we propose would bring tremendous advances in our understanding of cosmology and the universe. By measuring energy densities of matter and the unknown component, we would accurately determine flatness and energy contents of the universe. By measuring equation of state of the dark energy, we would drastically narrow the list of dark-energy candidates, and quite possibly leave a very small subset of previously-considered theories viable. Combining our data with that of other cosmological experiments, notably CMB, would help break parameter degeneracies and make cross-checks among different probes. Finally, with the data from our experiment cosmologists could perform a number of other exciting tests, some of which were already proposed in literature. Given our current lack of knowledge about energy contents of the universe, it is possible that some of these tests would give surprising and unexpected results.

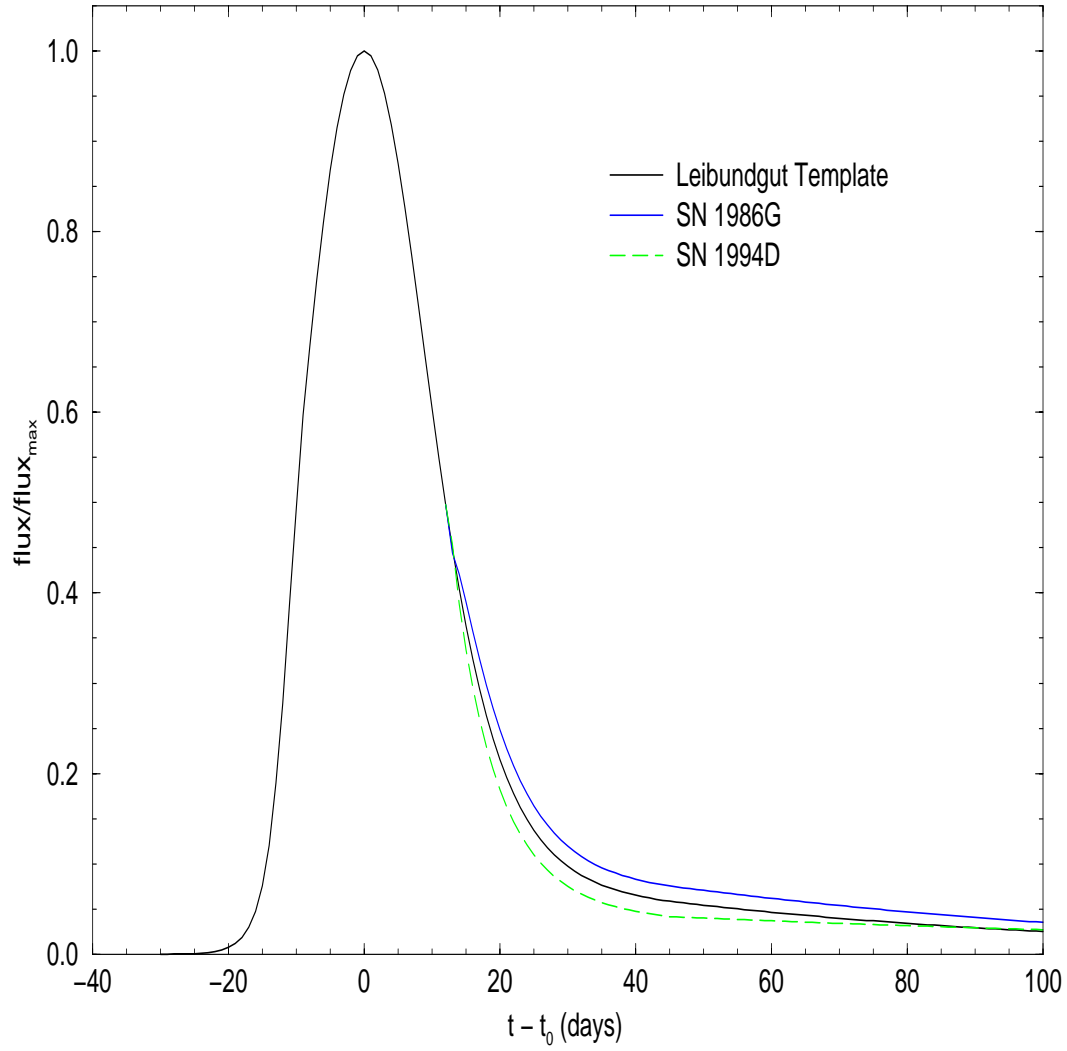


Figure 4.8: The black curve corresponds to the standard modified Leibundgut template. The solid-blue curve shows the late-time deviation exhibited by SN 1986G, while the dashed-green curve shows the late-time deviation for SN 1994D. These differences are expected for progenitors with differing C/O ratios.

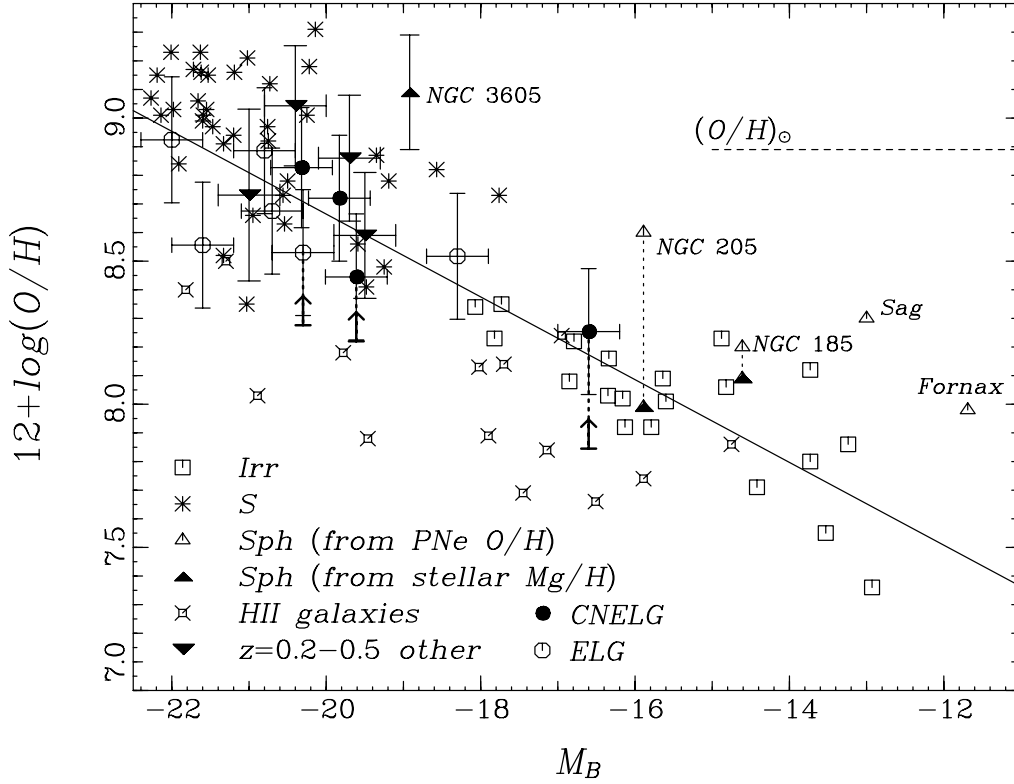


Figure 4.9: The oxygen abundance of $0.1 < z < 0.5$ star-forming galaxies, in comparison to those of nearby galaxies, versus the absolute blue magnitude, M_B , from Kobulnicky & Zaritsky (1999). This shows that metal-rich galaxies at $0.1 < z < 0.5$ (shown as inverted triangles) are common. It also shows that if desired photometric redshifts from SNAP can be used to estimate M_B , and thus (relative) O/H , in advance of selection of which supernovae to follow at high redshift, then M_B can also serve as a surrogate measurement of O/H . Normalization will have to be checked at even higher redshifts.

Chapter 5

Comparison with Alternative Approaches for Supernova Studies

5.1 Introduction

In choosing the best way to advance supernova cosmology, the capabilities, sensitivities, economics, and risk of various facilities need to be compared. Supernovae are point sources, and their study derives maximal benefit from the diffraction-limited imaging possible in space. This is nicely demonstrated by Fig. 5.1, which compares ground-based and HST images of the same supernova explosion.

The principle alternative to a dedicated space-based wide-field telescope like SNAP is to use large ground-based telescopes, possibly working in tandem with current (HST) and future (NGST) non-dedicated facilities in space. The current supernova work at high redshift involves the use of large ground-based telescopes equipped with wide-field imagers to find the supernovae near maximum light, followed by redshift determination and spectroscopic confirmation with the largest ground-based telescope (Keck 10-m) and subsequent photometric follow-up with HST. The quality and quantity of these current datasets are greatly inferior to what SNAP aims for. These data have been quite useful, but they are insufficient to fully test the underlying assumptions that the light-curve width-luminosity relation standardizes all Type Ia supernovae luminosities at all redshifts, that there is no intergalactic extinction, and that no dispersion exists in host-galaxy dust extinction curves. Combining the discovery rate of both the SCP and the High- z Team, at best 20 high-redshift supernovae per year have adequate follow-up observations. Fig. 5.2 shows how the sample of distant Type Ia supernova has been built-up over time. This rate, in and of itself, indicates that vastly improved facilities are necessary to advance supernova cosmology.

The discussion below will make the case that a dedicated SNAP mission has significant advantages over a number of alternatives. Here we summarize how several alternatives would perform were they to attempt the experiment for which SNAP is designed. This allows an examination of just which parts of the experiment would be

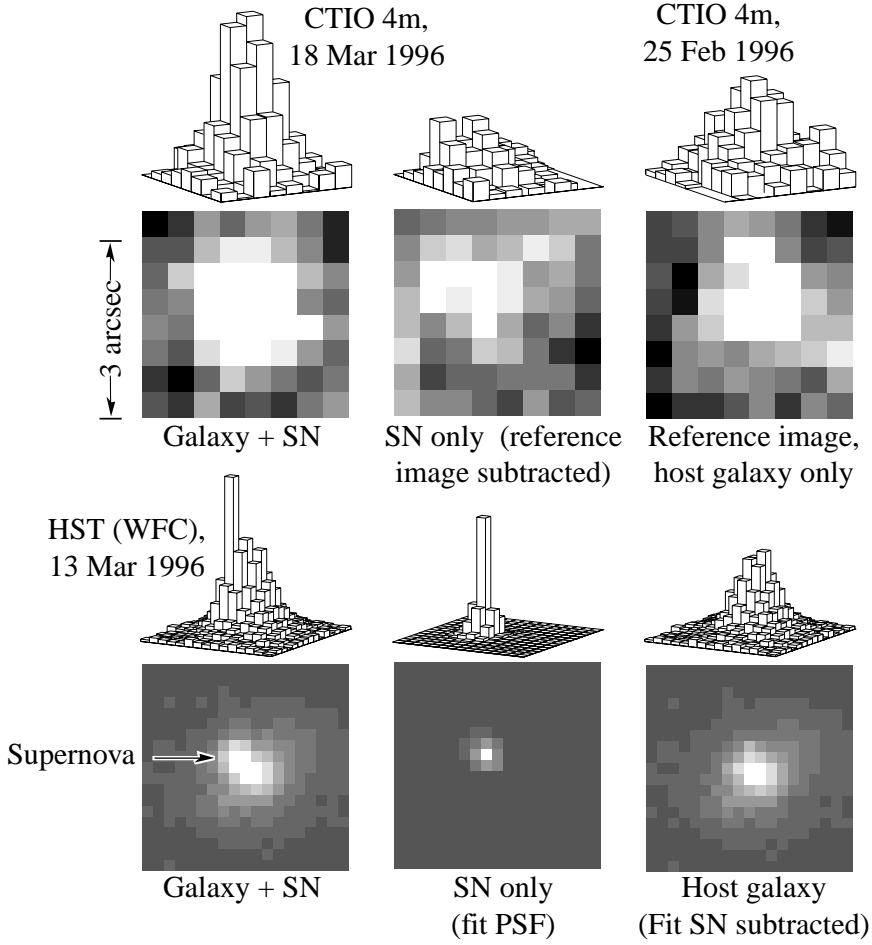


Figure 5.1: A comparison of ground-based and HST WF images of SN1996cl, a second $z = 0.83$ SN found by our project. This SN lies in the cluster MS1054.4-0321 which happened to be observed with HST when the SN was close to maximum light (HST image courtesy of Megan Donahue).

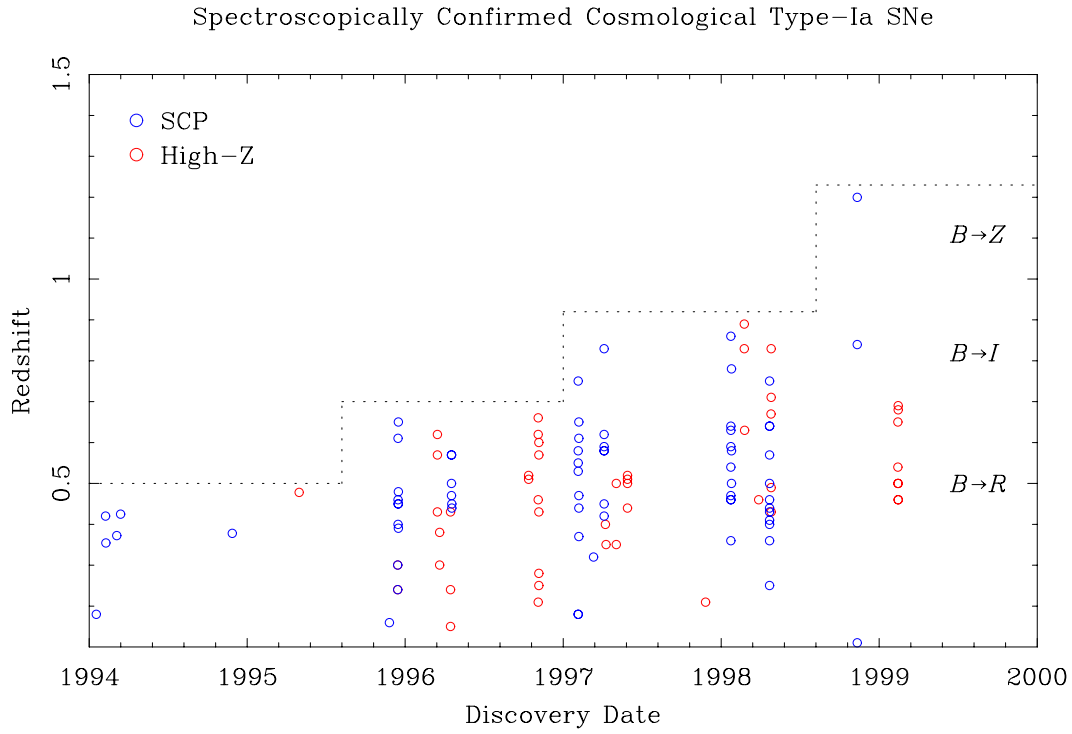


Figure 5.2: Distant, spectroscopically confirmed Type Ia supernova discoveries reported in the IAU Circulars this decade. Discoveries by the SCP and the High- Z Team are shown separately. The dashed boundary shows how the maximum distance has increased with time as facilities and time allocation have improved. Along the right margin the observer frame filter needed for restframe B -band discoveries and follow-up is indicated.

compromised with each alternative.

The alternatives considered assumed the following facilities:

Description	Location	Aperture	FOV	AO?	OH-suppression?
CFHT	ground	3.6-m	$1 \square^\circ$	no	no
Keck	ground	10-m	NA	no	yes
Keck+AO	ground	10-m	NA	yes	yes
Keck+AO+OH	ground	10-m	NA	yes	yes
WFT	ground	8-m	$7 \square^\circ$	no	no
OWLT	ground	24-m	$1 \square^\circ$	no	no
OWLT+AO	ground	24-m	NA	yes	no
OWLT+AO	ground	24-m	NA	yes	yes
HST+WF+NIC	space	2.4-m	NA	NA	NA
HST+ACS+NIC	space	2.4-m	NA	NA	NA
NGST	space	8-m	$0.004 \square^\circ$	NA	NA

Table 5.1: Alternative Facilities

We do not consider wide-field AO or OH-suppression systems; these are impractical as discussed in the next section.

We have determined how well these facilities, alone or in tandem, can actually execute the SNAP baseline mission. We examine whether discovery and follow-up photometry can be done in a batch mode, with several targets in a single field. The ability to discover distant supernovae within the allocated time, and to find supernovae shortly after explosion, are included in this comparison. In accord with the discussion of contrast in the next section, we assume in addition to Poisson errors a contribution equal to 10^{-6} of the foreground signal. We find that ground-based searches with wide-field imaging hit a noise wall set by this additional source of noise which prevents such facilities from finding distant supernovae early. The results of this analytic comparison are summarized in Table 5.2.

Facilities		Batch	SNe/yr	z Limit given time budget	Early Discovery (2 days)	Time (hrs) to Achieve S/N at max z	Magnitude Limit (AB)
Search	Photometry + Spectra						
SNAP	SNAP	Yes	2400	$z < 1.7$	Yes	4 ($S/N = 3$)	30
HST+ACS	HST+ACS+NIC	Yes	20	$z < 1.7$	Yes	2 ($S/N = 3$)	30
NGST	NGST	No	60	$z < 1.7$	Yes	0.1	-
CFHT	HST+ACS+NIC	No	350	$z < 0.6$	4 day	8 ($S/N = 5$)	26
WFT	Keck+AO	No	140	$z < 1.2$	Peak-0.5	8 ($S/N = 10$)	26
WFT	WFT	Yes	210	$z < 0.6$	Yes	6 ($S/N = 3$)	27
WFT	NGST	No	430	$z < 0.6$	4 day	8 ($S/N = 10$)	26
WFT	NGST	No	460	$z < 0.9$	6 day	7 ($S/N = 5$)	26.5
OWLT	OWLT	Yes	420	$z < 0.7$	Yes	9 ($S/N = 5$)	27.5
OWLT	OWLT+AO+OH	No	290	$z < 1.0$	5 day	4 ($S/N = 5$)	27

Table 5.2: Comparison of Alternative Facilities to SNAP for Baseline Mission

The one basic theme these simulations show is that supernovae cannot be discovered very early on the light curve from the ground.

5.2 Advantages of Space-Based Observations

5.2.1 Reduced Foreground Emission

The principle advantage of space-based observation of distant supernovae is the large reduction in foreground noise compared to ground-based observations. The major source of foreground noise arises from the Poisson statistics of atmospheric airglow, light from the supernova host galaxy, and zodiacal light. For imaging applications with modern detectors, noise from dark current and readout amplifier noise make minor contributions. In the typical case where the photon foreground flux exceeds that from the supernova, the exposure time to reach a given signal-to-noise ratio is directly proportional to the foreground. Significant foreground reduction can be achieved in space because atmospheric airglow is eliminated, leaving only the foreground from zodiacal light and host-galaxy light. Thus space-based observation offers a very direct means of obtaining better brightness measurements of more distant supernovae beginning when they are quite faint, just days after explosion.

Emission from the atmosphere is strongly wavelength dependent, as shown in Fig 5.3. In the range 0.7 - 1.8 μm , of interest in observing distant (redshifted) supernovae, the airglow is dominated by discrete emission lines from the OH radical. There is also a non-negligible continuum, thought to be caused by the reaction: $N + NO \rightarrow NO_2 + \gamma$. (Note that thermal emission is not important at these wavelengths, so observations at, e.g., the South Pole, do not lead to a significant reduction in sky emissions.) The relative contributions of important foreground sources are roughly as follows:

Wavelength (μm)	Airglow		Zodiacal
	Continuum	OH lines	Light
	(photons/ $\text{m}^2/\text{s}/\mu\text{m}/\text{arcsec}^2$)		
0.8	130	400	43
1.2	600	16000	32
1.6	600	25000	21

Table 5.3: Atmospheric and Space Foregrounds

These values indicate that for wide-field broadband imaging, as required for finding distant supernovae and obtaining light curve measurements simultaneously for all supernovae in the field of view, space-based images have an additional advantage of 12, 500, and 1200 at 0.8, 1.2, and 1.6 μm , respectively, from the reduced foreground emission alone. Some work has been done on filters attempting to suppress the OH emission lines; however, these filters also block significant spectral regions from the object being observed, making accurate photometry dependent on *a priori* knowledge of the spectral energy distribution of the target. For supernovae the spectral energy distribution is time dependent, and of course shifts with redshift. Some test-bed instrumentation has shown the ability to suppress OH lines using an intermediate spectral image where the OH lines are masked (Iwamuro et al., 1994). Such instruments can only work over very small fields, and their additional optics reduce system throughput by $\sim 2 - 3\times$. This

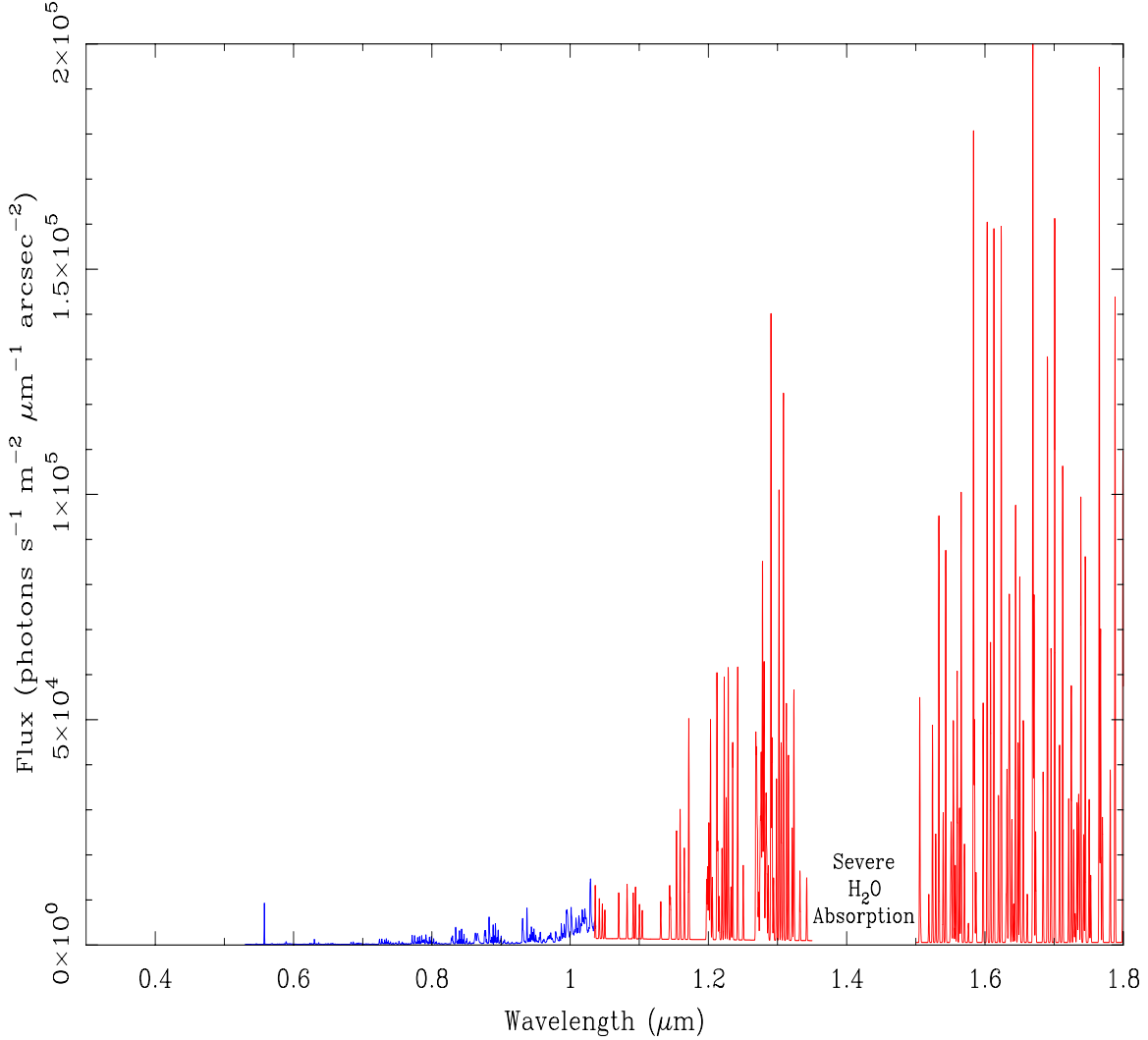


Figure 5.3: The optical and near-infrared spectrum of the atmosphere overhead at an excellent astronomical site such as Mauna Kea, Hawaii or Paranal, Chile. There is a faint continuum, punctuated by a series of bright emission lines, mostly due to OH. These emission lines are strong at the beginning of the night, and by midnight have decreased to the levels shown here. The sky brightness also correlates with increased solar activity, being roughly twice as bright as shown here at the peak of the solar cycle. Aside from these temporal variations, the sky brightness increases with the airmass of the source being observed. The intrinsic widths of the lines are quite narrow, thus their impact can be decreased for spectroscopic observations with resolution greater than $R \sim 10000$. The optical spectrum is from our own observations, while the NIR spectrum is constructed from the observations of Ramsay, Mountain, & Geballe (1992); Maihara et al. (1993); Oliva & Origlia (1992).

reduced efficiency and the need to observe each supernova individually eliminates any advantage of these systems compared to SNAP.

These benefits of space over ground-based observation are significant, but don't tell the whole story. Although calculations based on Poisson noise would indicate that ground-based telescopes of sufficiently large aperture can compete with a smaller space-based telescope, this ignores the difficulty inherent in obtaining accurate photometry of faint sources overwhelmed by a foreground $\sim 10^5\times$ brighter (typical of NIR observations). Photometry with an accuracy of 2% on such a source requires the foreground to be uniform to 2×10^{-7} on small scales. In our experience, accuracy of this type with CCD or NIR HgCdTe detectors has never been achieved. Indeed, we have found that whereas $S/N \sim 3.5$ supernova candidates discovered in *R*-band are generally genuine, candidates discovered in apparently well-flatfielded images at *I*-band – where the foreground is substantially brighter – with calculated S/N up to 5 have all been spurious. To achieve $S/N = 5$ rather than $S/N = 3.5$ requires twice the exposure; this penalty can only get worse as higher redshifts are attempted from the ground.

5.2.2 Reduced Atmospheric Distortion

Blurring by the atmosphere causes the light from a supernova to have a Gaussian point-spread-function (PSF) of ~ 0.7 arcseconds FWHM at optical wavelengths at the best ground-based sites (see Fig 5.5 and Fig 5.6), whereas in space the PSF is near the diffraction limit (0.12 arcseconds at a wavelength of $1\ \mu\text{m}$ for a 2-m telescope). This blurring means that considerably more sky light and host-galaxy light $((0.7/0.12)^2 = 34$ times more) is included in the (software) aperture used to measure a supernova from the ground. The improvement in image quality alone translates into a factor of 34 advantage for SNAP compared to a ground-based telescope of the same size. Prototype adaptive optics (AO) have demonstrated the ability to improve ground-based images to better than 0.1 arcsec. However, the corrected solid angle is small (less than one arcminute in radius), and laser guide stars are needed for observations near the preferred regions towards the Galactic poles. In addition, absolute brightness measurements may be complicated by the significant and varying skirt of light typical of AO point-spread-functions (\sim Lorentzian). Wide-field imaging with AO on a scale required for finding and simultaneously obtaining light-curves for many supernovae, is thus far beyond any instrumentation that could be built today.

The clear-weather transparency of the atmosphere also has a non-trivial effect on the quality of supernova data attainable from the ground. Fig 5.4 breaks the atmospheric transmission into a smooth component — which can be corrected fairly accurately using standard observing procedures — and a second, finely structured, component which is difficult to accurately correct. The second component is composed of discrete, narrow, absorption lines at differing levels of saturation, making the correction dependent on airmass and spectral resolution. Narrow spectral features observed in these regions would be suspect, and the relative accuracy of the absorption correction no better than $\sim 10\%$. It is clear from this figure that key supernova observations can not be accurately obtained for some redshifts from ground-based observations.

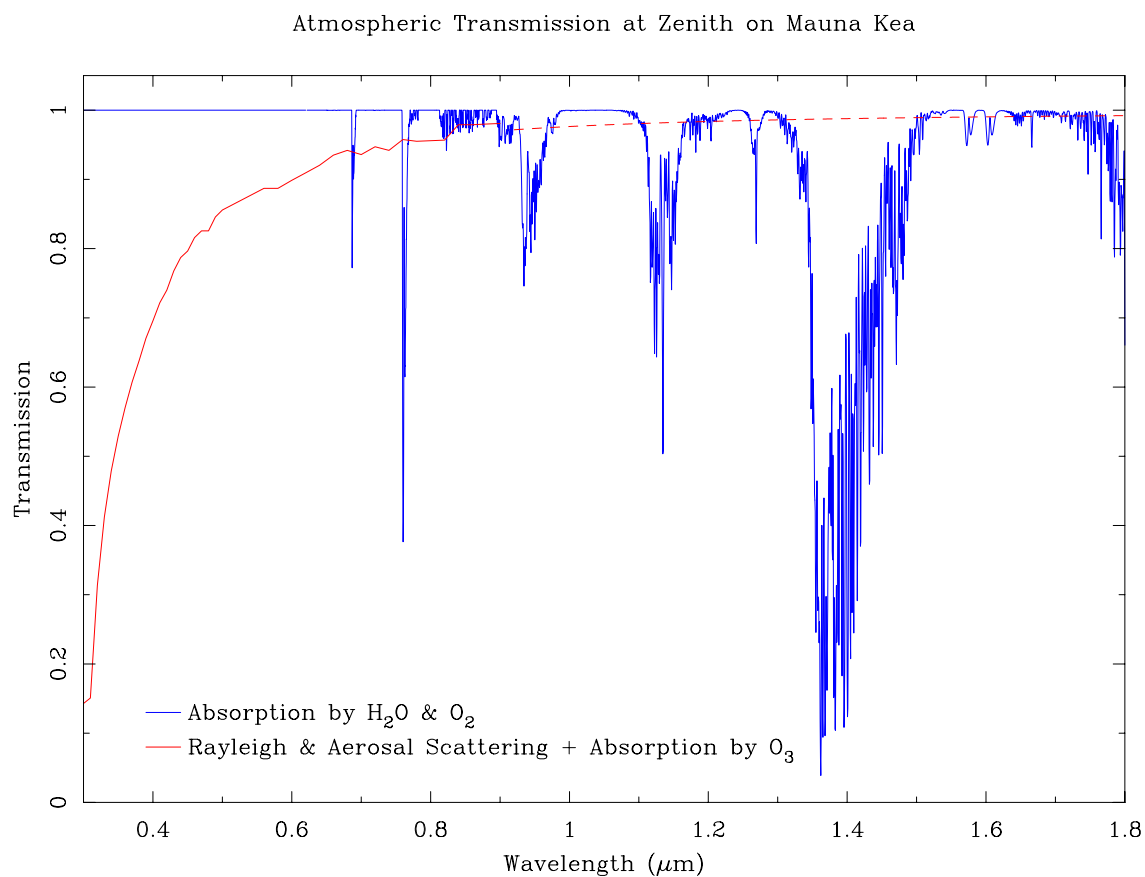


Figure 5.4: The optical and near-infrared transmission of the atmosphere at the zenith on Mauna Kea for an H_2O column of 1.6 mm. The transmission is broken into a smooth component mostly due to molecular and aerosol scattering, and a structured component due to H_2O and O_2 many discrete absorption lines. The resolution is approximately 1 nm, or $R \sim 10000$.

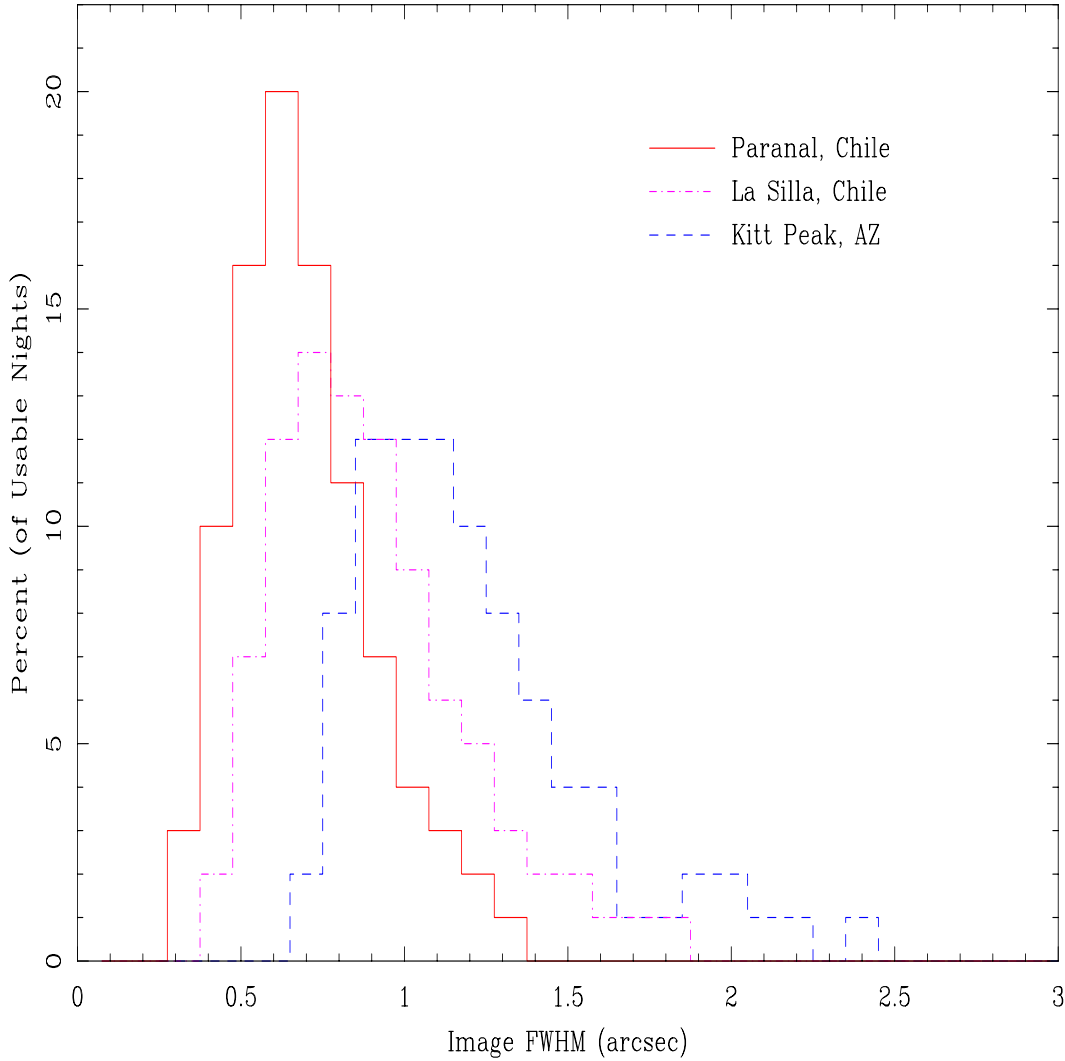


Figure 5.5: Percent of usable nights with given seeing for three representative sites and facilities. The Paranal data are applicable to an excellent site with state-of-the-art facilities, where careful attention has been paid to reducing telescope/dome seeing. The Kitt Peak data apply to a good site with old facilities which have been retrofitted to the extent possible to reduce telescope/dome seeing. La Silla is intermediate between these two. Measurements were obtained at optical wavelengths at zenith, using seeing measurement cameras and therefore do not include any degradation due to the astronomical instrument being used at the time. These measurements should scale with wavelength, λ , and airmass, X , roughly as $\lambda^{-0.2} X^{0.6}$. In determining the typical exposure time for foreground-limited observations, the appropriate value to use is not the mode, mean, or median of the seeing, but rather the RMS seeing, $\langle \text{FWHM}^2 \rangle^{0.5}$, since this reflects how seeing enters the signal-to-noise equation. $\langle \text{FWHM}^2 \rangle^{0.5}$ equals 0.80, 1.03, and 1.28 arcsec for Paranal, La Silla, and Kitt Peak, respectively.

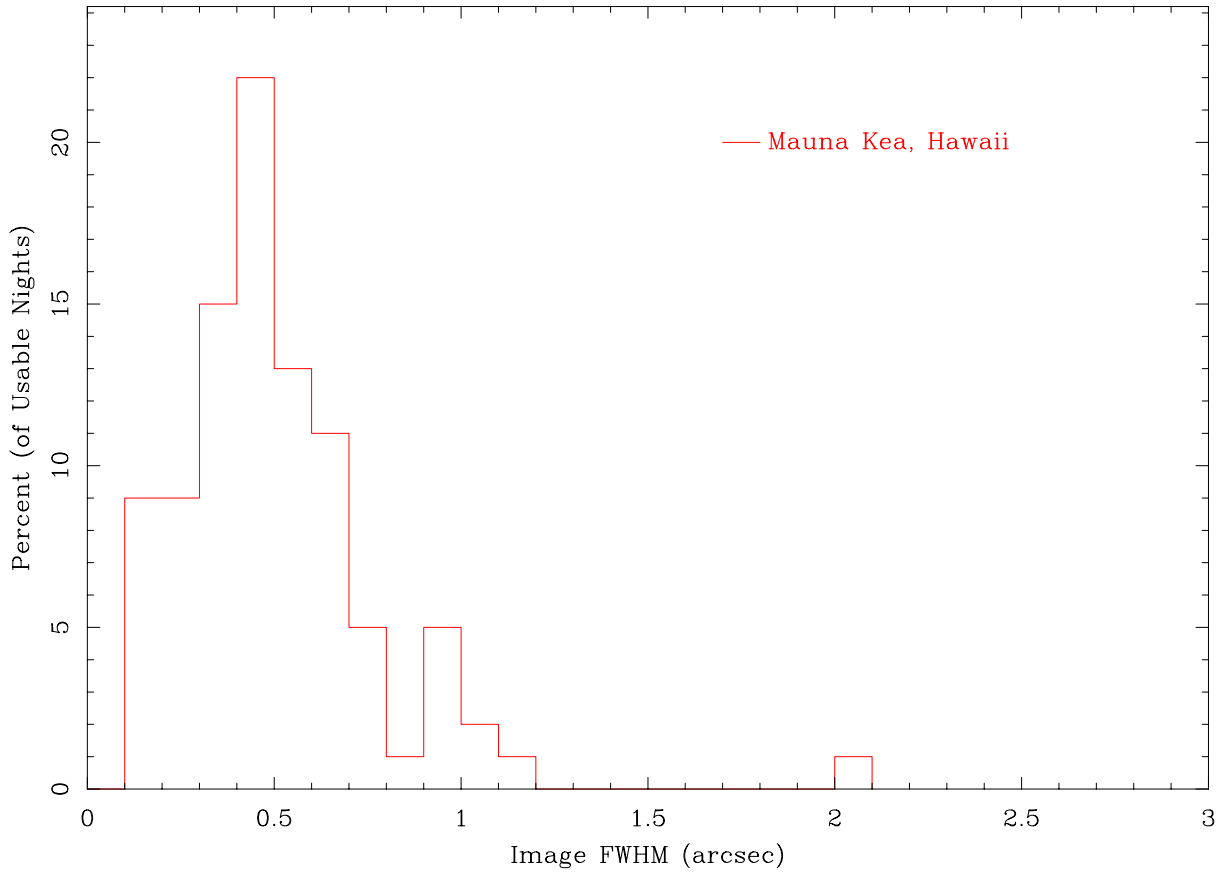


Figure 5.6: Percent of usable nights with given seeing in the near-infrared ($2.2 \mu\text{m}$) from the UK Infrared Telescope on Mauna Kea. UKIRT is at an excellent site, but the telescope and enclosure are not now state-of-the-art. The value of $\langle \text{FWHM}^2 \rangle^{0.5}$ equals 0.62 arcseconds if all the observations are included. Rejecting nights with seeing worse than 0.9 arcseconds (10% of nights) reduces $\langle \text{FWHM}^2 \rangle^{0.5}$ to 0.48 arcseconds.

5.2.3 Improved Detection Efficiency

Weather (cloudy skies, strong winds) make about $\frac{1}{3}$ of nights at the best sites unusable. For most astronomical observations this is simply counted as a direct loss in efficiency. However, for observations of transient sources, the impact of weather can be far greater. Our simulations indicate that a site with $\frac{2}{3}$ clear nights has an effective efficiency of 50%, assuming weather correlated on a timescale of 3 days. If this factor is combined with the fraction of each night that is dark ($\sim 40\%$) and the fraction of that time which is not severely degraded by moonlight ($< 75\%$), the effective duty-cycle of a ground-based telescope is $\sim 15\%$. In addition, interference from the moon will preclude early discovery with wide-field ground-based imaging for $\sim 25\%$ of supernovae.

5.3 Detailed Comparison of SNAP and Ground-based Viewing

A number of comparisons between SNAP and various ground-based observing factors are explored in Tables 5.4 through 5.7. We find that in no case – neither wide-field imaging, OH-suppressed photometry, AO-assisted photometry, nor AO-assisted spectroscopy – can ground-based facilities perform as effectively as a 2-m SNAP satellite for the types of measurements required for supernova-based cosmological studies, including the necessary checks on potential sources of systematic error. Details of the comparisons are provided in the footnotes to the table, and are based on the general discussion earlier in this section.

Wavelength (μm)	Degradation Factors						Ground/ Space Efficiency
	Image Quality	Night Sky Brightness	Trans- mission	Weather	Sun- light	Moon- light	
0.5—0.7	0.028	0.22	0.89	0.5	0.4	0.6	7×10^{-4}
0.7—0.9	0.031	0.079	0.95	0.5	0.4	0.7	3×10^{-4}
0.9—1.1	0.034	0.014	0.95	0.5	0.4	0.9	8×10^{-5}
1.1—1.3	0.049	0.0018	0.85	0.5	0.4	1.0	1×10^{-5}
1.3—1.5	0.071	0.0012	0.50	0.5	0.4	1.0	9×10^{-6}
1.5—1.7	0.098	0.00077	0.90	0.5	0.4	1.0	1×10^{-6}

Table 5.4: Wide-field Imaging Comparison. This comparison assumes background-limited wide-field imaging, where adaptive optics and OH line suppression is not practical. The image quality comparison assumes the maximum of four $0.1''$ square pixels or $1.86\lambda/D$ (80% encircled flux) for SNAP. The ground-based image quality was based on an aperture with diameter equal to $1.52\times$ the *RMS* seeing FWHM, which encloses 80% of the light for a Gaussian. An *RMS* seeing of $0.8''$ at $0.55 \mu\text{m}$ (as measured at Paranal, Chile) was assumed, and scaled as $\lambda^{-0.2}$.

5.3.1 Searching with HST or NGST

Space-based discovery with existing and currently planned imagers is impractical. The small fields of WFPC2 ($5.3\Box'$), WFPC3 ($7.1\Box'$), and ACS ($11.3\Box'$), and the poor red response of their CCD's (compared to an LBNL CCD) means that searching $20\Box^\circ$ to

Wavelength (μm)	Degradation Factors							Ground/ Space Efficiency
	Image Quality	Night Sky Brightness	Trans- mission	Weather	Sun- light	Moon- light	Suppressor Penalty	
1.1—1.3	0.049	0.015	0.85	0.5	0.4	0.7	0.50	4×10^{-5}
1.3—1.5	0.071	0.014	0.50	0.5	0.4	0.8	0.50	4×10^{-5}
1.5—1.7	0.098	0.012	0.90	0.5	0.4	0.9	0.50	1×10^{-4}

Table 5.5: OH Suppression (Follow-up) Imaging Comparison. This comparison assumes background-limited ground-based imaging with OH line suppression, but no adaptive optics. Other assumptions are as in Table 5.4. Here we add an additional column which is a rough estimate of the throughput penalty associated with the use of OH suppression devices. Only wavelengths where this penalty is potentially compensated by the gain due to sky suppression are shown. Note that with OH suppression, aerosol-scattered moonlight is more important at near-infrared wavelengths.

Wavelength (μm)	Degradation Factors							Ground/ Space Efficiency
	Image Quality	Night Sky Brightness	Trans- mission	Weather	Sun- light	Moon- light	AO Optics Penalty	
0.5—0.7	0.033	0.22	0.89	0.5	0.4	0.6	0.50	4×10^{-4}
0.7—0.9	0.041	0.079	0.95	0.5	0.4	0.7	0.50	2×10^{-4}
0.9—1.1	0.050	0.014	0.95	0.5	0.4	0.9	0.50	6×10^{-5}
1.1—1.3	0.081	0.0018	0.85	0.5	0.4	1.0	0.50	1×10^{-5}
1.3—1.5	0.144	0.0012	0.50	0.5	0.4	1.0	0.50	9×10^{-6}
1.5—1.7	0.262	0.00077	0.90	0.5	0.4	1.0	0.50	2×10^{-5}

Table 5.6: AO (Follow-up) Imaging Comparison. This comparison assumes background-limited ground-based imaging with adaptive optics with the diffraction limit of a 20-m telescope. Since in this case OH suppression is not as important, we do not include it. The quality of an adaptive optics system is often given by the Strehl ratio, which is the ratio of attained peak intensity relative to that expected from the diffraction limit. The point spread function resulting when adaptive optics is used consists of a (nearly) diffraction-limited core, surrounded by a broad skirt. Here Strehl ratios of 0.24, 0.32, 0.40, 0.48, 0.57, and 0.65 are assumed, respectively, for each of the wavelength ranges given in the table. These values are given or estimated from the study of Le Louarn et al. (1998), for median seeing conditions at Paranal and the use of nearby bright natural guide stars (which give better correction than laser guide stars). They are, however, optimistic in comparison with typical results to date from the AO system on Keck. We have further assumed that the skirt is a Gaussian with FWHM given by the uncorrected seeing. The ratio is evaluated as before for SNAP, and using the 80% encircled flux radius for AO. Here we add an additional column which is a rough estimate of the throughput penalty associated with the optics of the adaptive optics system. Note that the value chosen for this throughput penalty is quite generous in comparison to current working AO systems.

Wavelength (μm)	Degradation Factors							Ground/ Space Efficiency
	Image Quality	Night Sky Brightness	Trans- mission	Weather	Sun- light	Moon- light	AO Optics Penalty	
0.5—0.7	0.11	0.29	0.89	0.5	0.4	0.6	0.50	2×10^{-3}
0.7—0.9	0.16	0.17	0.95	0.5	0.4	0.7	0.50	2×10^{-3}
0.9—1.1	0.29	0.05	0.95	0.5	0.4	0.9	0.50	1×10^{-3}
1.1—1.3	1.2	0.03	0.85	0.5	0.4	1.0	0.50	3×10^{-3}
1.3—1.5	31	0.03	0.50	0.5	0.4	1.0	0.50	5×10^{-2}
1.5—1.7	127	0.034	0.90	0.5	0.4	1.0	0.50	4×10^{-1}

Table 5.7: AO (Follow-up) Spectroscopy Comparison. This comparison assumes background-limited ground-based spectroscopy with adaptive optics. (Note that it is possible that not all ground-based or space-based spectroscopic observations will be background-limited; the exact S/N is used to the SNAP mission analysis in Table 5.2, below). Observations at high resolution ($R > 10000$) automatically results in OH suppression, so we use the OH-suppressed foreground. The assumptions regarding the quality of AO are similar to this in Table 5.6, however, the comparison is made for a 50% encircled energy for the ground-based observations. This is justified under the assumption that the ratio between the 50%, 80% and total encircled energy apertures will vary slowly with wavelength, and that spectroscopic observations are deep enough that profile wings can be traced well beyond the 80% encircled energy aperture after smoothing over wavelength. A typical spectrum will cover a larger wavelength range than any of the ranges given in the table. Over the range of a real spectrum, the AO point spread function and sky foreground will vary, and an exposure will usually be taken to cover the worst case.

depths reached by SNAP would require about $6\text{--}12 \times 10^3$ exposures of $\sim 3\text{--}8$ orbits (each orbit has 52 minutes on-source, 44 minutes in Earth occultation and guide-star reacquisition); this amounts to 3—15 yrs! NGST ($16''$) would be more sensitive than SNAP, requiring discovery exposures of only 1 minute, but the 20 min repointing time (per 4 fields, assuming tertiary mirror throw can cover 4 adjacent fields) means that NGST would take 0.8 days *just repointing* to observe the 225 fields needed to cover 20° . Of course NGST can be an effective supernova-finder for redshifts beyond those in the baseline SNAP mission, where the surface density of supernova should be higher, and it could help in obtaining spectra of supernovae discovered by SNAP.

5.3.2 Ground-based searching with follow-up using HST or NGST

Ground-based discovery in concert with space-based follow-up using HST or NGST presents another alternative. This does involve some logistical problems, which we have already encountered with our current program. Namely, for observations with HST the location of, and observing sequence for, a potential supernova must be given three weeks in advance, and the exact location must be given one week in advance. If spectroscopic confirmation comes from the ground, and allowing for the time needed to analyze the discovery and spectroscopy data, a supernova must be discovered almost three weeks (observer frame) before maximum for space-based follow-up observations to begin even as late as one week before maximum. As we shall see in the analysis below, such early discovery is impractical beyond modest redshifts even for a wide-

field imager on a large ground-based telescope. Alternate schemes, such as obtaining spectroscopic confirmation with NGST can reduce the necessary lead time, but would require NGST to obtain an additional spectrum at maximum to ensure a homogeneous dataset. Also, such a scheme will result in a non-negligible number of wasted exposures due to spurious candidates or over-prescription of exposure times which cannot be tailored to each object. The time lost there may not be large in the overall scheme, but is likely to be taken with a dim view given that HST and NGST are user facilities.

Chapter 6

Other Scientific Objectives

6.1 Introduction

The detailed study of Type Ia supernovae is the driving science behind the SNAP satellite proposal. However, there are a number of other interesting scientific measurements that could be carried out with the proposed facility. In the following sections, a few examples of measurements that can provide independent information about cosmological parameters are described. In addition there are a wealth of possible measurements that will not be described here, but that would nevertheless be of general interest to the astronomical community.

6.2 Type II Supernova

Both Type Ia and Type II supernovae have been used as distance indicators. Type Ia supernovae have been used as (correctable) standard candles and are discussed elsewhere in this proposal.

The expanding photosphere method (EPM) was developed by Baade (1926) for use with variable stars and has been applied to Type II supernovae (Kirshner & Kwan, 1974; Branch et al., 1981; Schmidt, Kirshner, & Eastman, 1992; Eastman, Schmidt, & Kirshner, 1996) in order to estimate the value of H_0 . For a particularly lucid description of the empirical application of the EPM to supernovae see Branch (1987).

These previous applications of the EPM have all been semi-empirical in nature in the sense that the supernova is assumed to emit radiation as a blackbody or as a diluted blackbody. Then one simply needs to determine the color temperature and the velocity of expansion in order to determine the total luminosity. This method is plagued by the fact that supernovae are not dilute blackbodies, as well as by uncertainties in the absolute value of the “dilution factor” (Schmidt, Kirshner, & Eastman, 1992; Baron et al., 1995).

With the use of the detailed spectral modeling we have been able to overcome this difficulty and make the method much more precise (Baron et al., 1993; Baron, Hauschildt, & Branch, 1994; Baron et al., 1995; Nugent et al., 1995b; Baron et al., 1996). In the Spectral-fitting Expanding Atmosphere Method (SEAM) we use observed

spectra and photometry combined with detailed theoretical modeling of the observed spectra to actually determine distances to both Type Ia and Type II supernovae. It is unnecessary to make any assumptions about the intrinsic luminosity of the supernova. While previous use of the EPM has involved using observed colors to determine a temperature and then assuming the supernova is a dilute black body, we need to make no such assumptions. We have already demonstrated that SEAM method gives accurate distances for SN 1993J (Baron et al., 1993; Baron, Hauschildt, & Branch, 1994; Baron et al., 1995), which was a peculiar Type II supernova, and SN 1994I (Baron et al., 1996) a Type Ic, normal Type IIP supernovae should both be easier to model and give more reliable distances. Preliminary results on SN 1993W, SN 1999em (observed in the UV with HST) confirm that this is indeed the case. We also have shown (Mitchell et al. 2000; Baron et al., in preparation) that with accurate radiation hydrodynamical models exceptional precision to the spectra of SN 1987A can be achieved. Here, we are able to fit a long time series of spectra that have unprecedented coverage in both time and wavelength which will allow us both to assess the uncertainties in the method and to independently determine a distance to the LMC, which is still one of the major uncertainties in the *HST* measurements of Cepheids and hence in the uncertainty in the Hubble constant. We believe that our method rivals Cepheid based distances in quality and has a much greater range.

Clearly, with the thousands of SNe II to be discovered with SNAPSAT we will be unable to perform detailed modeling of nearly 10,000 spectra. However, our preliminary results on individual spectra already show that the method is extremely accurate. By detailed modeling of several selected well observed SNe, we should be able to produce a grid of theoretical models which, combined with Monte-Carlo simulations, will allow us to use the SNe II as independent distance indicators. This last point is in fact the most important aspect of the use of SNe II and the SEAM method for determining cosmological distances, i.e. the physics and astronomy is completely independent of that of the SNe Ia and hence the statistical and systematic errors are also uncorrelated with those of the SNe Ia search. This is a crucial check on the reality of the cosmological parameters determined by the SNe Ia search.

Figure 6.1 shows our current best fit for a typical plateau-type SN II. The agreement is remarkable.

6.3 Gravitational Strong Lensing

Mass concentrations along the line of sight to distant galaxies and quasars can distort and amplify the light from these objects via gravitational lensing. In the thin lens approximation, illustrated in Fig. 6.2, input angles are mapped to output angles according to:

$$\theta^I = \theta^S + \frac{D_{LS}}{D_{OS}}\alpha(\theta^I)$$

$\alpha(\theta^I)$ depends on the projected mass density of the lens, $\Sigma(\theta^I)$, and the angular-size distance from the lens, L , to the source, S , D_{LS} , and from the observer, D_{OS} , and

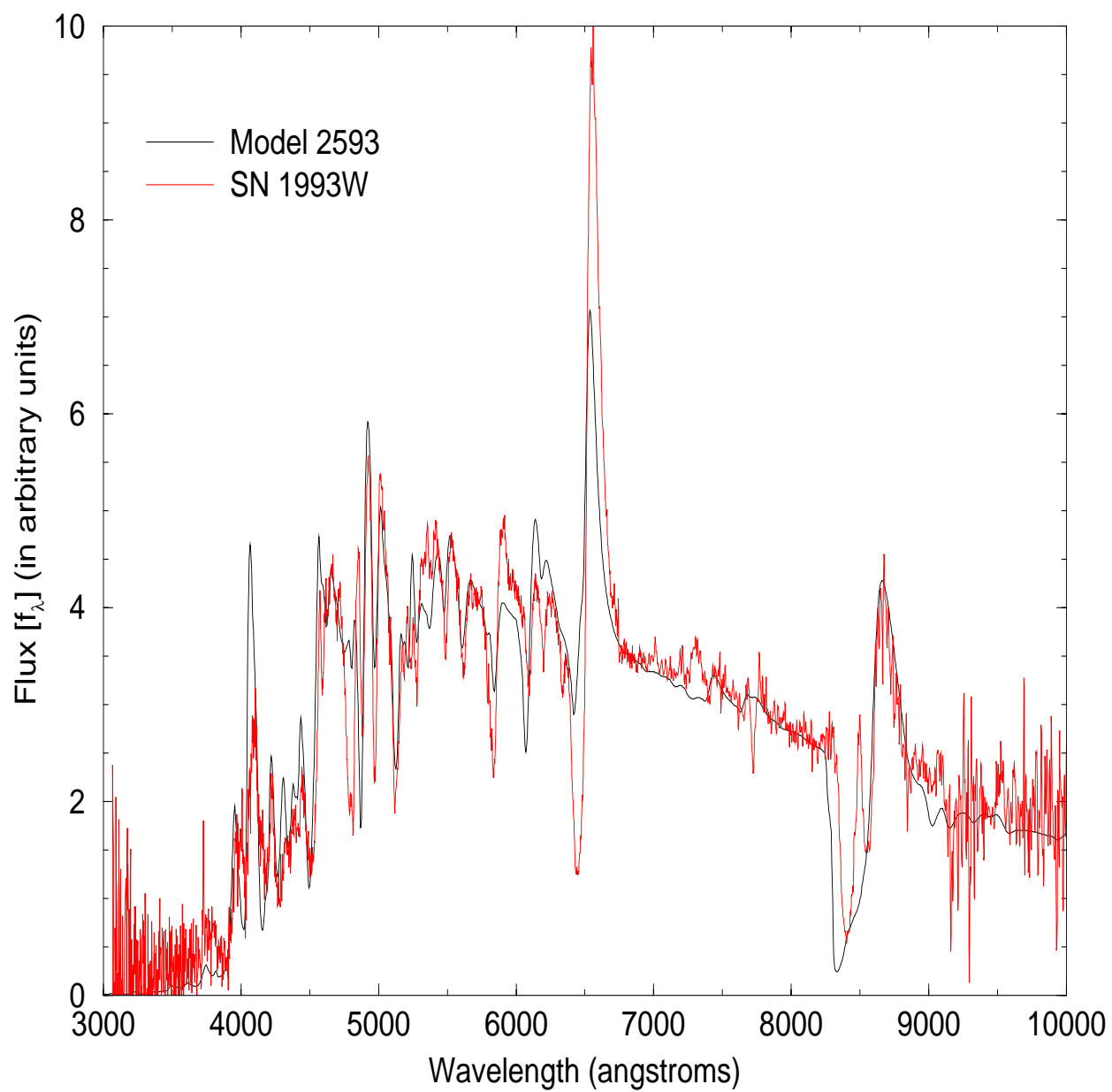


Figure 6.1: A fit to SN 1993W (courtesy D. Leonard) at roughly 40 days after max.

from the observer to the lens, D_{OL} :

$$\alpha(\theta^I) = \frac{4G}{c^2} \int \Sigma(\theta^I) \frac{\theta^I - \theta'}{|\theta^I - \theta'|^2} d^2\theta'$$

The surface mass density is related to the line-of-sight gravitational potential, φ , according to:

$$\frac{\Sigma(\theta^I)}{\Sigma_{crit}} = \frac{4\pi G}{c^2} \frac{D_{LS}D_{OL}}{D_{OS}} \Sigma(\theta^I) = \frac{1}{2} \Delta\varphi(\theta^I)$$

In the case of clusters of galaxies or elliptical galaxy halos, an singular isothermal sphere is often taken as an approximate model for the dark-matter dominated mass distribution. In which case the line-of-sight velocity dispersion, σ_{DM} completely describes the cross-section for lensing (Turner, Ostriker, & Gott, 1984). In this case, the deflection angle is simply

$$\alpha \sim 4\pi \left(\frac{\sigma_{DM}}{c} \right)^2$$

The halo of a typical massive elliptical galaxy with $\sigma_{DM} \sim 225$ km/s gives $\alpha \sim 1.5''$ while a rich cluster with $\sigma_{DM} \sim 1000$ km/s gives $\alpha \sim 30''$.

Counts of lensed quasars and galaxies can be used to constrain Ω and Λ (Kochanek, 1996; Falco, Kochanek, & Munoz, 1998) in a manner complimentary to the supernova limits since the probability of lensing is a strong function of the volume over which potential background sources are distributed. Based on gravitational lenses discovered in blind optical searches with HST (most of which would not be resolved from the ground; Ratnatunga, Griffiths, & Ostrander (1999); Cooray, Quashnock, & Miller (1999)), SNAP should easily find $\sim 10^3 - 10^4$ strong lenses over the 20° supernova monitoring region. Constraining Ω and Λ with strong lensing requires a knowledge of the lensing cross-section from foreground galaxies (or clusters), which goes roughly as $n (\sigma_{DM}/c)^4$, where n is the number of density of galaxies (which may evolve with redshift). SNAP will have excellent photometric redshifts for galaxies in the supernova monitoring region. It will also be able to obtain statistical information on typical galaxy halo mass surface density profiles from galaxy-galaxy lensing (Brainerd, Blandford, & Smail, 1996; Hudson et al., 1998). With these ingredients, the lensing cross-section, and even its evolution with redshift, can be determined completely internally with SNAP. The largest uncertainty then remaining is likely to be the correction for dust-extincted lenses which are missed (Falco et al., 1999; Malhotra, Rhoads, & Turner, 1997). SNAP may well be able to measure the differential extinction for strong lenses, from which it may be possible to tightly constrain the number of missed lenses. The SNAP strong lens dataset will also be a valuable target list for NGST.

Since SNAP will be monitoring these strong lenses for a number of years, it may find some in which the source is strongly variable on short timescales. The time delay between the variability light curves of the various lens components could then be used to place constraints on the Hubble constant. Since detailed lens modeling is required to interpret such observations, some follow-up spectroscopy with NGST would once again be an excellent complement to SNAP.

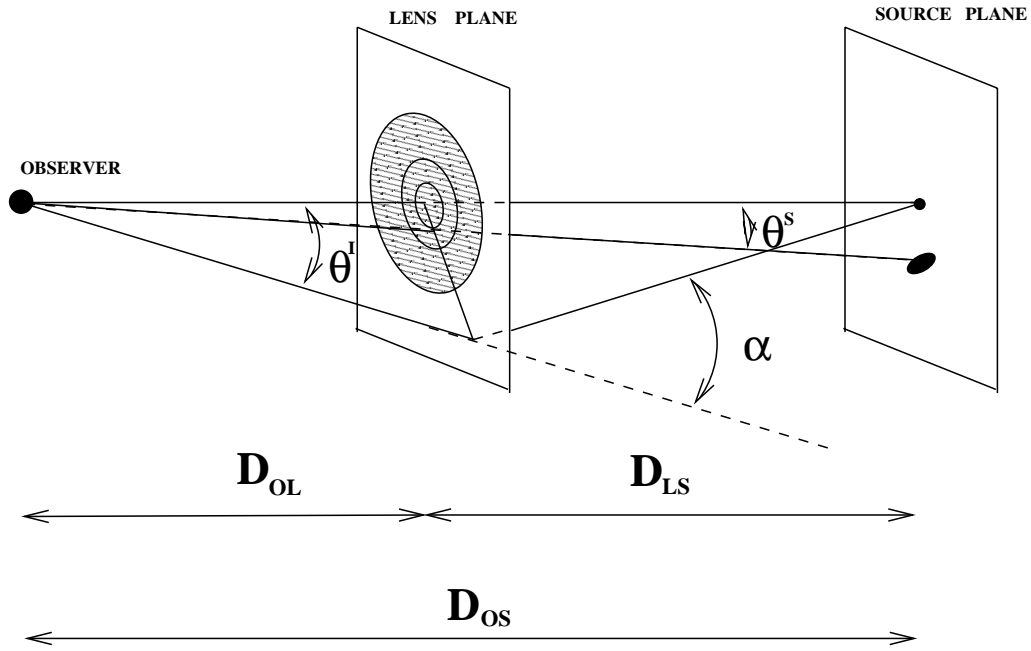


Figure 6.2: Schematic illustration of how light from a source, S , is deflected by an angle, α , as it passes by a mass concentration, L , acting as a gravitational lens. The distances between the observe, O , and the lens and source are angular-diameter distance, which depend on Ω , Λ , as well as any quintessence component.

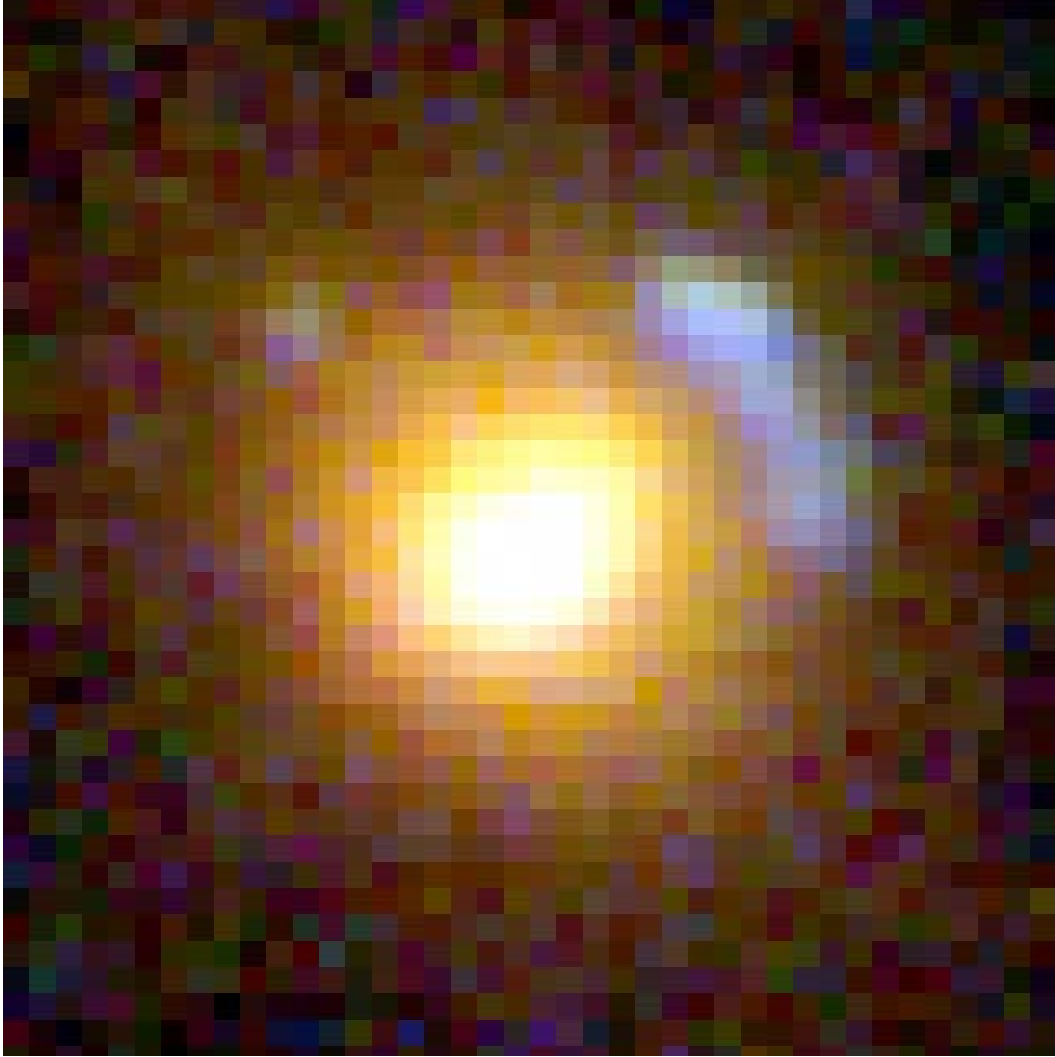


Figure 6.3: Strong lensing of a blue background galaxy with $V \sim 25$ by a foreground elliptical galaxy with $V \sim 22$, from the Hubble Deep Field South (Barkana, Blandford, & Hogg, 1999). North is up and East is to the left. The figure is centered on the lens galaxy and measures $3''$ on a side. The separation is 0.9 arcseconds, which ground-based observations could just barely resolve. SNAP would easily detect gravitational lenses like this.

SNAP may also discover gravitational microlensing by compact masses in foreground galaxies (e.g., primordial black holes, stellar remnants, MACHOS, normal stars, gas clouds, etc.; Walker (1999); Dalcanton et al. (1994)). If such a compact mass — in its orbit through its parent galaxy and as the galaxy moves through space — passes in front of a background quasar, it will produce a characteristic (nearly) achromatic light curve. SNAP would be sensitive to such events on timescales from 2 days to 2 years (in the observer frame). Fig 6.4 shows the mass ranges and time scales that could be probed. We have not yet performed a detailed calculation of various microlensing scenarios, so firmer statements would be premature.

Strong lensing of multiple galaxies at caustics in massive clusters allow yet another means of constraining Ω and Λ (Link & Pierce, 1998). A nice example of the strong-lensing phenomenon by a rich cluster of galaxies observed with HST is shown in Fig. 6.5. If the cluster potential can be mapped using weak and strong lensing, then the multiple images of highly magnified galaxies (located near caustics) can be used to obtain the angular-size distance. Several such cases with galaxies at different redshifts behind a given cluster form the ingredients for an angular-diameter versus redshift test, which is of course dependent on the cosmological parameters. It is unlikely that SNAP would happen to have a rich cluster with fortuitously-placed background galaxies in its survey field, so pursuit of this cosmological test would probably require special observations. Simulations for NGST show an abundance of low-surface-brightness, highly magnified arcs (beyond what HST can now see); if a rich cluster were in the SNAP monitoring region the total integration over the SNAP mission would provide images even deeper than NGST. SNAP would not have the resolution of NGST, so at a minimum special processing would be needed to recover the details of the thinnest arcs.

6.4 Gravitational weak lensing

6.4.1 Introduction

As a light from a high-redshift source traverses the universe on its way to us, it passes by and through a wide range of mass overdensities and underdensities which distort and (de)magnify the image of the source via gravitational lensing, as laid out by Kristian & Sachs (1966), Gunn (1967), Valdes, Jarvis, & Tyson (1983), Miralda-Escude (1991), Blandford et al. (1991), Kaiser (1992) and others. When these perturbations from gravitational lensing are $\ll 1$ in dimensionless units, they fall into the regime known as weak lensing. The net distortion and magnification contains information about the amount and locations of mass fluctuations along the line of sight, which can be used to determine the amplitude ($\sigma_8 \Omega_M$) and slope (n) of the power spectrum of mass fluctuations and the geometry of the universe. The mass power spectrum itself contains information on the primordial fluctuation spectrum, as well as the relative contributions of cold dissipationless particles (CDM), hot dissipationless particles (massive neutrinos), and baryons (which do dissipate) to Ω_M . In the case of sufficiently large mass concentrations, such as galaxy clusters, weak lensing also can be used to determine the total mass relatively independent of cosmological parameters (Tyson, Wenk, & Valdes, 1990; Luppino & Kaiser, 1997; Tyson, Kochanski, & Dell’Antonio,

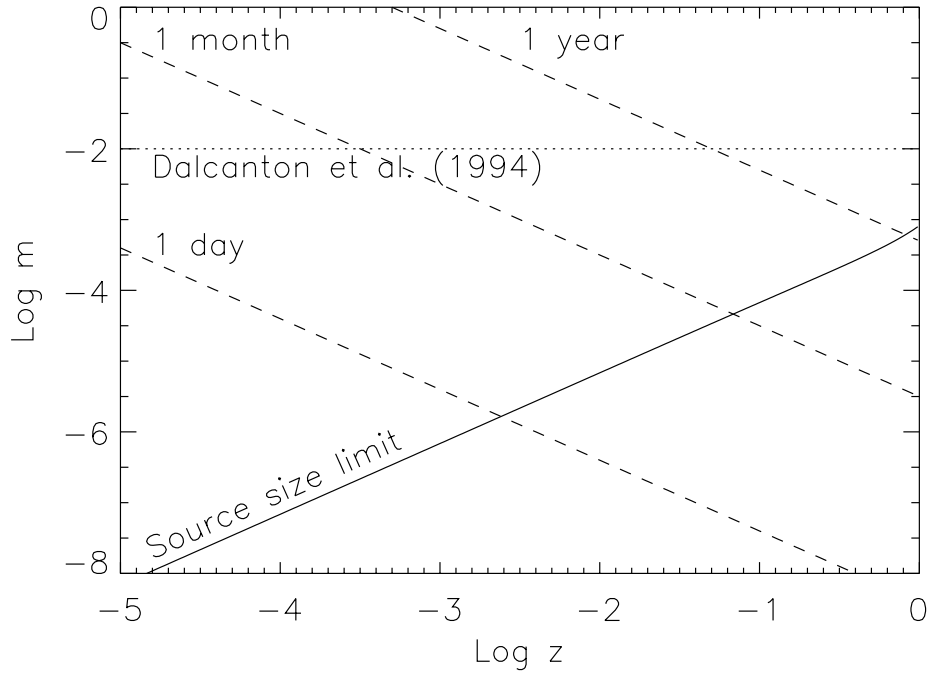


Figure 6.4: The microlensing detectability as a function of lens redshift, z , and lens mass, $m \equiv M/M_{\odot}$, from Walker (1999). In order for a microlens to introduce significant magnification, it must be more massive than indicated by the source-size limit. The adopted source size is taken as 10^{15} cm, located at $z \sim 2$, appropriate for a distant quasar. Approximate time-scales for microlensing events are shown by the dashed lines, assuming a transverse speed of 600 km/s. The limits already set by the Dalcanton et al. (1994) search for a change with redshift in quasar emission line equivalent widths which would be expected for lensing which resolved the quasar broad-line region are shown. SNAP would be most sensitive to planetary mass lenses in galaxies with redshift $0.1 < z < 1$ which varied on timescales less than 2 years.

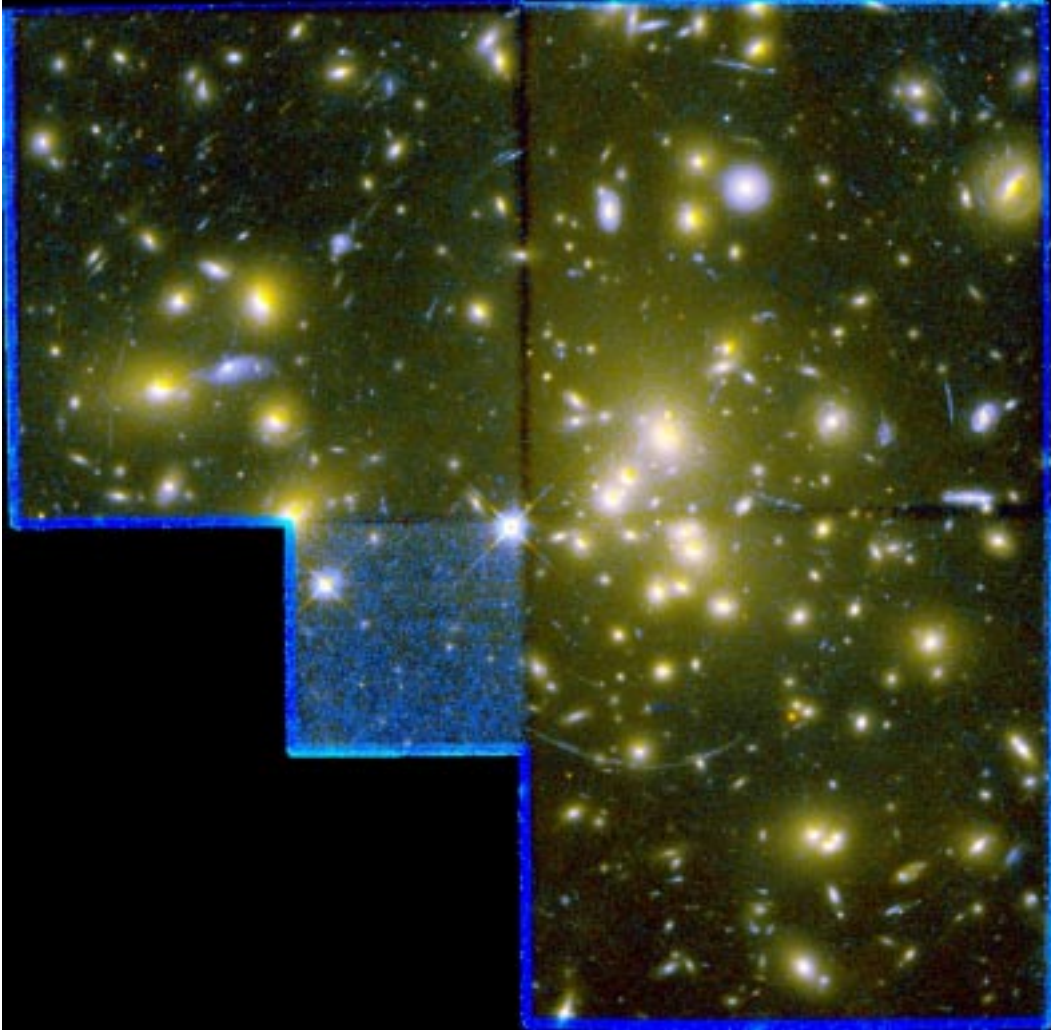


Figure 6.5: True-color image of the central portion of the massive cluster Abell 1689 ($z = 0.18$), taken with the Wide Field Planetary Camera 2 on the Hubble Space Telescope. The image shows the cluster members (bright oval-shaped blobs), two bright stars near the center, and the many faint, low surface-brightness arcs stretched tangentially about the cluster center. These are the magnified, brightened, and distorted images of background galaxies.

1998).

Since the effect of gravitational lensing on any given object is generally tiny ($\sim 1\%$), recovery of the weak lensing signal requires measuring the average effect over a large number of objects. The overwhelming majority of high-redshift sources are galaxies, so the basic ingredient for studies of weak lensing is very deep images of well-resolved galaxies covering a wide area of sky. Since SNAP will routinely monitor some 20° of sky to very low flux levels and 100° to intermediate flux levels, with image quality that will resolve most high-redshift galaxies, it can provide a weak-lensing dataset of unprecedented quality.

6.4.2 Weak Lensing Basics

Taking up from the discussion of strong lensing in the previous section, the perturbation of light traveling to us from a distant source is given by the Jacobian mapping input angles to output angles:

$$\frac{d\theta^I}{d\theta^S} = A(\theta^I)$$

Where the amplification matrix, A , is given by:

$$A(\theta^I) = \begin{bmatrix} 1 - \partial_{11}\varphi & \partial_{12}\varphi \\ \partial_{12}\varphi & 1 - \partial_{22}\varphi \end{bmatrix} \quad (6.1)$$

where, as in the previous section, φ is the projected mass surface density. The overall image magnification is given by $1/\det(A)$.

The amplification matrix can be broken down into an isotropic component called the convergence, κ , and an anisotropic component called the shear, $\gamma \equiv (\gamma_1, \gamma_2)$.

$$A(\theta^I) = \begin{bmatrix} 1 - \kappa - \gamma_1 & -\gamma_2 \\ -\gamma_2 & 1 - \kappa + \gamma_1 \end{bmatrix} \quad (6.2)$$

The complex shear can be determined by measuring the distortions in the ellipticity of lensed background galaxies. If the complex ellipticity is defined as $\epsilon = \frac{1-r}{1+r}e^{2i\phi}$ where ϕ is the position angle, $r = \frac{b}{a}$, and b and a are the major and minor axes of the ellipse, then the observed ellipticity ϵ_o is related to the intrinsic ellipticity ϵ_i in the weak lensing regime by

$$\epsilon_o = \frac{\epsilon_i + \mathbf{g}}{1 - \mathbf{g}^* \epsilon_i},$$

where $\mathbf{g} = \gamma/(1 - \kappa)$ is the reduced complex shear.

Using a large number of distant galaxies having random orientations, $\langle \epsilon_i \rangle = 0$, a map of the converge and shear fields due to lensing by foreground mass fluctuations can be obtained. If galaxies were intrinsically circular, measurement of the shear would be trivial. Rather, since the galaxies have a dispersion in ellipticity of about 0.4, the shear must be determined by spatially averaging over the ellipticities of many galaxies

to sort out the common distortion caused by lensing. The convergence map can then be reconstructed from the shear using

$$\langle \epsilon_o \rangle = \frac{|\gamma|}{1 - \kappa} \sim |\gamma| \text{ for } \kappa \ll 1,$$

or using a combination of shear information and galaxy surface density fluctuations (since the convergence component isotropically magnifies and demagnifies background galaxies).

A key ingredient in constructing and interpreting the highest signal-to-noise shear and convergence maps is knowing the redshift distribution of the galaxies. In particular, it is helpful to be able to statistically sort out the foreground (lensing) galaxies from the background (source) galaxies (Hui, 1999; Hu & Tegmark, 1999). Since the lensing power changes only slowly with relative distance, galaxy redshifts accurate to $\sigma_z \sim 0.1$ are more than adequate. The main SNAP SN monitoring fields will have deep photometry in XX filters spanning the wavelength range 0.35–1.0 μm . This will allow photometric redshifts good to $\sigma_z < 0.1$ to be determined for most detected galaxies.

Another key ingredient is controlling systematics. The principle source of systematic error in weak lensing work is the anisotropic component of the point spread function (PSF). Several techniques have been developed to help correct measured ellipticities for PSF anisotropy (Kaiser, Squires, & Broadhurst, 1995; Kaiser, 1998; Rhodes, Refregier, & Groth, 1999). However, given that the expected distortions are at the 1% level, the experiment would be much cleaner if only well resolved galaxies were used. Fig 6.6 shows that SNAP will better resolve galaxies, and will produce a much higher surface density of resolved galaxies than any ground-based experiment. For instance, requiring $\text{FWHM}_{\text{galaxy}} > 5 \text{ FWHM}_{\text{PSF}}$ eliminates most of the galaxies in the ground-based regime, demonstrating that ground-based weak lensing studies can succeed only if very careful corrections are applied. With this same over-resolution requirement there are still plenty of galaxies in the SNAP sample. The higher surface-density of the SNAP galaxy sample ($80\times$ ground-based) will provide cosmic-variance-limited uncertainties in $P_\kappa(l)$ up to $l \sim 1000$, whereas ground-based observations will be shot-noise limited down to $l \sim 100$.

6.4.3 Cosmological Measurements

With a map of the convergence in hand, a number of approaches can be used to constrain the cosmological parameters. Fig 6.8 gives an example of the constraints on Ω and Λ from a weak lensing survey of 100° (but with a galaxy surface density $10\times$ lower than SNAP). Fig 6.7, from Hu & Tegmark (1999), shows a theoretical prediction for the convergence power spectrum, $P_\kappa(l)$, and its uncertainty from a $3^\circ \times 3^\circ$ survey to $m_{AB}(R) \sim 25$. Also shown is $P_\kappa(l)$ from a cosmology which would be degenerate within 0.1σ using the expected MAP CMB data. The weak lensing power spectrum is able to significantly improve cosmological parameter estimates in combination with CMB or SN data by breaking degeneracies in those measurements. The uncertainties shown in Fig 6.7 can be improved by $2\times$ using galaxy redshift information (Hui, 1999). The larger sky coverage of the SNAP SN-monitoring fields would reduce the uncertainties

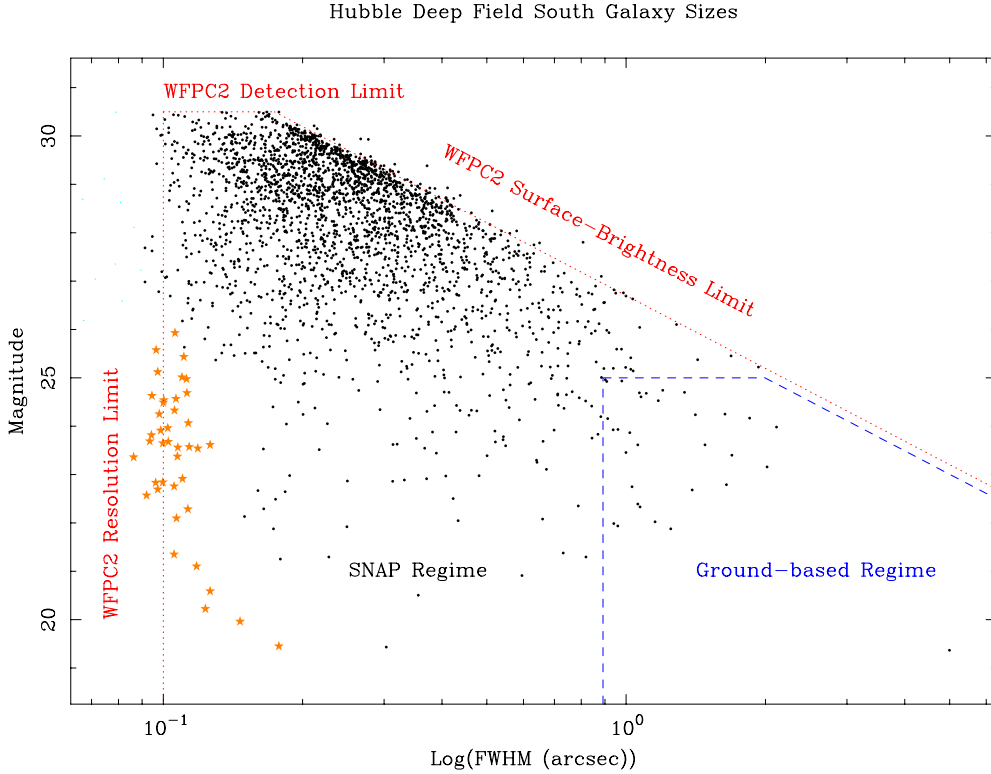


Figure 6.6: The sizes of galaxies detected by the HST Wide-Field/Planetary Camera (WFPC2) in the southern Hubble Deep Field (HDF-S) are shown, as a function of $V + I$ magnitude. The sizes plotted correspond to the FWHM of the best-fitting Gaussian. The limits on faintness, resolution, and surface brightness for this sample are shown with dashed red lines, and are labeled accordingly. Brighter sources at the resolution limit are probably stars (possibly quasars as well; orange star symbols). Detections which are faint and below the resolution limit are likely spurious (cyan dots). The remaining detections are predominantly galaxies (black dots). The SNAP SN monitoring fields would deliver data of quality comparable to the HDF-S — with perhaps very slightly lower resolution but probably deeper surface-brightness limits — over a region of sky roughly $10^4 \times$ larger. Galaxies which could be resolved with wide-field ground-based surveys are in the region bounded by dashed blue lines. Note that the resolution limits (vertical lines) indicate the point at which the FWHM of the point spread function (PSF) equals the FWHM of the galaxy, therefore, careful removal of PSF anisotropies is required or else the analysis must be confined to even larger galaxies. Given that the expected distortions are at the 1% level, it is very desirable to work only with well resolved galaxies.

by another $\sqrt{2}$, and the higher surface density of SNAP galaxies would reduce the uncertainties for $l > 100$ by another $\sim 5\times$. Finally, the higher mean redshift of the SNAP sample would increase the lensing signal, further improving the signal-to-noise. Better measurements for $l < 100$ would require observations in addition to the SNAP SN-monitoring fields. Cosmic-variance overwhelming dominates the statistical noise at these angular frequencies, meaning that only a significant increase in sky coverage can reduce the uncertainties. Conversely, since shot noise is not an issue, such additional observations could be relatively shallow. SNAP could easily perform a shallow survey covering $100\text{--}1000\text{Mpc}^2$ (possibly with sparse sampling, as suggested by Kaiser (1998)) which would allow determination of the slope of $P_\kappa(l)$ in the linear regime ($l < 100$).

There are several alternative schemes for constraining the cosmological parameters from weak lensing measurements include measuring the skewness, S_3 , of the convergence field (Jain & Seljak, 1997; Schneider et al., 1998; Van Waerbeke, Bernardeau, & Mellier, 1999; Bartelmann & Schneider, 1999) measured on angular scales of several arcminutes. This estimator is sensitive to the combination $\sigma_8\Omega_M$ (σ_8 measures the normalized RMS density fluctuations in an 8 Mpc top-hat sphere). Since its strongest signal is at high angular frequencies, where shot noise usually dominates, skewness measurements with SNAP can be much more accurate than those from ground-based surveys. (Benítez & Sanz, 1999) claim that by determining the correlation —induced by weak lensing amplification— of foreground galaxy surface density with the positions of background galaxies, it should be possible to determine Ω_M/b (b called the “bias” and is defined as the ratio of the normalized galaxy number density to the mass density field, $b = \frac{(\delta N_{gal}/N_{gal})}{(\delta\rho/\rho)}$). The amplitude distribution of peaks (not just the skewness) in maps of the convergence may be another way to constrain $\sigma_8\Omega_M$ (Jain et al., 1999; Van Waerbeke, Bernardeau, & Mellier, 1999).

The weak points of weak lensing are that very sophisticated modeling, with 7 unknown parameters (8 including w_Q), is needed to interpret results for cosmology, whereas really only 4 parameters (non-linear amplitude, non-linear slope, linear/non-linear transition wavenumber, and linear slope) can be determined from the convergence power spectrum, $P_\kappa(l)$. However, weak lensing is more of a geometric method and thus to first order is immune to evolution or dust extinction (indeed, it can be used to *measure* evolution in the dark matter distribution). In combination with either supernova constraints or CMB constraints, weak lensing is extremely powerful (especially in constraining neutrino mass, not just mass difference). Finally, gravitational lensing is the only means of directly probing the distribution of dark matter; this may be key in determining what dark matter is made of.

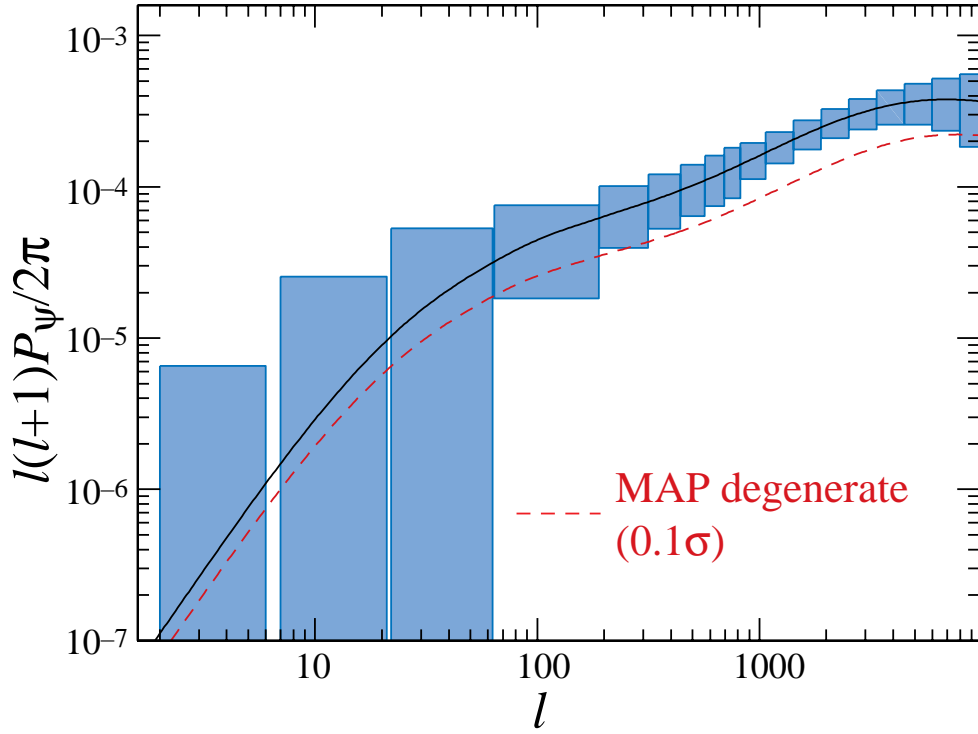


Figure 6.7: Example of the convergence power spectrum, $P_\kappa(l)$, and associated uncertainties, for a $3^\circ \times 3^\circ$ weak lensing survey (Hu & Tegmark, 1999). The surface density of galaxies assumed is roughly the geometric mean of what can be observed from the ground and what can be observed from space once spatial resolution requirements are imposed. Moreover, this example does not include the benefits of studies lensed galaxies in different redshift bins, as advocated by Hui (1999). The larger areal coverage of the SNAP supernova monitoring fields, in combination with these other improvements should allow SNAP to reduce the uncertainties on $P_\kappa(l)$ by an order of magnitude compared to what is shown here for $l > 100$. Wider-field SNAP images taken for search and follow-up of the lowest redshift supernova, or dedicated weak lensing images, can substantially improve $P_\kappa(l)$ for lower multipoles.

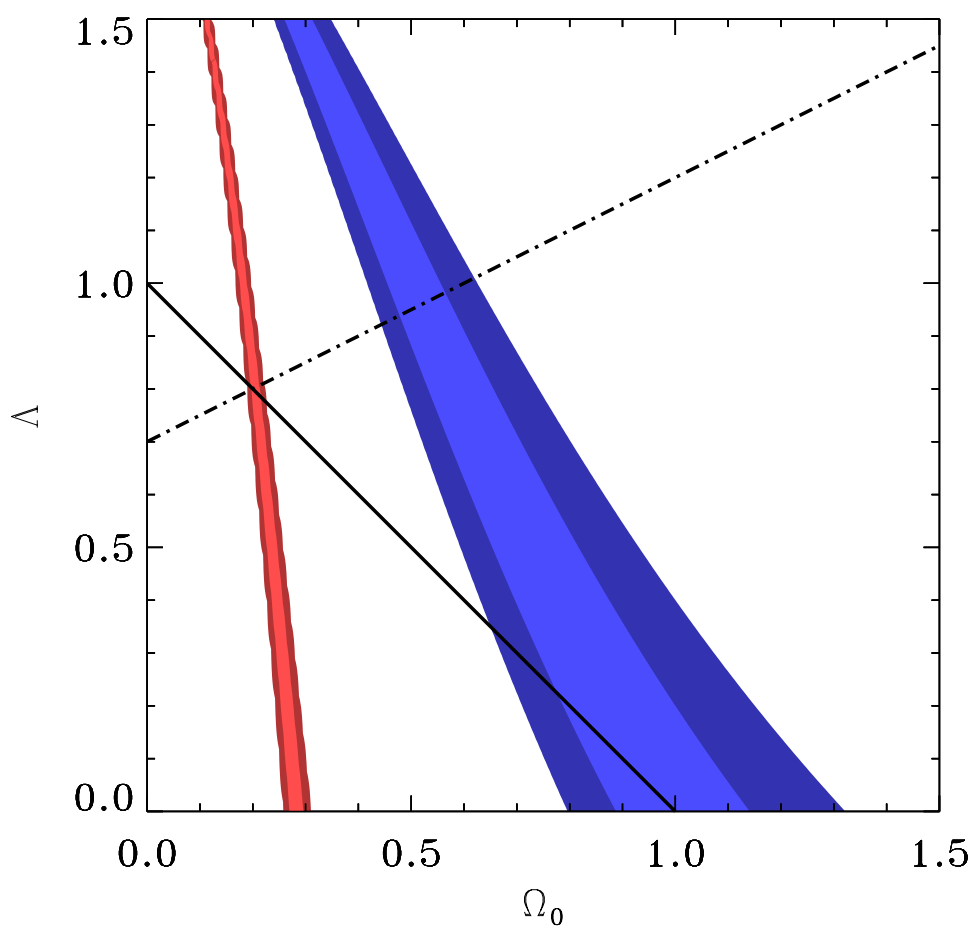


Figure 6.8: Example of the confidence regions in the Ω , Λ possible with a weak lensing survey of 100h^2 , adapted from Van Waerbeke, Bernardeau, & Mellier (1999). Confidence regions are shown for $\Omega_M = 0.3$ (left bands) or $\Omega_M = 1$ (right bands) and $\Lambda = 0$.

Part III

Baseline Instrument Description

Chapter 7

Observational Strategy & Data Package

7.1 Overview

The SNAP baseline science objective is to obtain a high statistics calibrated dataset of Type Ia supernovae to redshifts of 1.7 with excellent control over systematic errors. The statistical sample is to be 2 orders of magnitude greater than the current published set of ~ 42 supernovae, and is to extend much farther in distance and time. From this dataset we expect to obtain a 2% measurement of the mass density of the universe, a 5% measurement of the vacuum energy density, a 5% measurement of the curvature, and a 5% measurement of the equation of state of the “dark energy” driving the acceleration of the universe. Systematic studies will include a measurement of the “reddening” of spectra from “ordinary dust” at redshifts up to 1.7, and studying potential “grey dust” sources. Using type Ia supernovae as standard candles will require measurement of the key luminosity indicators: the light curve peak and width. The redshift of the host galaxy of the supernova needs to be measured, supernova type identified, and spectral features studied. Effects correlated with host galaxy morphology and the position of the supernova in the host galaxy will also be studied. These properties may indicate differences in stellar population from which the supernova came and therefore can be used to test whether the intrinsic brightness of the supernova changes systematically with redshift.

The baseline mission repeatedly samples a total of 20 fixed fields in the north and south ecliptic poles every four days searching for new supernova explosions. This “batch processing” method is a key to obtaining the required bias-free dataset. The discovered supernovae are then measured by photometry for the next four to eight months while the luminosity waxes and wanes. The observing fields selected minimize zodiacal light background. A medium-resolution spectrum is taken of each supernova at peak brightness. For supernovae with redshifts beyond $z = 1.2$ a greatly limited sample of the discovered supernovae are followed as these can only be measured very slowly in the infrared. The satellite is expected to be able to follow 2,000 supernovae per year with redshifts ranging from 0.1 to 1.7.

7.2 Observational Strategy & Data Package

The key measurement of the mission is the peak brightness vs. redshift relationship of type Ia supernovae out to a redshift of 1.7. These data will require taking accurate photometric observations of the supernova over the light-curve. An example of the restframe B-band light-curve is shown in Figure 7.1. It has been found experimentally that the supernova peak brightness can be standardized when viewed through a B-band filter where the B-band is defined in the restframe of the supernova (defined at rest with respect to the supernova). Therefore the photometry must seek to define an appropriate bandpass depending on the redshift of the supernova. The importance of this bandpass selection can be seen in Figure 7.2, where the B-band is superimposed over an example type Ia supernova spectrum. The bandpasses can be defined either by having an extensive set of “redshifted B-band” filters, one for each small range of redshift, or by defining the bandpasses synthetically using spectrophotometry. Both are suitable and viable options. Given that a large field-of-view optical photometer is in the baseline for the mission, it is possible to “batch process” large numbers of supernovae in a given observation so that the objectives can be met with a large number of filters. An example of a possible set of bandpasses with a average 25% non-overlap are given in Table 7.2 below.

<i>Effective redshift</i>	<i>B-band Center λ (μm)</i>	<i>B-band Bandpass $\delta\lambda$ (μm)</i>
0	0.44	0.11
0.1	0.48	0.12
0.2	0.53	0.13
0.3	0.57	0.14
0.4	0.61	0.15
0.5	0.66	0.16
0.6	0.70	0.17
0.7	0.75	0.18
0.8	0.79	0.19
0.9	0.83	0.20
1.0	0.88	0.21
1.1	0.92	0.23
1.2	0.97	0.24
1.3	1.01	0.25
1.4	1.05	0.26
1.5	1.10	0.27
1.6	1.14	0.28
1.7	1.19	0.29

Table 7.1: Redshifted B-band filters

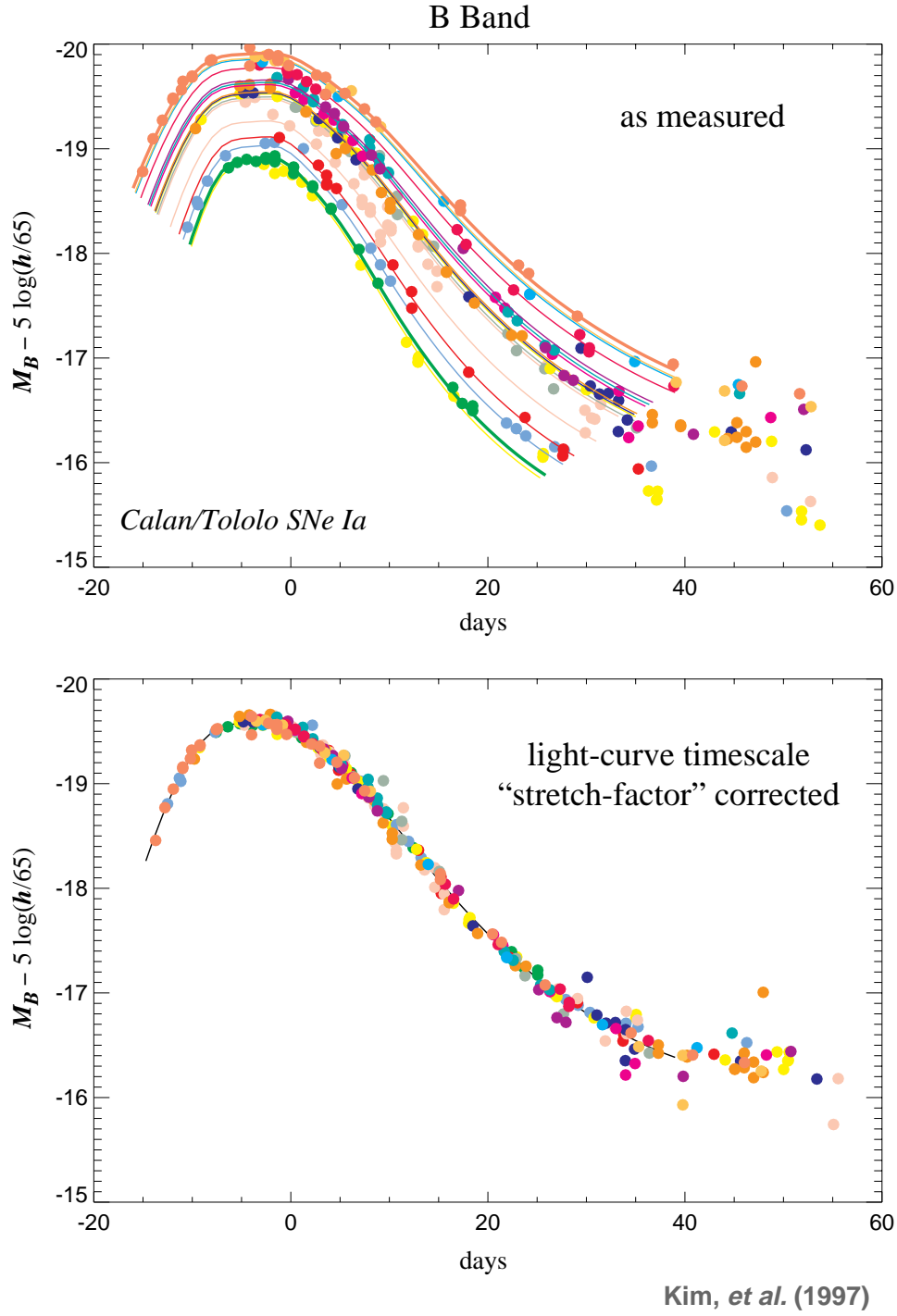


Figure 7.1: B-band Light-curve for Type Ia Supernovae corrected for redshift and light curve timescale.

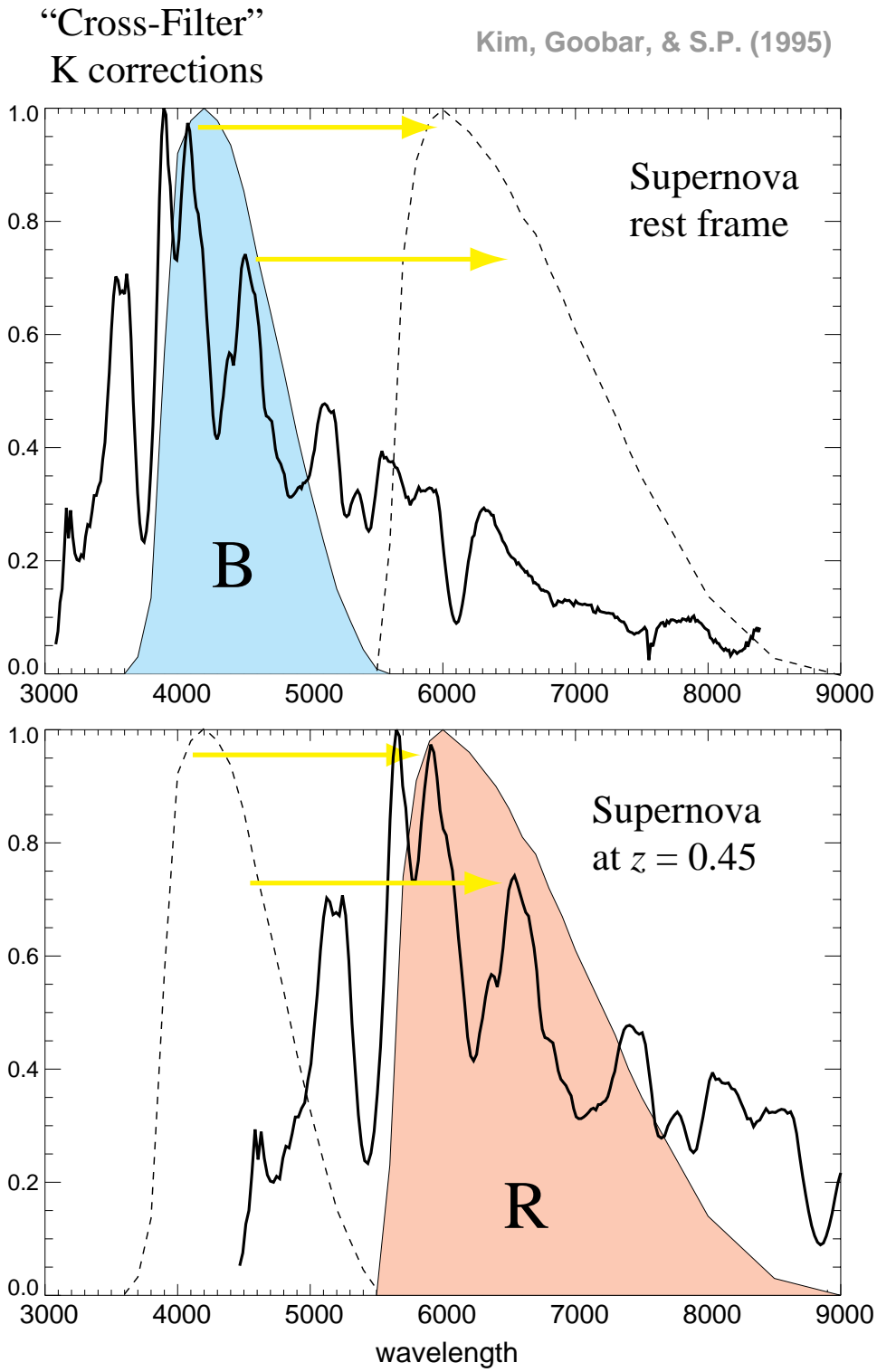


Figure 7.2: Example Type Ia supernova spectrum with B-band bandpass superimposed.

7.3 Objectives

The satellite is expected to carry four key instruments, a $1^\circ \times 1^\circ$ wide field optical imager/photometer, an optical spectrograph, a small IR imager/photometer, and an IR spectrograph. The capabilities of these instruments must be a good match to the science requirements for the satellite. In particular, the instrumentation must provide all the elements of the supernova studies, namely: 1) early detection of supernovae, 2) B-band restframe photometry to follow the photometric light curve of the supernova as it waxes and wanes, 3) supernova color at peak and near peak brightness, 4) spectra at near peak brightness to classify the supernova, 5) photometric redshifts of the host galaxies in advance of supernova follow-up, and 6) medium resolution spectra/photometry for a limited subset of supernovae sampled over the light-curve. Each of these elements can be expressed as a set of explicit requirements for the data products:

Detection. Early detection of Type Ia supernovae at $S/N > 10$, these would be obtained by comparing current images to a set of reference images. Early detection is required to identify the supernova within two days of explosion in the supernova restframe. Twenty $1^\circ \times 1^\circ$ fields would be repeatedly studied with a repetition rate of every four days for low redshift supernovae $z \leq 0.3$ with magnitude $m_{AB}(1.0\mu) \leq 27$, every six days for supernovae $0.4 < z < 0.8$ with magnitude $m_{AB}(1.0\mu m) \leq 28$, and every eight days for supernovae $0.8 < z < 1.2$ with magnitude $m_{AB}(1.0\mu m) \leq 28.5$. Two $1^\circ \times 1^\circ$ fields would be repeatedly studied with a repetition rate of every eight days for high redshift supernovae $1.2 < z < 1.7$ with magnitude $m_{AB}(1.0\mu m) \leq 30$. Only a sub-sample of the supernovae with $z > 1.2$ would be selected for further study.

Photometry. Photometric study of the supernova light curve by obtaining ten data points along the development of the light curve at specific intervals. Photometry for the supernova is obtained in the rest-frame B-band of the supernova using a filter set that approximates a redshifted B-band filter. Data points would be taken at peak brightness ($S/N > 30$), at 0.5 magnitude below peak ($S/N > 30$) (two measurements at rise and fall of light curve), at 1.0 magnitude below peak ($S/N > 20$), at 1.5 and 2.0 magnitude below peak ($S/N > 15$), and at 2.5 magnitude below peak on trailing edge of light curve ($S/N > 10$) only in the optical channel. Restframe photometry in B-band is redshifted into the observer frame by $(1+z)$. Photometry can be obtained by multiple fixed filters, an integral field spectrograph which preserves photometry, or other low resolution spectrograph provided there are no photometric losses. An optimal redshifted B-band filter or synthesized filters applied to spectrophotometry would eliminate a principal source of systematic error from the k-corrections. The photometry will require both optical and NIR coverage. Both optical and IR Photometry are expected to be performed with a systematic accuracy of better than 1% over the redshift $0.3 < z < 1.7$.

Spectra. In order to classify the supernova as type Ia a spectrum is obtained at peak magnitude. In the optical channel, for supernovae with redshift $0.02 < z < 0.4$ the resolution required is 15 \AA ($S/N > 10$), and 30 \AA ($S/N > 10$) for $0.4 < z < 1.2$, to study wavelengths between $3500\text{--}4800 \text{ \AA}$ in the restframe of the supernova. For supernovae with redshift $1.2 < z < 1.5$ the resolution required is 30 \AA ($S/N > 10$), to

study wavelengths between 3800-4200 Å (Ca II) in the restframe of the supernova. A single medium resolution optical spectrograph extending from 3500Å to 10000Å would appear to be sufficient to satisfy these requirements. For the highest redshift supernovae $z > 1.5$, a NIR channel would permit identification using the Ca II spectral features. In the IR channel, for supernovae with redshift $1.5 < z < 1.7$ the resolution required is 50 Å (S/N>10) to study wavelengths between 3800-4200 Å (Ca II) in the restframe of the supernova. For supernovae with redshift $0.02 < z < 1.2$ optical and IR spectra are obtained to 50 Å (S/N>10) at the Si II (6150 Å trough) to classify the supernova and study metallicity effects.

Color. To correct the data for supernova extinction from interstellar dust using color. As a minimum, restframe V-band photometry is obtained at peak brightness to S/N>30 band for all supernovae in the sample. Additional filter bands and near peak measurements (1 magnitude below peak) would be desirable.

Redshift. Measure photometric redshifts for host galaxies (only once per field) based on images in multiple filters to S/N>30.

Medium Resolution IR spectra (evolution). On a subset of the data obtain a medium-resolution spectrum at peak brightness (S/N>30 per 15 Å) for $z < 1.0$ to check for evolution of spectral features. Wavelength range is from 3000 Å to 6500 Å in the restframe of the supernova. For $z > 0.5$, this will require good near-IR spectroscopy capability.

NIR Photometry(dust). On a subset obtain spectrum or photometry at peak brightness in the laboratory frame wavelength range 4000 Å to 17000 Å to check for reddening of the supernovae for $z < 0.5$ from non-standard interstellar dust sources, emphasizing greater than 10000 Å. Only low-resolution of 1500 Å(S/N>30) is required for this systematic study.

7.4 Instrument Performance

In one year of study, as shown in Table 7.2, the satellite can discover, follow the light curve, and obtain spectra at peak brightness for 2366 supernovae. Most of these supernovae are obtained in the critical region of $0.5 < z < 1.2$ where the experiment has peak sensitivity to the value of the cosmological constant.

<i>Redshift</i>	<i>#SNe follow</i>	<i>Fields Fields</i>	<i>Photometry Photometry</i>	<i>Spectroscopy [days/yr]</i>	<i>Color [days/yr]</i>
0.1	14	20	8.4	0.06	
0.2	44	20	8.4	0.20	
0.3	82	20	8.4	0.38	
0.4	124	20	5.6	0.57	
0.5	162	20	5.6	0.75	
0.6	196	20	5.6	1.15	
0.7	226	20	5.9	2.24	
0.8	250	20	10.5	4.63	
0.9	270	20	12.6	5.00	2.13
1.0	286	20	16.9	6.07	3.31
1.1	298	20	25.3	8.81	5.52
1.2	304	20	35.1	12.12	6.74
1.3	30	2	20.9	3.66	
1.4	30	2	29.1	4.95	
1.5	22	2	28.8	4.77	
1.6	16	2	28.4	2.14	
1.7	12	2	28.0	2.03	
total			284	60	18

Table 7.2: Summary

Chapter 8

Telescope

8.1 Optical Requirements

The preceding material establishes a number of requirements that the SNAP telescope must satisfy. The most important of these are the optical performance specifications that establish the light gathering power, angular resolution, and wavelength coverage needed to deliver our planned supernova discovery rate. Furthermore, the final plate scale must allow us to properly oversample the image with existing CCD pixel sizes. We summarize our requirements in Table 8.1 below.

8.2 Optical Design

A key driver for our optical design is the requirement for a high quality field of view (FOV) that is one degree square. Telescopes that offer FOVs of this size or greater can be divided into several varieties:

8.2.1 One-Mirror with Corrector

This group includes the Schmidt telescopes which use a full-aperture refractive correcting plate and a concave spherical mirror. The focal surface is strongly curved and

Aperture	1.8 meter to 2.0 meter
Field-of-view	1° x 1°
Optical resolution	diffraction-limited at 1 μ m, \sim 0.1 arcsec for 2m primary
Wavelength coverage	350nm - 1700nm
Solar avoidance	70°
Temperature	< 200 K (well below thermal background for 1.7 μ m wavelength)
Fields of study	North and South Ecliptic Poles
Image stability	0.03 arcsec over each exposure
Plate scale	\sim 10 μ m/0.1 arcsec (for 2m diffraction limit)
Effective focal length	\sim 20m
Pupil Obscuration	<40%, preferably unobscured

Table 8.1: SNAP Observatory Requirements

is located midway between the corrector and the mirror. The refracting corrector is impractical for space use but can be replaced by a tilted reflecting corrector. However, sub-arcsecond performance has never been achieved in this way. Moreover, the inaccessible location of the focal surface makes this group unattractive for SNAP owing to requirements imposed by thermal design and spectrograph access to the focal plane.

8.2.2 Two-Mirror Ritchey-Chretien with Correctors

Although the uncorrected Ritchey-Chretien cassegrain telescope (e.g. the Hubble Space Telescope) has too small a field of view to be useful for SNAP, refractive correcting optics can be added to produce a wider field of view. These lenses need be only as large as the secondary. Examples are the DuPont telescope and the Sloan Digital Sky Survey telescope (see Figure 8.1 for an example); each uses a multi-element refractive Gascoigne corrector to achieve sub-arcsecond performance over a field of several degrees in size.

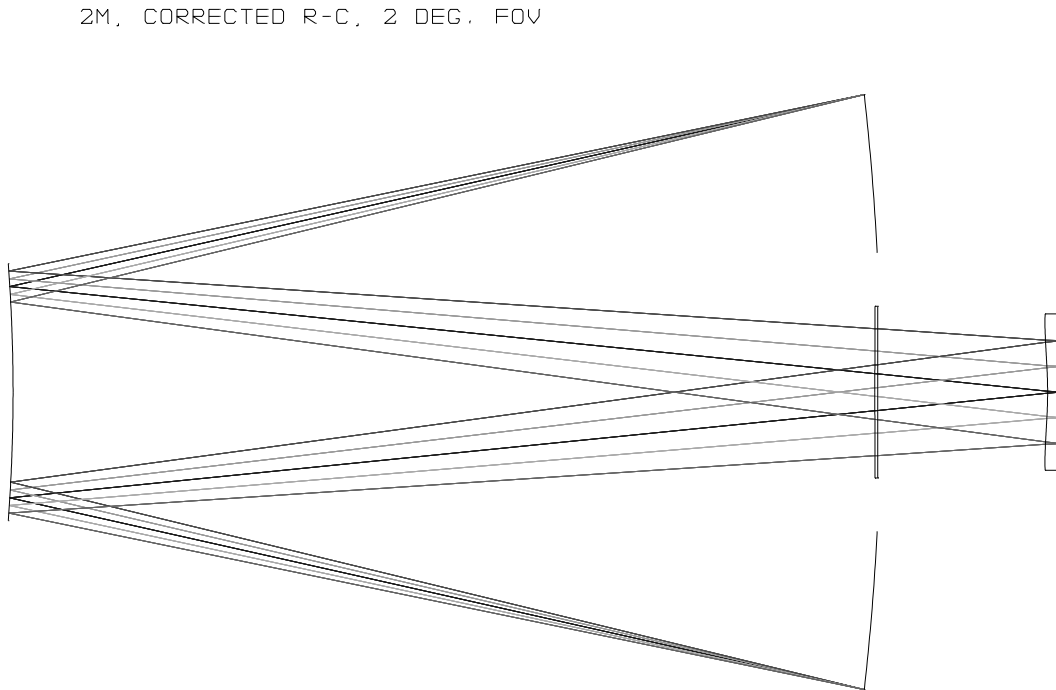


Figure 8.1: Example of a 2 meter Ritchey-Chretien with Gascoigne correctors to achieve a diffraction limited wide field, modeled after the Sloan Digital Sky Survey Telescope.

8.2.3 Two-Mirror Schwarzschild Telescopes

These can be designed to have a flat field without needing a refractive corrector, but their astigmatism is generally far too large to satisfy our requirements for sub-arcsecond image quality.

8.2.4 Three-Mirror Telescopes

This is an extremely large category, and quite a number of published optical designs meet our requirements for FOV and angular resolution. The presence of a third mirror allows for wide field correction without needing any refractive elements. As well as eliminating achromatism, this feature removes the mass and radiation damage susceptibility of near infrared glasses.

For SNAP we regard the three mirror family as the most attractive configuration. Some members of this group offer flat image surfaces, which are advantageous in simplifying the CCD array alignment. In addition, some members of this group offer intermediate field stops or beam waists, which are efficient locations for filters, shutters, lightweight beam steering mirrors and the like. Since a three-mirror telescope contains no refracting elements, it is inherently achromatic from the NUV to the IR. With the third mirror it is possible to design telescopes that are free of spherical aberration, coma and astigmatism with large *flat* image surfaces. Moreover, if curved focal surfaces are allowed, higher degree aberrations can be eliminated as well. There are further practical advantages to a subset of the three mirror family: baffling against stray light can be simplified, the accessibility of the focal plane can be improved, and the longer final optical path allows for interposing a variety of filters and steering mirrors into the train. A summary of the most important three-mirror, wide-field telescopes is given here.

Paul-Baker Three-Mirror Telescopes

The chief idea is to combine a concave primary paraboloid and a convex secondary paraboloid to produce an approximately afocal reducer. These two elements are followed by a highly concave spherical tertiary. The secondary, located at the center of curvature of the tertiary, is then modified to eliminate the spherical aberration of the system. A 1.8 meter telescope of this type with a 1° field-of-view and a worst case 0.1 arcsec rms radius image was described in Angel, Woolf, & Epps (1982); McGraw et al. (1982). In this design, shown in Figure 8.2, the short focus of the tertiary buries the detector deep within the secondary-tertiary space, being inaccessible and blocking its own light and also needs a fairly large secondary whose size is about 40% of the primary size.

Korsch's Three-Mirror Family

An analytic comparison of five variants of the basic three mirror layout (concave, convex, concave) was presented in Korsch (1980). Although not computer optimized, these five designs could serve as starting points for detailed engineering tradeoffs. In particular his layout 5 possesses an intermediate beam stop, very attractive for SNAP because filters and a shutter can be most economically placed there. In Figure 8.3 we show a flatfield, 1.5° FOV, $f/12$ Korsch design.

Willstrop's Mersenne-Schmidt Telescope

Placing the tertiary significantly behind the primary was shown by Willstrop (1984) to have significant advantages for wide-field imaging. With the increased space between tertiary and primary a 45° optical flat can be inserted to fold the optical paths. Moreover, this extra final-focus length allows us to tailor the final focal ratio to give the plate scale required so that our CCD pixels properly oversample our diffraction spot

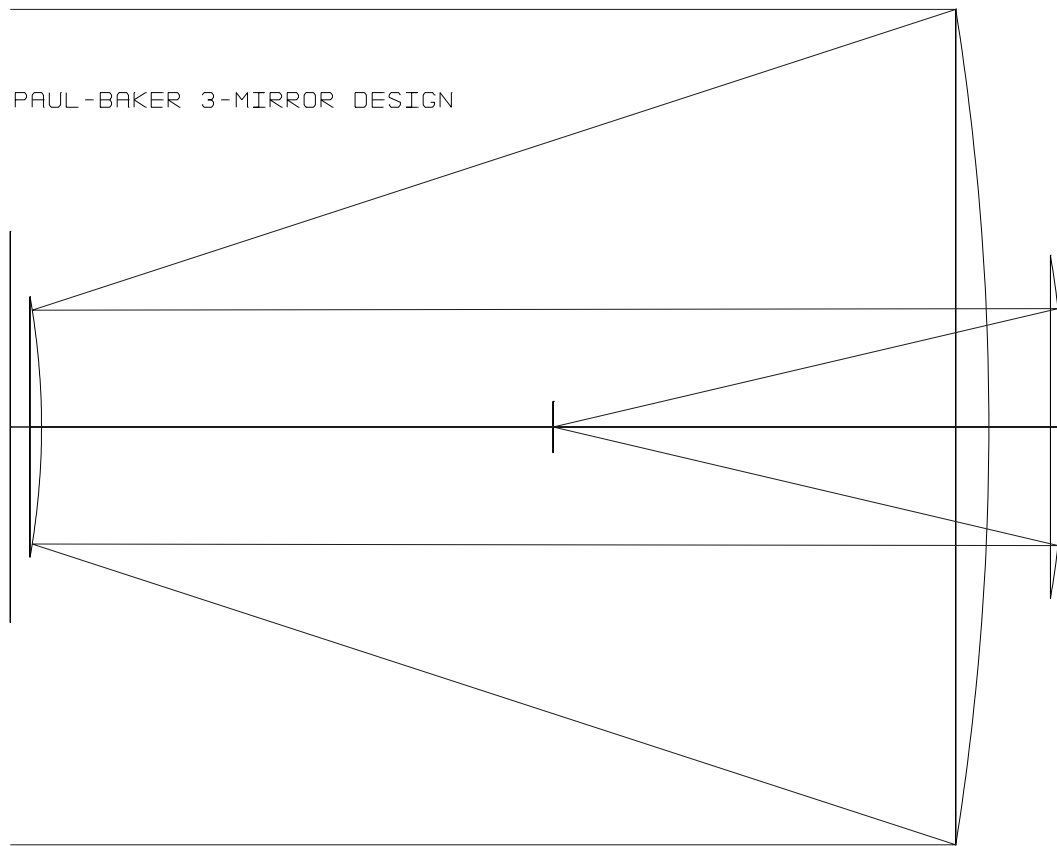


Figure 8.2: This is an example of a Paul-Baker three mirror design. Note that the image plane lies near vertex of the primary mirror.

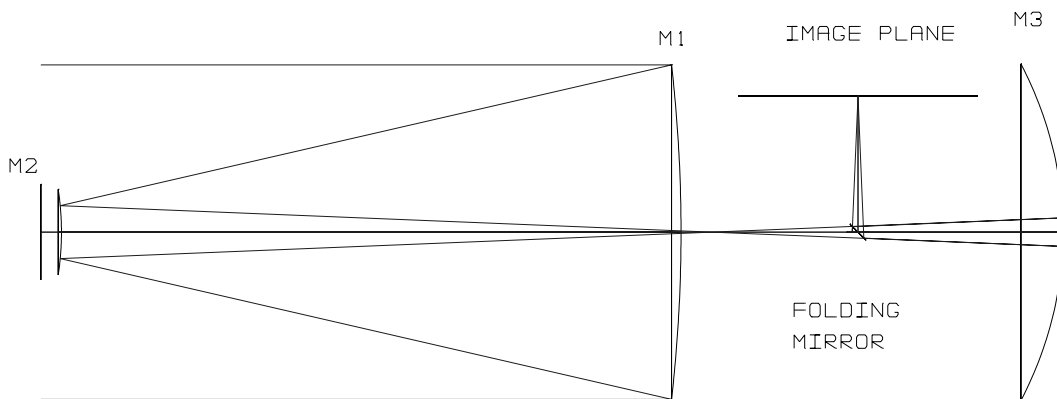


Figure 8.3: This Korsch design has an intermediate field stop at the exit pupil, a folding mirror puts the imaging plane in an accessible location behind the primary mirror.

size. However, the obscuration of the entrance pupil is nearly 50 % in the Willstrop design, and its length is nearly twice that of the Paul-Baker derivatives, so for SNAP we regard Willstrop's published configuration as unattractive. It does however offer a potentially attractive variant: if an off axis section of the Willstrop configuration is used, its baffling becomes hugely simplified and the long back focal position of its tertiary invites folding the final optical path behind the primary. Such a fold would place the detector plane near the boundary of the spacecraft envelope where thermal cooling is simplest and optical access is convenient.

Epps - Takeda Telescope

A thoroughly computer optimized three mirror telescope was published by Epps & Takeda (1983). This three mirror system was shown to deliver an average rms image radius of 0.01 arcsec over a 0.5 case, polynomials were used to correct both the secondary and the tertiary mirrors. Like Willstrop, the Epps-Takeda design places the tertiary behind the primary. In addition it features a relatively clean separation of the secondary and tertiary beams, so that in an off-axis configuration a baffle and folding mirror could be interposed to bring the final focal surface to a convenient location behind the primary.

Dark Matter Telescope

The Dark Matter Telescope (DMT) design is an on-axis variation of the Paul-Baker three mirror telescope (shown in Figure 8.4). The design specs are for a flat, 3° field of view with high resolution (51 micron/arcsec, 19.6 arcsec/mm), and an effective focal length of 10.5 meters.

The primary is a fast (f/1), hyperboloid, 8 meter diameter mirror. The secondary and tertiary mirrors are both prolate ellipsoids with diameters of 3.4 and 4.4 meters respectively. Total obscuration ranges from 26% at the field center to 38% at the field edge. The 3 degree imaging surface has a diameter of 55 cm. Eighty percent of the energy is encircled within a 1/3 arcsecond diameter. The detector is placed on axis, just behind the vertex of the primary.

New Planetary Telescope

The cleanest possible diffraction pattern is achieved with an unobscured pupil. An exhaustive study of this issue motivated by near-IR planetary research has recently been published (New Planetary Telescope WG Report 1999, Kuhn *et al.*). This group adopts a straightforward solution: use only an off-axis portion of each mirror, and scale the resulting optic to the size needed. They demonstrate mathematically that a 6.5 meter circular off-axis portion of a 15 meter f/1 mathematical primary optic yields a three mirror system meeting their needs for both wide field and high resolution. An example of this design is shown in Figure 8.5. Note that in the SNAP case, a 2-meter off-axis section will more easily produce 0% obscuration. Requiring only a one degree FOV leads to much better optical performance (G. Moretto, private communication).

8.2.5 Summary

The NPT design listed above opens an important avenue into wide field designs that are to achieve the best possible photometric accuracy. A fully unobstructed pupil avoids the diffraction of light normally caused by the secondary mirror and its support

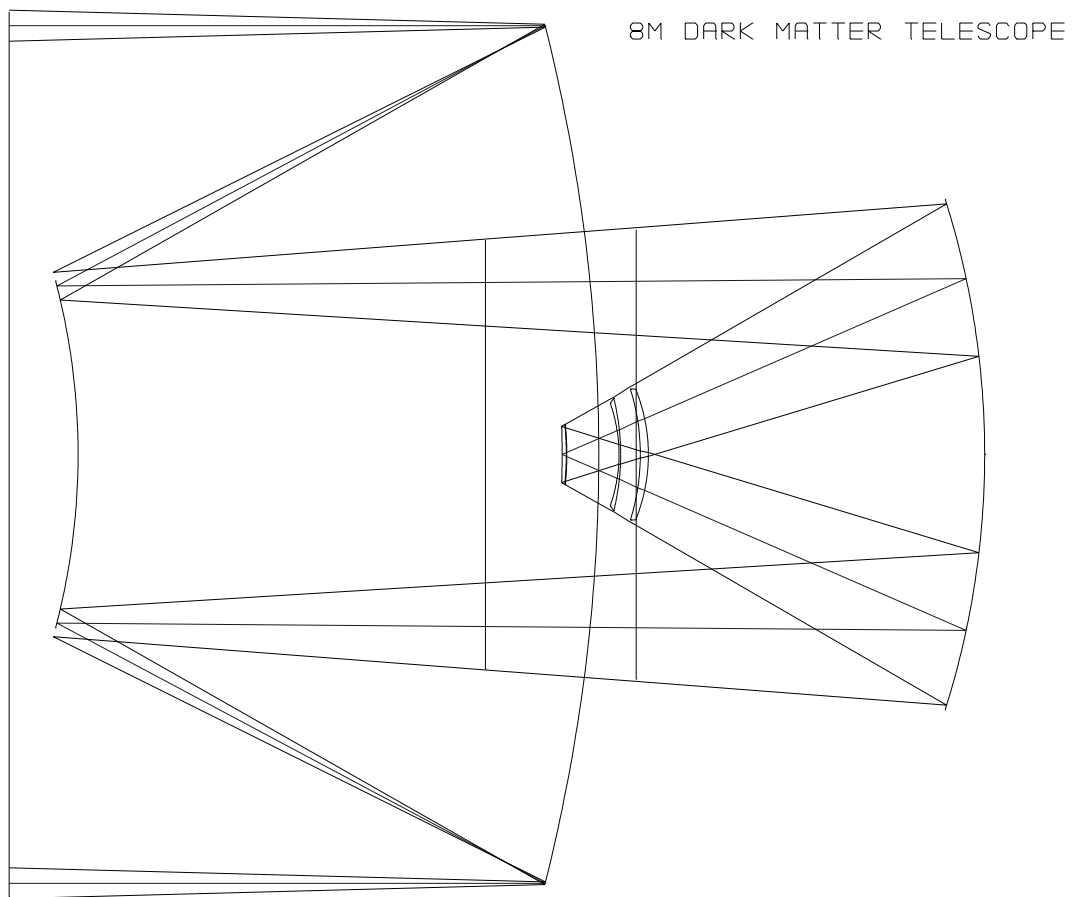


Figure 8.4: DMT Telescope (from R. Angel) a variant on the Paul-Baker three mirror telescope.

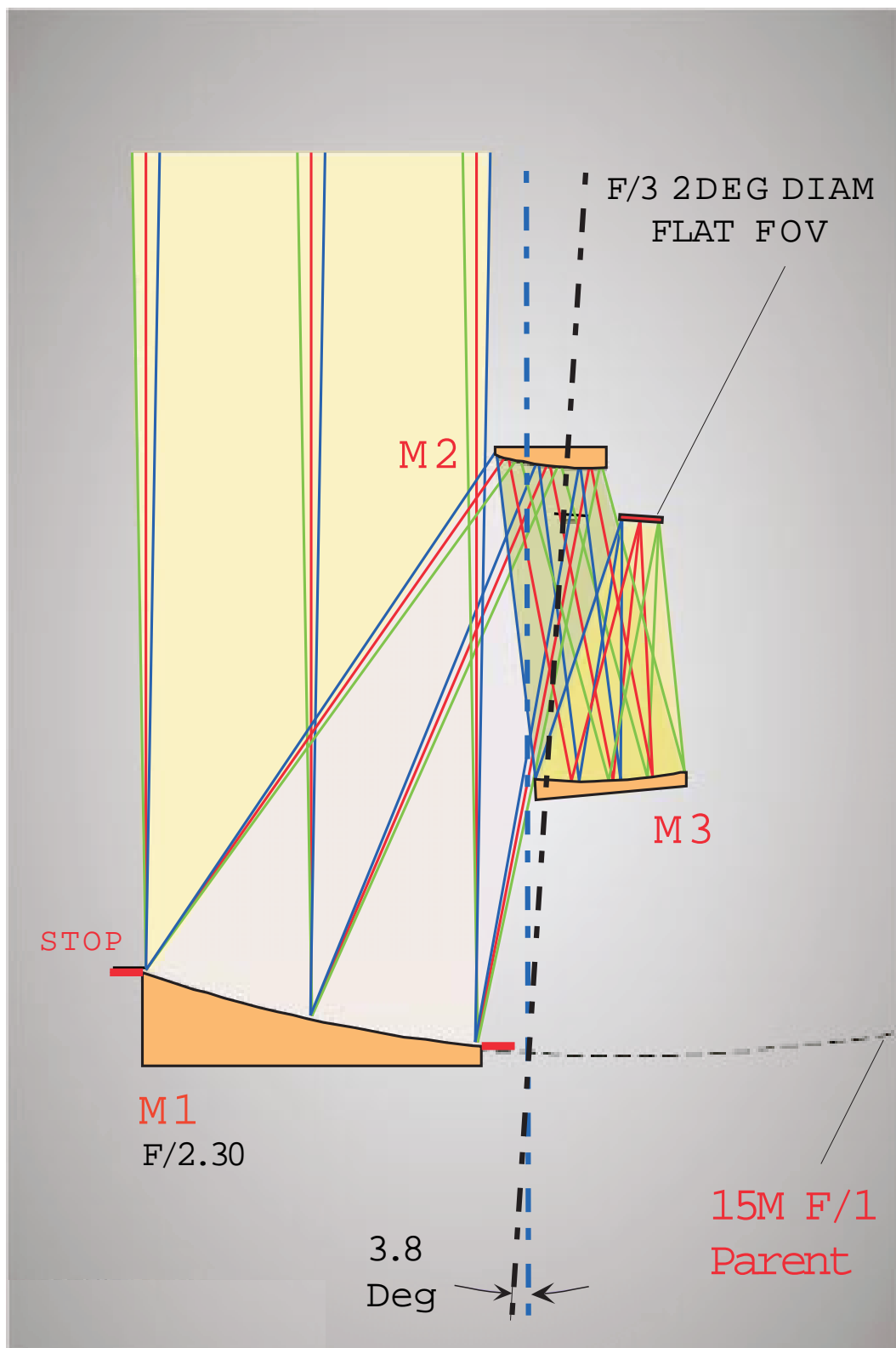


Figure 8.5: New Planetary Telescope, an off-axis wide field diffraction limited three mirror design with an unobscured pupil and excellent baffling. (Figure courtesy of G. Moretto/NOAO.)

structure. The net result is an improved ability to detect faint objects near brighter ones. An added bonus is the removal of the final focal plane from the space between the optical elements, which enormously eases the thermal design for the CCD detector plane where heat loads have to be carefully managed.

We emphasize that all of the three-mirror systems listed above will meet our fundamental requirements once scaled to a 2m aperture. Our final choice will depend on the results of our Phase A design study and will hinge on a number of practical factors:

- minimizing total mission cost
- minimizing total mission risk
- minimizing total mission schedule

8.3 Active Steering Mirror

Another key to the success of our optical design is the inclusion of a servo reflector in the optical path to stabilize the image over potentially long exposures while imposing a less stringent pointing stability specification on the spacecraft, thereby reducing total mission cost. An optic that can move in pitch, yaw, and piston can simultaneously allow us to stabilize our image in X, Y, and focus. For this purpose several CCDs will be located around the periphery of our principal focal plane. Each will be set up for video frame rate image analysis. Because there are ~ 100 stars/square degree at high galactic latitudes brighter than $m_V=15$, and because one star of $m_V=15$ delivers 10000 photons to a 30 ms video frame from a two meter telescope over a $1\mu\text{m}$ bandpass, the combined shot noise and readout noise in the video CCD signal will be the order of a few percent in each video frame. This SNR will give a pointing correction signal whose noise is a few percent of one pixel and will stabilize the image position to within a correspondingly small error box. The star servo concept will not unduly constrain our target field selection because there are seldom fewer than ~ 100 stars per field, any one of which can serve as the servo target.

8.4 Primary Mirror Size

The size of the SNAP primary mirror has a dramatic effect on the science capabilities of the mission. The combination of the light gathering power of the mirror and the diffraction limit imposed by the aperture determine the number of supernovae that can be studied in a given interval, and varies up to the *fourth power* of the aperture. The requirement of diffraction limited optics at 1000 nm has been selected to make best use of the capabilities of the photometric instruments and minimize exposure times. The wide-field optical photometry will also perform with the highest accuracy if the star images are over-sampled. A plate-scale of approximately $10\ \mu\text{m}/0.1\ \text{arcsec}$ has been selected assuming a 2m primary mirror diameter as a best compromise between a wide field of view and achieving the best photometric accuracy. The mission readily fits into the 14 foot diameter payload fairings for the Delta III rocket. Given the space required for spacecraft bus and telescope tube the aperture is not fixed by fairing diameter, rather by total length. The aperture will be limited by manufacturing, cost,

weight, and structural considerations (currently, the largest lightweight rigid beryllium mirror that can be manufactured is 1.9 meter diameter). The choice of primary mirror size is the most important single parameter to be explored during the Phase A tradeoff studies.

8.5 Mirror Technology

We are exploring a variety of light weight optical fabrication techniques suited to the requirements of the SNAP mission. The traditional materials, invar + zerodur, lead to designs that are potentially too heavy (~ 500 kg) for our mission payload constraints. However we are fortunate that existing programs, e.g. the NGST effort, solar programs, are developing high optical quality mirror technology whose mass/area ratio is an order of magnitude lower than conventional HST space optics. These new technologies include the following:

Passive Zerodur with carbon fiber epoxy support

A thin zerodur optical mirror surface is epoxied to a carbon fiber epoxy support structure that provides the requisite strength and stiffness. The compound structure is stiff enough and sufficiently stable that final figuring can be done in a one gravity environment and can be used in space. The measured thermal coefficients of expansion of the support structure and of the zerodur are comparable down to 70°K. A 1.6m test blank has been manufactured by Composite Optics, Inc as part of the NGST mirror research and development effort under contract to Ball Aerospace/TRW.

Active Zerodur with carbon fiber epoxy support

A rigid strongback composed of C-SiC or fiber reinforced epoxy ribs and a number of actuators upon which a thin zerodur faceplate is supported. This combination gives on-orbit control of the mirror figure. The actuators provide both coarse and fine adjustments, in a closed-loop mode, much like is used for the Keck Mirror segments. Surface densities as low as 20 kg/m² have been achieved in this way. COI has built a 1.5m diameter (across the points) prototype with this technology.

Passive SiC faceplate, C-SiC support

A single structure of a Carbon- Silicon Carbide composite which is figured, polished and coated on the front surface, ribbed on the back surface. The substrate is manufactured by IABG, a German company. To date good mirrors up to 0.5m in diameter have been successfully manufactured. Thin, 1 cm thick and 1 meter across structures have been demonstrated by IABG. IABG is continuing its R&D efforts into producing thicker (e.g. 70cm) and larger mirrors, While IABG has the furnace capability of making a 3.5 m diameter mirror substrate, it has yet to demonstrate a 2m diameter mirror. In the US, Union Carbide has demonstrated a 50cm C-SiC mirror.

Beryllium

A blank is produced by hot pressing a beryllium powder preform under vacuum. This blank is then weight relieved by machining, and the mirror surface is produced by machining, figuring, nickel-phosphorus plating, and polishing. Mirrors of this type have been produced up to 1.2 meters in diameter. The leading manufacturer, Brush-Wellman, envisions that with their existing furnace, they can manufacture mirror blanks up to 1.9 meters in size. Beryllium is lightweight, 34% lighter than aluminum, with a density of 1.84 g/cc. It is quite stiff, about seven times more than steel (which also makes it useful for structural components). Keck and VLT both use beryllium secondary mirrors. The VLT mirror is nickel plated. The SIRTf mirror is also made from beryllium, and is designed to operate down to 70 K, and has wavefront error of about 20 angstroms.

At present we are baselining the use of beryllium for the optics, combined with beryllium structural components to provide the metering structure that define the optical spacings and orientations. We intend to review this decision as new results emerge from the ongoing NGST studies.

8.6 Conclusion

During Phase A we will work closely with optics engineers, optical element fabricators, and spacecraft manufacturers to ascertain the confidence with which the optical system performance can be established. This is a complex subject because many factors interact to a considerable extent. For this reason, during the Phase A design period, we shall study the trade offs between the performance, cost, schedule, and science harvest that a variety of alternative optical trains offer the SNAP mission before adopting a baseline optics layout.

Chapter 9

Optical Photometry

9.1 Optical Photometer Requirements

The requirement for supernova detection and photometry is fulfilled by a large field imager based on CCD technology. The pixel size is chosen to be as low as attainable in science grade imagers to minimize the overall size of the device. The high-resistivity p-channel CCD technology provides high quantum efficiency at 1000 nm since the fully-depleted devices are 300 μm thick and back-illuminated. The shortest exposure time is 100 sec while the longest single exposure is set by cosmic ray contamination, approximately 400 to 1000 sec. Multiple frames, up to 24, would be stacked and cleaned of cosmic rays prior to ground transmission. The longest aggregated exposure in the imager is one hour. For the parameters given in Table 9.1, which assumes a 2 meter primary mirror, the imager sensitivity is limited only by zodiacal light background.

Field-of-view	1° x 1°
Plate Scale	$\sim 10 \mu\text{m}/0.1 \text{ arcsec}$ (diffraction 2m mirror)
Pixelization	28k x 28k CCD mosaic
Wavelength coverage	350nm - 1000nm
Detector Type	High-Resistivity P-channel CCD's
Detector Architecture	2k x 2k, 10.5 micron pixel
Detector Array Temperature	150 K
Detector Quantum Efficiency:	65% @ 1000nm, 92% @ 900nm, >85% @ 400-800nm
Photometric Accuracy	3% relative
Read Noise	4 e ⁻ @100kHz
Exposure Time	100 sec to 1000 sec (single exposures)
Number of Frames	1 to 24
Dark Current	0.08 e ⁻ /min/pixel
Readout Time	20 sec
Limiting Magnitude Sensitivity	30th AB magnitude in I-band
Exposure control	Mechanical shutter
Filter Wheel	15 bands (U, V, R, I, Z, & 10 special filters)
Spectroscopy	Fixed pick-off mirror to spectrograph

Table 9.1: Optical Imager/Photometer Requirements

9.2 Technology

The optical photometer will be fabricated using a new state-of-the-art CCD based on ultra-high purity high-resistivity n-type silicon. These CCD's are fully-depleted and back-illuminated with superior response. The largest devices currently in operation at Lick Observatory are 2k x 2k with $15 \mu\text{m}^2$ pixels. Larger 2k x 4k devices are currently in fabrication as well as devices with 12.0 and $10.5 \mu\text{m}^2$ pixels. The technology has also been moved to a commercial foundry with the first lot currently in manufacture. Since the devices do not require thinning to obtain high sensitivity with back-illumination the devices are extremely robust and easy to fabricate in volume. Early measurements at the LBNL 88" cyclotron also indicate enhanced radiation tolerance. Additional studies will be required to validate the devices for the SNAP mission. Further information about this technology can be found at URL, <http://ccd.lbl.gov>, and in the appendix.

Given the very large number of devices in the optical photometer, development of radiation hard multi-channel preamplifier/correlated double samplers developed on an integrated circuit has begun. Appropriate radiation hard 16-bit analog-to-digital converters are currently under investigation. These IC's would be fabricated in the radiation hard DMILL process through Temic Corp.

9.3 Supernovae Detection

Detection of supernovae is accomplished by a repeated comparison of fixed fields to reference images. The imager would obtain twenty discovery fields from dark regions around the north and south ecliptic poles. These discovery fields would have a limiting detection magnitude of $m_{AB}(1\mu\text{m}) < 27$. This set of discovery fields would be recorded at intervals of four days. At six day intervals detection fields would be obtained to a limiting magnitude of $m_{AB}(1\mu\text{m}) < 28$. At eight day intervals detection fields would be obtained to a limiting magnitude of $m_{AB}(1\mu\text{m}) < 28.5$. Two of these fields would have a limiting detection magnitude of $m_{AB}(1\mu\text{m}) < 30$ taken every eight days. This strategy is summarized in Table 9.2. This data would be obtained concurrently with the optical photometry, discussed next, and so would not require additional mission observation time. The average data transmission requirement from the discovery images assuming 50% loss-free compression is 0.38 Mbit/s, these images represent the majority of the data to be transmitted.

<i>Peak AB mag.</i> <i>B-band</i> <i>restframe</i>	<i>Peak SNe</i> <i>flux</i> <i>[e^-/s]</i>	<i>Peak</i> <i>Zody</i> <i>[e^-/s]</i>	<i>Total Time</i> <i>Time</i> <i>[hrs]</i>	<i>Filter Fields</i>	<i>Repeat</i> <i>Interval</i> <i>[days]</i>
27.0	0.4	0.27	0.1	Z-band	4
28.0	0.16	0.27	0.2	Z-band	6
28.5	0.06	0.27	0.3	Z-band	8
30.0	0.03	0.27	4.6	Z-band	8

Table 9.2: Observation strategy

9.4 Optical Photometer Performance

The follow-up optical photometry is obtained without specific knowledge of the location of new supernovae. The optical photometer obtains wide-field frames overlapping the positions of the discovery frames. Some of the photometry frames may be taken while the satellite is taking spectra of specific supernovae. The photometer obtains frames in each of a specified list of redshifted B-band filters with exposures of sufficient duration to obtain all the data points required to reconstruct the light curve. The longest optical photometric exposure is one hour. The photometry is also obtained at regular intervals in order to obtain data points that reasonably approximate the required ten photometric points along the light curve. As shown in Table 9.3, the B-band photometry is divided into ranges of redshift for photometry in a specific filter. Given the correlation between brightness and redshift the exposure times are known a priori. The parameters given in Tables 9.2 & 9.3 assume a 2 meter primary mirror.

<i>Red-Shift</i>	<i>SNe Rate yr/1°</i>	<i>Peak AB mag. B-band restframe</i>	<i>Peak SNe flux [e⁻/s]</i>	<i>Peak Zody [e⁻/s]</i>	<i>Peak [hrs]</i>	<i>Longest Expose [hrs]</i>	<i>B-band Filter Center [μm]</i>	<i>Fields</i>	<i>#SNe follow</i>	<i>Total Time [days]</i>	<i>Repeat Time [days]</i>	<i>Total Time/yr [days]</i>
0.1	0.7	18.95	553.2	634.0	0.16	0.11	0.48	20	14	0.09	4	8.4
0.2	2.2	20.59	122.1	145.3	0.18	0.11	0.53	20	44	0.09	4	8.4
0.3	4.1	21.60	48.1	57.8	0.20	0.11	0.57	20	82	0.09	4	8.4
0.4	6.2	22.33	24.6	29.5	0.22	0.11	0.61	20	124	0.09	6	5.6
0.5	8.1	22.91	14.4	17.3	0.24	0.11	0.66	20	162	0.09	6	5.6
0.6	9.8	23.39	9.27	11.1	0.25	0.11	0.70	20	196	0.09	6	5.6
0.7	11.3	23.80	6.35	7.6	0.26	0.12	0.75	20	226	0.10	6	5.9
0.8	12.5	24.16	4.56	5.5	0.26	0.21	0.79	20	250	0.17	6	10.5
0.9	13.5	24.47	3.43	4.1	0.27	0.33	0.83	20	270	0.28	8	12.6
1	14.3	24.76	2.62	3.2	0.27	0.44	0.88	20	286	0.37	8	16.9
1.1	14.9	25.02	2.07	2.5	0.27	0.67	0.92	20	298	0.56	8	25.3
1.2	15.2	25.25	1.67	2.0	0.26	0.92	0.97	20	304	0.77	8	35.1
total									2256	2.80		148.3

Table 9.3: Optical Photometry

The data payload from the photometry would saturate the available bandwidth, so transmitted data is limited to pixel sets around star images over a 3σ threshold and around locations already identified as being supernova candidates, analysis of HST images indicate that this will provide a ten-fold reduction in the data. Some of these techniques would require flattened and bias subtracted data to be computed aboard the spacecraft. Given these assumptions, the data transmission requirement for the optical photometry data is 0.20 Mbit/s.

Chapter 10

IR Photometry

10.1 IR Photometer Requirements

The IR photometer is constructed from one HgCdTe device with a 1.7 μm wavelength cut-off. This cut-off is a good match to the <150 K operating temperature of the payload. The requirements for the IR photometer are shown in Table 10.1. The IR photometer could have a single device with a filter wheel or there could be multiple devices each with a fixed filter. Using fixed filters may permit the placement of the HgCdTe devices within the focal plane of the optical photometer. The follow-up IR photometry will require specific knowledge of the location of each new supernova. The IR photometer obtains small frames determined by pointing the satellite at the supernova. Other options for the IR photometer are discussed in the "enhanced science mission" section.

Field-of-view	1' x 1'
Plate Scale	$\sim 10 \mu\text{m}/0.1 \text{ arcsec}$
Pixelization	256 x 256, 18.5 micron pixel
Wavelength coverage	1000nm - 1700nm
Location	TBD
Detector Type	HgCdTe (1.7 μm cut-off)
Detector Array Temperature	77K - 150K (to achieve dark current)
Detector Quantum Efficiency	56% @ 1000nm 400-800nm
Photometric Accuracy	3% relative
Read Noise	6 e ⁻ (multiple samples)
Dark Current	3 e ⁻ min/pixel
Readout Time	20 sec
Limiting Magnitude Sensitivity	30th magnitude (AB)
Exposure control	Mechanical shutter
Filters	J&H, plus five special filters

Table 10.1: IR Imager/Photometer Requirements

10.2 IR Photometer Performance

The IR photometer would be unable to follow all supernovae seen in each of the most distant discovery frames. Consequently a subset would be selected for follow-up. As shown in Table 10.2, the longest photometric IR observation is 8.3 hours and would require a total of 56 hours of observing time to follow the complete light curve of a $z=1.7$ supernova out to a limiting magnitude of $m_{AB}(1\mu m) < 28.2$. Following the supernova light curve in the infrared is the most “expensive” task of the satellite. This task will require the highest possible optical throughput and quantum efficiency. The parameters given in Table 10.2 assume a 2 meter primary mirror. With these parameters the IR photometer is only limited by zodiacal light background. Intra-pixel quantum efficiency variations need to be excellent in order for photometry to work with the coarse plate-scale. As an alternative, the plate scale can be changed, provided that detector noise can be tolerated. The data from the IR photometry would first require on-board processing to eliminate cosmic rays and reduce the overall read-noise by multiply sampling the HgCdTe device. The data transmission requirement for the IR photometry data is negligible.

<i>Red-Shift</i>	<i>SNe Rate</i> <i>yr/1°</i>	<i>Peak AB mag.</i> <i>B-band restframe</i>	<i>Peak SNe flux</i> <i>[e⁻/s]</i>	<i>Peak Zody</i> <i>[e⁻/s]</i>	<i>Peak [hrs]</i>	<i>Longest Expose</i> <i>[hrs]</i>	<i>Time per SNe</i> <i>[hrs]</i>	<i>B-band Filter Center</i> <i>[μm]</i>	<i>Fields</i>	<i>#SNe follow</i>	<i>Total Time/yr</i> <i>[days]</i>
1.3	15.4	25.47	1.09	0.54	0.7	2.4	16.7	0.95	2	30	20.9
1.4	15.5	25.67	0.91	0.53	1.0	3.4	23.3	1.01	2	30	29.1
1.5	15.4	25.85	0.77	0.52	1.3	4.6	31.4	1.07	2	22	28.8
1.6	15.3	26.03	0.65	0.51	1.8	6.3	42.6	1.13	2	16	28.4
1.7	15.1	26.19	0.56	0.50	2.3	8.3	55.8	1.20	2	12	28.0
total										110	135.2

Table 10.2: IR Photometry

The highest redshift supernova followed photometrically by the optical photometer will require measurement of the V-band restframe color of the supernova at peak magnitude using the IR photometer since the light will be redshifted into the infrared. Since these measurements are only performed at peak brightness the limiting magnitude for the measurements is $m_{AB}(1\mu m) < 25.2$, as shown in Table 10.3, and very little time is devoted to these measurements. It maybe necessary to assign additional observing time to obtain color at additional epochs near maximum brightness. The data transmission requirement for the IR V-band photometry data is negligible.

<i>Red-Shift</i>	<i>SNe Rate</i> <i>yr/1°</i>	<i>Peak AB mag.</i> <i>B-band restframe</i>	<i>Peak SNe flux</i> <i>[e⁻/s]</i>	<i>Peak Zody</i> <i>[e⁻/s]</i>	<i>Time SNe</i> <i>[hrs]</i>	<i>Filter</i>	<i>Fields</i>	<i>#SNe follow</i>	<i>Total Time/yr</i> <i>[days]</i>
0.9	13.5	24.47	2.74	0.55	0.19	J	20	270	2.1
1	14.3	24.76	2.10	0.55	0.28	J	20	286	3.3
1.1	14.9	25.02	1.65	0.55	0.44	J	20	298	5.5
1.2	15.2	25.25	1.34	0.54	0.53	J	20	304	6.7
total								1158	17.6

Table 10.3: IR V-band Photometry

Chapter 11

Spectroscopy

11.1 Optical/IR Spectrograph Requirements and Performance

11.1.1 Introduction

Spectroscopy of supernova candidates discovered by SNAP is necessary to confirm and assign a type to the supernova, to establish the redshift of the host galaxy, and to further characterize the supernova based on its expansion velocity, metallicity, and luminosity-indicator absorption line ratios. The defining signature for Type Ia supernovae is the Si II 6250Å absorption feature. Type II supernovae, from which the Type Ia supernovae are to be distinguished, are characterized by the presence of $H\alpha$ absorption and emission having a classic P-Cygni profile. In addition, numerous features, especially in the wavelength range 3800–5500Å can be used to distinguish Type Ia supernovae from other types. Host-galaxy redshifts can in most cases be determined from emission lines, such as OII 3727Å $H\beta$, and O III 5007Å, as well as absorption features like the Ca II H and K lines at 3933 and 3969Å. The supernova expansion velocity can be obtained from numerous absorption lines throughout the rest-frame optical spectrum, while the metallicity is best determined from pseudo-emission features produced by Fe absorption in the UV (2700–3800Å). Promising spectral luminosity indicators include the $\mathcal{R}(\text{Si II})$ and $\mathcal{R}(\text{Ca II})$ ratios (Nugent et al., 1995a). Thus, to fully exploit the spectral information from Type Ia supernova, rest-frame wavelength coverage from 2700–6600Å is desirable. For the redshift range of $0.3 < z < 1.7$ best probed by SNAP, a spectrograph covering 0.35–1.7μm is needed to obtain the optimal rest-frame spectral coverage.

11.1.2 Achieving Wavelength Coverage with a Three-Arm Spectrograph

The zero-th order requirements for a spectrograph capable of obtaining the above measurements are high throughput and broad wavelength coverage. These requirements, coupled with the need to prevent overlapping of spectral orders, lead naturally to the choice of a three-channel spectrograph. By initially splitting the light entering the

spectrograph into blue (0.35—0.55 μm), red (0.50—1.00 μm), and non-thermal near-infrared (0.95—1.70 μm) components, not only is order overlap handled automatically, but the detectors and optics (optical elements, materials, and coatings, and blaze wavelength for each grating) can be chosen to provide the best possible performance over the limited wavelength range of each channel. Conversely, no single dispersive element can cover the required wavelength range, so a single-channel spectrograph would require multiple gratings and serial observations of different wavelength ranges leading to a $2\text{--}3\times$ loss of observing efficiency. Even then, multiple detectors would be required since even LBL CCD's do not perform beyond $\sim 1\mu\text{m}$, while NIR detectors do not perform well, period, for space-based (low-background) spectroscopic applications. Finally, only reflective optics can perform over a large wavelength region, but their use would result in extremely low efficiency.

Several highly successful multi-channel spectrographs have been built for ground-based telescopes (Oke & Gunn, 1982; Miller, Epps, & others, 1992; Oke et al., 1995), so the design and construction of a three-channel spectrograph does not present fundamental technical challenges. An example of a two-channel optical spectrograph, the KAST spectrograph at the Lick 3-m telescope, is shown in Fig 11.1. One modest compromise over a static three-channel spectrograph design is required by the fact that current dichroic beam splitters — used to achieve color separation — only perform well over a range in wavelength that is slightly smaller than required for SNAP. This limitation is easily accounted for by allowing the NIR/optical dichroic to be removed from the beam for blue-channel observations of the lowest redshift supernova. With this dichroic in the beam, the blue-channel performance from 0.35—0.42 μm will be degraded, however higher redshift supernova ($z > 0.6$), which do require NIR coverage, will not require blue coverage in this wavelength range.

11.1.3 Resolution Requirements and Constraints

The next most important spectrograph design parameter is the resolution needed to measure supernova and host-galaxy features of interest. Typical supernova expansion velocities of $v \sim 15000 \text{ km s}^{-1}$ imply that supernova spectral information is undeniably lost for a resolution worse than

$$R = \lambda/\delta\lambda \sim \lambda/((v/c)\lambda) \sim c/v \sim 20.$$

At the other extreme, host-galaxy absorption and emission lines will be diluted if the resolution is not sufficient to resolve the velocity dispersion or rotation velocity of the host. These velocities are typically $100\text{--}300 \text{ km s}^{-1}$, and would require $R \sim 1000\text{--}3000$ to properly resolve. Although this higher resolution can be achieved, and would satisfy the resolution requirements for supernovae, for a 2-m aperture the light would then be so dispersed that detector dark current and read noise would dominate the noise budget, leading to lower performance compared to the photon-limited case. Thus, it is important to determine the maximum resolution needed for supernovae, and accept that this resolution is not ideal for galaxy spectroscopy.

Despite the large expansion velocities for supernovae, the locations and shapes of absorption and pseudo-emission features shift with changing metal abundance by

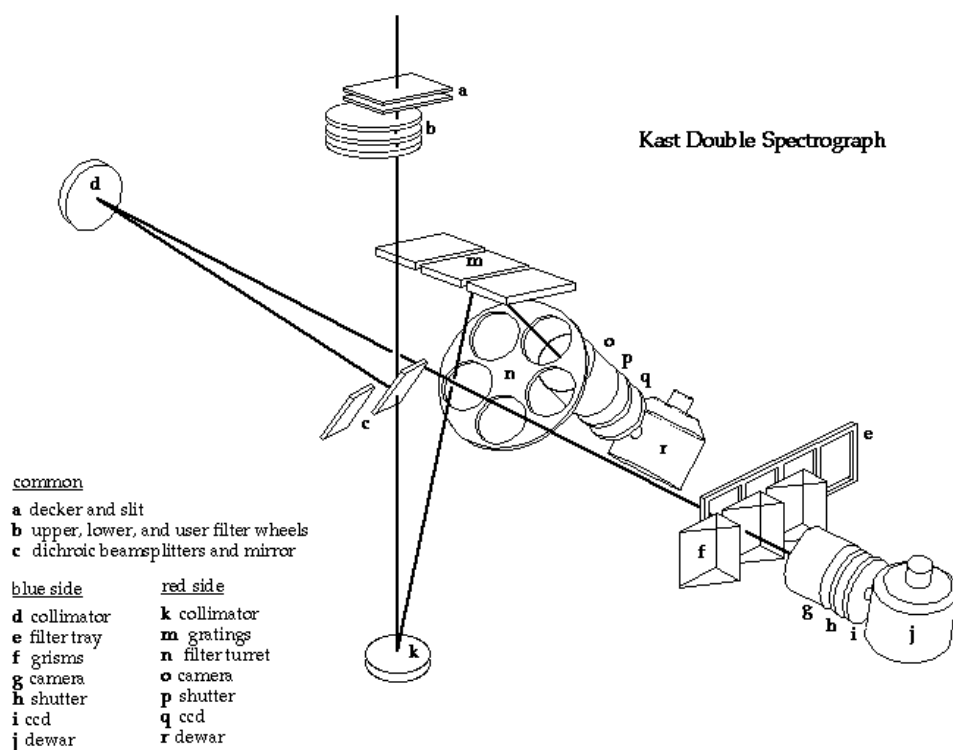


Figure 11.1: Schematic illustration of the light path for the KAST two-channel spectrograph of the Lick 3-m (Miller, Epps, & others, 1992). The three-channel spectrograph for SNAP would use similar concepts, although it would employ an integral field unit, rather than a single slit (see below), would have one more spectral channel, and would include a more limited selection of filters, gratings, and transmission gratings (a.k.a. a grism). Note that a wide variety of geometric layouts is possible in addition to that shown for KAST.

amounts much smaller than the line velocity width. For example, the locations of the UV pseudo-emission features shift by about 60\AA over a 2 dex change in metallicity. In order to achieve an approximate indication of supernova metallicity, say to 0.3 dex, a resolution of

$$R \sim (3000\text{\AA}/60\text{\AA}) (2 \text{ dex}/0.3 \text{ dex}) \sim 300$$

is desired. A similar, but more detailed analysis is summarized in Fig. 11.2, where the expected error on the velocity of the Ca II H&K features in Type Ia supernova for various combinations of signal to noise and resolution is shown. Also shown are the *statistical* errors in the supernova peak brightness associated with these velocity errors under the model discussed earlier where supernova absorption line velocity differences at a given light curve width lead to an additional source of error in the peak brightness. From this plot, and the previous discussion, it is clear that $R \sim 200\text{--}300$ is sufficient for obtaining the desired velocity measurements.

Assuming detectors with 2048 pixels in the wavelength direction and the wavelength coverage given above for each channel, the resolution limit set by the detectors (assuming Nyquist sampling of two pixels per resolution element) is $R \sim 2200, 1500$, and 1800 for the blue-, red-, and NIR-channel, respectively. Thus, the number of detector elements does not pose any significant limitation compared to the resolution desired for properly observing supernovae and their host galaxies.

11.1.4 Integral Field Unit

In typical spectroscopic observations a slit is placed at the focal plane of an astronomical telescope so that the region on the sky containing light from the object of interest can be selected (along with whatever background/foreground is superposed on the object), while light from regions on either side of the slit having only background light are prevented from entering the spectrograph. Along the spatial direction of the slit, background light does enter, and can often be used to estimate and subtract light contaminating the object of interest. Introduction of a slit is also necessary to preserve spectral resolution, which is otherwise set by the spatial width of the target (not always a point source). The drawback of using a slit is that either some light from the target is also rejected (when the slit is too narrow), or an undesirable amount of background is admitted into the spectrograph (when the slit is too wide). For very faint targets, extremely precise astrometry, pointing, and stability is required to place the slit accurately on the target object; for diffraction limited imaging in space these requirements are severe. Moreover, if there is any chromatic aberration in the telescope — or atmospheric dispersion for ground-based observations — the amount of light entering from the target is wavelength dependent. This is very undesirable because unless this effect can be exactly reproduced when calibration stars are observed (which it cannot be unless the pointing is perfect), the final target spectrum will not be properly flux-calibrated as a function of wavelength.

A solution to these acquisition, pointing stability, calibration, and slit-loss problems is to employ an integral field unit (IFU) in place of a slit. An IFU spatially subdivides the region of the focal plane near the target, and sends each subregion to the spectrograph where its spectrum is produced. If the filling factor of the IFU is 100%, all the

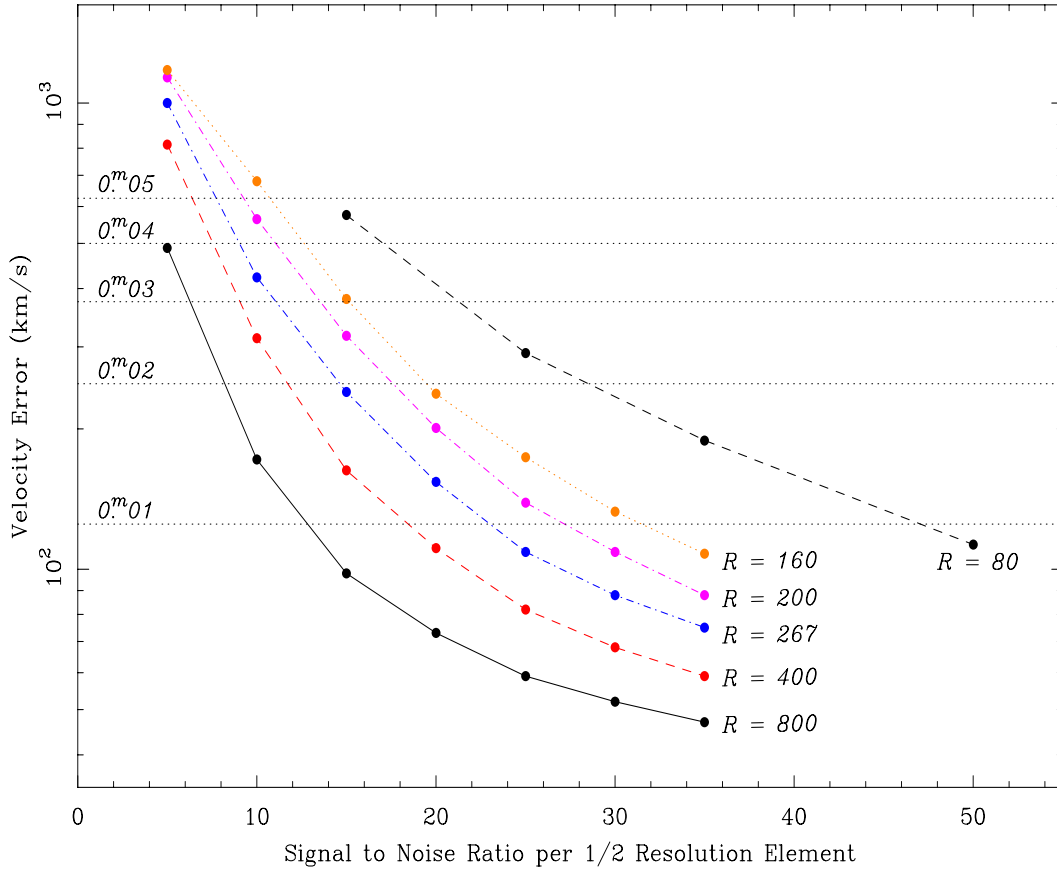


Figure 11.2: Calculation of the error in the position of the Ca H&K supernova absorption lines, expressed as a velocity, versus the signal-to-noise per spectral resolution element, for various values of the resolution, R . The horizontal lines give the statistical error in the peak magnitude at a given light curve width for variations in the Ca II H&K velocity, as discussed in § 4.5.3. As an example supernova absorption line velocities can be measured to 250 km/s, the peak magnitudes can be corrected to 0.02 magnitudes (2%). This accuracy can be achieved for a wide range of combinations of R and signal-to-noise. The ability of SNAP to meet such a goal is discussed in the text. Application of such a correction means that this effect will then be a statistical error rather than a systematic one.

light of the target object enters the spectrograph, although it may be spread amongst the spectra of several subregions. All information is available to completely reconstruct the 3-dimensional (2 spatial and 1 wavelength) spectral image, allowing the spectrum from the target object to be extracted in software, using optimal weighting.

The simplest form of IFU is an image slicer, typically composed of a stack of thin metal or glass plates, with each layer of the stack tilted slightly with respect to each other and with a reflective coating applied to the thin edge of each layer (Hunten, 1974). When the edge of such a stack is placed in the telescope focal plane, different slices of the focal plane image are reflected at slightly different angles. From the point of view of the spectrograph, this gives the appearance of a long slit (albeit with slight steps perpendicular to the slit along the length of the slit). An example of such an image slicer built for the Palomar 200-inch telescope is given in Murphy, Matthews, & Soifer (1999), while Content (1998b,a) discuss the advantages of image slicers for, e.g., use on NGST and Gemini. Alternative IFU designs using microlens arrays feeding optical fibers are presented by Iye, Ebizuka, & Takami (1998), Allington-Smith, Content, & Haynes (1998), Haynes et al. (1999) and Larkin, Quirrenback, & Graham (2000). A microlens-array IFU is illustrated in Fig 11.3 and Fig 11.4.

The drawbacks to using an IFU are minor; since the spectrograph sees a slit length that is longer than needed for a single slit, it must be designed with a wider field of view. Also, some loss of throughput will result from the reflection or transmission inefficiency of the IFU and any fore-optics required to produce a sufficiently large scale at the IFU.

Following the discussion of spectral resolution, above, the optimal spatial resolution for the IFU and the final spectrograph focal planes depends in part on the total effective area of SNAP and the properties of the spectrograph detectors. If the size of the IFU subregions is too small, the amount of background light will fall below that required for background-limited performance at a given spectral resolution. Sampling of a $2'' \times 2''$ region of the focal plane with $0.''07$ -wide slits would be more than adequate for SNAP. This would require 30 stack layers for an image slicer. Each would be about 30 pixels high, and could be formatted onto a $2k \times 4k$ CCD. Spatial resolution this fine would put the spectrograph in the detector-limited regime of operation for the dimmest targets for the most desirable resolution using current detectors; therefore some compromise in spatial or spectral resolution would be necessary. Alternatively, optics could be placed in front of the IFU to provide more than one scale; a coarse scale for the faintest objects and a finer scale of brighter objects or bright background (e.g., from the supernova host galaxy) situations. One final requirement for an IFU is that the size of image slicer slits or microlenses be sufficiently large that the IFU itself doesn't introduce significant diffraction effects.

11.1.5 Optics

A standard astronomical spectrograph consists of a slit, collimator, dispersive element, and camera lens. The SNAP telescope will have an $f/10$ beam, to which the focal ratio of the collimator should be matched. If the focal length of the camera is the same as that of the collimator, the spatial scale at the spectrograph focal plane will match that

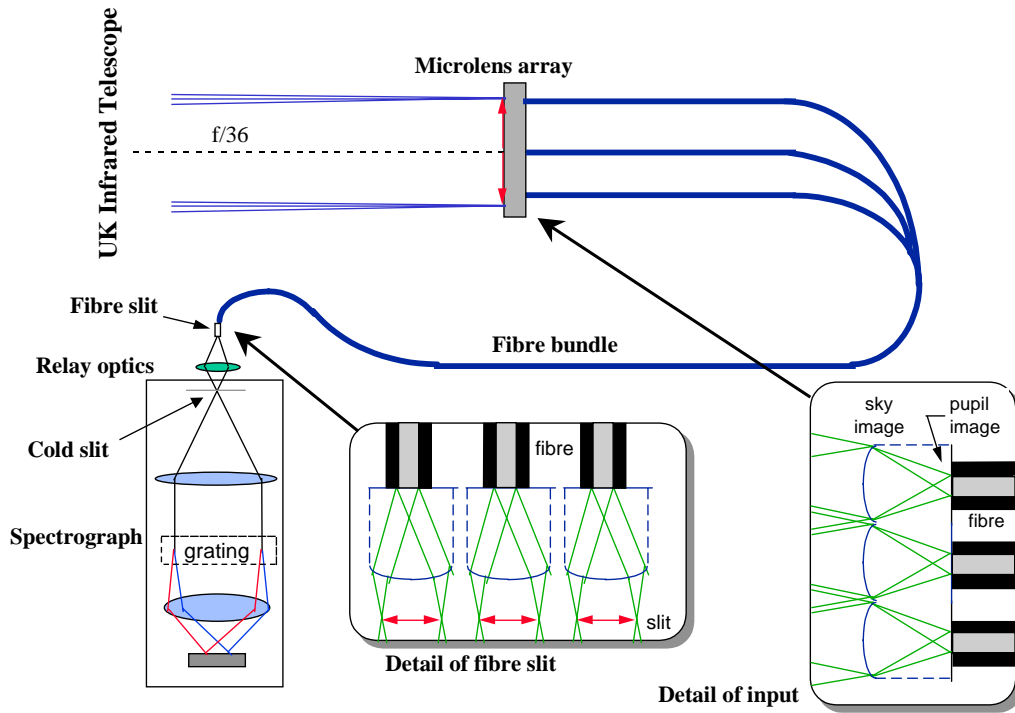


Figure 11.3: Schematic illustration of how an integral field unit based on a microlens array and fiber bundle works. (Adapted from Figure 9 of Haynes et al. (1999)). The measured throughput of this IFU is measured to be roughly 50%. However, this is a prototype IFU which was adapted to a pre-existing spectrograph. An image slicer IFU should have much better throughput, but may be more difficult to construct unless the image scale is increased.

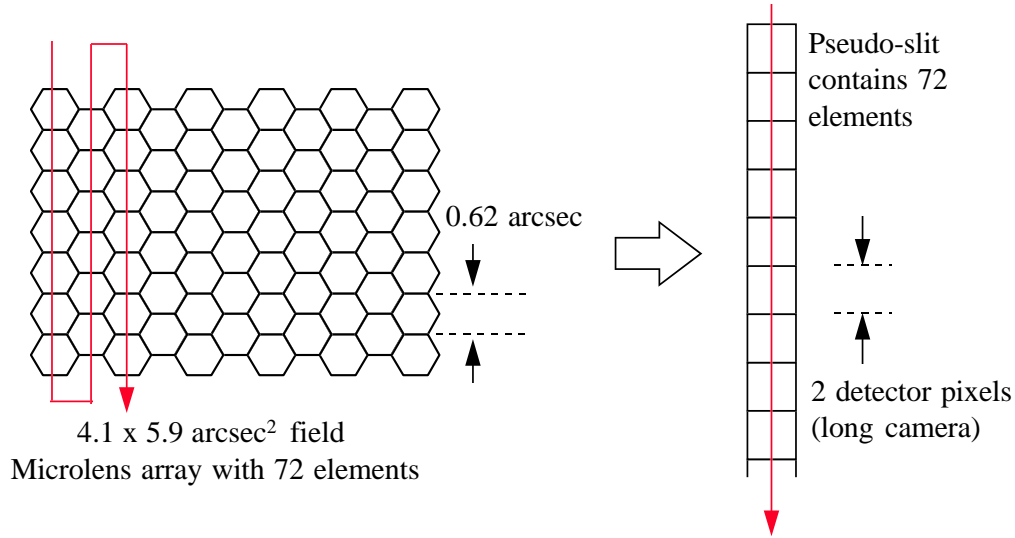


Figure 11.4: Illustration of how a microlens array is used to produce a pseudo-slit from an initially 2-dimensional region of the telescope focal plane. (Adapted from Figure 10 of Haynes et al. (1999)).

of the telescope focal plane. However, by choosing different camera lens focal lengths, the spatial scale can be changed to optimally match the properties of the detectors in each arm of the spectrograph.

The spatial scale at the telescope focal plane will be roughly $0.1 \text{ arcsec}/\mu\text{m}$. For a $2''$ square region in the image plane re-formatted as a slit using an IFU, the effective slit length with $0.1''$ slices and a $0.5''$ buffer between slits is $55''$. With such slow optics and limited field-of-view the spectrograph design should be straightforward, and the goal of high efficiency (35%, including detectors) should be attainable. If the spectrograph is feed by an optical-fiber IFU, the collimator focal ratio will be faster than that of the telescope to match the output focal length of the optical fibers. This can result in a more compact instrument. Conversely, if a classical image slicer IFU is used, the nominal telescope scale probably will be too small. In this case magnifying optics would be needed in front of the IFU. This in turn would lead to a longer focal length for the collimator, and would require the camera lens to then demagnify the scale.

As discussed earlier, the optics (including the image slicer, if placed after the dichroic beam splitters) can be optimized for image quality and throughput for each spectrograph arm. Thus, the design for the spectrograph could be quite different for each arm, if desired. A Phase A spectrograph design is necessary to determine further details and constraints for the spectrograph.

11.1.6 Dispersive Elements

Conventional Gratings and Grisms

The gratings and grisms in common use in astronomical spectrographs typically have efficiencies of 70% at the blaze wavelength, λ_B , and fall to half of peak efficiency at $\sim 2/3 \lambda_B$ and $\sim 3/2 \lambda_B$. These are off-the-shelf and space-ready components, but given their modest efficiency, it will be worthwhile exploring higher-efficiency alternatives for the SNAP spectrograph.

Volume Phase Holographic Gratings

Volume-phase holographic gratings are a relatively new concept for high-efficiency dispersive elements for astronomical spectrographs. Barden, Arns, & Colburn (1998) has performed extensive studies of the properties of these gratings and their suitability for astronomy, with encouraging results. One of these gratings has been put into use at the AAT, with good results (Glazebrook, 1998). It will certainly be worth exploring these as dispersive elements for the SNAP spectrograph. One critical issue when considering VPH gratings will be the reaction of the gelatin medium to the space environment.

A High-Efficiency NIR Dispersive Element

Oliva (1999) presents an Amici crown-crystal/neobium-flint/crown-crystal prism system, shown in Fig 11.5, which has roughly 85% efficiency over 0.85–2.5 μm . This would be a good starting point for the NIR channel of the SNAP spectrograph.

11.1.7 Very Low-resolution NIR Spectroscopy Option

There are advantages to trading high-efficiency for resolution for some NIR observations. Namely, with such a trade-off, observations of the faintest targets will be guaranteed to be in the photon-limited regime even if the noise properties of NIR detectors never improve over those currently available. Fig. 11.2 shows that $R \sim 80$ can be productive, and such low resolution might be necessary to overcome HgCdTe detector noise for the faintest, highest redshift Type Ia supernova ($z \sim 1.7$) for which rest-frame B -band is located at 1.2 μm and V -band is at 1.5 μm . One possible concept for a very low-resolution NIR spectroscopy option would be to use the feed an $f/30$ or slower beam to an image slicer and then directly on to the above high-index niobium-flint prism and through to the detector, eliminating a collimator and camera. Some optical aberrations may result, and these would have to be quantified in a Phase A study. Such a very low-resolution option would probably have to be separated from the main three-channel spectrograph. The economy and compactness of the design could allow SNAP to accommodate numerous such instruments.

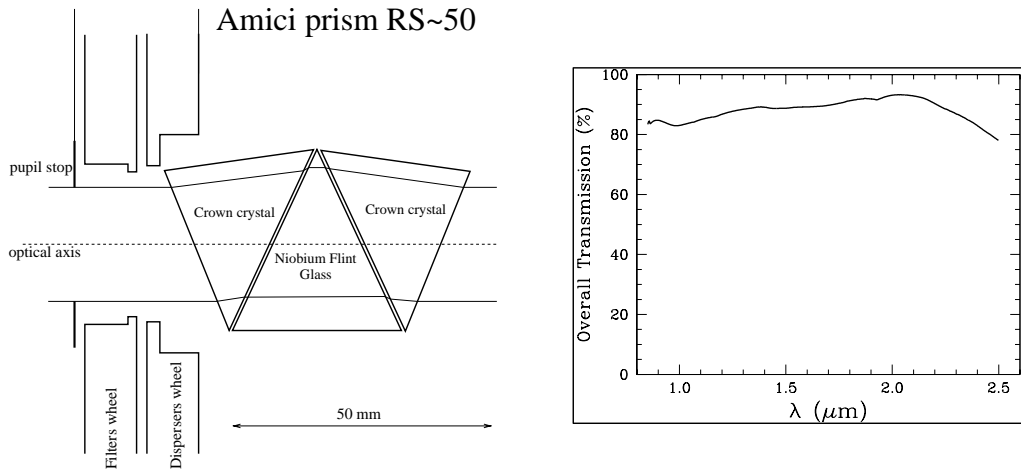


Figure 11.5: Example of a high-efficiency dispersion element which could be useful for the NIR channel of the SNAP three-channel spectrograph, or for a multiplexed very low resolution NIR spectroscopic option on SNAP. (Adapted from Figure 4 of Oliva (1999)).

11.1.8 Internal Adjustment and Calibration

Additional specifications for the spectrograph include an internal calibration module to provide wavelength calibration from arc lamps and pixel-to-pixel sensitivity corrections from a flat lamp, collimator or camera focus control, and possibly tilt control. The internal calibration unit must feed the spectrograph IFU with a beam having the same f-ratio and central obstruction as the SNAP telescope. Also, since the behavior of the dichroics depends on polarization, the internal calibration unit should mimic the (small) polarization of the SNAP telescope. A set of arc and flat lamps optimized for each of the three channels is desirable. The spectrograph focus can be checked using the width of arc lines. The alternative of using shifts in the positions of arc lines produced by the introduction of a Newall shutter into the collimator beam might be more sensitive, but involves added technical risk since the Newall shutter could stick and thus block half of the collimator beam. Focus control of the collimator is generally preferable over adjusting the camera due to the slower focal ratio of a collimator. Tilt of the detectors with respect to the spectrograph focal planes should be set prior to launch, however, it may be desirable to have tilt adjustments available on-orbit to handle any subsequent mis-alignments.

11.2 Spectrograph baseline

The architecture of both the optical and IR spectrograph is based on an integral field spectrograph with an image slicer. The image slicer eliminates the need for a slit and greatly reduces the pointing accuracy required to place the supernova within the

field of view of the spectrograph while preserving photometric accuracy because of the 100% filling factor. The pixel resolution for both spectrographs is set to contain the entire first lobe of the Airy disk within one pixel – this is severe undersampling and may be in conflict with required photometric accuracy and represents a change in scale from the imager. This however, relaxes the requirement for the readout noise of the IR imager, even so the spectrograph is still limited by the performance of the HgCdTe devices for the $z=1.7$ supernovae. Both optical and IR spectrographs will require selectable resolution in order to achieve an optimum of performance and exposure times. Furthermore, the spectral features of the high redshift supernovae are dilated by $1+z$, so that the reduced resolution is a good match to standardizing the performance over all supernovae followed. The performance features of the optical and IR spectrographs are shown in Tables 11.1 and 11.2, respectively. The optical spectrograph is assumed to have two channels, while the IR spectrograph one. The cross-over wavelength between the two optical channels would be determined by the availability of high throughput dichroics. It would be considered highly advantageous to be able to operate the longer wavelength channel of the optical spectrograph simultaneously with the IR spectrograph.

As opposed to the method of obtaining optical photometry on multiple supernovae simultaneously, we assume that the optical and IR spectroscopy is obtained by pointing the satellite at each individual supernova one at a time during its peak brightness. The resolution ranges from 15Å to 50Å for the most distant supernovae in the study. The parameters given in Tables 11.3 and 11.4 assume a 2 meter primary mirror.

Spectrograph architecture	Integral field spectrograph, two channels
Wavelength coverage	350 to 600 nm, 600 to 1000 nm
Spatial resolution of image slicer	0.07 arcsec
Field-of-View	2" x 2"
Location	TBD
Photometric Accuracy	1% relative
Resolution	15Å, 30Å, 100Å selectable
Detector Type	High-Resistivity P-channel CCD's
Detector Architecture	2k × 2k, 10.5 micron pixel
Detector Array Temperature	150 K
Detector Quantum Efficiency:	65% @1000nm, 92% @900nm, >85% @400–800nm
Read Noise	$\leq 4 \text{ e}^-$ @100kHz
Dark Current	$0.08 \text{ e}^-/\text{min/pixel}$
Readout Time	20 sec or longer to optimize readout nose
Exposure control	Mechanical shutter

Table 11.1: Optical Spectrograph Requirements

Spectrograph architecture	Integral field spectrograph
Wavelength coverage	1000 to 1700 nm
Spatial resolution of image slicer	0.12 arcsec
Field-of-View	2"x2"
Location	TBD
Resolution	30A, 50A, 200A selectable
Detector Type	HgCdTe
Detector Architecture	2k × 2k, 18.5 micron pixel
Detector Array Temperature	77K – 130K (to achieve dark I)
Detector Quantum Efficiency:	56% @ 1000nm
Photometric Accuracy	1% relative
Read Noise	≤ 5 e ⁻ (multiple samples)
Dark Current	1 e ⁻ /min/pixel
Readout Time	20 sec
Exposure control	Mechanical shutter

Table 11.2: IR Spectrograph Requirements

<i>Redshift</i>	<i>#SNe follow</i>	<i>Resolution</i> <i>[Angstroms]</i>	<i>Peak SNe</i> <i>Flux</i> <i>[e⁻/s]</i>	<i>Peak Zody</i> <i>[e⁻/s]</i>	<i>TimeSNe</i> <i>[hrs]</i>	<i>Total Time</i> <i>for Peak</i> <i>Spectra [days]</i>
0.1	14	15	8.86	0.010	0.11	0.1
0.2	44	15	2.03	0.010	0.11	0.2
0.3	82	15	0.80	0.009	0.11	0.4
0.4	124	15	0.41	0.009	0.11	0.6
0.5	162	30	0.48	0.017	0.11	0.7
0.6	196	30	0.31	0.016	0.14	1.2
0.7	226	30	0.21	0.015	0.24	2.2
0.8	250	30	0.15	0.015	0.44	4.6
0.9	270	30	0.11	0.014	0.44	5.0
1.0	286	30	0.09	0.013	0.51	6.1
1.1	298	30	0.07	0.012	0.71	8.8
1.2	304	30	0.06	0.012	0.96	12.1
total	2256					42

Table 11.3: Optical Spectroscopy

<i>Redshift</i>	<i>#SNe follow</i>	<i>Resolution</i> <i>[Angstroms]</i>	<i>Peak SNe</i> <i>Flux</i> <i>[e⁻/s]</i>	<i>Peak Zody</i> <i>[e⁻/s]</i>	<i>TimeSNe</i> <i>[hrs]</i>	<i>Total Time</i> <i>for Peak</i> <i>Spectra [days]</i>
1.3	30	30	0.031	0.023	2.9	3.7
1.4	30	30	0.025	0.021	4.0	4.9
1.5	22	30	0.022	0.020	5.2	4.8
1.6	16	50	0.030	0.031	3.2	2.1
1.7	12	50	0.026	0.029	4.1	2.0
total	110					17.5

Table 11.4: IR Spectroscopy

Chapter 12

Calibration

12.1 Introduction

SNAP will require excellent photometric, wavelength, and astrometric calibration in order to deliver its full scientific potential. Here the methods of obtaining this calibration are described.

12.2 Imager Photometric Calibration

12.2.1 Internal Calibration

The initial stages of photometric calibration are designed to put all pixels on an equal footing, such that measurements do not depend on where target objects are located on the CCD imager. The required steps are quite standard:

- bias subtraction
- dark current subtraction
- flat fielding

Bias Calibration

Bias subtraction corrects for the DC offset of the on-chip amplifier and subsequent electronics of each detector. Because the full electronics chain inevitably has imperfect behavior, this offset can vary slightly from pixel to pixel. Therefore, it is standard to obtain a series of zero-length exposures — bias images — with the shutter closed. These are combined and subtracted from science images. The number of bias images required depends on the detector readout noise and the number of particle hits occurring during the readout period, but 10—20 bias images are generally sufficient. Generally the 2-D bias pattern is stable over long periods, so a bias series is probably not required more than once per day. The bias level is likely to be temperature sensitive, but the bias level can be tracked using an 'overscan' region, produced by continuing to clock each CCD through another ~ 50 pseudo-pixels after the real image has been read. This adds a negligible amount to the total readout time. Typically systematic errors

in the bias subtraction should be far below the noise level set by the zodiacal light background, and uncorrelated between supernovae.

Dark Current Calibration

The dark current generated in the CCD silicon substrate will generally show modest 2-D structure, and will depend on temperature, which may vary slightly over the SNAP orbit. In addition, radiation damage incurred over the lifetime of the SNAP mission may result in hot pixels having elevated dark current. Such hot pixels have the potential to masquerade as supernova detections, so some attention must be given to monitoring their locations and stability. For these reasons, long-exposure images with the shutter closed must be taken periodically, and used to subtract the dark current from science images. Dark current images will have noise contributions from detector readout noise, dark current Poisson noise, and particle hits. An LBNL CCD has modest dark current of $\sim 1 \text{ e}^- \text{ min}^{-1}$, and the dark current Poisson noise will equal the $\sim 4 \text{ e}^-$ readout noise after ~ 10 minutes. In this time, the number of particle hits could be considerable. Therefore, dark current images can only last 15—30 minutes, and something like 50 such images requiring up to 25 hours of total integration would be desirable to obtain good signal-to-noise ($S/N \sim 20$; for the imager, the sky background dominates over the dark current, so higher S/N is not needed). Once the temperature dependence of the dark current is established (based on dark current images taken along the SNAP orbit during the initial calibration period), dark current calibration images should require updating only every month or so. The dark current will be much lower than the zodiacal light background, so random and systematic errors due to subtraction of the dark current should be negligible, and uncorrelated between supernovae.

Flat-field Calibration

After subtraction of the bias image, and subtraction of a scaled dark current image, the value of each pixel is directly proportional to the number of photoelectrons originally detected. Since each pixel can have a slightly different sensitivity, the pixel-to-pixel sensitivity must be corrected using a flat-field image in order for the value of each pixel to reflect the correct relative brightness of the astronomical scene. The standard means of obtaining a flat-field image on the ground is to image an illuminated screen in the telescope dome, the twilight sky, or the dark night sky. The idea being to produce a bright, uniformly illuminated scene. In the case of sky flats, astronomical objects are present and must be eliminated by obtaining, e.g. a median, of many sky images obtained for different telescope pointings. The response of each pixel depends on the angle of incidence, so the flat-field light must come from (near) infinity and traverse the complete optical path. In addition, the sensitivity variations between pixels are generally slightly wavelength dependent, so the spectral energy distribution of the flat-field scene should be fairly featureless.

The lack of a projection screen — and source to illuminate it — in space (analogous to a dome flat), or any high surface brightness uniform natural sources (analogous to a twilight flat), leads us to first investigate whether adequate signal-to-noise and object

elimination can be obtained with sky flats with SNAP. Future investigation is required, but it is quite likely that the zodiacal light (sunlight reflected by interplanetary dust) near the northern and southern ecliptic poles is sufficiently uniform to serve as a flat-field source. For the typical zodiacal background near the ecliptic poles, SNAP would require about 18 hrs of exposure in a given filter to collect enough photons to produce a flat-field with Poisson errors of less than 1% per pixel. Accounting for pixels lost due to the presence of astronomical objects and particle hits in individual exposures, up to 30 hrs would realistically be required. Since 30 hrs worth of images would typically be collected in many filters every 2 weeks, flat-fielding using sky flats is a practical method for constructing flat-field images. For less frequently used filters, some extra time above that needed for science observations may be required. It will be essential to achieve excellent elimination of real astronomical sources. Our analysis of the Hubble Deep Field South (HDF-S) indicates that 1 of every 16 pixels of 0.025 arcsec on a side contains light from an astronomical source of sufficient brightness to perturb a sky flat by more than 2%. To meet a requirement that contaminating objects this bright be eliminated from all sky flats over the $\sim 10^9$ pixels of the imager and over the mission lifetime of SNAP, deep exposures at a minimum of ~ 10 different pointings would be needed. The baseline plan calls for SNAP to monitor some 20 fields, so the object rejection requirement for constructing clean sky flats can be met.

Alternatively, it may be possible to construct a reasonably good flat-field module for SNAP. Using lamps placed on the SNAP secondary mirror support, perhaps in concert with a diffusing screen in the intermediate focal plane, might provide sufficient uniformity to correct sensitivity variations on small spatial scales. Then, smoothed sky flats (requiring much lower S/N per pixel) could be used to make corrections on large spatial scales. It is unlikely that a completely uniform internal flat-field module can be constructed for such a wide-field imager, especially if the risk associated with such a device getting stuck in the optical path is to be avoided.

Yet another alternative would be to use the (mostly) full moon to map pixel to pixel sensitivity variations. This approach would require numerous dithered images, from which both the correct illumination pattern of the moon and the detector sensitivity pattern would have to be determined. The only potential advantage of this approach is that flat-field images could be constructed quite rapidly, although it remains to be seen to what extent sharp, unresolved features (crater rims) will cause problems. The full moon subtends 30 arcminutes as seen from Earth, and has an apparent optical magnitude of -12.5; at a pixel scale of 0.1 arcsec pixel⁻¹ the effective brightness in each pixel would be 8.5 magnitudes, requiring the use of a neutral density filter. As the orbit of SNAP takes it closer to the moon, the moon could fill the field of the CCD imager, making the construction of a flat-field somewhat more efficient. A project to photometrically calibrate the surface of the moon as seen from Earth at a wide range of lunar phases and over a wavelength range of 0.35–2.5 μm is underway by the USGS (Anderson et al., 1999).

As the above discussion makes clear, unlike bias and dark calibration, some R&D will be required to determine optimal flat-field strategies for the SNAP wide-field imager. Since the CCD quantum efficiency is temperature dependent at the reddest wavelengths, some effort should be made to obtain flat-field images over a range of

temperatures. It is worth noting that an external estimate of the quality of a flat-field can be obtained by observing a given field using many dithered pointing and then checking that the photometry of each object is independent of location.

Point Spread Function Calibration

Another component of internal calibration which is not necessary for all applications, but which is desirable for the detection and follow-up photometry of supernovae is the determination of the optics point spread function as a function of location on the imager. For detection of supernovae, reference and search images are subtracted from each other, and remaining objects are flagged as potential supernova candidates. In this process, slight differences in the point spread function between these two images can produce spurious candidates, especially around bright objects. A standard procedure is to determine the convolution kernel needed convolve the higher resolution image to that of the lower resolution image. This convolution kernel is typically a function of location on the imager, if for no other reasons than that diffraction effects will necessarily change slightly over the imager and individual CCD's will be offset slightly from the true focal plane. It will also be a function of time since the focus, as scattering properties of the optics, are likely to drift slightly (behavior seen with HST), and it will be different for each filter. In addition, optimal photometry employs the point spread function for weighting, and to determine the "aperture correction" needed to account for light in the extended wings of the point spread function which are too weak and contaminated by other sources to measure for each target object individually.

It is desirable to obtain the PSF from its core well out into the wings (say, to a radius with 99% encircled energy). This requires a very large dynamic range, as only the brightest stars will have adequate signal in the wings but they may be saturated in their cores. Moreover, the wings will likely be littered with contaminating objects. By using stars covering a wide range in brightness, or by employing a range of exposure times if performing special calibration observations, the point spread function can generally be determined using stars in each target field. Fig 12.1 shows the number of stars as a function of magnitude from a combination of high Galactic latitude fields observed with HST, scaled to give the number of stars which should be present on each CCD of the SNAP imager. This indicates that each SNAP CCD will have a few stars of sufficient brightness to construct a point spread function. The number of stars bright enough to have good S/N in the wings is low, so variations in the wings of the point spread function will have to be determined by collecting stars from several CCD's.

12.2.2 External Flux Calibration

Once the above internal calibration procedures have been applied, target objects can be photometered, giving their correct relative brightnesses in the system defined by the effective instrumental bandpass (optics+filter+CCD) of the imager. Using this information for science requires converting these relative fluxes onto an absolute system. This involves determining a zero-point, as well as a term proportional to the color of

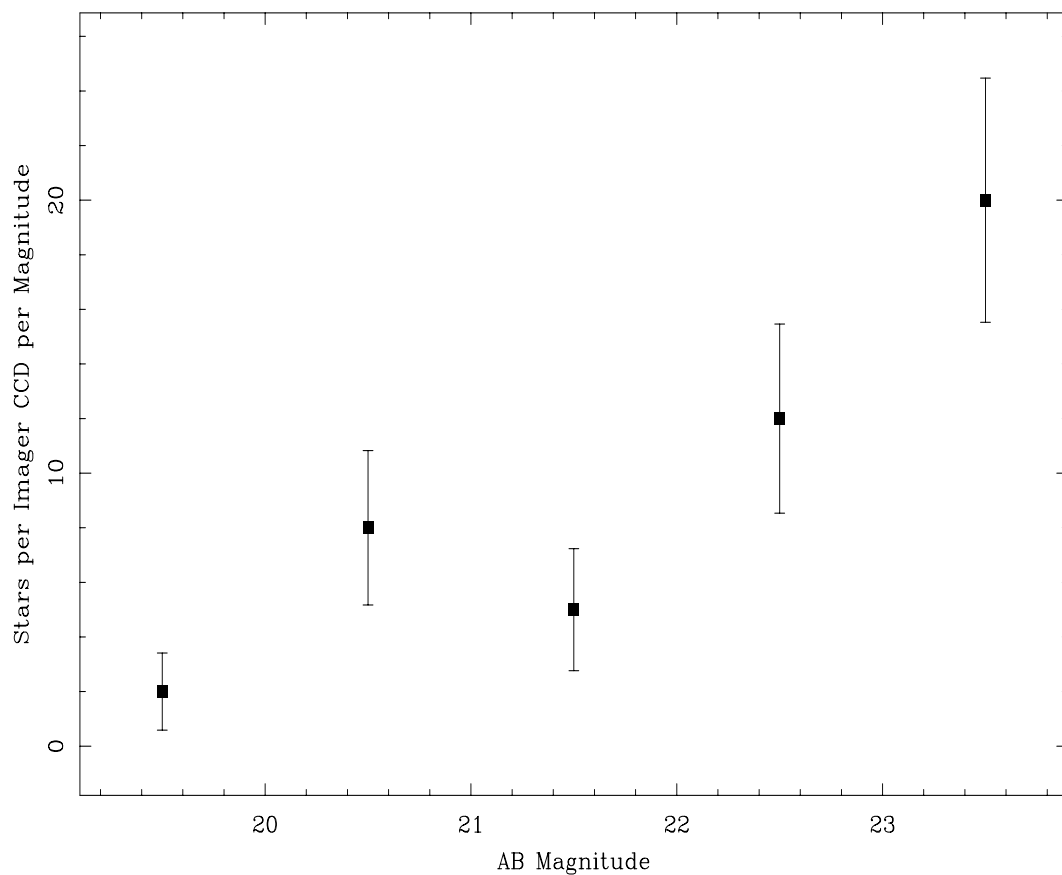


Figure 12.1: The number of stars per magnitude expected on average for each CCD on the SNAP imager. These counts were constructed by combining unresolved objects detected with WFPC2 in the HDF (Williams et al., 1996) and HDF-S, and with STIS in the HDF-S. Fainter than $m_{AB} > 24$ an increasing number of galaxies become unresolved and begin to contaminate the star counts. For typical SNAP search images, stars with $m_{AB} < 24$ will be bright enough to be used to construct the point spread function.

each object to allow for differences between standard and instrumental bandpasses.

The most common photometric system employed for ground-based astronomy over the wavelengths to be covered by SNAP is the Johnson *UBVRI,J(H)K* system, based on Vega and five other bright stars of type A0. Megessier (1995) summarizes numerous subsequent recalibrations of this system and presents preferred absolute fluxes, while Bessell (1979), Bessell & Brett (1988), and Bessell (1990) provides an absolute calibration and filter definitions which include the revised, Kron-Cousins, versions of *R* and *I* more commonly in use.

An alternative system in the optical is the Gunn *uvgriz* system, defined by Thuan & Gunn (1976), and extended by Kent (1985) and Wade et al. (1979). This system is related to the AB magnitude system of Oke (1974) and Oke & Gunn (1983) which provides a direct conversion to flux density, f_ν , with a zero-point also determined by Hayes & Latham (1975). A slightly modified version of the Gunn system is being used to carry out the Sloan Digital Sky Survey (Fukugita et al., 1996).

Systems of secondary and tertiary standards have been set up around the sky using both of these magnitude systems (Landolt, 1983, 1992; Thuan & Gunn, 1976; Kent, 1985). In addition, the number of stars having spectra defined on the Hayes & Latham (1975) system is growing. Bootstrapping from these systems, and aided by accurate model atmosphere calculations, Bohlin (1996) has developed a handful of relatively featureless hot white dwarf and solar-analog stars into spectrophotometric calibrators spanning the UV through NIR. Bohlin (1996) estimates that the absolute calibration is good to 1–2%, and that the error in the relative calibration of his system across the optical–NIR is less than 1%. He also finds that systematic differences of up to 2% exist for some of the other spectrophotometric photometric systems. This analysis is consistent with the extensive independent assessment by Megessier (1995).

The key component of flux calibration for determining cosmological parameters with SNAP is the relative calibration between restframe *B* and redshifted *B*. That is, it is important that relative calibration over the range 0.4–1.7 μm be correct to better than the brightness difference from SNAP target 1- σ changes in the cosmological parameters, i.e. $\sim 1\%$. Based on the assessment of Bohlin (1996), the current system of white dwarf and solar-analog spectrophotometric standards — comprised of only 8 stars — can just barely deliver this accuracy. Ideally the core SNAP supernova search fields should be peppered with well calibrated standards. These would serve not only to zero-point the photometry, but to provide a robust check on the accuracy of SNAP photometry. Since bright white dwarfs of the type used by Bohlin (1996) are not common, an improved set of calibration standards for SNAP would require bootstrapping from the Bohlin (1996) stars, perhaps including redoing the absolute calibration, to ensure that after all uncertainties are propagated SNAP photometry will be flux-calibrated to better than 1%. Establishing secondary standards and redoing the absolute calibration would be a major undertaking in itself, however there is broad interest in the astronomical community in doing this so finding experts to help with such an undertaking should be possible.

12.2.3 Imager Calibration Summary

Internal calibration of SNAP should be relatively straightforward, although some further study of the quality attainable with sky flats would be prudent. The external calibration steps — flux calibration and correction for Galactic extinction — currently have some weak points, to which a wide range of cosmological studies have some sensitivity. These weaknesses are not irreducible, and improvements can be made between now and the launch of SNAP. Our current estimated of the calibration error budget for the SNAP wide-field imager is given in Table 12.1, below. The statistical error quoted refers to the expected worse-case Gaussian/Poisson degradation introduced by each calibration step. The relative systematic error quoted refers to systematic errors between the lowest and highest redshift supernovae due to relative calibration errors over the entire optical to NIR spectral range. The absolute systematic error reflects the accuracy to which the true brightness of supernovae can be determined. These absolute errors do not matter for determination of the cosmological parameters exclusively from the SNAP supernova dataset. They could apply when comparing with ground-based observations (e.g., due to the PSF error).

Calibration Step	Statistical Error	Relative Systematic Error	Absolute Systematic Error
Bias	negligible	negligible	negligible
Dark Frame	negligible	negligible	negligible
Flat-Field	$< 1\%$	$< 0.1\%$	$< 0.1\%$
PSF Calibration	$< 3\%$	$< 1\%$	$\sim 2\%$
Flux Calibration	$< 1\%$	$\sim 1\%$	$\sim 2\%$

Table 12.1: Imager Calibration Error Budget

12.3 Spectrograph Wavelength and Photometric Calibration

Like the SNAP imager, the spectrograph will require initial subtraction of a bias image and a scaled dark current image. Since the background zodiacal light is dispersed, these corrections require more attention than for the imager. In particular, the dark current from an LBNL CCD or HgCdTe device will be comparable to this background level, so the quality of the dark current image will have to be several times better than needed for imaging. For both of these corrections, the precepts discussed for the imager apply, with the additional requirement that the dark current calibration image have a total exposure time several times longer than the longest target spectrum to prevent degradation of the signal-to-noise ratio.

For flat-felding of the spectra, the methods used are quite different than for the imager. Because the dispersed zodiacal light background will be dispersed and contains numerous stellar features since it is reflected sunlight, sky flats are not suitable for flat-

fielding. Rather, the standard approach is to make use of an internal flat lamp. This is much more practical than it would be for the SNAP imager since the spectrograph field is so much smaller. The flat lamp spectrum is fit in the wavelength direction, leaving only the pixel-to-pixel variations. The result is then used to correct for pixel-to-pixel sensitivity variations of the detector. Alternatively, the lamp spectrum can be divided directly into the object spectrum, leaving the true lamp wavelength to be corrected at the flux calibration stage (as described below). A crucial aspect of this procedure is that the functional form of the lamp spectrum in the wavelength direction be well described by a function of modest order, or that it be extremely reproducible. If this is not the case, each flat lamp spectrum would have to be externally calibrated with observations of spectrophotometric standard stars.

After correction by the lamp flat, the resulting spectrum will still contain either the spectrograph response and low-resolution detector response or the (inverse) spectrum of the flat lamp, depending on which of the above flat-fielding methods is used. (Technically, wavelength calibration, described below, is applied prior to flux calibration with a spectrophotometric standard.) Correcting either of these signatures requires observations of spectrophotometric standard stars, such as those of Bohlin (1996) discussed above. This same step provides the absolute flux calibration for the target spectrum. The final accuracy of the relative flux calibration is limited by the 1–2% accuracy of extant spectrophotometric standards. This is further motivation for working to improve this situation. With the use of an integral field unit, during the initial SNAP science verification phase such standard stars should be placed at numerous locations on the IFU to confirm that the lamp flat is providing accurate correction everywhere in the IFU field.

Wavelength calibration uses internal arc lamps — a very straightforward procedure. Slight differences in the optical path of the arc calibration lamps and that of celestial objects can lead to small zero-point errors in the wavelength calibration. This is especially important for very low resolution spectra obtain, e.g., using a dispersive element option for the NIR photometer. Such a zero-point should be quite stable, and can be determined from observations of planetary nebula (having narrow emission lines) or radial velocity standard stars.

12.4 Imager Astrometric Calibration

Astrometric calibration of the wide-field SNAP imager is necessary for the purposes of aligning images prior to subtraction, locating an aperture or point-spread-function for photometry, obtaining correct surface brightnesses for galaxies, or correcting weak lensing shear maps. At a minimum, the orientation and scale of each CCD needs to be determined. Since it is likely that the scale will change slightly across each CCD, especially near the field edges, higher order fits for the scale will likely be necessary. Lithography mask errors will also be present, as in the 34th row defect on WFPC2. Roughly speaking, there are almost 10^4 terms to solve for, for each filter. By observing a given field with many dithered pointings with offsets as large as one degree, a “plate-overlap” solution can be obtained for these various parameters. In typical SNAP

images, objects with $m_{AB} < 25$ should have plenty of signal-to-noise such that centroids can be determined to 0.1 arcsecond or better. Based on HDF number counts there should be more than 10^5 such objects per SNAP field. Multiple dithered fields should easily reduce SNAP astrometric errors to less than 0.01 arcsec. The remaining question then is how often astrometric calibration needs to be obtained; this depends principally on the stability of the optics, optics supports, and CCD mounting plate, etc. Since SNAP will re-observe the same fields every few days, frequent differential adjustments to the astrometry will be possible.

12.5 Spectrograph Astrometric Calibration

In order to reconstruct a spatially and wavelength rectified data cube from spectroscopic observations with an IFU, the relative mapping onto the sky of the slitlets must be known. The exact relative physical locations of the slitlets can be determined from measurements in the lab, however, the telescope and spectrograph optics, and orientation of the detector — which can change once in orbit — will effect the mapping onto the sky. Furthermore, in order to be able to subtract final reference spectra from supernova plus host galaxy spectra obtained at maximum light, the correct relative positions of these spectra in the IFU must be known. This requires that the location of the IFU relative to the wide-field imager be well determined. Obtaining this calibration consists of taking dithered observations in both the wide-field imager and with the IFU spectrograph of a field having a very high surface density of objects, such as the outskirts of a global cluster. The dithering must be large enough so that over the course of the calibration observations the same objects are detected both with the spectrograph and the imager, but needn't cover nearly the area required for astrometric calibration of the imager. Such calibration should be straightforward.

12.6 NIR Imager Calibration

The HgCdTe detectors to be used for the NIR imager have electronics for each pixel capable of performing non-destructive reads during the course of an exposure. The electronics still have a bias voltage level, as well as dark current and pixel-to-pixel sensitivity variations. These can be addressed in much the same way as for the CCD imager. Because the field of the NIR imager is small, flat-fielding using an internal lamp should be possible. External verification will come from deep sky exposures, and possibly Earth or Moon flats.

Each field observed with the NIR imager will be comparable in size to that of a single CCD on the CCD imager. Therefore, astrometric and point spread function calibration can be accomplished using basically the same methods used for the CCD imager.

12.7 Extinction from Foreground Dust in the Galaxy

The final step before the absolute photometry can be used to address cosmological questions, is to correct for extinction by dust in our own Galaxy. The amount of dust can be estimated by its emission in the far-infrared, as measured by IRAS and COBE (Schlegel, Finkbeiner, & Davis, 1998) (shown in Fig 12.2 and Fig 12.3, or by measuring the column of HI and assuming a constant ratio of dust to gas (Burstein & Heiles, 1982). Using these data as guides, SNAP fields can be chosen which have low amounts of extinction. It is worth pointing out that since discovering lower redshift supernovae ($z < 0.1$) will require searching even larger regions of sky, there is the potential for errors in the dust extinction maps or in the extinction law (relating the extinction at each wavelength to the total column of dust) to cause systematic differences at the level of a few percent. For this reason it will be important to select supernovae of all redshifts over the same regions on the sky. Naturally, any improvements in the dust extinction maps and in verifying the extinction law will be of great benefit. In particular, there is an uncertainty of up to 6% in the minimum B-band dust extinction near the Galactic poles (Schlegel, Finkbeiner, & Davis, 1998). Since a given column of dust absorbs blue light more strongly than red light, such an error will translate into errors in the relative brightnesses of lowest and highest redshift supernovae. SNAP will automatically collect multi-wavelength observations of thousands faint Galactic stars in each field, many of which will lie in the halo of the Galaxy and thus presumably above the dust layer. Of these, ~ 100 should be very hot, featureless subdwarfs whose intrinsic spectra can be calculated fairly well. The calculated spectra can be compared to the observed multi-color photometry, allowing the amount of reddening to be determined. Application of a standard dust extinction law gives the total extinction from the reddening (relative) extinction. These, and similar measurements using halo stars (Szomoru & Guhathakurta, 1999; Gilmore, Reid, & Hewett, 1985) should allow an improved determination of Galactic extinction in the SNAP fields. Internal comparison of the extremely deep galaxy counts that will be available across the SNAP survey region will provide a means of obtaining the correct relative Galactic extinction in each color, without having to assume a dust extinction law, using magnitude offsets for the counts in different fields. Ideal SNAP survey regions, having low Galactic extinction and which also have low zodiacal background and are free of very bright stars, are given in Table 12.7.

Field Name	Right Ascension	Declination	Ecliptic Latitude	Galactic Latitude	Blue Extinction
SNAP-North	$16^h 25^m$	$+57^\circ$	$+74^\circ$	$+41^\circ$	~ 0.035
SNAP-South	$04^h 30^m$	-52°	-70°	-42°	~ 0.047

Table 12.2: Survey regions with low zodiacal background

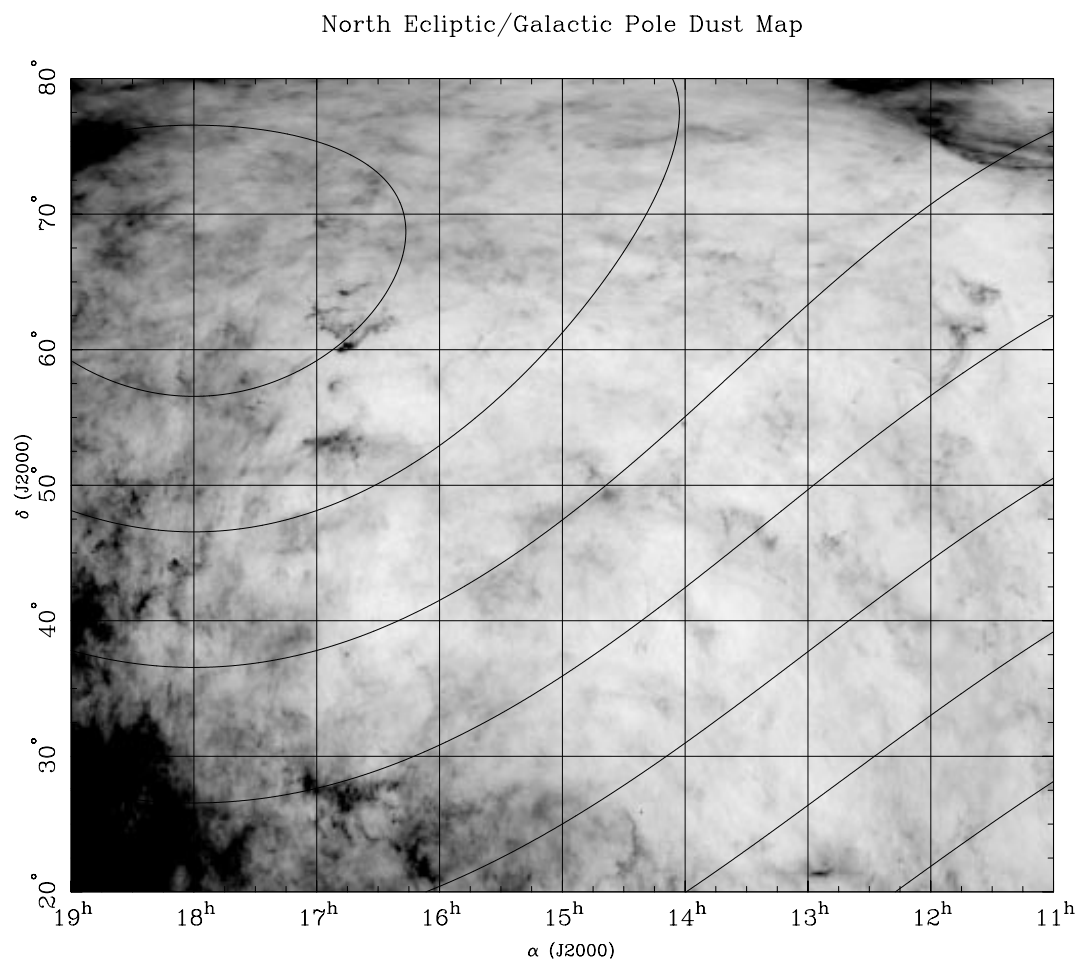


Figure 12.2: Map of the Galactic dust towards the north ecliptic pole and north Galactic pole, from Schlegel, Finkbeiner, & Davis (1998). The greyscale ranges from a B -band extinction of 0.0 (white) to 0.4 (black) magnitudes. The rectilinear coordinate grid is equinox J2000 celestial coordinates. Also shown are lines of constant ecliptic latitude. SNAP fields should be located in regions of low Galactic dust extinction, and at high ecliptic latitude where the zodiacal light background is the lowest.

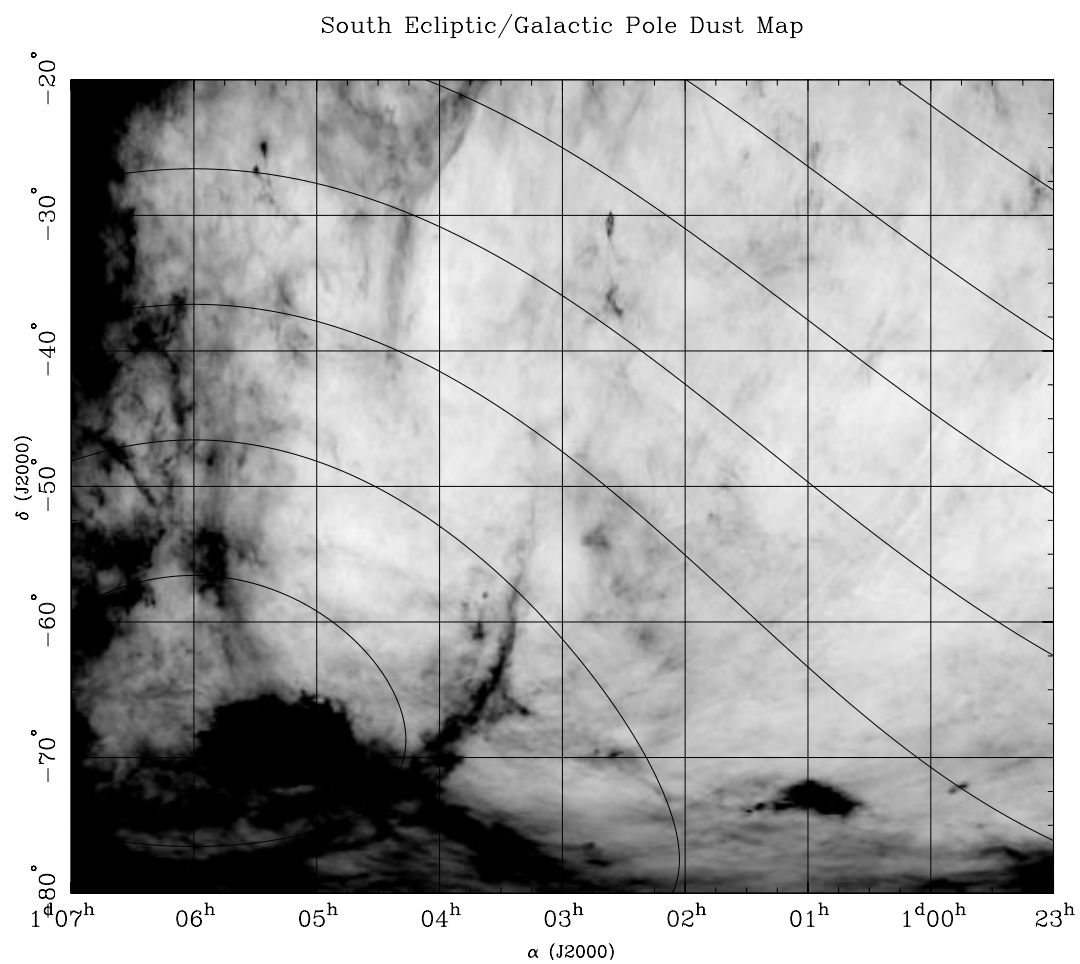


Figure 12.3: Same as Fig. 12.2 for the south ecliptic pole and south Galactic pole.

12.8 Photometric Redshift Calibration

For the SNAP mission there will be a great advantage to knowing in advance the approximate redshifts of newly discovered SNe. With an approximate redshift, an initial guess can be made as to the type (Ia, or other) of a SN, allowing the appropriate follow-up prescription to be executed. This will be especially important for faintest (high redshift) targets, especially since SNAP will have time to observe only a fraction of these.

If a SN candidate can be associated with a host galaxy — which should be true more than 90% of the time — knowledge of the host galaxy redshift provides a good estimate of the SN redshift. The advantage here is that host galaxy redshifts can be measured in advance of any SN explosion. The difficulty is that all galaxies must have redshift determinations since we cannot predict which galaxies will host a SN during the lifetime of SNAP.

Obtaining spectroscopic redshifts for all (10^6) galaxies is clearly out of the question. However, given that galaxies typically have spectra with a few strong features (most notably the “4000 Å break” in the continuum), redshifts can be estimated from broadband photometry. This technique is known as a “photometric redshift”. The accuracy of this technique depends on the number and widths of the filters. In order to cover a large range in redshift, the wavelength coverage of the filter set must also be large.

Photometric redshifts have been determined from UBVRI photometry of galaxies in the Hubble Deep field (HDF; Williams et al. (1996)). Hogg et al. (1998) present a blind comparison of Keck spectroscopic redshifts with HDF photometric redshifts presented by several groups. In this relatively small sample they find $\sigma_z \sim 0.1$. It is important to note that their sample includes very few galaxies with $z > 1$. This is because LRIS on Keck II has trouble securing redshifts for such distant galaxies due to a lack of prominent galaxy spectral features below the OII3727 emission line, coupled with night-sky lines, fringing, and poor response in the red. In principle, with an LBNL CCD these Keck redshift surveys should be easily extended, and thus provide training data, to at least $z \sim 0.95 \mu\text{m}/0.3727 \mu\text{m} - 1 \sim 1.55$.

Since SNAP will have ~ 11 filters for the wide-field CCD array, it should be able to determine photometric redshifts with a standard deviation of 0.1 out to $z \sim 1.3$. Beyond $z \sim 1.3$ the signal from the 4000Å break will fade away, and by $z \sim 1.5$ it will be redshifted off of the CCD response altogether. This leaves the follow-up program vulnerable to faint SNe with hosts in the range $1.3 < z < 2.2$. Note however that by these redshifts there is a non-negligible distortion of the galaxy continuum due to absorption by Lyman-alpha forest metal lines which can help set redshift limits (this will need to be quantified). The next feature of note is the continuum break blueward of Lyman-alpha, which will enter the B-band at $z \sim 2.3$. Note that CCD response down to 2800Å would be required to enable the Lyman-alpha break to predict redshifts as low as $z \sim 1.3$, which is infeasible.

An alternative approach would be to determine photometric redshifts from the SNe themselves. This approach is mostly unexplored at this time. The expectation would be that various Fe II lines in the restframe UV may present a noticeable photometric signature. Other techniques might include constraints from early photometry since the

SNe will brighten $2\text{--}3\times$ more slowly than in the restframe. Again, further study of this question is needed.

In order to have the photometric redshift estimation in place at the start of the SNAP mission, redshifts of several hundred galaxies in the SNAP fields out to redshift $z \sim 2$ will be needed. These can be obtained using multi-object spectrographs on large ground-based telescopes (e.g., DEIMOS on Keck).

Chapter 13

Electronics

13.1 Electronics

An array of approximately 200 CCD's of 2k x 2k $10.5 \mu m^2$ pixels would be installed in the focal plane of the SNAP telescope. Single exposure times from 100 to 1000 seconds in the wavelength range of 350-1000 nm are foreseen.

The current thinking is that the satellite would be able to transmit all images obtained given the availability of high performance Traveling Wave Tube Amplifiers. However, as our baseline solution we have assumed the requirement of compressing images on-board. In particular performing the necessary cosmic ray rejection which will require post-processing multiple frames. Frames of up to 24 images are correlated in order to send to the earth images filtered of cosmic rays that can be rejected using on-satellite digital filtering.

The array of back-illuminated CCDs is read and digitized by low noise electronics in a range from a few to 300,000 electrons, at speeds of the order of one to three hundred kHz. The required dynamic range is 16-bit for the electronics and has to be tolerant of 10 krad, under a wide range of temperatures.

The proposed readout architecture (Figure 13.1) comprises:

- Clock Driving for the CCDs,
- Amplification and Correlated Double Sampling (CDS) providing the kT/C on-CCD reset transistor noise reduction.
- Gain selectable amplifiers,
- Analog to Digital conversion,
- Readout control of the analog electronics.
- Digital storage for at least 24 exposures: $24 \times 196 \times 8 \text{ MByte} = 37 \text{ GByte}$, and provision for buffering during the processing time, depending on the number of Digital Signal Processors (DSP).

- DSPs for CCD and readout calibrations, digital filtering, lossless and lossy data compression, main control of the analog sections. A block diagram of the analog electronics readout section is shown in Figure 13.1.

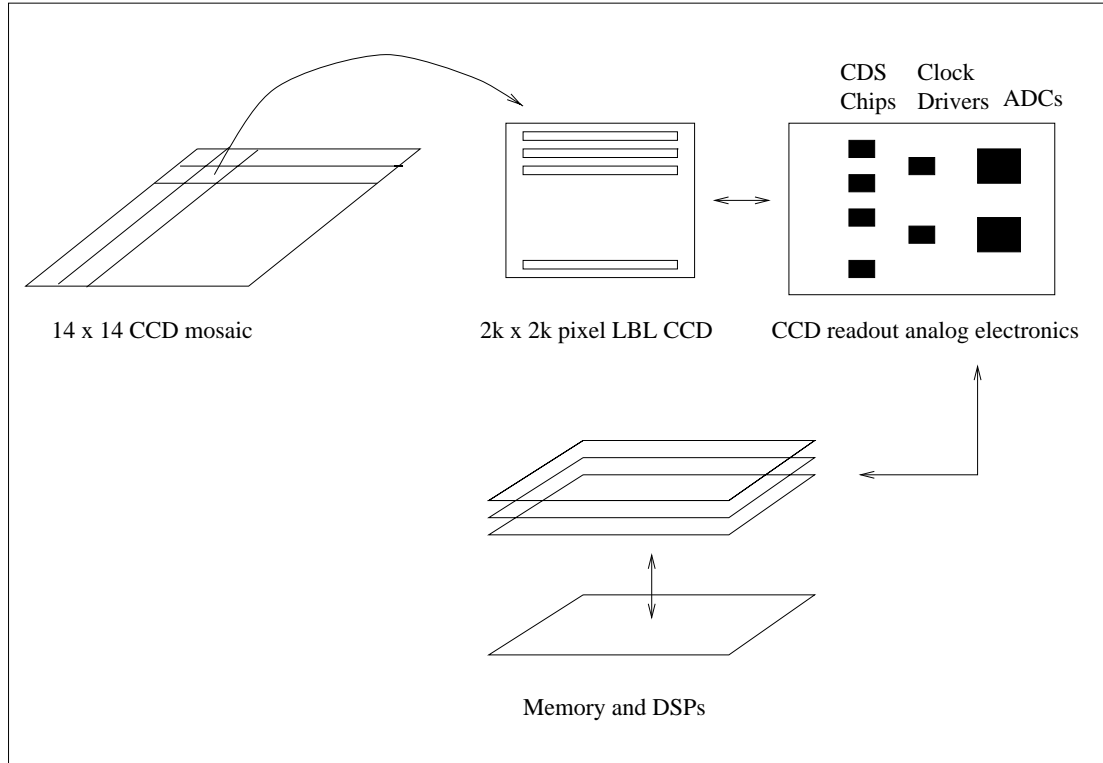


Figure 13.1: CCD Array Readout Chain.

13.1.1 CCD Clocking

The CCD capacitance is of the order of 5 nF for the pixel (horizontal) clock lines, and 85 pF for the register (vertical) clock line. A voltage level of 12 V is needed, with a slope depending on the readout speed. Current sources switched to a capacitor can generate the waveform, they have to be heavily buffered to drive the capacitive loads. Corresponding power for CCDs and the clock drivers is of the order of 14 W during a 100 kHz readout. The power for the CCD output stage is 50 mW per channel. Assuming a duty cycle of 50% for the clock driver chip, the total power for CCDs and clock driver chip are 27 W and 14 W respectively. The CCD and clock drivers only consume power during image transfer. This power scales with the readout frequency. The clock driver can be integrated using a radiation hard process able to hold 15 V voltages, and deliver large currents. Dentan et al. (1998, Toronto); Ardelean et al. (1996).

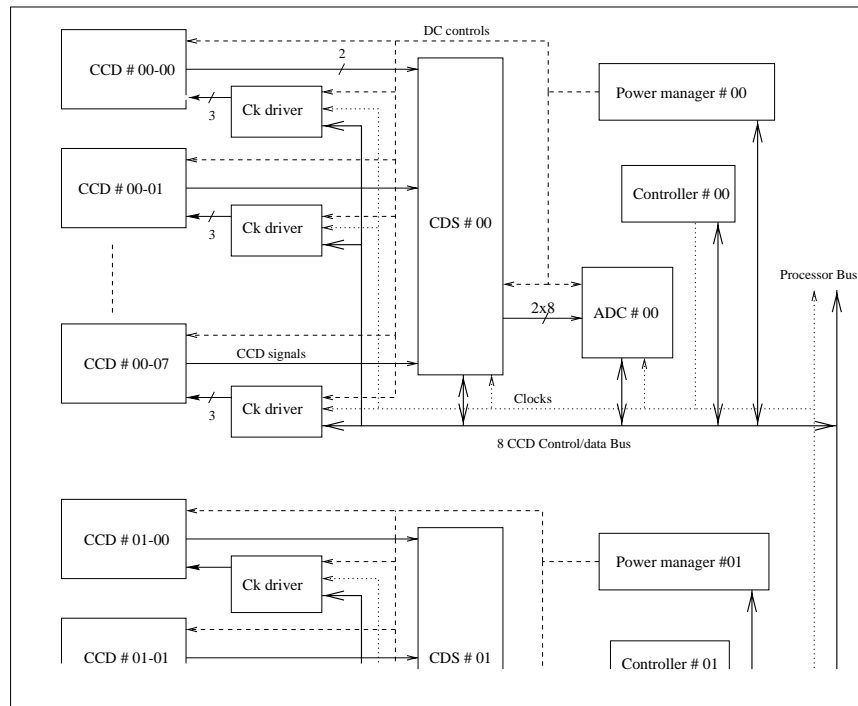


Figure 13.2: Analog readout electronics.

Correlated Double Sampler for CCD Readout

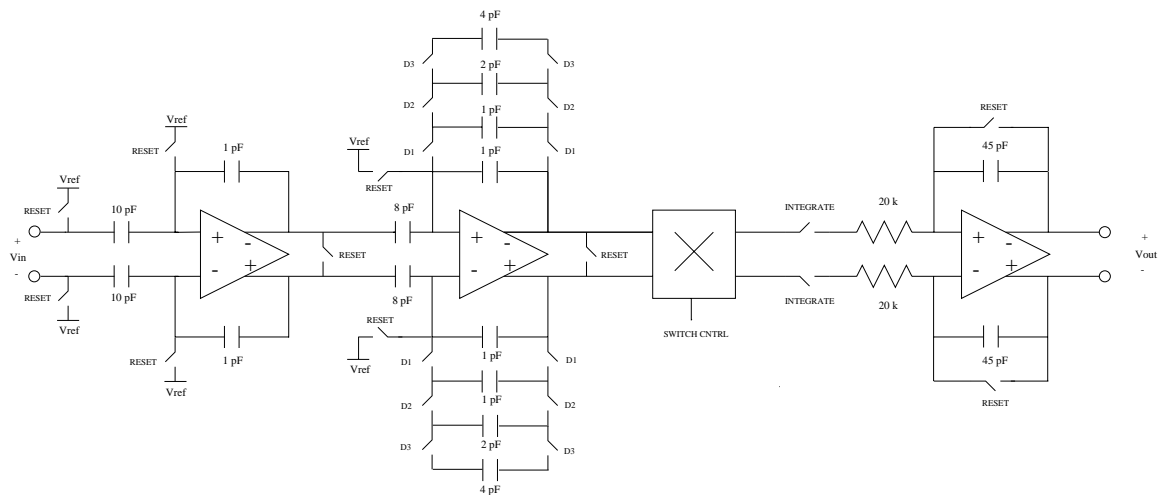


Figure 13.3: Correlated Double Sampling chain Block-Diagram.

13.1.2 Double Correlated Sampling

The present CCD sensitivity is $3 \mu\text{V}$ per electron. In order to reject the low-frequency reset noise, the CCD output is sensed two times, during a clock phase where it is clamped to a voltage reference through a MOS transistor switched on, and when the signal is present. The Correlated Double Sampler integrates and subtracts the two voltages, resulting in a voltage corresponding to the actual CCD pixel signal. Depending on the sensitivity required by the objects to be observed, a gain of 1, 2, 4, or 8 is selected. These function can be integrated in the same radiation-hard CMOS chip operated at 5V power supply. The leads to an input referred noise of $3 \text{ nV}/\sqrt{Hz}$ corresponding to a noise of 1 electron with the actual CCD output sensitivity. This device has been simulated using the DMILL process. The noise/speed performance requires a total power of 40 mW/channel. There are two differential readout channels per CCD. This function is to be de-powered after CCD have been read, the actual signal levels digitized, and data stored in memory. A block diagram is shown in Figure 13.1.1.

13.1.3 Analog to Digital Conversion.

Analog to digital converters that have 16-bit precision and can survive 10 kRad is limited to the 330k Hz LTC1604 currently on HESSI. Higher speed, or more radiation tolerant devices are currently under investigation. Power is managed in each analog readout module (there are 24 modules processing 8 CCDs each), switching off the sections that either are not in use at a given time, or dissipate an excessive amount of power.

13.1.4 Digital Processing

In order to reject cosmic induced noise and other irrelevant objects in the images, median filtering is performed by Digital Signal Processors accessing a main memory where a set of consecutive frames are stored. The processing time required using the Texas Instrument TMS320C6200 DSP chip to median filter 32 CCD frames of 2k X 2k pixels is estimated to 40 seconds based on benchmark measurements using this processor family assuming programmed memory accesses. If Direct Memory Access mode (DMA) from memory to processor is used, together with a median filtering depth of 24, this time is reduced down to 20 seconds, as DMA saves half of the processing time, and the sort algorithm scales in $N \log N$.

The TMS320C6203 processor offers 512 KBytes of internal data memory, with the same computing performance than the TMS320C6200 (2.4 GIPS). These processors have not been measured for radiation tolerance. On the market, A rad-tolerant version of the PowerPC chip is able to run 300 MIPS up to 200 kRad with 10^{-10} Single Event Upset/bit/day.

The huge amount of required data storage dictates the use of dynamic RAM. Synchronous Dynamic RAM (SDRAM) integrated in 3D technology conditioned for space operation, are manufactured (e.g. Lockheed-Martin) as solid state recorders and housed in units of 27 GByte (error correction code included) of 80 lb weight, dissipating 110 W for simultaneous Read and Write access, 75 W for Read or Write operations,

40 W for Data Retention. Scaling these numbers to our needs (assume 24 frames and 8 DSPs) lead to 47 GByte for a total weight of 140 lb, and a total power dissipation of 130 W for data Read or Write, 70 W for data retention. This technology is radiation hardened.

13.1.5 Power

Memory is written when the CCDs data are transferred, read when the DSPs access for processing. A pixel can be seen as a memory page sized as the median filtering depth. A depth of 24 is foreseen. The time when memory is written and read (i.e. full powered), is 20s at 100 kHz (4M pixels x 100 kHz / 2 channels) for write, and DSPs DMA accesses when processing. Assuming these accesses take place during the whole processing time, (pessimistic), the power (average and peak) required by CCDs, memory, DSPs and control is shown in Table 13.1.

A power of 5 W is assumed for one DSP and its associated components. Actually, a C6203 processor running at 200 MHz dissipates 1.05W in typical conditions. It is assumed that memory can be partitioned in blocks of a few Gigabytes (eight to sixteen CCDs), allowing us to de-power sections where data are not to be accessed for processing. Power is a nearly linear function of the number of frames to be median filtered. It appears that it is possible to keep the average power to 100 Watts and the peak power at approximately 200 Watts.

A summary is given Table 13.1, for CCD readout at 100 kHz, median filtering depth of 24 frames, with an overlap of four frames, eight TMS320C6200 DSPs, that optimize average power, peak power, and memory size. Average power is 117 W, peak power 235 W.

Subsystem	Power peak (W)	Power average	Rad hard	Quantity
CCD	27	4.25	yes	196
CDS Chip	16	3.3	possible	
Clock Drivers	14	4.25	possible	
ADC	9	1.9	?	40
Memory	130	95	yes	47 GB
DSP	40	8.4	?	8
Total	235	117		

Table 13.1: Power consumption of CCD readout chain.

Chapter 14

Spacecraft Description

14.1 Orbit Properties

The choice of orbit is governed by the effect of the orbit on five aspects of the mission design: 1) The requirement to operate the detectors at 150° K (suggests a high orbit to reduce heat load from the earth and allow the use of a passive radiator system for detector thermal control), 2) The requirement to view in the direction of the ecliptic poles over the entire year with out interference from light from the earth, 3) The requirement to maximize viewing time and link margin for the receiving antenna(s) used to downlink science data from the observatory, 4) The requirement to survive the effects of trapped radiation and cosmic rays in the orbit which may degrade performance of the detector systems, and 5) The requirements on the launch vehicle necessary to attain the orbit. A preliminary analysis has identified two orbit strategies which appear likely to provide a solution which meets all requirements: a polar sun synchronous “terminator” orbit, and a very high lunar assist “Prometheus” orbit. Since the choice of orbit affects the design, weight, power and cost of virtually every spacecraft subsystem, the determination of the optimum strategy is an involved and iterative process which will be re-visited in detail during the forthcoming mission study phase. The result of the present trade study is shown in Table 14.1.

Orbit	Radiation	Thermal	Telemetry	Launch	Stray Light	SCORE
LEO/Polar	High at Poles	Mechanical	High BW	Excellent	Earth Shine	2.9
LEO/28.5	Lowest Dose	Mechanical	High BW	Excellent	Earth Shine	2.9
LEO/Equatorial	Lowest Dose	Mechanical	High BW	Fair	Earth Shine	2.5
HEO/GEO	Poor	Passive	24 hr	Fair	Dark	3.2
HEO/Prometheus	Very Good	Passive	Low BW	Fair	Dark	3.4
HEO/L2	Very Good	Passive	Low BW	Fair	Dark	3.4

Table 14.1: Orbit Trade Study Matrix

For the purpose of the present proposal, we will present a solution based on the Prometheus orbit which we believe meets all requirements. Figure 14.1 shows the proposed Prometheus orbit. As is seen from the figure, the strategy involves selection of an orbit which devotes virtually all of the launch vehicle energy to achieving a very high apogee. The position of the apogee is carefully chosen to interact with the moon

in such a way as to bring the perigee up to approximately 122,000 Km on the first apogee pass. Propulsion on the spacecraft is then used to supply a velocity change of 35 meters/second to reduce the apogee to approximately 300,000 Km. The final step is necessary to achieve a final orbit which does not have instability due to interaction with the moon.

Advantages of this orbit are: 1) Since the spacecraft is always far from the earth, the effect of earth albedo on the detector thermal control system, and in causing thermal changes to structural components which would compromise performance of the attitude control system (ACS) is small. 2) The orbit can be designed to go for long periods with out eclipse. This simplifies thermal control, power management, and most importantly, reduces thermally induced disturbances to the ACS. 3) By adjusting the inclination, the orbit can be configured so that the spacecraft is visible from the Berkeley Satellite Ground Station antenna for a substantial fraction of the orbit, while limiting the maximum time between contacts. 4) The orbit is entirely outside the radiation belts.

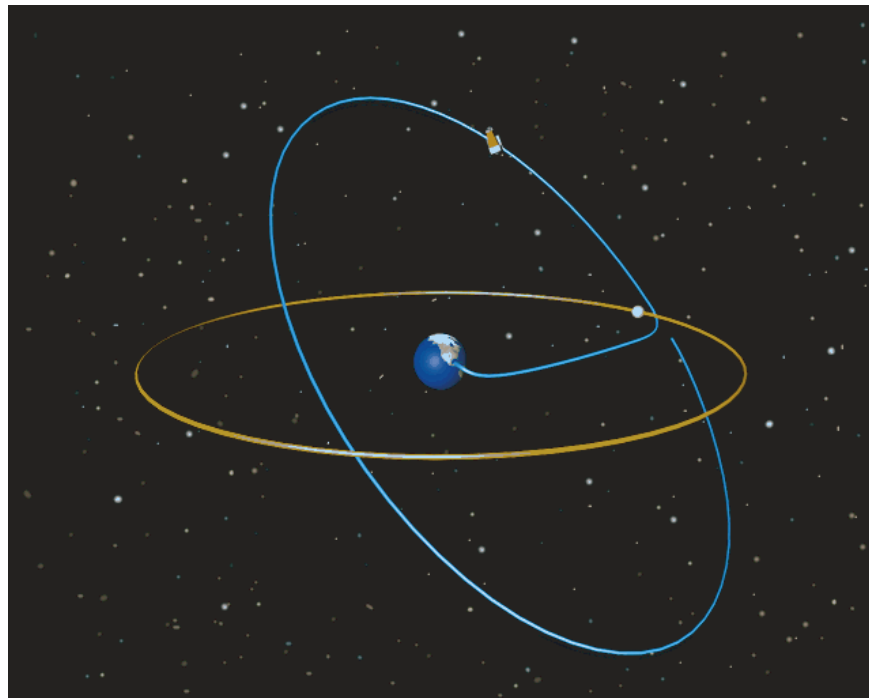


Figure 14.1: Lunar assisted "Prometheus" orbit.

14.2 Spacecraft Description

The SNAP Team is in the process of recruiting and selecting an aerospace industrial partner with whom to team in the preparation of a detailed proposal for the SNAP mission. The partner would be expected to provide a substantial portion of the spacecraft systems and may also participate in development of portions of the payload. A Letter of Interest/Opportunity for Partnership has been sent to a number of companies, with at least 5 firms indicating that they will respond. While it is expected that details of the spacecraft design will depend on the particular teaming partner chosen, a preliminary design is presented in the following sections which we believe will meet all mission requirements. Figure 14.2 is a block diagram of the entire observatory which shows the relationship between the science payload and the various spacecraft subsystems. The intent in the design is to break the system into a number of sub-systems with well defined requirements and very simple and well defined interfaces. The choice of provider for each block is intended to play to the strengths of each of the teaming partners. The spacecraft portion of the system is comprised of four major functional blocks which are described in the sections below.

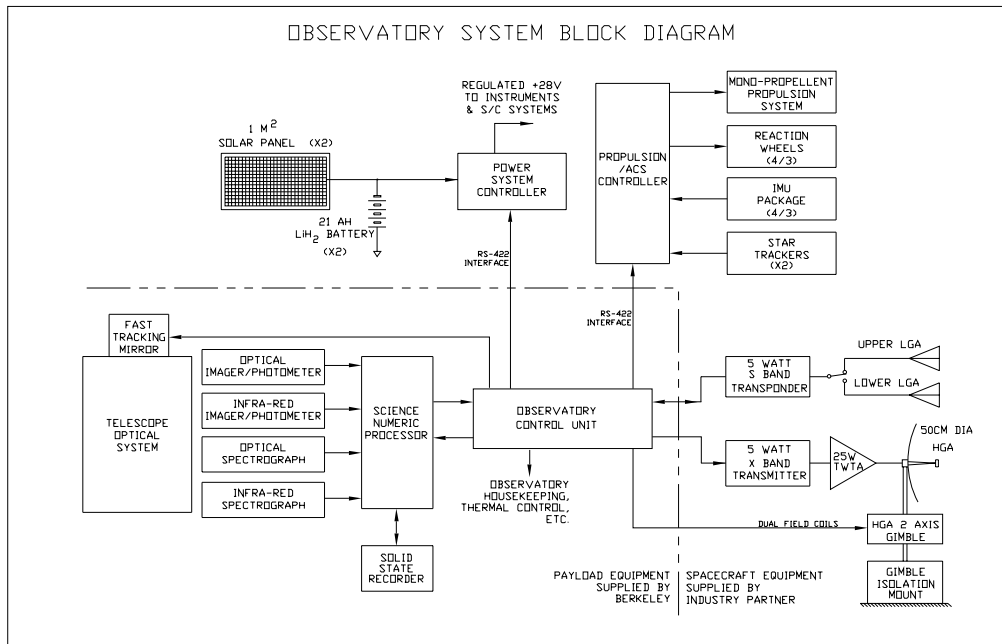


Figure 14.2: Block diagram of the relationship between the science payload and the spacecraft subsystems.

14.2.1 Power system

The Power System includes 2 solar arrays, each of which has 11 strings of 37 each 2.2 cm square GaAs solar cells. The cells are mounted to array panels and equipped with 1 mm cover glasses for radiation protection. Each array has an overall size of approximately 1 square meter, and when aligned with the sun will produce 209 watts at the beginning of the mission and 170 watts at the end of the mission. OR'ing diodes for each string and power control shunts are mounted on the rear of the panel. The arrays are mounted on panels which swing out from the spacecraft and lock into position with both arrays in the same plane perpendicular to the telescope bore sight. Careful attention is paid to the design of the array support and locking system to keep the frequency of the first vibration mode sufficiently high to avoid degrading the performance of the attitude control system. Since the science targets are generally in the direction of the ecliptic poles, the arrays can be maintained in an orientation approximately normal to the sun direction by controlling the roll of the spacecraft about the telescope bore sight axis. The control of roll angle will also have the effect of keeping the CCD thermal control radiator panels always pointed away from the sun, and by keeping a constant sun direction with respect to the spacecraft will minimize thermally induced distortion of the telescope and structure. The Power System is a direct energy transfer type, with each array connected to one of a pair of 21 AH LiH₂ batteries. The partially redundant system will allow reduced operation of the observatory even in the event of failure of one of the arrays or batteries. A dedicated controller in the power system performs maintenance of the battery state of charge, provides regulated 28 volt DC power to the other observatory systems, and collects housekeeping and status information on the power system. A single RS-422 interface between the Power System Controller and the Observatory Control Unit (OCU) serves to transfer control information to the Power System, and power system engineering data back to the Observatory Control Unit.

14.2.2 ACS/Propulsion System

The ACS/Propulsion System consists of a pair of star trackers, an Inertial Measurement Unit (IMU), a set of reaction wheels, and a control unit which is used to determine and maintain the attitude of the spacecraft. The ACS control unit also manages a mono-propellant hydrazine system which is used to provide the 35 meters/second velocity change needed to circularize the Prometheus orbit, and to provide the angular momentum to unload the reaction wheels. For the preliminary spacecraft design, the ACS components shown in Table 14.2.2 are suggested.

The controller uses information from the star trackers and the reaction wheels to generate control signals to the reaction wheels to bring the spacecraft to a specified pointing direction. Experience on previously flown spacecraft indicates that a system based on the components listed in Table 14.2.2 can achieve a pointing accuracy of approximately 2 arc-seconds on a spacecraft with a suitably rigid structure. This "course" pointing supplied by the spacecraft system is augmented by the payload fast tracking mirror system described in § 8.2 above to achieve the required .03 arc-second

<i>Description</i>	<i>Mfr & P/N</i>	<i>Mass</i>	<i>Cost</i>
Roll Axis Star Tracker	Ball CT 602	6.0 kg	\$600K
Cross Axis Star Tracker	Ball CT 602	6.0 kg	\$600K
Reaction Wheel Package	Ithaco Type B 16 nmsec		\$800K
	With special balancing		
	for low noise		
IMU Package	Litton HRG (4/3)		\$900K
Controller	TBD		\$500K

Table 14.2: Attitude control system components

observatory system pointing accuracy.

The mono-propellant propulsion system includes a 5 pound engine which is used to provide the orbit velocity change and a redundant set of six 0.2 pound engines used for reaction wheel management, along with fuel tanks with a total capacity of 49.2 kg of hydrazine and necessary valves and plumbing. The Table 14.3 lists the components with their mass.

<i>Quantity</i>	<i>Description</i>	<i>Mfr & P/N</i>	<i>Mass</i>
1	5.0 lbf Main Engine	Primex MR-50M	.68 kg
12	0.2 lbf Attitude Engine	Primex MR-1003g	12 X .22 kg
3	Latch Valve	Moog 51-204	3 X .36 kg
2	Fill/Drain Valve	Moog 50-837	2 X .02 kg
3	Filter	Wintec 1524-772	3 X .18 kg
2	Pressure X-ducer	Paine 213-76-570-01	2 X .20 kg
4	Bladder Tank	PSI 80266-1	4 X 2.20 kg
A/R	Plumbing		1.0 kg
		TOTAL	13.18 kg

Table 14.3: Propulsion system components

Approximately 40 minutes of operation of the main engine are required to provide a velocity change of 35 m/sec on a 1550 kg spacecraft. This will consume approximately 25 kg of fuel, leaving 24 kg for orbit injection, reaction wheel management, and margin.

Control of the engine catalyst bed heaters, the tank heaters, and the propellant latch valves, as well as the valves on the individual engines is also done by the same controller as performs the attitude control. When the reaction wheels become saturated the attitude control engines are operated by the controller to unload them. The interface between the Propulsion/ACS and the rest of the observatory is a single RS-422 line in each direction between the Propulsion/ACS Controller and the OCU.

14.2.3 Telecommunications System

The Telecommunications System is comprised of two parts. An S-band transponder switched between a pair of mechanically fixed low gain antennas (LGA's) is used for

transmission of commands from the ground system to the spacecraft and for low rate engineering data from the spacecraft to the ground. Science data are transmitted to the ground via a 5 watt X band transmitter driving a 25 watt Traveling Wave Tube Amplifier (TWTA) which is connected to a 50 cm diameter steered high gain antenna (HGA). The high gain antenna is mounted to a 2 axis gimbal tied to the spacecraft structure through an isolation mount which is designed to decouple the vibration modes of the antenna from the spacecraft structure to reduce the demand on the ASC system. At a range of 300,000 Km, a data rate of 50 megabits per second with a link margin of +3.3 dB can be supported with the 50 cm diameter antenna on the spacecraft transmitting to the Space Sciences 11 meter dish. Assuming a gain of 1.5 dB for the LGA's, an S band down link rate of 7 Kb/sec will be supported, and using the 100 watt transmitter in the Space Sciences ground station, an uplink rate of 150 Kb/sec will be possible. While the telecommunications system presented here is single string, it may be desirable to introduce redundancy in the transmitters and/or receiver. This issue will be investigated during the study phase.

14.2.4 Observatory Control Unit

The remaining major spacecraft system block is the Observatory Control Unit (OCU). The OCU serves as the central interface between the other major subsystems and is the interface to the science payload. Functions of the OCU include the receipt and processing of ground commands, the control of the Propulsion/ACS system, the management of ranging operations, and control of the power system. The most computation intensive task of the OCU is management of the science payload systems, and the management and control of the data flow between the science payload and the telemetry downlink. The OCU will also manage the Solid State Recorder (SSR) used to store science data prior to downlink. The OCU hardware consists of a RAD6000 processor system coupled to a hardware data processing and interface system based on radiation hardened Actel FPGA's which is used to manage the high speed data flow between the science payload and the X band transmitter. This system architecture is patterned after that used with great success on the FAST spacecraft. The OCU will also collect both spacecraft and payload engineering data and will perform thermal control of the spacecraft and the payload systems.

14.2.5 Spacecraft Structure

The spacecraft structure consists of a disk shaped section approximately 150 cm in diameter and 40 cm thick which makes connection between the science payload and the the launch vehicle. The deployable solar array panels are attached to and are considered a part of the structure, as is the HGA isolation mount. The LGA's are attached to the structure, and all Power System, Radio System, and Propulsion/ACS System components are mounted inside it with the exception of a portion of the attitude control engines which are mounted higher on the science payload. Mathematical modeling and analysis of the spacecraft structure and the payload will be done as a single unit by the industrial teaming partner, and the results of the analysis used to refine the designs

of all observatory systems, including the ACS, the payload, the solar arrays, and the spacecraft and payload structure.

14.3 Launch Vehicle

While it is expected that the final choice of launch vehicle for the SNAP mission will be made by NASA code L, the Berkeley team has identified a number of candidate launchers. The Boeing Delta III easily meets all SNAP requirements. Figure 2-11 from the Delta III Payload Planners Guide which is reproduced below shows that the Delta III can supply sufficient energy to place a 2850 kg in the initial orbit, well in excess of the current estimated mass of 1550 kg for the SNAP. The excess lift capability will be used to relax the mass constraints on the mission which will greatly reduce payload development risk and cost.

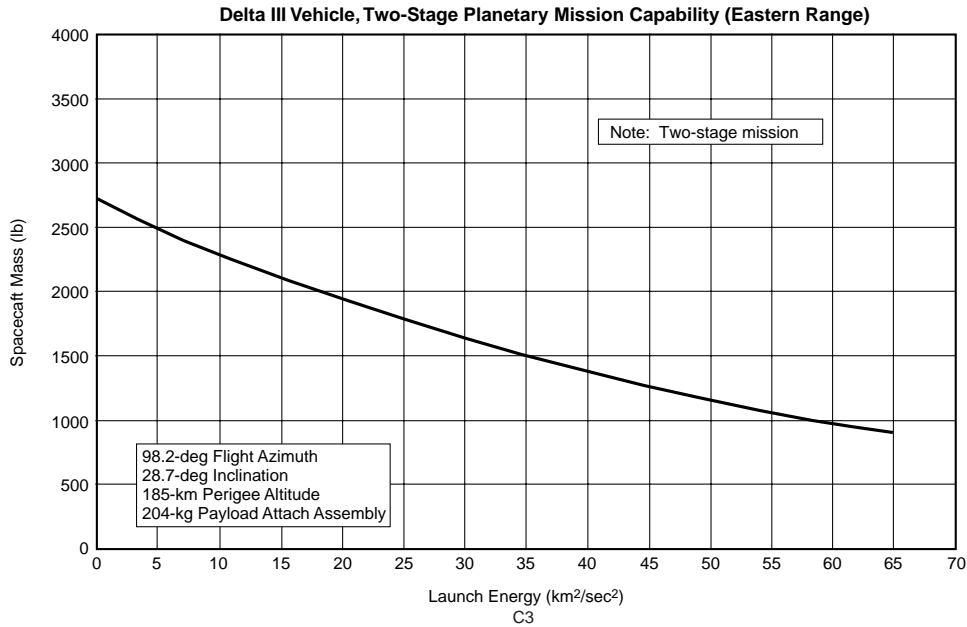


Figure 14.3: Planetary mission capability of the Delta III rocket. A lunar assist orbit requires a $C3 = -2.0 \text{ km}^2/\text{s}^2$ (slightly negative due to the gravity of the moon).

The Delta III will be operated with a single second stage burn to go directly to the lunar intercept orbit. According to Boeing, the orbit injection accuracy for the Delta III is ± 0.03 degrees in both angles, and ± 3 meters/second in velocity. The Propulsion/ASC system on the SNAP spacecraft will be used to perform two mid-course correction maneuvers to achieve the necessary accuracy for the Prometheus swing-by and will be used again on the first perigee pass to supply the 35 meters/second velocity change needed to lower the apogee to prevent interaction with the moon on

subsequent orbits. The Figure 14.3 shows dimensions of the Delta III fairing. In Figure 14.3 the fairing is shown enclosing the observatory and spacecraft where we have used an optics concept from the Ball Aerospace feasibility study. In Figure 14.3 the fairing is shown enclosing the observatory and spacecraft where we have used an off-axis optics concept showing the differences between the various schemes for the optical paths.

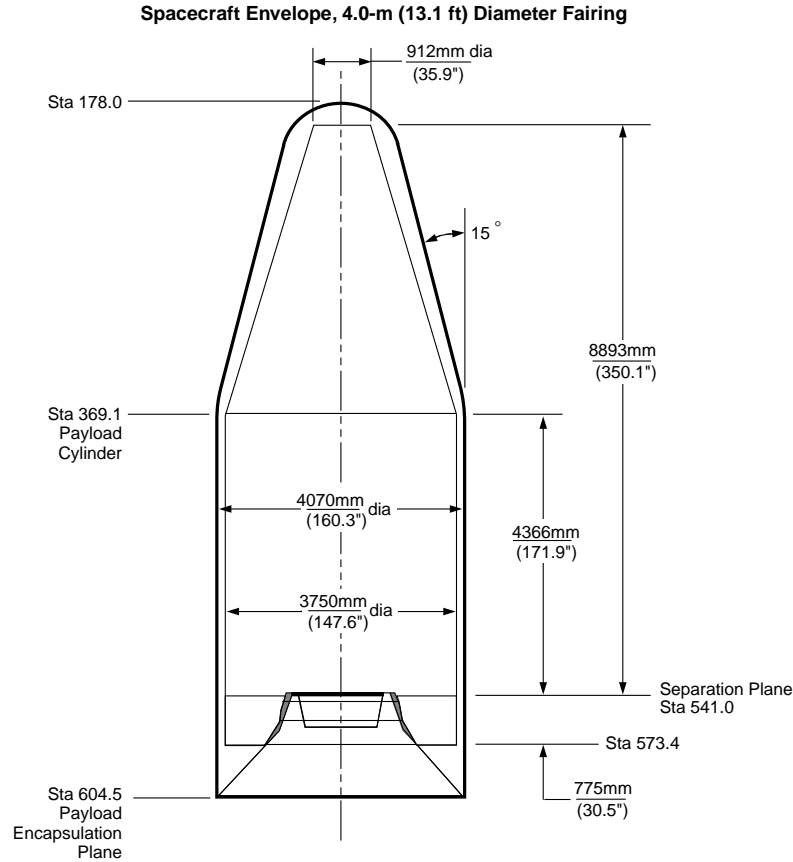


Figure 14.4: The 4.0m diameter composite spacecraft fairing for the Delta III launch vehicle.

14.4 Observatory Integration and Testing

Integration and Test of the SNAP systems is a large and complex task which dictates the need for a carefully developed plan to insure the delivery of a properly functioning observatory with the minimum cost and schedule risk to the program. A detailed I&T plan will be developed during the study phase which utilizes the particular strengths, capabilities, facilities, and experience of the collaboration team, the aerospace partner,

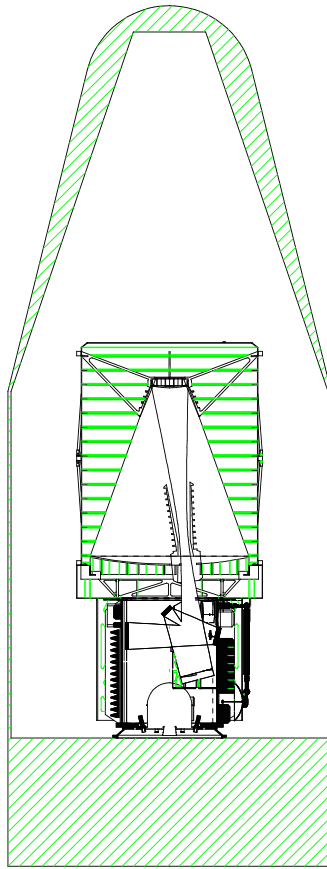


Figure 14.5: The 4.0m diameter composite spacecraft fairing for the Delta III launch vehicle enclosing a 2m primary optics design from the Ball Aerospace feasibility study.

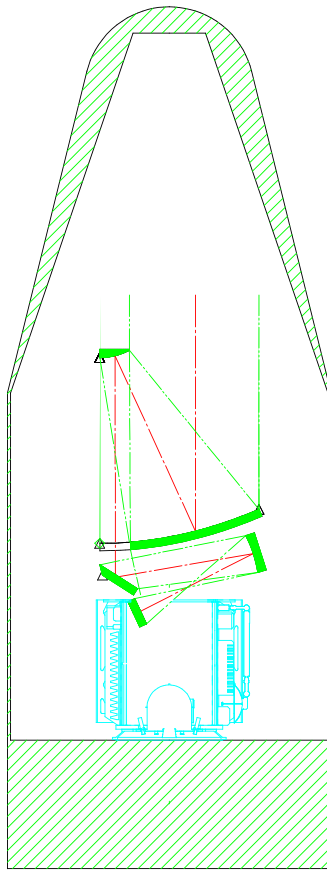


Figure 14.6: The 4.0m diameter composite spacecraft fairing for the Delta III launch vehicle enclosing a 2m primary off-axis optics design.

and the other sub-contractors involved in development of the observatory components. While the details of this plan will be developed only after a period of careful study and will depend on the particular industry partners(s) chosen, the overall outline is expected to be as follows: A detailed mechanical mathematical model will be developed early in the program and used to specify limit loads for the various subsystems. Vibration and thermal vacuum testing will be done at the component level by the unit developers. Testing of the optics elements as well as the completed telescope will be done by the optics sub-contractor. Mechanical and electrical integration of the payload will be done in the Space Sciences Laboratory high bay facility. A mechanical engineering model of the payload assembly will be provided to the spacecraft contractor to do antenna tests, testing of the ACS, and verification of the structure, including vibration and thermal vacuum testing of the spacecraft components. Final mating of the observatory components and the associated electrical testing including end-to-end RF testing will be done in the Space Sciences Laboratory high bay facility. Vibration and thermal vacuum of the observatory will be done by at a Bay Area contractor facility, and a final end-to-end optical test will be done in an appropriate facility.

Chapter 15

Mission Operations

15.1 Mission Operations

SNAP mission operations is based on short periods of autonomous operation of the observatory coincident with rapid ground analysis of the data collected to determine optimum targets for further observation. All missions operations will be controlled and performed from the SNAP Mission Operations Center (MOC) located at the Space Sciences Laboratory and at the Science Operations Center (SOC) located at the Lawrence Berkeley Laboratory. Figure 15.1 shows the close coupling required between the MOC and the SOC in order to identify supernova and redirect the satellite in a timely manner.

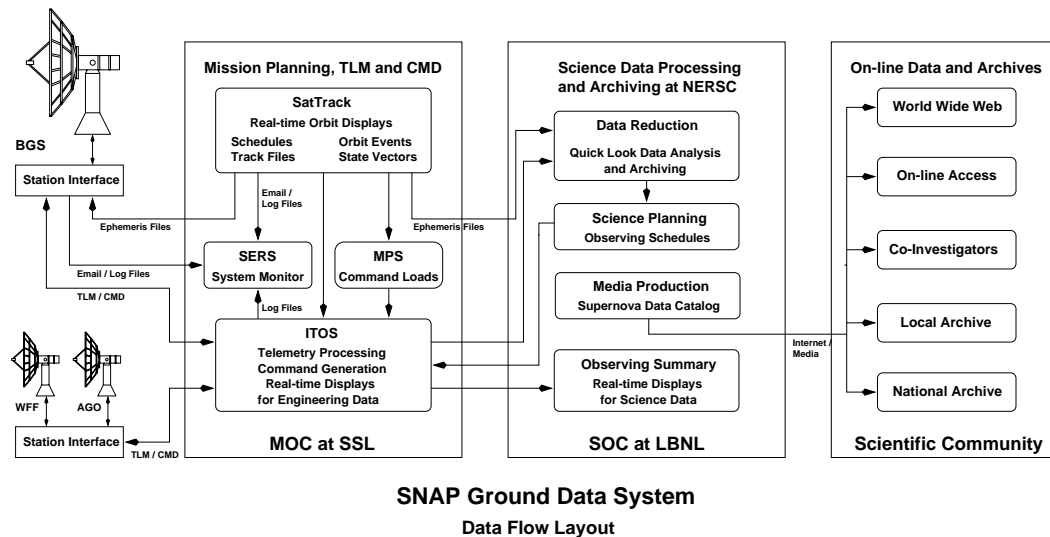


Figure 15.1: Ground system showing the flow of data and the close coupling required between the missions operations center and the science operations centers. The data flows from the satellite to the mission operations center, then to the science operations center where new supernova are identified and commands can then be sent back to the satellite.

Routine operations will be done on a four day period with a command load of approximately 1 megabyte sent up to configure the instruments. Science data will be collected, compressed, and evaluated for figure of merit by on board processing, and the maximum data value transmitted to the ground by autonomous software in the Observatory Control Unit. In parallel with this activity, scientific review and automated ground software will evaluate the transmitted data and build the target lists and instrument configuration loads for the next four day cycle.

15.2 SNAP Operations

Figures 15.2 & 15.3 show the portion of the time that the SNAP spacecraft will be visible from the BGS. Of the approximately 14 hours a day that the spacecraft is visible, it is estimated that about 5 hours a day will be required at a data rate of 50 megabits/sec to download the up to of up to 1 terrabit of science data per day. This would allow all mission scenarios including those with no on-board science data compression to be accommodated. Additional bandwidth can be added if needed by adding time on additional ground stations.

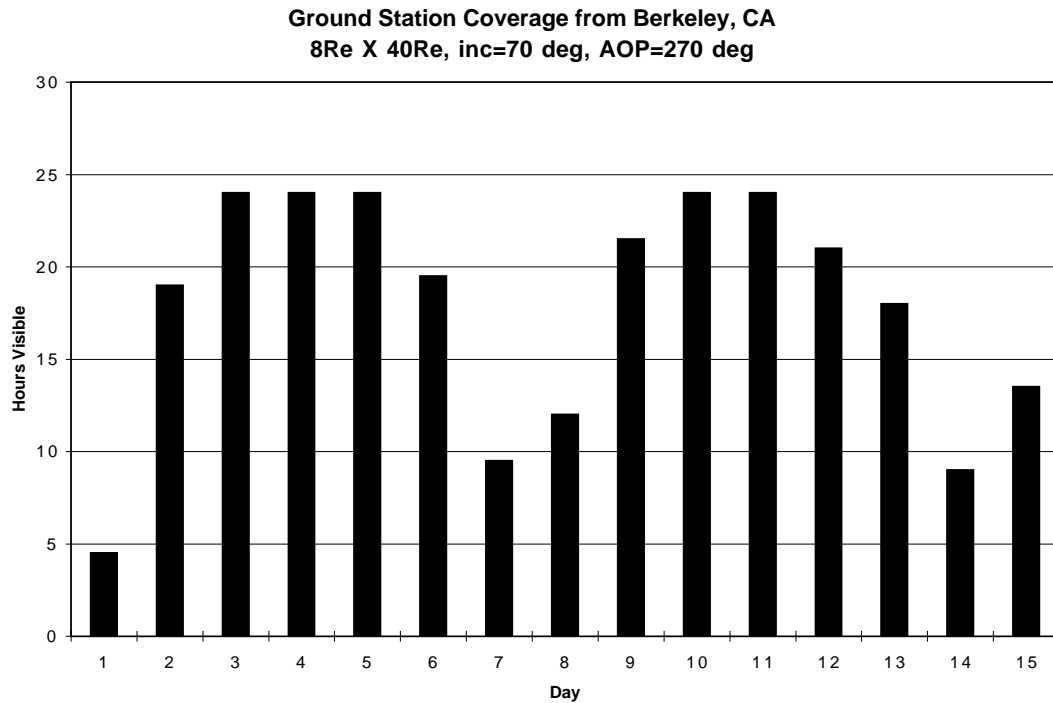


Figure 15.2: Daily coverage from from the SSL ground station for the Prometheus orbit.

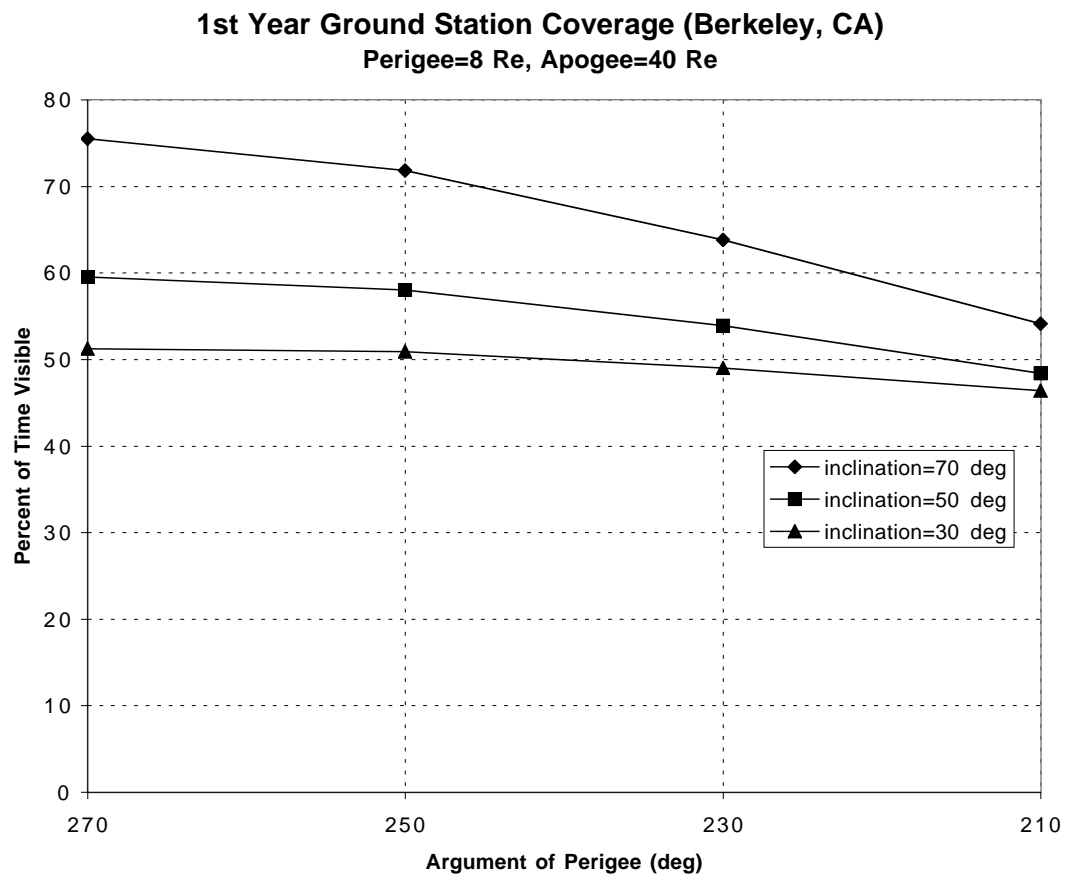


Figure 15.3: Percentage coverage from the SSL ground station as a function of the Prometheus orbit inclination and for different values of the angle of perigee.

15.3 Data Handling & Signal Processing

Data bandwidth from the spacecraft is expected to be limited to 50 Mbit/s or less. This high rate would permit the transmission of lossless compressed images at the rate of one per 160 seconds. Alternatively, identical fields can be processed prior to transmission to reduce the bandwidth requirement and eliminate cosmic-rays from the images. This would reduce the bandwidth requirement on the average four-fold. Additionally, transmitted data from the photometry measurements (but not discovery images) can be limited to pixel sets around star images over a 3σ threshold and around locations already identified as being supernova candidates, analysis of HST images indicate that this will provide a ten-fold reduction in the photometry data. Some of these techniques would require flattened and bias subtracted data to be computed aboard the spacecraft. Given these assumptions, the data transmission requirement for the photometry and discovery images is 0.70 Mbit/s on average.

15.4 NERSC

SNAP data is transmitted from satellite to a receiving station at Space Sciences Laboratory and then transferred to LBNL. High performance computing and mass storage are locally provided by NERSC, the National Energy Research and Scientific Computing Center. Multiple petabytes of raw and processed data may be stored in HPSS, the NERSC tape robotic facility for long term storage. High speed networks link the mass storage to the CPU farms and supercomputers. Raw data can be extracted for processing, computations performed and then results sent back quickly for uplink to the satellite for mission operations. NERSC high performance computing facilities include a T3E, a RS6000, and several clusters of 30 to 100 Linux PCs. These computers are currently being phased out and replaced with new supercomputers and processor farms. Each of these high performance machines has fast networks to a substantial local disk cache and HPSS. For a complete description of these facilities, please visit the NERSC web site: <http://www.nersc.gov/aboutnersc/facilities.html>.

Processing begins by converting the data to a format amenable to analysis and calibrating digital numbers into physically meaningful units. Pattern recognition algorithms reconstruct features in the data such as photon fluxes and spectral-line positions. Data are then reduced with software filters into smaller, signal-enhanced samples based on reconstructed features. If all CPU intensive processing is accomplished on a supercomputer, final analysis can proceed on the average desk-top PC. If analysis is also CPU intensive, software systems exist to accommodate the needs of the experimenters.

The essential supernova discovery algorithms have already been run on the NERSC "Millennium Cluster," and semi-automatically handled ~ 40 Gbytes of data per night for a ground-based low-redshift supernova search. This low-redshift search will be scaled up over the next year and run fully automatically, providing the test-bed for the satellite discovery analysis system, the single most time-critical element of the analysis.

Part IV

Research and Development

Chapter 16

Research and Development Plan

This chapter describes the identified areas of R&D for SNAP and a summary of our plans to address each of these areas. Between now and the proposed official project start, there are several areas where the feasibility of identified technologies and solutions in underdeveloped areas need to be determined. By performing these tasks early, we intend to reduce our exposure to technical risk during the construction phase of the project, where the cost implications are large.

Table 16.1 lists these major R&D areas and the funding needed to address them adequately over the next 3 years. The development of the project plan, or Cost and Schedule Preparation, and Concept/Mission Definition are also part of this up front effort.

16.1 Concept/Mission Definition

This task is in recognition of the fact that the SNAP Satellite concept needs to be developed further. The major activities associated with this task include the up front science and engineering studies, the further refinement of a viable organization and management team, and the traditional early systems engineering tasks: requirements refinement, concept models and trade-offs, defining effective interfaces between systems, and so forth. Performance of this task over time will lead to a better definition of the SNAP Construction Project, and the identification of viable and cost effective technical solutions for each subsystem. The end goal is a fully defined and optimized project technical baseline.

The companion task to this is the development of the project plan. Many of the same people will be involved in pulling together the overall plan, but the individual engineering cost and schedule estimates will be performed by small groups of specialists in the respective technologies for each subsystem as described in the next section.

16.2 Cost & Schedule Preparation

The process of developing detailed cost & schedule estimates will begin with the further refinement of the Work Breakdown Structure (WBS) to a reasonable lowest level (for

SNAP R&D Cost Plan (K\$)

Assumes that official project start occurs FY '03

Task	FY '00	FY '01	FY '02
Ground Supernova Factory	----	500	600
Concept/Mission Defin. Study	600	650	1800
Cost & Schedule Prepar.	250	350	800
CCD Development	----	400	900
Electronics Technology	300	400	900
Instrum. Proof-of-Prin./Early Develop.			
1) Optical Imager	350	500	1200
2) Optics	150	400	1200
3) IR Imager	100	300	700
4) Spectrograph	100	300	900
Total by FY:	1850	3800	9000

Figure 16.1: Research and Development Plan

estimating and tracking purposes). Individual technical people who will be responsible for performing the various tasks will be required to develop a basis of estimation (quotes, previous similar work, engineering estimates, etc.) for cost, schedule, and risk scoring. Each of the individual estimations are reviewed and entered into a relational costing database which performs all of the necessary roll ups through the WBS and allows the examination of the various cost elements (personnel, procurements, and other costs) across the WBS. These rolled up costs and risk assessment scores are used to determine the total costs, contingency and the schedule is then used to determine the application of the appropriate DOE escalation.

The end product of this task is an approved project cost and schedule baseline. It is foreseen that this task will parallel the development of the technical baseline and will thus be accomplished over the next 2 and 1/2 years.

16.3 CCD R &D

The LBNL CCD technology is currently being transferred to a commercial vendor, Mitel Corp, Bromont Canada. Mitel is in the middle to two simultaneous processing runs that will evaluate the process at their foundry. The two runs consist of 1) an adaptation of the LBNL process recipe for the Mitel process equipment that is fairly true to the original recipe, and 2) a version that is highly optimized for the standard Mitel CCD process flow and would produce the devices at higher volume. We would expect Mitel to be able to manufacture CCD's in volume to our specification in approximately twelve to eighteen months. This time is needed to optimize furnace recipes, validate process steps and characterize intermediate devices. Funds are required to continue this development work at Mitel and to support the characterization of the wafers and verify CCD performance. Detailed radiation hardness studies would require use of the LBNL 88" 55 MeV proton cyclotron to make systematic studies of dark current and CTE as a function of proton fluences and to characterize the performance of the CCD's in a radiation environment.

As an alternative, EEV or Sarnoff deep-depletion devices can be considered as an alternative technology although with some diminution of the science return of the experiment. In order to mitigate project risk optimization of an imager based on these devices would be required.

16.4 Electronics R &D

16.4.1 Analog to Digital Conversion.

To date the only 16-bit precision analog-to-digital converters that are being used for space flight operate at 50 kHz (CD5016 currently on FAST), or 330kHz using the LTC1604 part (about to be flown aboard the HESSI satellite). There have recently been a wealth of new 16-bit high speed ADC's released on the market in the past 18 months. We are aware of several programs currently evaluating these new devices. Given that many of these new devices are manufactured with processes that typically

have good radiation tolerance (thin gate-oxide), there is reason to hope that devices can be found that will meet our requirement of radiation tolerance (> 10 krad) and even higher speed operation.

16.4.2 Correlated Double Sampler

The requirement for having an integrated correlated double sampler for CCD readout has already been discussed in a previous chapter. This would be a new radiation-hard circuit developed in the DMILL process. Although this circuit is relatively straightforward as an analog design, it would be a very long lead item that would require extensive development, evaluation, and testing.

16.4.3 Processors

Assuming that the design of the spacecraft telemetry requires that data be stored and reduced on-board, then the radiation tolerance of the signal processing becomes an immediate issue. Radiation tolerant processors would need to be found through an extensive testing program. PowerPC and R6000 chips already exist in radiation hardened forms; however, given the thin gate-oxide processes now used for advanced processors it is very likely that other radiation tolerant processors can be found (e.g. WE32).

16.5 Instrument R &D

Significant R&D will be required to mitigate risk in the optical imager, spectrograph (with an integral field unit), the IR imager, and the observatory optics.

These studies will include sufficient engineering to identify the trade-offs between scientific requirements and practical reality. In the case of the optical and IR imagers these studies will include design of the "sensor sub-assembly" (sensor chip bonded to a substrate with electrical connectivity), followed by simple implementations and testing sufficient to identify critical processes. Followed by the development of a small scale "proof-of-principle" array. In the case of the spectrograph, there are a number of existing implementations (described in the early section on Spectroscopy) which will require evaluation and selection as a best fit to the requirements to the optical design for the observatory.

Finally, a key development will be the selection of a strategy and design for the observatory optics. There are several potential candidates for the choice of optical system and it is expected that several candidates will be fully developed to a level of detail that will permit study of both performance and to permit detailed cost analysis.

16.6 Ground Based Studies of Supernova

During the R&D phase the study of supernova from ground based telescopes will continue. This period will be used effectively to study observing strategies, validate instrument concepts such as spectrographic wavelength coverage and resolution, and

further refine concepts that will enhance fully-automated supernova detection and follow-up.

These studies are not just extensions of the current scientific studies, but will be aimed at obtaining specific engineering numbers. Areas which would require further investigation for example are the required UV and near-IR spectroscopic resolution. There is additional interest in obtaining a reference set of very nearby supernovae in order to understand the very early development of the light curve.

16.7 Optics Design

During the concept design study we expect to work closely with optics engineers, optical element fabricators, and spacecraft manufacturers to ascertain the confidence with which the optical system performance can be established. This is a complex subject because the factors interact to a considerable extent. For example the autocollimation testing for an axisymmetric optic is simpler than for an off axis system, yet the glare and stray light testing is simpler for an off axis system. For these reasons we shall trade off the performance, cost, schedule, and science harvest that a variety of alternative optical trains offer the SNAP mission before adopting a baseline optics layout. Below we outline the main concerns regarding telescope design.

Principal Issues:

The main issues that we need to address during the study, which will affect the final design of the SNAP telescope, can be divided into two principal groups. The first deals with the mechanical structure of the telescope itself, namely

- a) Amount of physical space within the payload vehicle which is allocated for the telescope,
- b) Total allowed payload for the selected launch vehicle, and hence, weight trade-offs between the telescope structure and other observatory components,
- c) Materials for the optics (mainly the mirrors): composites vs. glass vs. beryllium for example.
- d) Telescope structure supports: depending on the design, we will have to consider mass, strength, and thermal properties of probable structural materials. These include Beryllium, Invar and Carbon composites. Beryllium is a lightweight metal, used for lightweight metal structures, optical platforms, mirror substrates and space telescopes among other uses. Invar is a nickel-iron alloy which has a rate of thermal expansion approximately one-tenth that of carbon steel at temperatures up to 204C. It is used for applications where dimensional changes due to temperature variation must be minimized. Carbon composites (C-C, C-SiC) are lightweight, have high specific strength (strength/weight) and are thermally stable. They are used in mirrors, trusses and other structures.
- e) Accessibility of the various instruments.

The second group of issues revolves specifically around the optical design, and must address the tradeoffs between the specified requirements for spatial resolution, field of view, wavelength range, imaging and spectroscopy instruments and the reality of physical materials. This includes, but is by no means limited to the following,

a) Investigating image quality versus the need to have an intermediate field stop or “beam waist” in the optical path. Some of the 3-mirror designs described previously in this document, allow a beam waist, by using a Gregorian secondary mirror (cf. 8.3). While this may well permit savings in the filter system design by allowing smaller filters, it lengthens the optical path between primary and secondary and may limit the speed or aperture that can be accommodated within the confines of a Delta rocket launch shroud.

b) Carrying out detailed tests of the optical design viz a viz misalignment, aberrations, and tolerance limits. General analysis of the effect of mirror misalignment across the imaging field in two-mirror systems have been discussed in the literature (Shack & Thompson, 1980; Wetherall & Rimmer, 1972; Schroeder, 1987) and thus is fairly well understood.

c) Comparing the advantages and disadvantages of off-axis and axisymmetric designs. Naturally this analysis must include the manufacturing costs of aspheric optics, as well as the cost-benefits of obscured and clear apertures in terms of scattered light, vignetting, thermal loads, collimation and the like. It also includes investigating efficient “packaging” schemes. For example, the thermal design is simplified when the optical elements can be divided into distinct optical compartments with well-defined beam access between these, although the design of a unified optical bench for such a layout may become more complex.

In fact, the constraints on physical dimensions, payload weight, manufacturability, risk, and cost will be the key factors in the ensuing optical design studies.

Part V

Education/Public Outreach

Chapter 17

Education/Public Outreach

17.1 Overview

This E/PO project is designed to investigate why supernovae are useful probes for cosmology research, and how scientists use models to understand observed phenomena. We will use the internet to bring the excitement and immediacy of cutting-edge scientific inquiry into the hands of students.

17.2 Program Goals and Objectives

The web provides an effective means of disseminating up-to-the minute scientific results. It also provides easy access to engaging, interactive learning programs through the use of e.g. JAVA applets. Building upon the experience developed by the SCP in using the internet in myriad ways to carry out research, we can share the excitement of the ongoing work on the accelerating universe.

17.3 Proposed Education Product

The result of this E/PO effort is the creation of web-based activity modules with the necessary background scientific information. The target audience is secondary school students in 10th to 12th grade, and 1st and 2nd year college students. The activities will be developed in collaboration with teachers and scientists at the Lawrence Berkeley National Laboratory.

17.4 Activity Modules

This project's product is a set of Java activity modules focused on supernovae. They will be freely available to the public via the internet, and may also be used as classroom lessons. The activities are intended to introduce the two common types of supernovae, Type Ia and Type II, and understand why astronomers find them interesting.

Each activity provides the appropriate science background and is designed to engage learners. Links to complementary web sites (e.g. SEGWAY) that explore related topics

in more depth will be included. The science content and the activities will be designed and field-tested in collaboration with science teachers in the San Francisco Bay area.

17.5 What are Supernovae?

Supernovae (SNe) are produced when a star that is at the end of its evolution explodes. The Type II (core collapse) supernova occurs when a massive star collapses after producing iron in its core by nucleosynthesis. Type Ia supernovae presumably occur in binary systems composed of a white dwarf and a red giant. The white dwarf accretes material from the red giant until its total mass reaches 1.2 solar masses, at which point a thermonuclear runaway process leads to an explosion. Observationally, Type Ia and Type II SNe are distinguished by the shape of their light curves and by their spectral features. Additionally, supernova ages (time from the peak luminosity) can be determined by the evolution of spectral features and the change in brightness. Spectra are also used to measure the redshift to each supernova. Furthermore, Type Ia have an additional useful property— they are “calibratable” standard candles. It is these characteristics that the SCP exploits in its use of SNe as tools in determining cosmological parameters.

17.6 Activity 1: A Simulation of SNe explosions

This is intended to qualitatively illustrate the basic concepts of supernovae explosions. For Type II SNe this would be a “cross-section” animation of the process of nucleosynthesis in an 8+ solar mass star, followed by the explosion. Simultaneously, we would show the corresponding light curve points. We would create a similar animation for a Type Ia SNe.

17.7 Activity 2: Making a Hubble Diagram

Given photometric data and observation dates for a set of SNe, learners place each SN’s light curve points on a graph. Then, they can fit a template light curve to their SNe data. Once this step is done, learners determine the peak (apparent) magnitude of the SNe. Corresponding spectra are used to measure the redshift. Armed with this information, learners now make their own Hubble diagram, complete with an overlay of cosmologies with different values for the cosmological parameters. Now learners can see how well the data fit the various models. Corresponding spectra can also be consulted to determine the SN type and, say, age at first discovery.

17.8 Activity 3: Supernova Models

Learners use a user-friendly, graphical interface (GUI) which submits “jobs” to the PHOENIX code. The interface allows learners to choose physical parameters and to make their own SNe models. The output from the modeling code are spectra, which

can then be compared to the observed data as in Activity 2. The goals of this activity are to understand why scientists build and use physical models and how models are used to interpret observed phenomena. In this particular case, the focus is on the physics of supernovae.

17.9 Alignment with E/PO Guidelines

The developed web materials will

- be designed by scientists and master teachers at LBNL;
- be field tested in Bay Area high schools, where a significant proportion of students come from underrepresented populations;
- be translated into standard Spanish (especially important in California);
- be aligned with the NRC National Science Education Standards for content and pedagogy
- be evaluated according to standard practices, with particular attention paid to front-end and formative evaluations during the design and field testing phases. Final report will include the summative evaluation of the project;
- have links to the SEGWAY project;
- work with the Bay Area Project Astro Coalition as a teacher resource.

17.10 Experience of the E/PO team

The Lawrence Berkeley National Laboratory has a long history of providing research experiences to undergraduates through academic and summer research programs. It also provides high school students with the same kinds of experiences through week-long and summer internship programs. The Supernova Cosmology Group regularly provides its data and expertise to the Hands-On Universe high school asteroid search project. Due to the international nature of the SCP collaboration, the SCP has experience in JAVA programming for efficient data collection and communication.

Dr. Deustua will lead the EP/O project. The materials will be designed and developed during the first two years using SCP data. Field testing will begin during the second year. Material revision and testing will continue through the out years. Dissemination will begin in the third year.

Part VI

Project Management

Chapter 18

Management of the Project

18.1 Organization and Management Plan

This section describes the SNAP project organization and management plan. The approach that SNAP is implementing is an adaptation of the successful STAR detector project directed by LBNL and the HESSI project directed by SSL. The desired approach and configuration of projects as described in DOE Order 4700.1 and the Project Management Institute (PMI) Standards Committee A Guide to the Project Management Body of Knowledge (BMBOK) form the organization and execution background for the SNAP project. The goal is an efficient, focused, flexibly staffed, project that will allow scientists to have overall technical control while utilizing the talents of technical managers and their supporting organizations to ensure proper scope execution within cost and schedule.

18.2 Organization

18.2.1 Organization Chart

The SNAP Project Organization Structure is shown in Figure 18.2.4. This configuration covers the research and development activities, the construction activities and the operations portion of the project. Clearly, the organization should be viewed in a dynamic context where major activities and emphasis will shift during the course of the project.

18.2.2 Element Function and Responsibility

The functions and responsibilities of each of the elements shown in the Organization Chart are given in the following subsections.

18.2.3 DOE and NSF Organization

The SNAP project is seen as a joint DOE/HEP and the NSF/MPS project. It is anticipated that these organizations will work together with the SNAP Project Office

to organize a Joint Oversight Group that will be responsible for establishing external monitoring, reviews and overall programmatic guidance for the project.

The Joint Oversight Group will include representatives of each of the funding agencies or of the collaborating institutions if duly empowered. The role of the JOG includes approval of MOUs and modifications to the structures and tasks proposed to the project as a whole. It also includes monitoring common funds and general financial and manpower support, and endorsement of the annual budgets for construction, maintenance and operation of the detector. The Principal Investigator reports regularly to the JOG on administrative, financial and technical matters.

The Project Directorate

The body responsible for scientific, technical, scope, schedule and cost execution of the project is the Project Directorate. The Project Directorate consists of the Principal Investigator / Project Scientist, the Co-Principal Investigator / Project Director, and the Project Manager. To assist the Project Directorate in this regard it has the services of the Project Office, the Systems Engineering Office, and the Safety, Quality, and Reliability Office. Serving in both advisory and control capacities to the Project Directorate are the Collaboration Executive Board, the Project Technical Committee, and the Project Advisory Council.

Principal Investigator / Project Scientist

The Principal Investigator / Project Scientist has principal responsibility for the project with regard to its scientific mission and execution. He is directly responsible to ensure that as specifications and requirements are developed and trades conducted that the scientific goals are not compromised. The Project Scientist serves as the Principal Investigator (PI). He is the spokesperson for the project and oversees the R&D, design, construction and deployment of the satellite and subsequent operations efforts. He is directly responsible to the DOE, NSF and the Joint Oversight Group.

The PI will be an ex-officio member of the Collaboration Board. The PI will be in frequent contact with the other members of the Board and obtain from the Board advice on all major collaboration issues. On financial matters, the PI authority will be consistent with the requirements of the funding agencies represented in the Joint Oversight Group. The PI is responsible for keeping the Joint Oversight Group informed about the status of the project.

The Project Director / Co-Principal Investigator

The Project Director / Co-Principal Investigator has responsibility for the direction of all SNAP activities. He has full responsibility and authority for all phases of the project. The Project Director coordinates the R&D, design, construction and deployment of the satellite and subsequent operations efforts through systems managers. The Project Director is the Co-Principal Investigator for the project. He assumes the role of the PI whenever the PI is unavailable. He is also an ex-officio member of the Collaboration Executive Board.

The Project Manager

The SNAP Project Manager (PM) is responsible to the PI for the execution of the project within the schedule, cost and resource constraints available. The PM with support from the project office (PO), the Systems Engineering Office (SEO) and the Safety, Quality and Reliability Office (SQRO) will establish tasks, interfaces, requirements, work statements, Memoranda of Understanding (MOU), deliverables, schedules, and changes to those elements.

The PM is responsible for day-to-day project management which includes: requirements tracking; project status; risk management; documentation; cost and schedule tracking, configuration management; major make or buy decisions; subcontract management and procurement; MOU facilitator; coordination with team members; and focal point of communication for project construction.

The PM will be responsible for establishing a baseline project plan. This plan will establish the schedule, cost phasing, and resource needs to carry out the SNAP project consistent with experiment science requirements. This proposal is the first step in defining the project plan. The complete project plan require the approval of the Project Scientist, Project Director, the Joint Oversight Group, DOE/HEP and NSF/MPS Co-PI, before being accepted as the baseline.

Collaboration Executive Board

The SNAP Collaboration Executive Board (CEB) is comprised of a lead scientist from each of the collaborating research institutions. The Collaboration Board along with the Project Scientist and Director establishes scientific goals and objectives of the SNAP project. It advises the Principal Investigator on all scientific, financial and organizational matters of the project. It will develop a policy for membership and for publication. The Board will decide on controversial issues within the collaboration by consensus or by voting.

An elected member of the Board will chair the CEB. Elections for Chair will be held once each year. The Project Scientist and the Project Director will be ex-officio members of the Board. Official Board meetings will be held on an as needed basis and no less frequently than twice a year. Teleconferencing will be used to resolve urgent issues and minimize travel expenses.

The CEB will appoint (with concurrence from the Joint Oversight Group) a Project Advisory Council to monitor and review the execution of the SNAP project. The Board is responsible for organizing briefings to the EAC.

Project Advisory Council

The Project Advisory Council (PAC) will be comprised of several outstanding individuals from the US, Europe, and elsewhere with expertise in all facets of the SNAP project. PAC members will be appointed by vote of the CEB with input and approval of the JOG to minimum two-year terms. Expertise will be sought in the relevant areas of science, engineering, space flight, operations, education and outreach, and management. Each of these areas will be represented by at least one individual.

The PAC will meet once per year with the SNAP collaboration to review performance and progress of the SNAP project. These reviews will be held in the form of short briefings given by members of the SNAP science, engineering and management teams. The CEB is responsible for organizing briefings to the PAC. The PAC will provide the Collaboration CEB and the Program Directorate with a summary report on their recommendations, suggested plan of action, and observations shortly after the conclusion of each PAC meeting.

Project Technical Committee

The SNAP Project Technical Committee (PTC) is responsible for working with and advising the Project Directorate with respect to the execution of the project as a whole. Its membership consists of the leads from the Systems Engineering Office, the Project Management Office, the Safety, Quality, and Reliability Office, the individual systems managers and additional members as determined appropriate by the Project Directorate.

The PTC shall meet on a regular basis to discuss technical, cost and schedule issues and will form the basis of the Change Control Board (CCB). Its main goal is to help ensure that all systems of the project are being adequately integrated and executed toward the scientific and technical goals of the project within the constraints of budget and schedule.

Safety, Reliability and Quality Office

The Safety, Reliability, and Quality Office (SRQ) has primary responsibility to the Project Directorate in ensuring that all aspects of the project are conducted to the appropriate levels of safety, reliability, and quality.

The SRQ will aid the Project Directorate in the definition of the system safety implementation plan (SSIP) by developing and maintaining a detailed system description and by supporting safety working group meetings. SRQ will document in a safety data package all identified hazards to instrumentation and personnel, hazardous procedures, and the methods used to control them. The instrument design will incorporate safety features such as encapsulation of high voltages and cryogenic surfaces (as required). All work will be done in accordance with the requirements of DOE and Laboratory, Health and Safety standards, as well as applicable NASA and flight safety standards.

Based on the project quality guidelines most of the instrument and mission level systems will undergo extensive failure modes and effects analysis (FMEA). The SRQ will perform these FMEA in concert with the spacecraft and systems engineers to determine vulnerability.

The SRQ will work with the systems managers and engineers to ensure that as the design is developed that cost-effective, easily serviceable units are developed for use during assembly, integration and testing. Any part that is replaced as the result of an alert of failure during testing, that unit will undergo a new round of testing before integration.

The SRQ will establish the requirements for needed for quality and reliability within

the project, and ensure, under the Project Directorate, that all policies, procedures and design approaches are consistent with mission goals and agency requirements.

Systems Engineering Office

The Systems Engineering Office (SEO) is charged with developing and maintaining the system hardware and software requirements and specifications. The SEO reports to the Project Manager within the SNAP Project Directorate. The SEO has primary responsibility for all system level issues. Early in the project the SEO will be primarily concerned with top level requirements flow-down so that design and planning decisions are made with overall systems considerations in mind. The other key role that the SEO has is in the development of interfaces between the various systems. As such, the SEO will be working continuously with system managers to ensure that interfaces are properly defined and that technical issues affecting more than one system are resolved efficiently and effectively.

In the definition phase the SEO will also work with the spacecraft designers to identify requirements on the spacecraft and on the instrument. Both instrument-level and spacecraft-level requirement documents will require Project Directorate approval. Requirements, specifications, and Interface Control Documents (ICD) will be entered into configuration management by the end of the definition and R&D phase.

The payload system and payload-to-spacecraft interface will be managed by the SEO. The SEO will develop and maintain a set of requirements on the flight segment and from this will develop an approach to meeting those requirements.

Systems management will be performed through regular reviews of the design activity. All drawing will receive SEO approval prior to initial release to manufacturing and procurement and all Engineering Change Orders (ECOs) will require SEO sign-off. ECOs that do not affect form, fit, or function may be given a preliminary release by the subsystem manager with a courtesy copy to the SEO. Other ECOs will require SEO approval prior to release. To expedite operation of this system with design groups from all parts of the project, ECO review meetings will be held via teleconference or video-conference, with exchange of drawings, ECO forms, and signatures done electronically.

Project Office

The project office is responsible for monitoring the technical scope, cost and schedule performance of all portions of the SNAP project and providing timely reports to JOG. The Project Office will maintain the SNAP master resource-loaded schedule with a software package (most likely Primavera) capable of determining and monitoring the progress of the project and reporting the status of the project to the JOG and sponsoring entities in a complete manner.

18.2.4 SNAP Systems and Subsystems Management

As can be seen in the organization chart shown in Figure 18.2.4 the SNAP project is divided into its principal systems and subsystems beneath the Project Directorate. Each

```

graph TD
    FA[Funding Agencies] --> JOG[Joint Oversight Group]
    JOG --> SPM[S. Perlmutter Proj Scientist/PI  
M. Levi Proj Director/Co-PI  
XXXX Proj Manager]
    SPM --> CEB[Collab. Exec. Board]
    SPM --> PTC[Proj. Tech Committee]
    SPM --> PO[Project Office]
    SPM --> QRS[Quality, Reliability & Safety]
    SPM --> SEO[System's Engr'g Office]
    SPM --> PAC[Proj. Advisory Council]
    SPM --> ISM[Instrumentation Sys Mgr]
    SPM --> TSM[Telescope Sys Mgr]
    SPM --> OSM[Ops & Ops Center Mgr]
    SPM --> STM[Science Team Mgr.]
    SPM --> SM[Spacecraft Manager]
    SPM --> MIT[Mission Integration & Test]
    
    ISM --> IO[Opt. Imager Subsys]
    ISM --> IIR[IR Imager Subsys]
    ISM --> ISS[Spectrograph Subsys]
    ISM --> ES[Electronics Subsys]
    ISM --> DHS[Data Handling Subsys]
    
    TSM --> OS[Optics Subsystem]
    TSM --> SS[Structure Subsystem]
    TSM --> OBS[Optical Bench Subsys]
    TSM --> IT[Integr. & Test]
    
    OSM --> OCD[Ops Center Devel.]
    OSM --> GAD[Ground Antenna Devel.]
    OSM --> PDP[Prep. for Data Handling]
    OSM --> MOP[Mission Ops Planning]
    
    STM --> SRD[Science Reqmt's Devel.]
    STM --> DA[Data Analysis]
    STM --> EPO[Educ. & Public Outreach]
    STM --> SWG[Science Working Groups]
    
    SM --> IT2[Instrum/Telesc. I&T]
    SM --> SPS[Sci Paylod/Spacecr. I&T]
    SM --> SLV[Satellite/Launch Veh. I&T]
    
    MIT --> IT2
    MIT --> SPS
    MIT --> SLV
  
```

Figure 18.1: SNAP Project Organization Chart

As previously stated the Project Technical Board is comprised of system managers, representatives from the SEO, and SQR, and the Project Directorate. These will convene on a weekly basis in person, or by teleconference or video-conference (as required) to discuss project progress. The Project Director chairs the technical board and will run weekly meetings and set the agenda.

18.2.5 Management Processes

The Project Director (PD) is responsible to the Principal Investigator, the International Oversight Group, the DOE, and the NSF for day-to-day operations including performance, schedule, and budget tracking. The PD, with the support of the SNAP project office, will assure that clear channels exist for official communication including establishment of tasks, interfaces, requirements, work statements, deliverables, schedules, and changes to those elements. Working level communication, on the other hand, is encouraged among all participants to assure that technical information is freely and efficiently disseminated and thoroughly discussed. The management approach is designed to communicate clearly to all team members the tasks to be done, the require-

ments for those tasks, and the schedule and resources available, and to track progress so that problems can be identified and resolved at the earliest possible time.

A Work Breakdown Structure (WBS) is the key planning and control document. The WBS is designed to implement the project as defined in project documents. The present WBS is shown in the Appendix to Level 3. This includes the top-level requirements document from which the lower-level requirements documents are derived by the flow-down process, and the contract requirements, which include the budget and schedule. The detailed work of the SNAP project will be planned in the form of a resource-loaded schedule using the WBS as the basis of the individual tasks. The order of tasks, the relationships between the tasks, and the schedule boundary conditions will be incorporated into the schedule. The groups that will actually perform the tasks provide estimates of time and other resources. This increases their commitment to meeting the schedule and budget and serves as a basis for internal monitoring.

Tracking progress will be accomplished primarily by review of the schedule, particularly the near-term milestones. Any task that is falling behind schedule, is consuming more resources than planned, or is encountering unforeseen difficulties becomes the focus of corrective action. The process of evaluating progress is constant: estimating what remains to be done, iterating the schedule, budget, and requirements to maintain an optimum balance, and communicating the results to all concerned. Project management software will be used to assimilate, analyze, display, and maintain the key schedule and resource information. Primavera and MSPProject have been successfully used on recent projects within LBNL General Sciences Project Office (GSPO) to maintain schedules, analyze alternative resource-loaded plans, and maintain cost-to-complete estimates. It is anticipated a combined use of Primavera and Excel will provide the basis for the resource loaded schedule and monitoring. The Project Technical Committee (PTC) will convene weekly to discuss current project, plans and issues. The PTC also forms the basis of the Change Control Board.

Financial and schedule control will be exercised via review of monthly earned-value and financial reports detailing all SNAP. The amount of labor charged will be regulated by the PM, before the monthly reports are compiled, by monitoring the actual effort applied as it occurs and comparing it to the plan. In addition, the PM will review a detailed breakdown of all expenses contained in the monthly financial report. Financial control of consultants will be accomplished by means of the subcontract and continuous review of technical and financial progress.

Design, development, technical, and engineering progress will be measured by the schedule milestones, design reviews, testing, informal reviews, and day-to-day communication. System managers report to the PM and keep him informed of progress, problems and potential solutions, operational needs, and weekly status. The single point of contact model is used for aspects of subcontract activity including all official communications. However, day-to-day working-level direct communication on technical matters among the parties directly involved is encouraged.

Change Orders

Changes to baseline technical, schedule, and cost specifications are inevitable. These changes will follow a change control process over-seen by the PM. A technical board composed of all system managers, the SEO, the SQR, and others designated by the PM will function as the Change Control Board (CCB). The PD chairs the technical board and the CCB. The PI is a member of the technical board and the CCB to ensure that the scientific requirements of the project are met.

Proposed changes will require different levels of approval based on severity and impact on the project. At the lowest level, involving a relatively small redistribution of funds within a given subsystem, only approval of the subsystem manager is required. At a much higher level, involving a major change in scope or scientific goals, the change must be brought to the Change Control Board (CCB) and approved by the Collaboration Board and the PI. The PD must be informed of all changes at any level. System managers will bring changes in cost and/or schedule to the CCB. Changes in scientific scope will first be brought to the CCB and in turn taken to the Collaboration Board by the PI for approval.

Requirements and Specifications Development and Control

A top-level project scientific requirements document will be developed during the initial phase of the program by the science team and the Collaboration Executive Board. Systems requirements and definition is the responsibility of the SEO. The SEO will lead the definition of lower level system and subsystem requirements using a documented flow down process. All hardware and software elements of the SNAP system will be defined in these specifications. At the appropriate point in the program, the specifications will be placed under configuration control, after which changes are made by means of formally controlled Engineering Change Orders (ECO) which assure proper review by all affected project elements. Updated documentation will be made available to all affected parties and a straightforward system of verification of the latest current version of any project document is continuously maintained and is readily accessible by all. The SRQ has responsibility for planning and oversight of the configuration control process in order to ensure efficient and successful implementation.

Manage and Conduct Systems Engineering

The SNAP SEO has primary responsibility for all systems level issues. It is critical in this process to view all elements of the SNAP project as a single entity and properly allocate requirements and design approaches across the entire system. Early in the design process the SEO will be primarily concerned about top level requirements flow-down and precisely how the system will operate once in operation so that design decisions are made with system considerations in mind. The other key role that the SEO has is in the development of interfaces between subsystems. As such, the SEO will be working continuously with system and subsystem managers to ensure that interfaces are properly defined and that technical issues affecting more than one system are resolved efficiently and effectively.

Manage, Control, and Allocate Contingency

Contingency requirements are developed as part of the costing and estimating cycle. These form part of the initial risk assessment. Development of an overall contingency consistent with DOE and NSF guidelines is part of this estimation process and within the total, contingency is reserved for the various systems and subsystems based on their perceived risk. During the preliminary phase of the project, a contingency depletion schedule will be established. Schedule and budget depletion will have established time-phased benchmarks. The amount of reserve needed depends on the level of maturity and heritage of the particular item. An existing subsystem requires less reserve than one in the early stages of development. As the subsystem develops, the reserves may be expended to resolve problems, meet unanticipated needs, or simply to accommodate the as-built actual parameter.

Contingency is controlled in the central project office and any call by a system or subsystem on contingency must be made through the CCB. This permits the PD and PM the ability to manage the progress of the project and efficient use of resources and funds by the effective management of contingency. The management of resources by the PM will balance the reserve available against its use as appropriate to preserve performance, budget, and schedule.

Manage Collaboration Agreements

Memoranda of Understanding (MOU) will be written between the members of the SNAP collaboration. These agreements will cover the cost, schedule, and specifications of elements to be provided by respective collaborators. The MOUs specify inter-institutional conduct within the collaboration as well as the scope of efforts, the resources, and the schedule for the respective collaborators. The MOUs will be reviewed along with progress each year as part of the yearly financial planning cycle.

The members of the SNAP collaboration will subcontract to LBNL and SSL. The subcontract will be established by means of a proposal that contains a statement of work, technical requirements, specification where appropriate, schedule, and cost of elements to be provided. A subcontract manager from the SNAP project office will monitor progress and be the point of contact for contractual matters between the project office and collaboration institutions. The subcontract manager reports to the PD.

Progress Reports

Monthly financial and project (earned-value) reports will be submitted to the DOE, NSF and the Joint Oversight Group. Technical progress reports will be submitted to summarize progress, concerns, problems, changes, and plans for the next period.

Risk Management

The basic approach to risk management is to minimize risk by using proven designs, existing hardware, and conventional fabrication methods to the maximum extent pos-

sible. However, it is not possible that in a project the size and scope of SNAP that all elements of it can be of a fully developed technology and maturity. It is also to be anticipated that unexpected events or developments during the various phases of the project will influence the resources, cost and schedule of the final configuration. It is in recognition of the inherent uncertainty within the general scope of project execution and more specifically R&D projects that the GSPO has adopted an aggressive, global and proven approach to the management of risk on projects within General Sciences. SNAP being part of General Sciences will employ this same approach.

The approach that the GSPO follows is in recognition that risk may impact any of all of the dependent project variables (scope, schedule, and cost). Typically, there are two general types of risks, insurable (those that can only result in a loss) and leveraged (those with a positive outcome will benefit the project). Developing contingencies for all the dependent project variables provides for the mitigation of risk.

The first step in the management of risk is its assessment. This is done initially in conjunction with the estimation and determination of the work to be done. Each element used in costing is assessed and scored as to its stage of development and potential impact on the project. Specifically, each element is rated for design/approach maturity, complexity, dependency, technical development, cost uncertainty, and potential schedule variance.

The data thus obtained are then scored following procedures adapted from the PMI and STAR approaches. Calculations are then done on the assessed risk score to determine an appropriate level of cost and schedule contingency. In parallel, possible scope contingencies are identified with decision points established where technical trade-off choices must be made.

Once the project is underway, issues identified with risk to the project are monitored and contingency is allocated where necessary. In addition, reliability assessments and trade-off studies directed by the SRQ also seek to minimize incidental as well as project risk.

18.2.6 Schedule

Figure 18.2.6 shows the schedule of the major activities and milestones. A more detailed schedule will be developed in the next six months. This schedule serves as a basis for the developing of refined cost estimates, resource requirements and task phasing for the project.

18.2.7 Cost

At present only rough order of magnitude (ROM) top-down estimates exist for the overall costs of the SNAP project. This ROM estimate was obtained by scaling from an initial feasibility Phase A Study for the Kepler spacecraft with the assistance of Ball Aerospace. The ROM presented here includes the telescope and instruments package. It does not include the launch, spacecraft bus, or ground support. We are presently soliciting a letter of intent (LOI) from suppliers of the spacecraft bus and ground support and until the LOI process is completed it is premature to present numbers

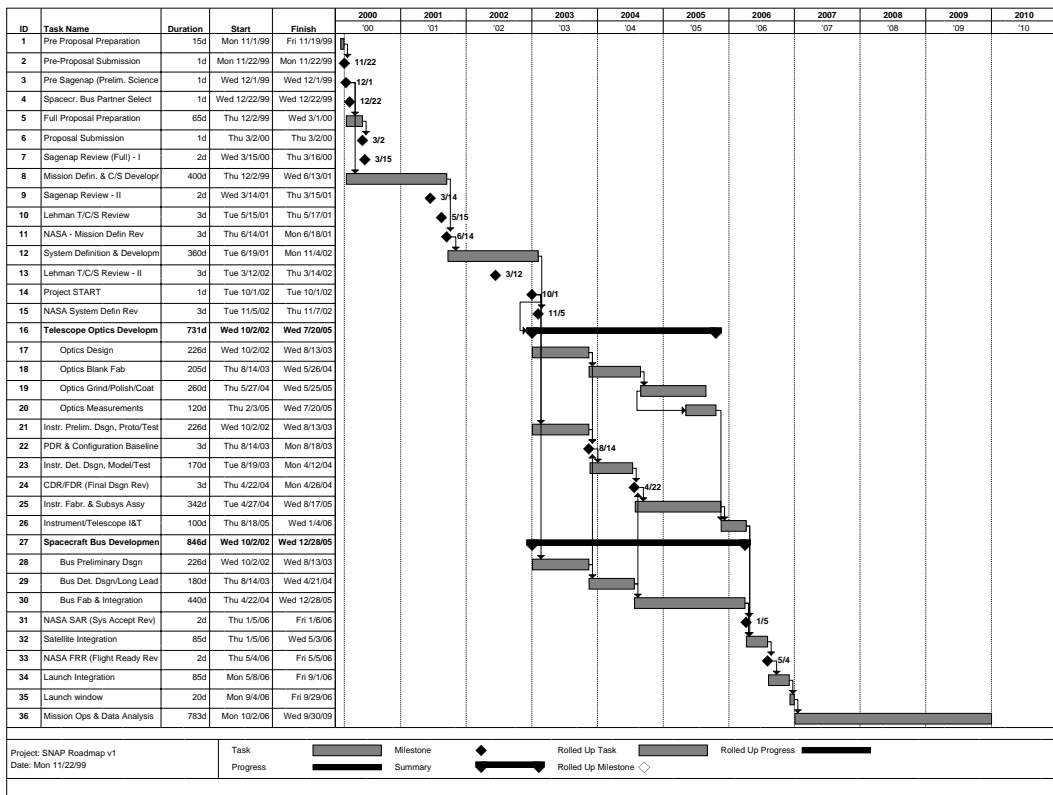


Figure 18.2: SNAP Project Schedule

associated with those elements. Likewise, the launch and launch vehicle are provided by NASA and so are not included in these numbers. These are shown in Table 18.1. Table 18.2 shows the initial estimated required funding profile to achieve completion and operation of SNAP in an effective and efficient timescale.

Detailed estimation of the cost will be by detailing the WBS to the lowest level achievable in the available time. Individual technical people who will be responsible for performing the various tasks will be required to develop a basis of estimation (quotes, previous similar work, engineering estimates, etc.) for cost, schedule, and risk scoring. Each of the individual estimations are reviewed and entered into a relational costing database which performs all of the necessary roll ups through the WBS and allows the examination of the various cost elements (personnel, procurements, and other costs) across the WBS. These rolled up costs and risk assessment scores are used to determine the total costs, contingency and the schedule is then used to determine the application of the appropriate DOE escalation.

Experience with \$100M scale science projects indicates that a contingency level of 28% is appropriate in order to complete science-driven project scope.

WBS #	Element	BASE (M\$)
1	Instrument Systems	34
2	Telescope	28
3	Spacecraft	
4	Launch Vehicle	
5	Mission Integration & Test	8
6	Mission Operations Center	5
7	Operations	
8	Special Studies	4
9	Science Team	5
10	Program Management	6
11	Systems Integration	5
	Contingency	30
	TOTAL	125

Table 18.1: SNAP Rough Order Cost Estimate (FY'00\$) Does not include Launch, Launch Vehicle, Spacecraft Bus or OPS/Ground Support

Task/Milestone	FY '00	FY '01	FY '02	FY '03	FY '04	FY '05	FY '06	FY '07
Estimated Fund- ing								
R&D Phase – \$14.6M	1.8	3.8	9					
Construction Phase – \$125M				25	40	45	15	

Table 18.2: Funding By Fiscal Year (excludes launch and spacecraft)

Bibliography

- Aguirre, A. N. 1999, *ApJ*, 512, L19
- Aguirre, A. N., & Haiman, Z. 1999, *astro-ph*, 9907039
- Allington-Smith, J. R., Content, R., & Haynes, R. 1998, *SPIE*, 3355, 196–205
- Anderson, J. M., Becker, K. J., Kieffer, H. H., & Dodd, D. N. 1999, *PASP*, 111, 737–749
- Angel, J. R. P., Woolf, N. J., & Epps, H. W. 1982, *SPIE*, 332, 134
- Ardelean, J., et al. 1996, *Nucl. Instrum. Meth.*, 376, 217
- Arnett, W. D. 1982, *ApJ*, 253, 785
- Arnett, W. D., Branch, D., & Wheeler, J. C. 1985, *Nature*, 314, 337
- Baade, W. 1926, *Astr. Nach.*, 228, 359
- Bahcall, N., & Fan, X. 1998, *ApJ*, 504, 1
- Barden, S. C., Arns, J. A., & Colburn, W. S. 1998, *SPIE*, 3355, 866–876
- Barkana, R., Blandford, R., & Hogg, D. W. 1999, *ApJ*, 513, L91–L94
- Baron, E., Hauschildt, P. H., Branch, D., Wagner, R. M., Austin, S. J., Filippenko, A. V., & Matheson, T. 1993, *ApJ*, 416, L21
- Baron, E., Hauschildt, P. H., & Branch, D. 1994, *ApJ*, 426, 334
- Baron, E., Hauschildt, P. H., Branch, D., Austin, S., Garnavich, P., Ann, H. B., Wagner, R. M., Filippenko, A. V., Matheson, T., & Liebert, J. 1995, *ApJ*, 441, 170
- Baron, E., Hauschildt, P. H., Branch, D., Kirshner, R. P., & Filippenko, A. V. 1996, *MNRAS*, 279, 779
- Bartelmann, M., & Schneider, P. 1999, *A&A*, 345, 17–21
- Benítez, N., & Sanz, J. L. 1999, *ApJ*, 525, L1–L4
- Bessell, M. S. 1979, *PASP*, 91, 589–607
- Bessell, M. S. 1990, *PASP*, 102, 1181–1199

- Bessell, M. S., & Brett, J. M. 1988, *PASP*, 100, 1134–1151
- Blandford, R. D., Saust, A. B., Brainerd, T. G., & Villumsen, J. V. 1991, *MNRAS*, 251, 600–627
- Bohlin, R. C. 1996, *AJ*, 111, 1743+
- Bond, J., Efstathiou, G., & Tegmark, M. 1997, *MNRAS*, 291, L33
- Brainerd, T. G., Blandford, R. D., & Smail, I. 1996, *ApJ*, 466, 623+
- Branch, D. 1987, *ApJ*, 320, L27
- Branch, D., et al. 1983, *ApJ*, 270, 123
- Branch, D., & Miller, D. L. 1993, *ApJ*, 405, L5
- Branch, D., & van den Bergh, S. 1993, *AJ*, 105, 2231
- Branch, D., Falk, S. W., McCall, M. L., Rybski, P., Uomoto, A. K., & Wills, B. J. 1981, *ApJ*, 244, 780
- Branch, D., Livio, M., Youngelson, L., F.Boffi, & Baron, E. 1995, *PASP*, 107, 1019
- Branch, D., Romanishin, W., & Baron, E. 1996, *ApJ*, 465, 73
- Bredthauer, R., Pinter, J., Janesick, J., & Robinson, L. 1991, *SPIE*, 1447
- Burke, B., Mountain, R., Harrison, D., Bautz, M., Doty, J., Ricker, G., & Daniels, P. 1991, *IEEE*, 38(5)
- Burke, B. E., et al. 1994, *IEEE Trans. Nucl. Sci.*, 41, 375
- Burke, B. E., et al. 1997, *IEEE Trans. Elec. Dev.*, 44(10), 1633
- Burstein, D., & Heiles, C. 1982, *AJ*, 87, 1165–1189
- Caldwell, R., Dave, R., & Steinhardt, P. 1998, *PRL*, 80, 1582
- Carlstrom, J., et al. 1999, *astro-ph/9905255*
- Coble, K., Dodelson, S., & Frieman, J. 1997, *PRD*, 55, 1851
- Content, R. 1998a, *SPIE*, 3354, 187–200
- Content, R. 1998b, *SPIE*, 3356, 122–133
- Cooray, A. R., Quashnock, J. M., & Miller, M. C. 1999, *ApJ*, 511, 562–568
- Copi, C., Schramm, D., & Turner, M. 1995, *Science*, 267, 192
- Dalcanton, J. J., Canizares, C. R., Granados, A., Steidel, C. C., & Stocke, J. T. 1994, *ApJ*, 424, 550–568

- Dentan, M., et al. 1998. Industrial Transfer and Stabilization of a CMOS-JFET-Bipolar Radiation-Hard Analog -Digital SOI Technology. In IEEE NSS98 Conference. Toronto
- Donahue, M., Aldering, G., & Stocke, J. T. 1995, *ApJ*, 450, L45–+
- Eastman, R., Schmidt, B. P., & Kirshner, R. 1996, *ApJ*, 466, 911
- Efstathiou, G., & Bond, J. 1999, *MNRAS*, 304, 75
- Efstathiou, G., Bond, J., & White, S. 1992, *MNRAS*, 258, 1
- Eisenstein, D., Hu, W., & Tegmark, M. 1999, *ApJ*, 518, 2
- Epps, & Takeda 1983, *Ann.Tokyo Astron. Obs.*, 19, 401
- Falco, E. E., Kochanek, C. S., & Munoz, J. A. 1998, *ApJ*, 494, 47+
- Falco, E. E., Impey, C. D., Kochanek, C. S., Lehar, J., McLeod, B. A., Rix, H. W., Keeton, C. R., Munoz, J. A., & Peng, C. Y. 1999, *ApJ*, 523, 617–632
- Filippenko, A. V. 1997. In 18th Texas Symposium on Relativistic Astrophysics, A. Olinto, J. Frieman, and D. Schramm, editors, Singapore: World Scientific. in press
- Frieman, J., et al. 1995, *PRL*, 75, 2077
- Fukugita, M., Ichikawa, T., Gunn, J. E., Doi, M., Shimasaku, K., & Schneider, D. P. 1996, *AJ*, 111, 1748+
- Garnavich, P., et al. 1998, *ApJ*, 493, L53
- Gilmore, G., Reid, I., & Hewett, P. 1985, *MNRAS*, 213, 257+
- Glazebrook, K. 1998, *AAO Newsletter*, 87, 11
- Goobar, A., & Perlmutter, S. 1995, *ApJ*, 450, 14
- Groom, D., et al. 1999, *SPIE*, 3649
- Gunn, J. E. 1967, *ApJ*, 147, 61+
- Hamuy, M., Phillips, M. M., Wells, L., & Maza, J. 1993, *PASP*, 105, 787
- Hamuy, M., Phillips, M. M., Maza, J., Suntzeff, N. B., Schommer, R. A., & Aviles, R. 1996, *AJ*, 112, 2391
- Hayes, D. S., & Latham, D. W. 1975, *ApJ*, 197, 593–601
- Haynes, R., et al. 1999, *astro-ph/9909017*
- Heyes, P. S., Pool, P., & Holton, R. 1997. In *Solid State Sensor Arrays: Development and Applications*, page 201

- Höflich, P., & Khokhlov, A. 1996, *ApJ*, 457, 500
- Höflich, P., Wheeler, J. C., & Thielemann, F. K. 1998, *ApJ*, 495, 617
- Hogg, D. W., Cohen, J. G., Blandford, R., Gwyn, S. D. J., Hartwick, F. D. A., Mobasher, B., Mazzei, P., Sawicki, M., Lin, H., Yee, H. K. C., Connolly, A. J., Brunner, R. J., Csabai, I., Dickinson, M., Subbarao, M. U., Szalay, A. S., Fernández-Soto, A., Lanzetta, K. M., & Yahil, A. 1998, *AJ*, 115, 1418–1422
- Holland, A. 1996, *Nucl. Instrum. Methods*, A337
- Holland, A., et al. 1991, *IEEE Trans. Nucl. Sci.*, 38(6)
- Holland, A. D. 1997, *SPIE*, 3114, 586
- Holland, S. 1989, *Nucl. Instrum. Methods*, A275
- Holland, S., et al. 1996, *IEDM Tech. Digest*, 911
- Holland, S., Wang, N., & Moses, W. 1997, *IEEE Trans. Nucl. Sci.*, **44**(3)
- Holland, S. E., et al. 1997. Development of back-illuminated, fully-depleted CCD image sensors for use in astronomy and astrophysics. In 1997 IEEE Workshop on Charge-Coupled Devices and Advanced Image Sensors
- Holmes-Siedle, A., Holland, A., & Watts, S. 1996, *IEEE Trans. Nucl. Sci.*, **43**(6)
- Hopkinson, G., Dale, C., & Marshall, P. 1996, *IEEE Trans. Nucl. Sci.*, **43**(2)
- Hu, W. 1999, *ApJ*, 506, 485
- Hu, W. 1999, private communication
- Hu, W., & Eisenstein, D. 1999, *PRD*, 59, 083509
- Hu, W., & Tegmark, M. 1999, *ApJ*, 514, L65–L68
- Hu, W., Eisenstein, D., & Tegmark, M. 1999, *PRD*, 59, 023512
- Hudson, M. J., Gwyn, S. D. J., Dahle, H., & Kaiser, N. 1998, *ApJ*, 503, 531+
- Huey, G., et al. 1999, *PRD*, 59, 063005
- Hui, L. 1999, *ApJ*, 519, L9–L12
- Hunten, D. 1974. Part A: "Optical and Infrared. In *Methods of Experimental Physics: Astrophysics*, volume 12, Academic Press, New York, page ???
- Huterer, D., & Turner, M. 1999, *PRD*, 60, 081301
- Iwamuro, F., Maihara, T., Oya, S., Tsukamoto, H., Hall, D. N. B., Cowie, L. L., Tokunaga, A. T., & Pickles, A. J. 1994, *PASJ*, 46, 515–521

- Iye, M., Ebizuka, N., & Takami, H. 1998, SPIE, 3355, 417–423
- J. Mohr, B. M., & Evrard, A. 1999, ApJ, 517, 627
- Jain, B., et al. 1999, astro-ph/9901191
- Jain, B., & Seljak, U. 1997, ApJ, 484, 560+
- Janesick, J. 1997, CCD Astronomy
- Janesick, J., et al. 1991, SPIE, 1447, 87
- Janesick, J., Elliot, T., & Pool, F. 1989, IEEE Trans. Nucl. Sci., **36**(1)
- Janesick, J., Elliot, T., Winzenread, R., Pinter, J., & Dyck, R. 1995, SPIE, 2415
- Kaiser, N. 1992, ApJ, 388, 272–286
- Kaiser, N. 1998, ApJ, 498, 26+
- Kaiser, N., Squires, G., & Broadhurst, T. 1995, ApJ, 449, 460+
- Kamasz, S., Farrier, M., & Smith, C. 1994, SPIE, 2172
- Kent, S. M. 1985, PASP, 97, 165–174
- Khokhlov, A. 1991a, A&A, 245, 114
- Khokhlov, A. 1991b, A&A, 245, L25
- Kim, A., et al. 2000, ApJ, in preparation
- Kirshner, R. P., & Kwan, J. 1974, ApJ, 193, 27
- Knox, L., & Dodelson, S. 1999, astro-ph/9909454
- Kobulnicky, H. A., & Zaritsky, D. 1999, ApJ, 511, 118–135
- Kochanek, C. S. 1996, ApJ, 466, 638+
- Korsch, D. 1980, Appl.Opt., 19, 3640
- Kristian, J., & Sachs, R. K. 1966, ApJ, 143, 379+
- Landolt, A. U. 1983, AJ, 88, 439–460
- Landolt, A. U. 1992, AJ, 104, 340–371
- Larkin, J., Quirrenback, A., & Graham, J. 2000. Image Slicing with Infrared Fibers.
In Imaging the Universe in Three Dimensions: Astrophysics with Advanced Multi-Wavelength Imaging Devices, W. van Breugel and J. Bland-Hawthorn, editors, ASP Conference Proceedings
- Le Louarn, M., Foy, R., Hubin, N., & Tallon, M. 1998, MNRAS, 295, 756–768

- Leibundgut, B. 1988. Ph.D. thesis, University of Basel
- Lentz, E., et al. 1999, astro-ph/9906016
- Lesser, M. P., & McCarthy, B. 1996, SPIE, 2654
- Link, R., & Pierce, M. J. 1998, ApJ, 502, 63+
- Lumb, D. 1990, Nucl. Instrum., A288
- Lumb, D., Chowanietz, E., & Wells, A. 1987, Optical Eng., 26
- Luppino, G. A., & Kaiser, N. 1997, ApJ, 475, 20+
- Maihara, T., Iwamuro, F., Yamashita, T., Hall, D. N. B., Cowie, L. L., Tokunaga, A. T., & Pickles, A. 1993, PASP, 105, 940–944
- Malhotra, S., Rhoads, J. E., & Turner, E. L. 1997, MNRAS, 288, 138–144
- McCann, D., et al. 1980, SPIE, 217
- McGraw, J., et al. 1982, SPIE, 331, 137
- Megessier, C. 1995, A&A, 296, 771+
- Meidinger, N., Struder, L., Soltau, H., & Zanthier, C. 1995, IEEE Trans. Nucl. Sci., **42**(6)
- Miller, J., Epps, H., et al. 1992, Lick Observatory Technical Report, 66
- Minkowski, R. 1939, ApJ, 89, 156
- Miralda-Escude, J. 1991, ApJ, 380, 1–8
- Murphy, T. W., J., Matthews, K., & Soifer, B. T. 1999, PASP, 111, 1176–1184
- Nomoto, K., Thielemann, F., & Yokoi, K. 1984, ApJ, 286, 644
- Nugent, P. 1997. Ph.D. thesis, University of Oklahoma
- Nugent, P., et al. 1999, PASP, in preparation
- Nugent, P., Phillips, M., Baron, E., Branch, D., & Hauschildt, P. 1995a, ApJ, 455, L147
- Nugent, P., Branch, D., Baron, E., Fisher, A., Vaughan, T., & Hauschildt, P. 1995b, Phys. Rev. Lett., 75, 394
- Nugent, P., Baron, E., Branch, D., Fisher, A., & Hauschildt, P. 1997, ApJ, 485, 812
- Oke, J. B. 1974, ApJS, 27, 21+
- Oke, J. B., & Gunn, J. E. 1982, PASP, 94, 586+

- Oke, J. B., & Gunn, J. E. 1983, *ApJ*, 266, 713–717
- Oke, J. B., Cohen, J. G., Carr, M., Cromer, J., Dingizian, A., Harris, F. H., Labrecque, S., Lucinio, R., Schaal, W., Epps, H., & Miller, J. 1995, *PASP*, 107, 375+
- Oliva, E. 1999, *astro-ph/9909108*
- Oliva, E., & Origlia, L. 1992, *A&A*, 254, 466+
- Peckerar, M., McCann, D., & Yu, L. 1981, *Appl. Phys. Lett.*, **39**(1)
- Perlmutter, S., et al. 1997, *ApJ*, 483
- Perlmutter, S., et al. 1998, *Nature*, 391
- Perlmutter, S., et al. 1999, *ApJ*, 517, 565
- Phillips, M. M. 1993, *ApJ*, 413, L105
- Ramsay, S. K., Mountain, C. M., & Geballe, T. R. 1992, *MNRAS*, 259, 751–760
- Ratnatunga, K. U., Griffiths, R. E., & Ostrander, E. J. 1999, *AJ*, 117, 2010–2023
- Ratra, B., & Peebles, P. 1987, *PRD*, 37, 3406
- Rhodes, J., Refregier, A., & Groth, E. 1999, *astro-ph/9905090*
- Riess, A., et al. 1997, *AJ*, 114, 722
- Riess, A., et al. 1998, *AJ*, 116, 1009
- Riess, A. G., Press, W. H., & Kirshner, R. P. 1995, *ApJ*, 438, L17
- Riess, A. G., Press, W. H., & Kirshner, R. P. 1996, *ApJ*, 473, 88
- Sandage, A., & Tammann, G. 1995, *ApJ*, 452, 16
- Schlegel, D. J., Finkbeiner, D. P., & Davis, M. 1998, *ApJ*, 500, 525+
- Schmidt, B. P., Kirshner, R., & Eastman, R. 1992, *ApJ*, 395, 366
- Schmidt, B. P., Suntzeff, N. B., Phillips, M. M., Schommer, R. A., Clocchiatti, A., Kirshner, R. P., Garnavich, P., Challis, P., Leibundgut, B., Spyromilio, J., Riess, A. G., Filippenko, A. V., Hamuy, M., Smith, R. C., Hogan, C., Stubbs, C., Diercks, A., Reiss, D., Gilliland, R., Tonry, J., Maza, J., Dressler, A., Walsh, J., & Ciardullo, R. 1998, *ApJ*, 507, 46–63
- Schneider, P., Van Waerbeke, L., Jain, B., & Kruse, G. 1998, *MNRAS*, 296, 873–892
- Schroeder, D. J. 1987. *Astronomical Optics* 2nd Edition.
- Shack, & Thompson 1980, *Proc. SPIE Int. Soc. Opt.Eng.*, 251, 146

- Starkman, G., Trodden, M., & Vachaspati, T. 1999, PRL, 83, 1510
- Steinhardt, P., Wang, L., & Zlatev, I. 1999, PRD, 59, 123504
- Stover, R. 1999, private communication
- Stover, R., et al. 1997, SPIE, 3019, 183
- Stover, R., et al. 1998, SPIE, 3505
- Sze, S. M. 1981. Physics of Semiconductor Devices, Wiley
- Szomoru, A., & Guhathakurta, P. 1999, AJ, 117, 2226–2243
- Tegmark, M., Taylor, A., & Heavens, A. 1997, ApJ, 480, 22
- Thuan, T. X., & Gunn, J. E. 1976, PASP, 88, 543–547
- Trimble, V. 1987, ARAA, 25, 425
- Tsoi, H. 1985, IEEE Trans. Elec. Dev., **32**(8)
- Turner, E. L., Ostriker, J. P., & Gott, J. R., I. 1984, ApJ, 284, 1–22
- Turner, M. 1999, Physica Scripta (in press)
- Tyson, J. A., Wenk, R. A., & Valdes, F. 1990, ApJ, 349, L1–L4
- Tyson, J. A., Kochanski, G. P., & Dell’Antonio, I. P. 1998, ApJ, 498, L107–+
- Umeda, H., et al. 1999, ApJ, 513, 861
- Valdes, F., Jarvis, J. F., & Tyson, J. A. 1983, ApJ, 271, 431–441
- Van Waerbeke, L., Bernardeau, F., & Mellier, Y. 1999, A&A, 342, 15–33
- Vaughan, T. E., Branch, D., Miller, D. L., & Perlmutter, S. 1995, ApJ, 439, 558
- Vilenkin, A. 1984, PRL, 53, 1016
- Vilenkin, A., & Shellard, E. 1994. Cosmic strings and other topological defects, Cambridge University Press
- von Ammon, W., & Herzer, H. 1984, Nucl. Instrum. Meth., A226
- Wade, R. A., Hoessel, J. G., Elias, J. H., & Huchra, J. P. 1979, PASP, 91, 35–40
- Walker, M. A. 1999, MNRAS, 306, 504–508
- Wang, L. 1999, private communication
- Weinberg, S. 1989, RMP, 61, 1
- Wetherall, W., & Rimmer, M. 1972, Applied Optics, 11, 2817

- White, M. 1998, ApJ, 506, 495
- Williams, R. E., et al. 1996, AJ, 112, 1335
- Willstrop, R. V. 1984, MNRAS, 210, 597
- Woosley, S. E. 1991. In Gamma-Ray Line Astrophysics, P. Durouchoux and N. Prantzos, editors, New York: AIP, page 270
- Yamashita, et al. 1997, IEEE Trans. Nucl. Sci., **44**(3)
- Zlatev, I., Wang, L., & Steinhardt, P. 1999, PRL, 82, 896
- Zwicky, F. 1937, Helv. Phys. Acta, 6, 110

Appendix A

WBS

1. INSTRUMENT SYSTEMS

- (a) INSTRUMENTS
 - i. IMAGER
 - ii. SPECTROGRAPH
 - iii. INSTRUMENT CALIBRATION
- (b) INSTRUMENT ELECTRONICS
 - i. READOUT ELECTRONICS
 - ii. DATA HANDLING
 - iii. CRATES & POWER MANAGEMENT
 - iv. CONTROLS & STATUS SENSORS
- (c) INTEGRATION & TEST
- (d) GROUND SUPPORT EQUIPMENT
- (e) SUBPROJECT MGM'T & SYS ENG

2. TELESCOPE

- (a) OPTICS
 - i. PRIMARY
 - ii. SECONDARY, ETC.
- (b) STRUCTURE
 - i. METERING STRUCTURE
 - ii. SUN SHIELD & PM BAFFLES
 - iii. M & TM SHIELDS & BAFFLES
- (c) OPTICAL BENCH ASSY
 - i. OPTICAL BENCH
 - ii. FAST STEERING SYSTEM
 - iii. MATCHING OPTICS

- iv. SPLITERS
 - v. FILTER WHEELS
 - (d) INTEGRATION & TEST
 - (e) GROUND SUPPORT EQUIPMENT
 - (f) SUBPROJECT MANAGEMENT & SYS ENG
- 3. SPACECRAFT
 - (a) ATTITUDE CONTROL
 - (b) PROPULSION
 - (c) MECHANICAL
 - (d) POWER
 - (e) COMMUNICATIONS
 - (f) THERMAL
 - (g) COMPUTING & DATA HANDLING
 - (h) INTEGRATION & TEST
 - (i) GROUND SUPPORT EQUIPMENT
 - (j) SUB-PROJ. MGM'T & SYS ENG
- 4. LAUNCH VEHICLE
 - (a) PROCUREMENT
 - (b) LAUNCH SERVICES
- 5. MISSION INTEGRATION & TEST
 - (a) INSTRUMENT TO TELESCOPE I&T
 - (b) INSTR/TELESCOPE TO SPACECRAFT BUS I&T
 - (c) PAYLOAD TO LAUNCH VEHICLE I&T
- 6. MISSION OPERATIONS CENTER
 - (a) MISSION OPERATIONS CENTER DEVELOPMENT
 - (b) GROUND ANTENNA DEVELOPMENT
 - (c) REPARATION FOR DATA HANDLING/SOC
- 7. OPERATIONS
 - (a) LAUNCH & EARLY ORBIT SUPPORT(30 Days)
 - (b) POST-LAUNCH SUPPORT
 - (c) FACILITY MAINTENANCE
 - (d) SOFTWARE MAINTENANCE

- (e) PERSONNEL TRAINING
- (f) INSTRUMENT TROUBLE SHOOTING/REPAIR
- (g) MISSION GROUND STATION OPERATIONS
- 8. SPECIAL STUDIES
- 9. SCIENCE TEAM
 - (a) SCIENCE REQUIREMENTS DEVELOPMENT
 - (b) IMPLEMENTATION
 - (c) DATA ANALYSIS
 - (d) EDUCATION & PUBLIC OUTREACH
- 10. PROGRAM MANAGEMENT
 - (a) TECHNICAL
 - (b) PLANNING
 - (c) TRACKING
 - (d) SUBCONTRACTING & PROCUREMENT
 - (e) DOCUMENT CONTROL
 - (f) PERFORMANCE/QUALITY ASSURANCE
 - i. CALIBRATION
 - (g) ES&H
 - i. INSTRUMENT & TELESCOPE EH&S PROGRAM
 - ii. GLOBAL SPACECRAFT EH&S PROGRAM
 - iii. ORBITAL DEBRIE ASSESSMENT
 - (h) SUPPLIES & EQUIPMENT
 - (i) REVIEWS, MEETINGS & TRAVEL
 - (j) BUDGET RESERVE/CONTINGENCY
 - (k) CONFIGURATION CONTROL BOARD
- 11. SYSTEMS ENGINEERING
 - (a) REQUIREMENTS DEVELOPMENT & CONTROL
 - (b) CONFIGURATION & INTERFACE CONTROL
 - (c) TRADE STUDIES
 - (d) SYSTEM ANALYSIS
 - (e) MATERIALS & PROCESS CONTAMINATION CONTROL
 - (f) SYSTEMS QUALIFICATION
 - (g) INTEGRATION & LOGISTICS

Appendix B

Appendix. Fully Depleted High Resistivity CCDs

B.1 Overview

A key technological innovation in the SNAP instrumentation is a large one billion pixel camera. In order to maximize the sensitivity of SNAP to discover high red-shift supernova ($z < 1.7$) this camera requires excellent sensitivity in the I or Z optical bands. Consequently, we have assumed in the baseline design the use in this camera of a new kind of CCD with excellent I and Z-band sensitivity.

We have successfully developed a new type of large-format CCD's on n-type high-resistivity silicon. The back illuminated CCD's are fabricated on 300 μm thick silicon substrates. The substrate is fully depleted by the application of an independent voltage through an optically transparent backside contact. Multiple science-grade $2\text{k} \times 2\text{k}$ pixel ($15 \mu\text{m}^2$ pixels) CCD's have been obtained and tested (Fig. B.1). Furthermore, devices on these wafers have shown excellent charge transfer efficiency (> 0.999995), read noise of $4.3 e^-$, dark current of $0.003 e^-/\text{pixel/s}$, and a well depth of $300,000 e^-$ ($15 \mu\text{m}^2$ pixels). With back illumination, the QE at 1000 nm is 65% ($T = 150^\circ\text{K}$). As shown in Fig. B.1, commercially available CCD's with proper coatings reach 15% or less at 1000 nm at this temperature. This is a major achievement in the development of n-type high-resistivity CCD's (Holland et al., 1996; Stover et al., 1997; Holland et al., 1997).

Early measurements indicate that as expected [J. Janesick, private communication] this technology results in significantly improved radiation tolerance of the CCD. For long duration missions this could prove to be a major benefit. Since devices do not need to be thinned, the CCD's are self-supporting and four-side buttable (with back-illumination thinned devices require an underlying mechanical support that interferes with traditional wire bonding). Consequently, the new CCD's are ideal for a wide-field mosaic array. A space-based wide-field imager taking advantage of the 4-side abutment would require much smaller pixel sizes than ground based telescopes for reasonable cost and weight of the optics. In this context, we currently have in fabrication large-format, smaller pixel size (10.5 and 12 μm) devices, and we are exploring light weight four-side

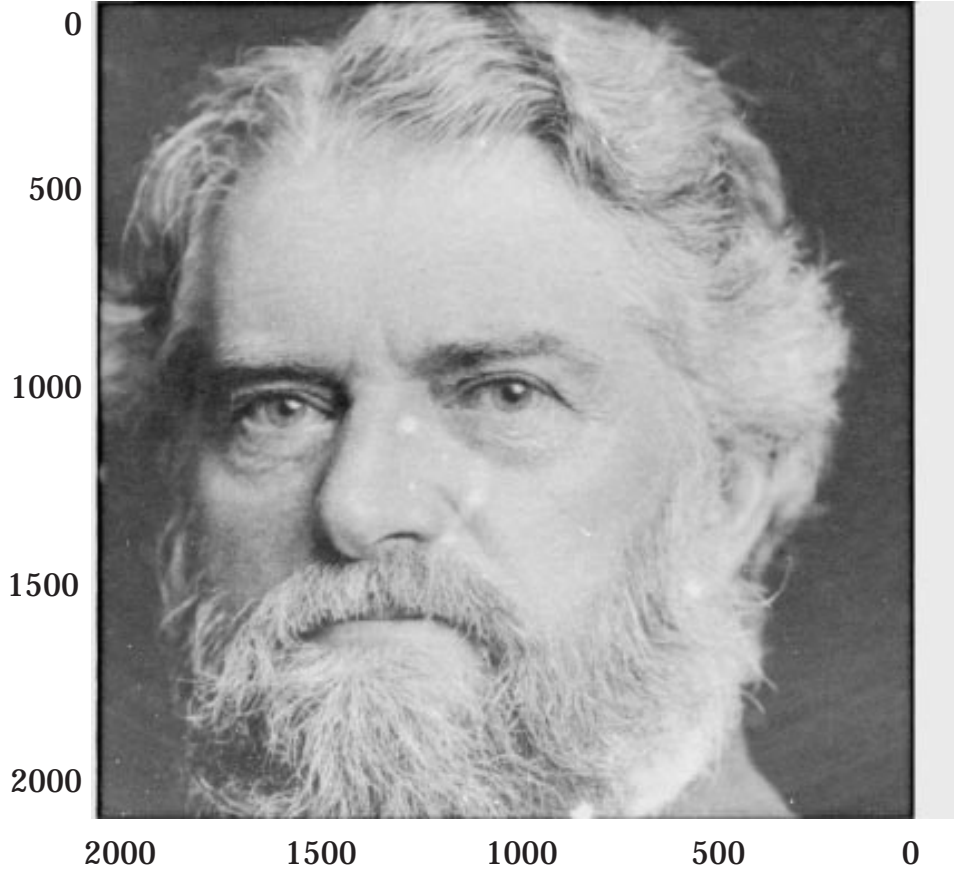


Figure B.1: Raw test image obtained at Lick Observatory of a back-illuminated $2k \times 2k$ ($15 \mu\text{m}^2$ -pixel) LBNL high-resistivity CCD. The chip is cosmetically and electrically perfect. A 20V bias voltage transports the charge from the rear surface through the fully-depleted substrate to the CCD potential wells on the front surface. The substrate is $300 \mu\text{m}$ thick. Parallel CTE is 0.999998 and serial CTE is 0.999999, well depth is $300,000 e^-$, and the read noise is $4.3 e^-$.

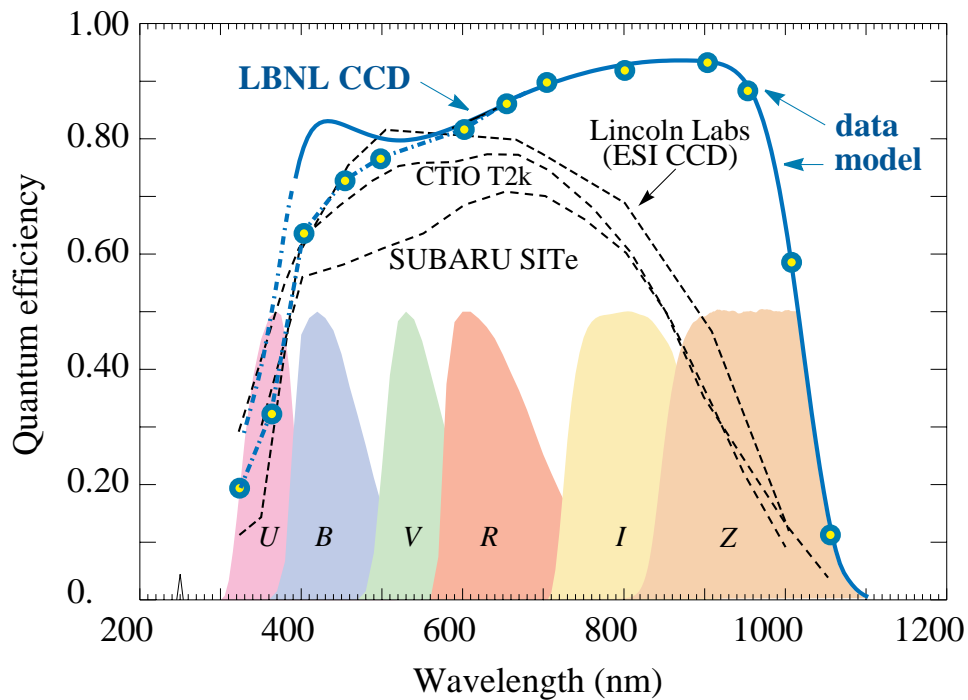


Figure B.2: Measured response of the LBNL “fully-depleted” CCD at -100°C (open circles) for an unoptimized two-layer AR coating (the dark curve through the points is a model calculation). Response is expected to be significantly higher for optimized AR coatings. For comparison, measured response of the $2\text{k} \times 4\text{k}$ “deep-depletion” back-illuminated MIT/Lincoln chip on Keck ESI is shown, as are measurements for two different SITe CCD’s on SUBARU and CTIO. Relative spectral responses of standard wide-band filters are shown.

abutment packaging technologies.

This technology is currently being transferred to a commercial vendor, Mitel Corp, Bromont Canada. Mitel is currently in the middle to two simultaneous processing runs that will evaluate the process at their foundry. The two runs consist of 1) an adaptation of the LBNL process recipe for the Mitel process equipment that is fairly true to the original recipe, and 2) a version that is highly optimized for the standard Mitel CCD process flow and would produce the devices at higher volume. This is the second vendor that has taken this process over for device fabrication. The first vendor Digirad, has now been successfully using the process for the manufacture of photodiode arrays. From this experience we would expect Mitel to be able to manufacture CCD's in volume to our specification in approximately twelve to eighteen months. This time is needed to optimize furnace recipes, validate process steps and characterize intermediate devices. If funds were available this time period could be greatly accelerated as the development work is currently paced by funding.

LBNL is also engaged in further in house fabrication runs. Now that the process steps have been completed for fabrication, development of specific science devices is underway. Currently, we have devices in use or about to be in use at Lick Observatory and we have a $2k \times 4k$ pixel device in fabrication for the ESI spectrograph at Keck Observatory. With the completion of the process development we have hired a process technician to help us with regular manufacture. The time expected now to process a lot (25 wafers) is 6 months. To date we have been able to obtain one science grade large format device per wafer.

Were SNAP to proceed into an R&D phase we would very seriously consider other options available to mitigate the technical risk present in the new technology for the imager. For slightly higher cost and lower performance we would seriously consider EEV or Sarnoff deep-depletion devices. These thinned devices, when back-illuminated and placed over a mirrored surface (effectively doubling the apparent thickness) can achieve 30% quantum efficiency at 1000 nm ($T = 150^\circ\text{K}$). Design of the imager would proceed such that these devices could be substituted if necessary.

B.2 Benefits and Goals

Although the LBNL CCD's use a normal three-phase gate structure, the CCD's differ dramatically from the thinned CCD's currently used in astronomy. They are made on float-zone refined high-resistivity ($\sim 10,000 \ \Omega\text{-cm}$) n-type silicon $300 \ \mu\text{m}$ thick. Holes, rather than electrons, are collected in the potential wells. An indium-tin oxide coating on the back surface provides three functions: (a) as a contact to which an up to $\gtrsim 80 \text{ V}$ bias is applied to deplete the substrate completely, so that photo-generated charge from the whole volume is collected, (b) as a transparent window, permitting back illumination for normal operation, and (c) as part of the back-surface anti-reflective (AR) coating. The photo-produced charge from near the back surface is then collected in the potential wells. Since the devices are thick, they exhibit excellent quantum efficiency as shown in Fig. B.1, until just below the silicon bandgap at 1050 nm, and at the same time interference "fringing" is completely absent.

Since blue light is strongly absorbed in the gate structure of any front-illuminated CCD, the CCD's used in astronomy are usually thinned and back-illuminated. For most devices (with a 20 μm thick 10 to 50 $\Omega\text{-cm}$ epitaxial layer), this means thinning to about 20 μm . The thinning results in transparency in the red, resulting in a loss of quantum efficiency (QE) and “fringing” due to multiple reflections. For the LBNL devices this expensive, time-consuming, and low-yield thinning process is both unnecessary and undesirable. Advantages of the novel LBNL CCD's include:

- a. High quantum efficiency (QE) up to wavelengths approaching the silicon bandgap at just above 1050 nm, where silicon becomes transparent.
- b. Absence of fringing. The interference patterns that are present in thinned spectroscopic CCD's are completely absent in these thick devices.
- c. Good blue response without special processing and without UV flooding. A normal CCD exhibits field inversion near the back surface, resulting in the loss of QE for blue light, where the absorption length is very short. A variety of methods have been invented to avoid this problem. Since holes, rather than electrons, are collected in the LBNL CCD's, the problem does not exist and the fully-depleted substrate has no field-free region.
- d. The very low concentrations of phosphorus and oxygen in the n-type high-resistivity device result in excellent radiation tolerance. Preliminary measurements at the 88” cyclotron indicate that these devices have superior tolerance to previous CCD technologies.
- e. Exceptionally large well-depth of 300,000 e^- (15 μm^2 pixels) with low noise readout can be traded-off for smaller pixel sizes.
- f. Capitalizing on the device thickness, the CCD's can be readily packaged for four-side abutment with standard wire bonding techniques enabling the manufacture of very large mosaic arrays.
- g. The new CCD's can be manufactured at low cost in a traditional CCD foundry. Since no thinning is required, the overall cost will be significantly less than conventional thinned devices.

B.3 Uniqueness of Fully-Depletion Devices

To overcome a variety of technical problems discussed below, high-performance CCD's for astronomy are obtained by “thinning” conventional CCD's (where the active region is a thin 30–50 Ωcm epitaxial layer grown on a lower-resistivity p-type substrate), leaving only the epitaxial layer and gate circuitry. After back-surface preparation they are used with back illumination. There are severe cost, quality, and availability problems associated with the process. For example, a defect-free 2048×2048 pixel CCD in a modern mosaic camera costs approximately \$50,000, about an order of magnitude higher than the cost of the CCD as it leaves the foundry (Janesick, 1997).

All of these problems are avoided by the full-depletion technology, in which the final CCD emerges directly from the MOS foundry. There are additional gains: high blue sensitivity is achieved with standard technologies, therefore easing the transfer of the technology to a commercial foundry. These CCD's are more radiation resistant

than standard CCD's, because boron, rather than phosphorus, is used for doping, and because the high-resistivity substrate contains comparatively little oxygen. Because they are thick, red sensitivity is extended to near the bandgap cutoff at 1050 nm ($T = 150^\circ\text{K}$) (Sze, 1981). No other MOS CCD process offers these improvements.

These "fully-depleted" 300 μm thick high-resistivity MOS CCD's exhibit significantly improved performance over existing "deep-depletion" CCD's which still require thinning to 40–50 μm for good performance and are technically quite different.

Full depletion of a standard low-resistivity silicon substrate is not technically feasible, so the technical developments for expanding the wavelength sensitivity of scientific CCD's have focussed on high-resistivity substrates. Unique among MOS CCD developers is the use at LBNL of a lightly doped high-resistivity n-type silicon substrate. The community of developers of MOS CCD's on high-resistivity silicon is small, limited to LBNL, Sarnoff Laboratory, MIT/Lincoln Laboratory (Burke et al., 1997, 1994, 1991), and EEV Ltd (Heyes, Pool, & Holton, 1997; Holland, 1997, 1996; Lumb, 1990; Lumb, Chwanietz, & Wells, 1987).

The MOS CCD's developed at MIT/Lincoln Laboratory, Sarnoff Laboratory, and EEV Ltd. are of the "deep-depletion" type. In these devices partial depletion of the substrate is achieved to depths of typically 40–80 μm through the potential applied at the charge transfer gates. The devices must still be thinned to 40–50 μm in order to eliminate the field-free region between the depletion layer and the backside (Burke et al., 1997; Heyes, Pool, & Holton, 1997). Thinning unfortunately undermines the long wavelength sensitivity and introduces large amplitude interference fringes at long wavelengths. The need to apply the depletion potential at the charge-transfer gate makes these devices harder to optimize.

In contrast, the LBNL "fully-depleted" CCD utilizes conventional MOS technology. This implies that technology transfer to any of a number of CCD manufacturers is possible without the need for customized fabrication equipment to handle the double-sided lithography. The major difference for wafers used by LBNL compared to industry standard wafers is the thickness (300 μm versus industry standard 550 μm for 4 inch diameter). However, we have shown that conventional lithography tools used in CCD manufacturing can operate with both wafer thicknesses (demonstrated on both 1:1 scanners and 5:1 steppers) and our expected commercial partner has already agreed to work with the 300 μm thick substrates. The "fully-depleted" thick MOS CCD's will in the future be inexpensive to manufacture due to the lack of thinning and backside lithography.

B.4 Comparison of CCD's

The CCD design dilemma is summarized in Fig. B.3. At the atmospheric cutoff at the blue end ($\lambda \equiv 320$ nm), the absorption length of light in silicon is about 10 nm. It is four orders of magnitude larger, or 100 μm , at $\lambda = 1000$ nm. The problem at the blue end is to collect electrons (or holes, in the case of this work) produced very near the entrance window. At the red end, quantum efficiency (QE) decreases as the device becomes transparent. In the case of a thinned device, the loss of QE is accompanied

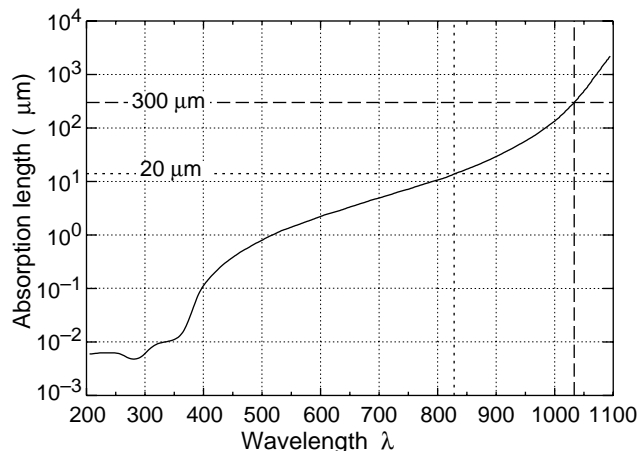


Figure B.3: Absorption length of light in silicon (solid curve). Except at wavelengths approaching the bandgap cutoff at $\lambda_b \approx 1100$ nm, essentially all absorbed photons produce e-h pairs. The sensitive region of a conventional CCD is the ≈ 20 μm -thick epitaxial layer, indicated by the dotted line, while in the LBNL high-resistivity CCD's the fully-depleted 300 μm substrate is active (dashed line).

by the production of interference fringes due to multiple reflections. Typical QEs for astronomical CCD's are shown in Fig. B.1, along with the predicted QE for the LBNL CCD with a two-layer AR coating.

The “fully-depleted” thick CCD's have a wider range of wavelength sensitivity than backside illuminated conventional CCD's or “deep-depletion” CCD's, including improved blue response due to the optical contact, and significantly better IR response. The best MIT/Lincoln Laboratory “deep-depletion” CCD is measured to have 16% quantum efficiency at 1000 nm (Stover, 1999, private communication) whereas our devices have a 65% quantum efficiency at 1000 nm and $T = 150^\circ\text{K}$.

In Table B.1 the characteristics of LBNL CCD's are given along with the performance characteristics of other competitive devices. One favored substitute for CCD's in the near-IR region are HgCdTe active pixel devices. A HgCdTe array is grown on a sapphire substrate, illuminated through the sapphire, and indium bump-bonded to silicon readout chips. Charge transfer efficiency (CTE), quantum efficiency (QE) as a function of wavelength, noise, and full well capacity, have been characterized on the $2k \times 2k$ prototypes. The CCD's were characterized in detail at the Lick Observatory CCD Laboratory. Measured serial and vertical CTEs were 0.999999 and 0.999998, respectively. Fig. B.4 shows a test pattern imaged by a back-illuminated $2k \times 2k$ CCD tested. Excellent CTE was also measured on an 1100×800 CCD. (Holland et al., 1996; Stover et al., 1997; Holland et al., 1997; Stover et al., 1998)

Astronomical images using a 200×200 pixel back-illuminated high-resistivity CCD fabricated at LBNL were first obtained on 1996 Dec 4. In a test at the Lick Observatory 1 m telescope, a heavily obscured region of the Orion Nebula was imaged using an R filter, which has maximum transmission near 600 nm, and a narrow bandpass 1000 nm

Characteristic	LBNL measured	LBNL future	Typical CCD [‡]	MIT/Lincoln*	HgCdTe [†]
Typical format	2k×2k	2k×4k	2k×2k	2k×4k	2k×2k
Pixel size	15μm×15μm	8μm×8μm	15μm×15μm	15μm×15μm	18μm×18μm
Operating Temp.	150K	150K	150K	150K	78K
CTE	> 0.999995	> 0.999995	> 0.999995	> 0.999995	—
Read noise	4.3 <i>e</i>	2 <i>e</i>	3–6 <i>e</i>	2–4 <i>e</i>	4 <i>e</i>
Dark current	0.18 <i>e</i> /m/pix	0.05 <i>e</i> /m/pix	0.03 <i>e</i> /m/pix	0.03 <i>e</i> /m/pix	1 <i>e</i> /m/pix
Full-well (<i>e</i> 's)	300 k	100k	150k (non-MPP)	105k	90k
Fringing @ 800 nm	0%	0%	9%	9%	—
Fringing @ 900 nm	0%	0%	22%	22%	—
Fringing @ 1000 nm	< 2%	< 2%	46%	46%	—
QE @ 900 nm [◊]	92%	92%	38%	47%	—
QE @ 1000 nm [◊]	65%	65%	5–10%	11%	56%
QE Variation @ 350 nm	0% **	0% **	45%	45%	—
QE Variation @ 500 nm	0% **	0% **	2%	2%	—
Cost	—	10K	50-100K	—	300K

LBNL 2k×2k CCD's measured at UCO/Lick, expected performance taken from ref. Groom et al. (1999).

[‡] Thinned CCD, <http://sauron.as.arizona.edu/ccdlab/>

* <http://gardiner.ucolick.org:80/~ccdev/lincoln>

[†] Hawaii-2 array prospects/cost as reported by K. Hodapp (priv. comm.), QE is from Hawaii-1 array

[◊] At cold temperatures ($T = 150^\circ\text{K}$) where QE drops due to bandgap widening Lesser & McCarthy (1996).

** expected

Table B.1: LBNL $2k \times 2k$ ($15 \mu\text{m}$)² CCD's as compared with other detectors.

B.5 Technical features of high-resistivity CCD's

The use of a high-resistivity substrate permits fully depleted operation at reasonable bias voltages. The effect of the bias voltage is to remove the mobile electrons resulting from the extremely small number of dopants atoms (phosphorus) in the high-resistivity silicon. The resistivity, $\approx 10,000 \text{ } \Omega\text{-cm}$, corresponds to a doping density in the mid- 10^{11} cm^{-3} range, about four orders of magnitude smaller than in conventional CCD's. The substrate thickness used here, $300 \text{ } \mu\text{m}$, is significantly thicker than previous conventional, deep-depletion CCD's with typically $40\text{-}80 \text{ } \mu\text{m}$ thick depletion regions (Burke et al., 1997, 1994, 1991; Heyes, Pool, & Holton, 1997; Holland, 1997, 1996; Lumb, 1990; Lumb, Chohanietz, & Wells, 1987; Kamasz, Farrier, & Smith, 1994; Tsoi, 1985).

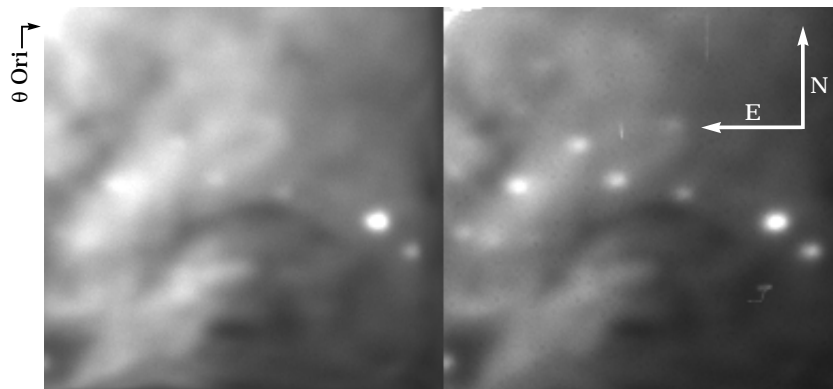


Figure B.5: Lick test CCD images of a heavily obscured region in the Orion Nebula, observed under poor conditions on 1996 Dec 4 with the Lick Observatory 1-m telescope on Mt. Hamilton. The left image was a 50 s exposure with a Harris R filter, with a peak transmission at 600 nm and a FWHM of 120 nm. The right image was a 100 s exposure through a special filter with maximum transmission at 1000 nm and FWHM 88 nm. Each field is about 57 arc-sec squared.

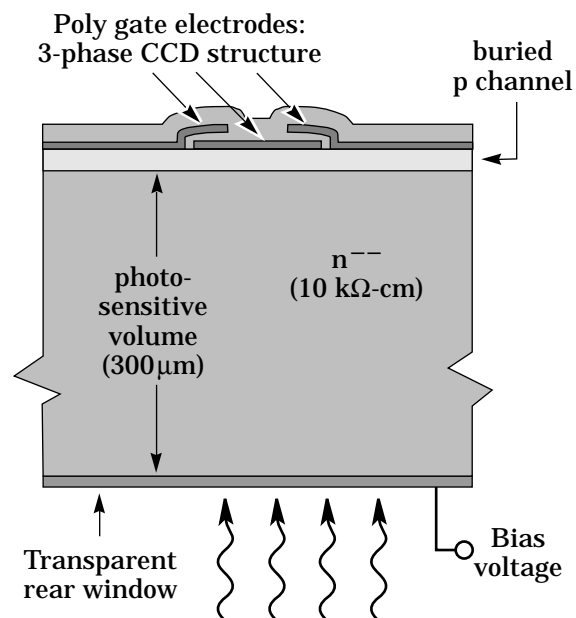


Figure B.6: Cross-section of the back-illuminated, fully-depleted CCD. A conventional buried channel CCD is fabricated on a high-resistivity silicon substrate. A bias voltage applied to the backside contact results in full depletion of the substrate.

The removal of the mobile electrons from the substrate results in an electric field due to the dopant atoms that are now ionized and positively charged. This electric field extends essentially all the way to the backside contact, hence the term full depletion. This element is key to the proper operation of the back illuminated CCD. Short wavelength light is absorbed very near the backside contact. In order to minimize the loss of spatial resolution due to thermal diffusion, it is important the the photo-generated charge be directed towards the CCD buried channels by an electric field.

In order to realize the benefits of such a CCD, several technical challenges needed to be overcome. One concern was maintaining low dark currents with a substantially thicker depletion region as compared to thinned CCD's. A technique for processing high-resistivity silicon while maintaining low dark currents had been previously developed for high-energy physics detectors(Holland, 1989), and this active gettering technique was also used for the CCD fabrication. It consists of the deposition of a phosphorus-doped, backside polycrystalline silicon layer which getters harmful impurities during the fabrication process. High dark currents were a significant problem with initial attempts to develop CCD's on high-resistivity substrates(McCann et al., 1980; Peckerar, McCann, & Yu, 1981).

Another significant challenge was the development of a transparent back-side window that allows transmission of short-wavelength light and application of the bias voltage necessary for full depletion of the substrate. A backside window consisting of a thin layer of in-situ doped polysilicon with an indium-tin oxide antireflection coating was developed(Holland et al., 1996; Holland, Wang, & Moses, 1997).

B.6 Radiation Tolerance

Radiation damage is relevant to space applications. J. Janesick has been pointed out (private communication) that the major bulk damage effect due to space protons, for example, is the generation of trapping states due to formation of phosphorus-vacancy centers (Janesick et al., 1991; Janesick, Elliot, & Pool, 1989; Yamashita et al., 1997; Holmes-Siedle, Holland, & Watts, 1996; Hopkinson, Dale, & Marshall, 1996). This defect results in hot pixels (high dark current) and degrades CTE. Typical CCD's have phosphorus implanted channels, with peak phosphorus concentrations in the low 10^{16} cm^{-3} range(Janesick et al., 1995). Our p-channel CCD has a boron implanted channel, and the background phosphorus concentration is extremely small in the high-resistivity substrate (in the low 10^{11} cm^{-3} range). Therefore it is expected that P-V centers will not limit radiation hardness, but instead oxygen-related defects as observed by Meidinger et al. (1995). High-resistivity silicon has significantly reduced oxygen levels as well(von Ammon & Herzer, 1984). The type of CCD under development here should have significantly improved radiation hardness when compared to conventional CCD's. A 200×200 prototype has been irradiated at the LBNL 88" cyclotron with 55 Mev protons to a fluence of $1 \times 10^9 \text{ cm}^{-2}$. The equivalent 10 Mev fluence was $5 \times 10^8 \text{ cm}^{-2}$, and the CTE degradation, was below the level of detection 2×10^{-6} . This limit is already is a factor of ten less than that reported in the literature for CCD's on p-type silicon with the same dose(Holland et al., 1991), and a factor of two less than recent

measurements of a SiTe CCD as shown in Figure B.6.

Detailed radiation hardness studies will require use of the LBNL 88" 55 MeV proton cyclotron to make systematic studies of dark current and CTE as a function of proton fluences.

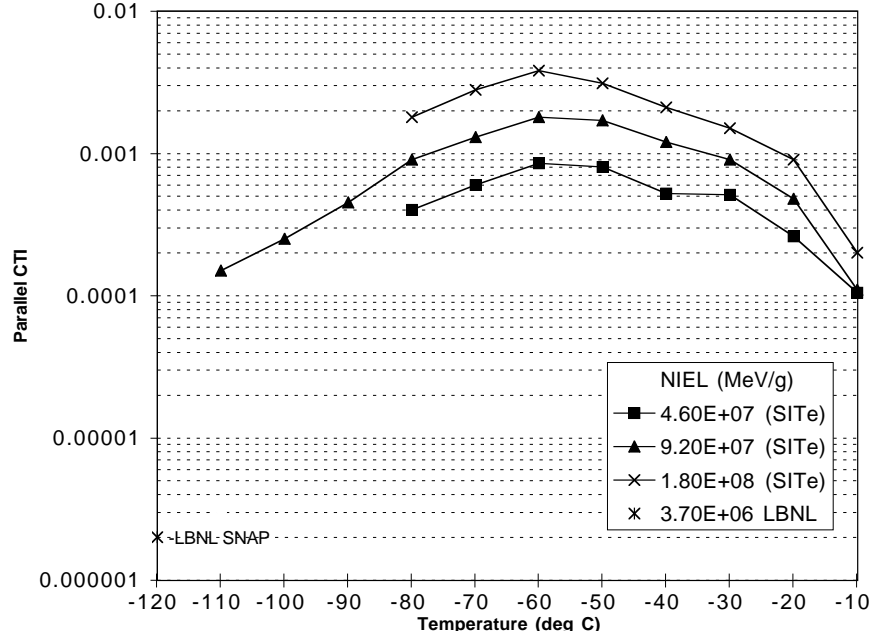


Figure B.7: Degradation of CTE as a function of the Non-Ionizing energy loss (NIEL). The data for an irradiated SiTe 502AF CCD is compared to the limit of detection for an LBNL CCD. The LBNL CCD in this test did not have a narrow channel insert needed for improved radiation tolerance and yet already exceeds the performance of the SiTe CCD.

The Non-Ionizing energy loss (NIEL) for 55 MeV protons at $1 \times 10^9 p/cm^2$ that the CCD has been tested to is 3.7×10^6 MeV/g. For the SNAP mission, if we assume a 3 year mission during solar maximum outside the earth's geomagnetic field, the NIEL behind a nominal 1" of aluminum shielding is 1.85×10^7 MeV/g – a factor of 5 lower than what the device has been tested to. See Figure B.6 for the dependence of the non-ionizing dose (during solar max) as a function of shielding thickness. The amount of shielding required to reduce the environment to the test level is about 10" of aluminum.

If we assume the mission during solar minimum, then the current models would predict no coronal mass ejections and thus, no solar proton damage. Computing the NIEL for the cosmic ray protons for a 3 year period, it comes out to 6.7×10^5 MeV/g – much lower than what the device has been tested to. Clearly, a flight during solar minimum is best from a total radiation damage point of view.

High CTE is essential for such large area devices, and several design and process

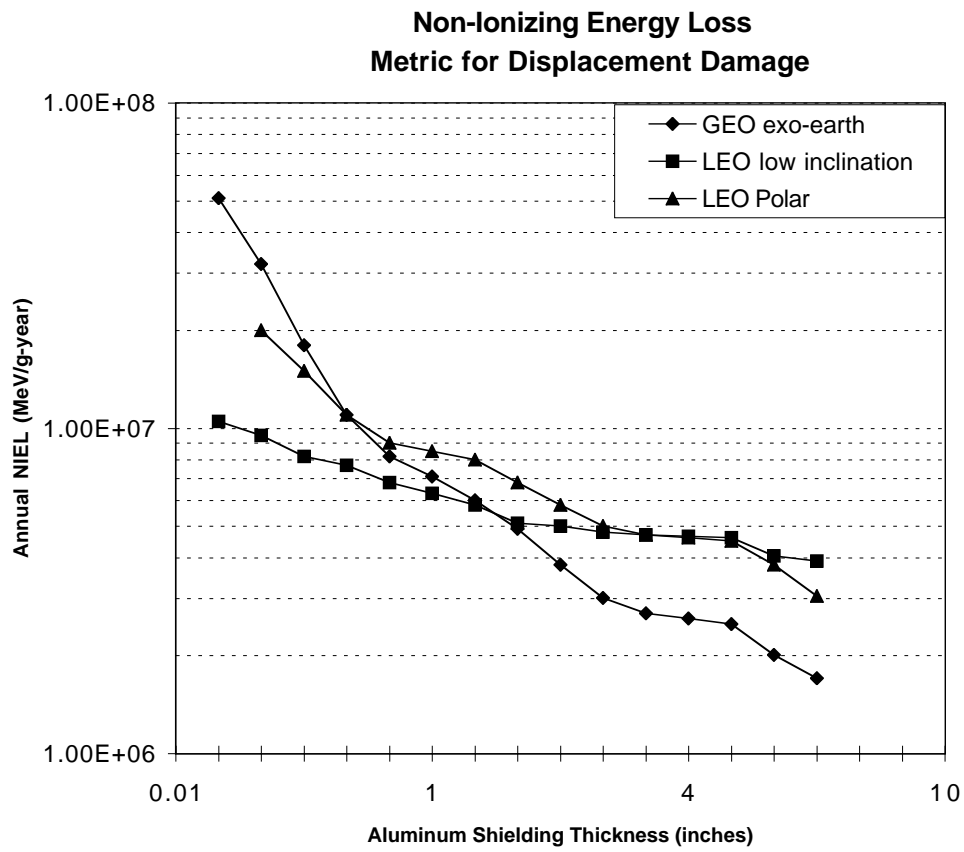


Figure B.8: Non-ionizing energy loss metric for CCD displacement damage during solar max.

techniques have been implemented in the current mask set in order to enhance CTE in a radiation environment (not present in the previous radiation tests). The channel implant region, where the charge carriers reside, is slightly offset from the channel stop region in order to avoid possible trapping sites at the channel to channel stop interface (Janesick et al., 1995). The serial register is wider than the imaging channel in order to allow for on-chip binning with large full well capacity. However, this results in a larger volume for charge trapping in the serial register. A second implant, $3\text{ }\mu\text{m}$ wide, is included in the serial register in order to improve CTE, especially for small signals (Bredthauer et al., 1991).

B.7 Cosmic Rays

Fully-depleted CCD's have an increased sensitivity to cosmic rays due to the thicker active region. So that a passing particle will leave a longer trail of particles in the detector eventually destroying any accumulated optical image. This phenomena is well known in previous and current space flights and we are current beginning to receive excellent data from Chandra on the performance of the "deep-depletion" devices especially numerical values of the cosmic ray fluence. This can be used for engineering numbers in determining our expectation for CCD's in SNAP.

Our current best estimate, summarized in Table B.2, for the worst case cosmic ray fluence in high earth orbit (assumes 0.1" aluminum shielding) is $4.4\text{ protons/cm}^2/\text{s}$ at solar min (drops to $1.5\text{ protons/cm}^2/\text{s}$ at solar max). This flux of protons, shown in Figure B.7, peaks around 300 MeV and is consequently difficult to shield further.

Solar Condition	Al Shielding	Integrated Flux/ cm^2/s
Maximum	None	1.7
Maximum	100 mil	1.6
Maximum	1 inch	1.5
Minimum	None	4.7
Minimum	100 mil	4.4
Minimum	1 inch	4.2

Table B.2: Prometheus Orbit Cosmic Ray Hit Rate

With a typical 45 pixels/particle contaminated by the passage of the ionizing trail in a CCD with $10.5\text{ }\mu\text{m}$ pixels, then 10% of the image will be contaminated after a 500 second exposure. This calculation is consistent with the assumptions used for NGST. This level of contamination is acceptable and we assume that multiple images of the same region of space must be taken in order to obtain a single "clean" image. The methods for removing cosmic ray signatures from images are well known.

B.8 Packaging with 4-side Abutment

For a normal thinned CCD, pad contacts are etched through the wafer and are available at the back surface. The packaging normally includes a circuit board which substantially extends the dimensions on any CCD edge with pads. External wiring is attached

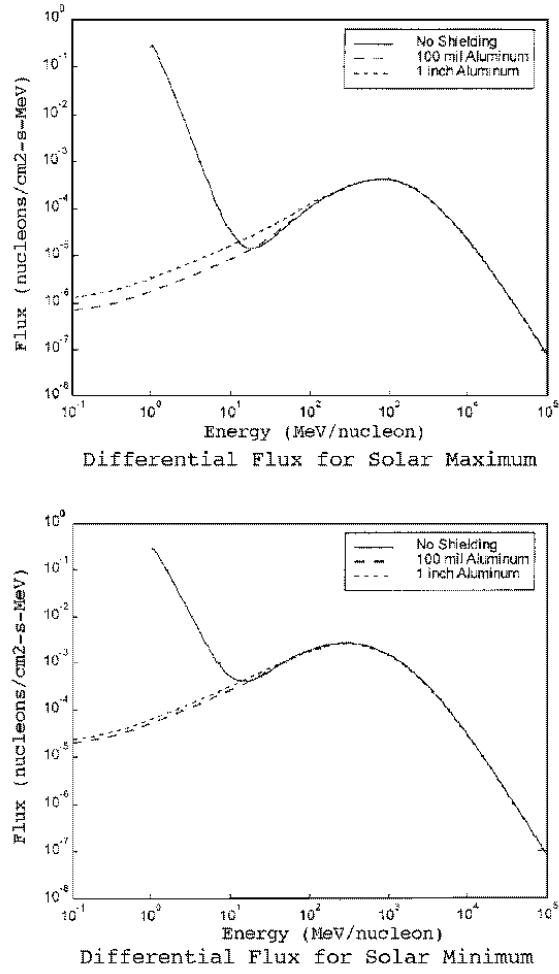


Figure B.9: Differential proton flux in high earth orbit for solar maximum and solar minimum for different shielding thicknesses calculated using CREME96.

to this board, as are the wire-bond connections to the CCD. Thus if a CCD mosaic is extended in the direction of any pad-containing edge, close abutment along this direction is impossible and the wiring obstructs light. These problems are normally dealt with by (a) making the connections on only two of the four sides and achieving two-side abutment; (b) using rectangular 3-side abutable CCD's with all the connection pads on the narrow end, so that the array is two CCD lengths wide and four or more wide; or (c) allowing wide gaps between the CCD's, as is done in the Sloan Digital Survey mosaic.

For our thick, totally-depleted CCD's, back surface access to the pads is out of the question. In a packaging scheme under consideration, the edges cantilever from a 3-layer aluminum oxide structure. The first is a thin insulating layer cemented to the front of the CCD. The second is a ceramic circuit board with edge pads to which the CCD pads are wire-bonded. The traces go to a center miniature connector through which wiring is brought out perpendicular to the CCD package and through the cold plate. The third layer is an additional insulator which also captures three indexing pins. Screw-on extensions facilitate installation and removal without hitting adjacent CCD's. Four-side abutability and a certain amount of assembly jiggling is therefore automatic. This scheme is shown in Fig. B.10.

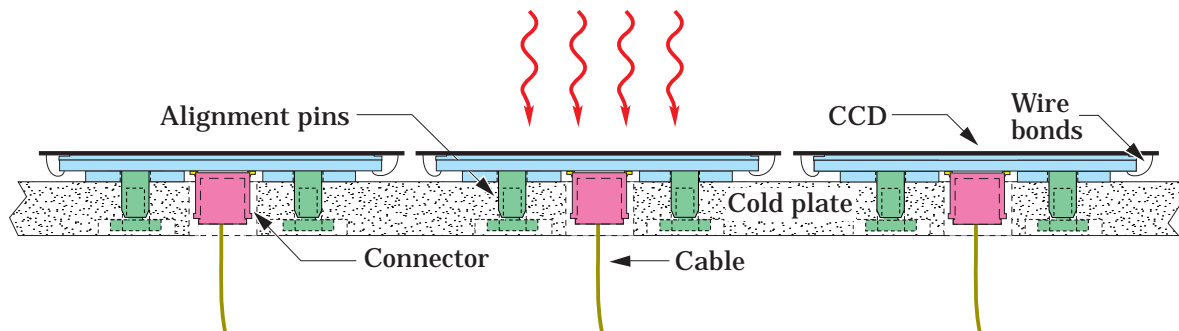


Figure B.10: Conceptual design for “fully-depleted” CCD packaging. The CCD is cemented to a three-layer aluminum oxide substrate. The middle layer is a circuit board to which the cantilevered CCD pads are wire-bonded. Connections exit through the cold plate via a miniature connector in the center of the board. The third layer provides insulation and captures three indexing and mounting pins